NOVEL METHODS OF TRANSDUCTION FOR ACTIVE CONTROL OF HARMONIC SOUND RADIATED BY VIBRATING SURFACES

KYM A. BURGEMEISTER

Department of Mechanical Engineering

University of Adelaide

South Australia 5005

NOVEL METHODS OF TRANSDUCTION FOR ACTIVE CONTROL OF HARMONIC SOUND RADIATED BY VIBRATING SURFACES

CONTENTS

Contents

Contents

Contents

Contents

NOVEL METHODS OF TRANSDUCTION FOR ACTIVE CONTROL OF HARMONIC SOUND RADIATED BY VIBRATING SURFACES

ABSTRACT

Large electric transformers such as those used in high voltage substations radiate an annoying low frequency hum into nearby communities. Attempts have been made to actively control the noise by placing a large number of loudspeakers as control sources around noisy transformers to cancel the hum. These cancellation systems require a large number of loudspeakers to be successful due to the imposing size of the transformer structures. Thus such systems are very expensive if global noise reduction is to be achieved.

The aim of this thesis is to investigate theoretically and experimentally the use of thin perforated panels closely placed to a heavy structure (eg. a transformer) to reduce the radiation of unwanted harmonic noise. These panels can themselves be vibrated to form a control source radiating over a large surface surrounding the primary source. The problem of the equipment overheating inside the enclosure is alleviated because the holes in the panels still allow natural cooling.

An initial study is carried out to determine the resonance frequencies of perforated panels. The use of previously determined "effective" elastic properties of the panels and Finite Element

Abstract

Analysis to theoretically calculate their resonance frequencies is examined.

Secondly the attenuation provided by active noise control using perforated panels as control sources is explored by use of a coupled analysis, where the primary source is assumed to influence the radiation of the perforated control panel. This analysis was found to predict poorly the amount of attenuation that could be achieved, so an uncoupled analysis is undertaken, where both the primary and control sources are assumed to radiate independently of each other. Not only does this greatly simplify the theoretical analysis but it also enables prediction of attenuation levels which are comparable to those determined experimentally. The theoretical model is reformulated to enable comparison of the sound power attenuation provided by perforated panel control sources with that of traditional acoustic and structural control sources.

Finally, the use of modal filtering of traditional acoustic error sensor signals to give transformed mode (or "power mode") sensors is examined. The independently radiating acoustic transformed modes of the panel are determined by an eigenanalysis and a theoretical analysis is presented for a farfield acoustic power sensor system to provide a direct measurement of the total radiated acoustic power. The frequency dependence of the sensor system, and the amount of global sound power attenuation that can be achieved is examined. Experimental measurements are made to verify the theoretical model and show that a sound power sensor implemented with acoustic sensors can be used in a practical active noise control system to increase the amount of attenuation that can be achieved. Alternatively the sound power sensor can be used to reduce the number of error channels required by a control system to obtain a given level of attenuation when

Abstract

compared to traditional error criteria. The power mode sensor analysis is then applied to the

perforated panel control system, with similar results.

STATEMENT OF ORIGINALITY

To the best of my knowledge and belief all of the material presented in this thesis, except where otherwise referenced, is my own original work, and has not been presented previously for the award of any other degree or diploma in any University. If accepted for the award of the degree of Doctor of Philosophy, I consent that this thesis be made available for loan and photocopying.

Kym A. Burgemeister

ACKNOWLEDGMENTS

Chapter 1

INTRODUCTION AND LITERATURE REVIEW

1.1 INTRODUCTION

In this thesis, two novel methods of transduction are examined for use in active noise control systems for reducing sound radiated by heavy structures. The first is a control source; a perforated panel, which has been chosen for study because of possible application to control of harmonic noise radiated by large heavy structures (such as electric transformer tanks) where direct vibration control of the sound radiating surface is difficult. The second transducer system investigated is modal filtering of vibration and in particular, the use of traditional acoustic error sensor signals to provide transformed mode (or "power mode") sensors. The minimisation of the signals from these sensors results in direct minimisation of the total radiated acoustic power. This type of error sensor is examined for the case of radiation from a single simply supported rectangular panel controlled directly by vibration actuators on its surface and finally applied to radiation from the perforated panel control source.

As a precursor to examining perforated panels as control sources, a study of their simply supported modal response is undertaken in Chapter 2. Parameters defining the geometry of the holes in a perforation array are introduced, as well as the ratio of the modal resonance frequencies of a perforate to those of a corresponding solid panel, termed the *effective resonance frequency*.

Two theoretical analyses, a Finite Element analysis (F.E.A) and an experimental study are compared, where applicable, for thirteen perforates to determine the most accurate method for calculating the effective resonance frequency. A cubic function is derived to fit the F.E. analysis results, and so provide a convenient way of determining the effective resonance frequency of panels with a wide range of perforation geometries. This is a prerequisite for the following work, as an estimate of the resonance frequencies is necessary for calculation of both the on and off resonance sound radiation characteristics of perforated panels.
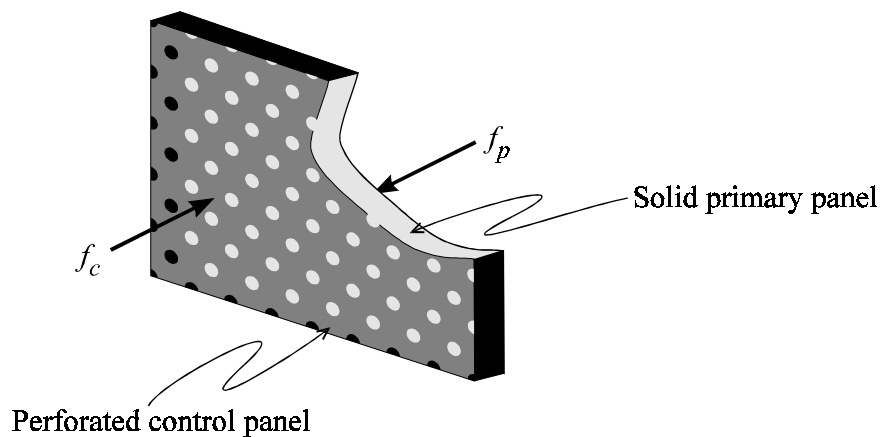
Figure 1.1   Control source arrangement; a perforated control panel closely mounted in front of a solid radiating source.

A coupled analysis of a simply supported rectangular perforated control panel vibrating in front of a solid primary radiating panel is performed in Chapter 3. A previous analysis for a simple, single hole - single mode system is extended to account for multiple holes in a perforation array and many modes of vibration. The air in the holes of the perforate is modelled as an array of air pistons individually coupled, together with the vibration response of the perforated control panel, to the vibration of the primary panel via the acoustic pressure in the air cavity between them. The total farfield acoustic pressure is calculated by adding the sum of the farfield contribution of all

of the individual air pistons to the farfield response from the solid part of the perforated control panel. An optimum control force is calculated using traditional quadratic optimisation theory to minimise the acoustic pressure at a single error sensor in the farfield. The theoretical analysis is computationally cumbersome due to the coupling between the panels and experimental validation of the model fails to attain the very high levels of sound attenuation that are predicted. The reasons for this overprediction and methods to simplify the model are suggested.

These simplifications are applied in Chapter 4, where an uncoupled analysis of the panel system is considered. Both the solid primary panel and the perforated control panel are assumed to radiate independently of each other, greatly simplifying the theoretical analysis. This analysis has been generalised to allow for any number of primary point forces, control point forces and error sensors in the farfield. Quadratic optimisation is again used to determine the optimum control point forces to minimise the sum of the mean square pressures at the error sensors. The problem is reformulated so that the error criterion to be minimised is the total acoustic power output in the farfield of the panel system.

Experimental verification of the uncoupled analysis is given for two perforated panels, the first only lightly perforated with a small open area and the second with many perforations and a relatively large open area.

The uncoupled analysis is used to compare the control force magnitude required to provide reasonable attenuation using the perforated control panel with the control force required for

active structural acoustic control (ASAC) of the panel. The effect of the perforation density (in particular, the open area) on the achievable attenuation is examined. Finally a comparison is made between the attenuation provided by minimising the sum of the mean square pressures and minimising the system acoustic power.

Practical methods for measuring the total system acoustic power radiated by a single simply supported solid panel are discussed in Chapter 5. The independently radiating acoustic "power modes" of the panel are determined by an eigenanalysis and a theoretical analysis is presented for a farfield *acoustic* power sensor system (using microphones) to provide a direct measurement of the total acoustic power radiated. The frequency dependence of the sensor system, and the amount of global sound power attenuation is examined. Finally the acoustic power mode sensor analysis is applied to the perforated panel control system.

1.2   RELEVANCE AND MOTIVATION

Active control of noise radiated by heavy structures (such as electrical transformers) with acoustic control sources has been attempted by a number of researchers (Leitch and Tokhi, 1987; Yannucci, 1979; Hesselmann, 1978; Berge *et al.*, 1987/88; Angevine, 1981/90/91/92/94). However global noise reduction (Hesselmann, 1978; Angevine, 1991/92; Craig and Angevine, 1993) has only been achieved when the structure has been surrounded by a large number of acoustic sources or by a complex multipole source (Bolton *et al.*, 1995). In other work, (Berge *et al.*, 1988) where only one or a few loudspeakers were used, noise levels were reduced at some locations at the expense of increased levels at other locations, with no demonstrated overall reduction in radiated sound power. The reason that many acoustic sources are needed to achieve global sound reduction lies in the physical mechanisms responsible for the active control of sound radiation using acoustic sources. To achieve global noise control, it is necessary to acoustically "unload" the radiating structure by changing the radiation impedance it "sees". Clearly, when using acoustic control sources, this can only be done for a large heavy structure by using enough sources to completely surround the structure and have a total area of the same order of magnitude as the radiating surfaces of the structure.

As it is often inconvenient or impractical to use a large number of acoustic control sources surrounding the structure, vibration actuators can be used to modify the structural vibration and hence its sound radiation. Although this technique has been used in the past by a number of researchers to control sound radiation from thin structures (Snyder and Hansen, 1990; Meirovitch and Thangjitham, 1990) and sound transmission through thin structures (Fuller and Jones, 1987;

Eatwell, 1989; Thomas *et al.*, 1993*a*), the control of vibration of heavy structures with a large internal impedance is much more difficult because of the large forces required and requires a correspondingly large number of control sources (McLoughlin *et al.*, 1994). It is generally inconvenient and expensive to enclose electrical transformers completely, because of the requirement to provide a cooling system to dissipate the heat generated by the transformer. However, an alternative is to enclose the radiating structure in a lightweight enclosure made of perforated sheet metal to which vibration actuators are attached. The holes in the sheet metal still allow cooling by natural convection. This type of control arrangement has not been examined elsewhere and is considered in the first section of this thesis.

The performance of any control transducer used for active noise or vibration control will depend greatly upon the accuracy of the control signal and the error criterion to be minimised. The accuracy of the control signal is generally bound by the mathematical precision of the signal processing electronics that make up the control system; however the type and method of measurement of the error criterion is the choice of the system designer. For active noise control a microphone (Conover, 1956; Angevine, 1981; Berge *et al.*, 1988; Pan *et al.*, 1992*b*; Baumann and Greiner, 1992) or an array of microphones (Silcox *et al.*, 1987/89/90; Simpson *et al.*, 1989/91; Zander and Hansen, 1993) has traditionally served as an acoustic error sensor system. These have been used in the simplest case to measure (as an error criterion) the acoustic pressure at the sensor location (Fuller *et al.*, 1991*a/b*; David and Elliott, 1994). More complicated error criteria, such as transmitted power have been measured in the case of active vibration control of a beam (J. Pan and Hansen, 1990) and a plate (Tanaka *et al.*, 1992; X. Pan and Hansen, 1995).

For active noise control in ducts and enclosures, error criteria such as energy density (Bullmore *et al.*, 1986; Nashif and Sommerfeldt, 1992; Sommerfeldt and Nashif, 1994; Sommerfeldt and Parkins, 1994; Sommerfeldt *et al.*, 1995) or acoustic potential energy (Tohyama and Suzuki, 1987; Curtis *et al.*, 1987; Thomas *et al.*, 1993*b*; Zander, 1994) have been used. For controlling structural radiation into semi-infinite space employing ASAC, measurement of various error criteria has been attempted using structural sensors (Clark and Fuller, 1991/92; Rex and Elliott, 1992; Naghshineh and Koopmann, 1993; Naghshineh *et al.*, 1995; Charette *et al.*, 1995; Snyder and Tanaka, 1993*b*; Snyder *et al.*, 1995*b*). Although these sensors can be applied to a single radiating source with ASAC, they are not suitable when a second acoustic control source (such as a loudspeaker or the perforated panel discussed above) is introduced, as they are no longer able to measure the total power output of the system. In the second section of this thesis (from Chapter 5), transformed modal radiation from a panel is examined in a new way, using the decomposition of the acoustic field rather than the structural vibration field as a measure of the efficiently radiating modes and hence the power radiated from the panel - control source system.

1.3   LITERATURE REVIEW

1.3.1   HISTORICAL OVERVIEW OF ACTIVE CONTROL

The origins of active noise control are attributed to the German inventor and physician Paul Lueg (Guicking, 1990), whose U.S. patent was filed in 1932. However the concepts it detailed were impossible to implement with the technology available at that time. Olson (1953, 1956) resurrected the idea and proposed its use in enclosures, ducts and active headsets, but the electronics technology was still insufficiently advanced to take his laboratory tests and turn them into a practical reality. At around the same time, Conover (1956) applied an active noise control system to a large 15MVA transformer using loudspeakers arranged around the tank, but achieved only local control at the error microphone located over 30m away. His system was non-adaptive and relied on an operator to continually adjust the noise cancelling signal.

After another two decades of disinterest, the advent of digital electronics in the early 1980's (and its rapid advances thereafter) prompted a resurgence in attempts at active noise control, with relatively simple control systems in ducts (Chaplin, 1980; La Fontaine and Shepherd, 1983) and then more difficult applications such as transformers (see Section 1.3.2) and aircraft fuselages (Fuller and Jones, 1987; Silcox *et al.*, 1987; Simpson *et al.*, 1989).

1.3.2   NOISE CONTROL OF ELECTRIC TRANSFORMERS

Electric transformers, particularly those used in large electric substations - which can have capacities of the order of 25-750 MVA, have long been identified as important contributors to environmental noise. With recent trends in housing development necessitating dwellings being

much closer to substations, electricity utilities have identified the noise produced by transformers as a great concern, particularly considering the tightening of Acts concerning environmental noise (for example the German Noise Nuisance Act (1979)).

Schuller (1982) identifies the magnetostrictive forces within the laminated core of the transformers as the well accepted source of noise. It is suggested that the manufacturers of the transformers are making continual improvement to their products through use of innovative materials and construction methods, which is resulting in a reduction in noise output of their products of about 1 dB(A) each year. A large number of possible methods for reducing the noise emission from transformers are given including: vibration isolation of the core in the transformer tank; decreasing the induction used; vibration isolated covering of the tank; and double tank construction, all of which contribute to approximately 5 dB(A) reduction in far field noise levels.

The possibilities for reducing the transmission of the emitted noise rely on surrounding the transformer with a large, heavy structure - often a dedicated building or barrier. The cost of these is estimated at between $150,000AUD to $230,000AUD (Yannucci, 1979). Craig and Angevine (1993) also note that as a way of reducing complaints the utility may need to buy the complainant's property.

Yannucci (1979), in his report to the United States Department of Energy - Environmental Control Technology Division, studied the feasibility of an active noise control (ANC) system to reduce the transmission of noise from electrical transformers. He estimated that United States

electrical utilities at that time spent over $100US Million each year in transformer noise abatement. A cost analysis by Yannucci put the cost of active control systems for transformers at about half that of conventional methods. His work also reports transformer noise levels as low as 36dB(A) causing complaints. Yannucci's experiments on a two dimensional transformer model produced over 20dB of noise reduction in narrow angular locations, which he claimed to be sufficient to considerably reduce the number of complaints. This was achieved using a primitive feedback-only control system, with no adaptive component. Further, Yannucci stated that "the amplitude and phase adjustments of the control system may be predetermined before applying the system to a full-scale transformer". Clearly with environmental conditions being so critical to the performance of active control systems this could not be the case.

The current methods of measurement and prediction of transformer noise by major Canadian utilities were discussed by Gosselin *et al.* (1992/93), Laroche *et al.* (1992), Sakuta *et al.* (1992), Kowalewski *et al.* (1992) and Savard (1992), and by U.S. utilities in work by Craig and Angevine (1993) and Angevine (1994). It is established that transformer noise is a cause of community complaint, and acceptable noise level criteria are discussed. They of course identified the fundamental frequency at twice the power supply frequency, and its harmonics, as comprising the main spectral content of transformer noise. A new IEEE test code for transformer noise evaluation is reviewed positively by Teplitzky (1995).

One of the earliest researchers in active noise control, Conover (1956), saw its potential application to the control of electric transformer noise, and carried out field trials to test its

effectiveness. He placed a loudspeaker near a 15 MVA transformer and adjusted the phase and amplitude of a 120Hz, 240Hz and 360Hz combined tone to produce attenuation of the transformer's noise. He achieved over 15dB reduction in narrow regions away from the transformer which he called "Beams of Silence", but recognised the limitations of the system in achieving global noise control. Conover also recognised the need for an adaptive controller to account for the 'drift' in achievable control caused by changes in ambient conditions.

Ross (1978) took a purely experimental approach to the control of transformer noise, in an attempt to assess its practicality. Using only a single loudspeaker and a crude electronic control system to control the noise from two transformers, Ross achieved at least 10dB reduction in a nearby office space where a disturbance was reported. A local noise level reduction of 28dB was attained and it was stated that better control could be achieved by using more control sources. Unfortunately the noise control system also increased levels in other areas. Hesselmann (1978) also carried out experimental work on a single 100kVA transformer approximately 1.2m wide and 0.8m high using two control sources which when coupled with the dipole-like radiation of the transformer itself created a longitudinal quadrupole radiator, to reduce the efficiency of the transformer noise radiation. Large noise reductions were achieved, though the small physical size of the transformer made it easier than could be expected using a larger substation transformer.

In further field measurements conducted by Berge *et al.* (1987,1988) on 20MVA transformers, only very narrow cancelling zones were achieved, again attributed to the random fluctuations in

environmental conditions and the large physical size of the transformer relative to the control sound sources.

A concentrated effort has been made by Angevine (1981/90/91/92/94) to actively control transformer hum. Angevine implemented an array containing as many as 26 tripole control sources arranged around a model transformer, and using the "suck and see" method to adjust the system achieved a reasonable global attenuation of between 10 and 20dB at a single frequency. Tests were not performed with multiple frequencies that could be expected to be present from an actual transformer, and little theoretical treatment of the system was presented. Recent work by Craig and Angevine (1993) on actual substation transformers controlling the first four harmonically related tones has produced better results, however attenuation has still only been limited to angles of 30 to 60 degrees away from the transformer because of the limited number of control sources that were implemented.

Cheuk *et al.* (1994) also used a large number of loudspeakers (8) surrounding an already passively controlled 66KV transformer. Both the control sources and a single error sensor were placed inside the transformer enclosure, with the resulting external sound pressure measured at a single point close to the front of the enclosure. The work demonstrated up to 20dB attenuation at 100Hz at the measurement position, with no demonstrated global or farfield reduction.

The most recent variation of the loudspeaker control source concept was by Sugiki *et al.* (1995), who put them in ducts terminating at the top edge of a conventional passive acoustic barrier, in

an attempt to improve the overall control attenuation that they provide. Experimental work carried out in an anechoic chamber with an single point source as the primary source achieved large levels of control (15dB) in localised areas, close to the barrier with no demonstrated control on a global basis.

The first departure from traditional acoustic control sources to ASAC of a transformer is that reported by McLoughlin *et al.* (1994). Thirty two piezoceramic control actuators were located directly on the transformer tank (a comparatively large number of sources), and 64 closely spaced microphones used as error sensors. Though not reported in this work, it has been suggested that this system may also have used tuned radiators placed close to the surface of the transformer. A global tonal noise reduction of 10-15dB was demonstrated in the farfield, but the expense and large size of the control system for such a small transformer make application of this control solution unattractive.

It is apparent from this body of work that traditional acoustic sources (loudspeakers) are difficult to apply to large structures, such as transformers, due to the large number required to be effective. ASAC has only been attempted once, with surprising effectiveness, though the dimensionality of the electronic controller was large. The control methodology outlined in this thesis aims to fill the gap between traditional acoustic sources and application of ASAC.

1.3.3   THE EFFECT OF PERFORATIONS ON MATERIAL PROPERTIES

With the construction of many large nuclear power plants in the late 1950s came the need for accurate stress analysis of the stress-bearing perforated panels (tubesheets) used to support the tubes in the heat exchangers in both the boiler and condenser (Horvay, 1952; O'Donnell and Langer, 1962; Duncan and Upfold, 1963; Soler and Hill, 1977) or the reactor core itself (Bailey and Hicks, 1960). The most convenient way, adopted by most of the authors, is to calculate "effective" material properties for an "equivalent" solid panel. In this way the effective properties of Young's Modulus (E^*), Poisson's ratio (v^*) and density (ρ^*) can be used simply in standard procedures to design the panels required for the load application. Two types of penetration pattern are generally considered because of the application to heat exchanger design. These are the diagonal (sometimes called triangular) and rectangular arrays as shown in Figure 1.2. These regular arrays are characterised by their ligament efficiency, η, which is defined as $\eta = l/p$.
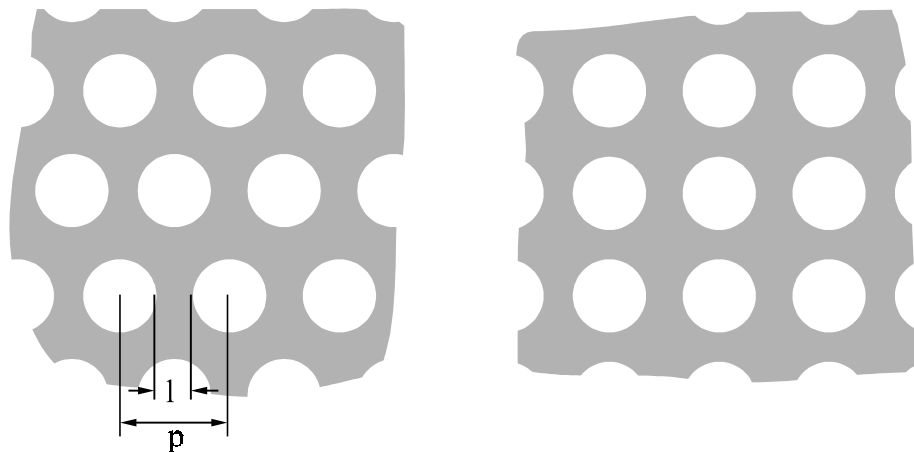
Figure 1.2   Diagonal and Rectangular array geometries.

Bailey and Hicks (1960) presented a detailed theoretical stress analysis of circular holes in both regular diagonal and rectangular arrays, which was supported not only by their own experimental work, but also the subsequent work of Duncan and Upfold (1963), where it was shown to be in much better agreement with experimental results than the earlier work by Horvay (1952).

Other work (O'Donnell and Langer, 1962) noted the inaccuracies of Horvay's theoretical formulation of effective elastic constants, and instead relied solely on experimental results (Sampson, 1960) to provide a basis for perforated panel design practice. Further work (O'Donnell, 1973) provided experimental results from a limited number of perforated aluminium samples, and investigated the effect of the panel thickness on the effective material properties. This was favourably compared to the theoretical analysis of very thin panels conducted by Meijers (1967).

In an attempt to simplify what had become a very complicated stress analysis problem, Soler and Hill (1977) defined the deflection efficiency of a panel as the ratio of effective bending stiffness to the actual bending stiffness. A function describing deflection efficiency based on the perforation dimensions and panel thickness was obtained by curve fitting experimental results of Meijers (1967), O'Donnell (1973) and others. This work can only be used in the case where circular perforations are in a regular array.

In the most recent work (Forskitt *et al.*, 1991), a finite element analysis of a simple perforated element was used to determine the effective Young's modulus and Poisson's ratio. Results from

this work are useful because the concept of a perpendicular and parallel ligament efficiency was introduced to allow for different spacing between layers of holes in the array, and it also examined elliptical holes as a general case. The effective material properties determined by Forskitt *et al.* (1991) for the case when the perforation is circular are in close agreement with those calculated by Meijers (1967), though it will be shown in Chapter 2 that these effective material properties do not allow accurate calculation of the resonance frequencies of the perforates.

1.3.4   MODAL FILTERING

The concept of modal filtering was first introduced for vibration control by Meirovitch and Baruh (1982). An eigenanalysis was applied to the modes of vibration of a generalised structure, to determine the set of transformed modes (sometimes called *basis functions*) that contributed independently to the structural velocity distribution. A practical demonstration of controlling these transformed modes on a beam (Meirovitch and Baruh, 1985) used discretised measurements at a finite number of sensors, and compared the use of several interpolation techniques to estimate the continuous displacement. It was shown that observation and control spillover were negligible, confirming the usefulness of the modal filters. The technique was further applied theoretically to travelling waves in a string and beam (Meirovitch and Bennighof, 1986).

Studies by Borgiotti (1990) and Photiadis (1990) involved the application of modal filtering to determine the transformed modes that contributed independently to the farfield acoustic power

radiated by a structure, in particular, by application of the singular value decomposition (SVD) of the radiation transfer function matrix. An important result was that the eigenvalues corresponding to the orthonormal basis functions (ie. the transformed mode) are indicators of the radiation efficiency of the transformed mode, and as a corollary, that the majority of the acoustic power is radiated by only the first few transformed modes, thus making it possible to limit the number considered with little loss of accuracy in the calculated acoustic power. A numerical study of transformed modal surface velocity and corresponding 2-dimensional radiation patterns of a cylinder with end caps was presented (Borgiotti, 1990).

By exploiting the transformed mode shapes that exhibited poor radiation efficiency, Cunefare (1991) and Naghshineh *et al.* (1992) were able to specify the physical design of beam structures which would passively feature low acoustic power radiation.

The application of modal filters to active control was first demonstrated by minimising the modal vibration power to actively control vibration of a beam (Morgan, 1991). It was noted that the importance of modal filtering to active control would be in the reduction of the numbers of sensors, actuators and hence the controller dimensionality, due to a reduced set of important modes.

Realising that the previous work on control of sound radiation where structural velocity was minimised could actually result in an increase in radiated acoustic power, Snyder *et al.* (1993) then applied modal filtering to structural sensors to determine the transformed modes that

contributed orthogonally to the acoustic power radiated from a simply supported panel. Practically, two important steps were made: the first was the use of shaped Polyvinylidene Fluoride (PVDF) film to directly sense the *transformed modes*, without the need for other prefiltering (see Section 1.3.5); the second was the eigenvalue weighting of these shaped sensor error signals, to account for the frequency dependence of the radiation efficiency (and of the transformed modes themselves). At around the same time, Naghshineh and Koopmann (1993) theoretically studied a discretised model of a beam, demonstrating numerically the small variation of the transformed mode shapes (basis functions) as a function of frequency and their use for optimising placement of discrete sensors. As an alternative to using discrete sensors, which required this optimisation of their placement to give an accurate measure of the transformed modes, Naghshineh and Koopmann conceived that PVDF might be used to create shaped sensors to give a *distributed* measure of the transformed modes. Similarly, Elliott and Johnson (1993) theoretically studied discrete models of the so called *power radiation modes* of beam and plate structures, and identified the minimum number of discrete structural sensors and power radiation modes required to accurately estimate the sound power output.

Continuous models of the orthogonally contributing transformed modes corresponding either to structural kinetic energy or radiated acoustic power for a simply supported panel and acoustic potential energy in an enclosure were developed by Snyder and Tanaka (1993*b*). It was shown that in the case of the simply supported rectangular panel, minimisation of the structural kinetic energy is equivalent to minimising the *untransformed* structural modal velocities.

Burdisso and Fuller (1994) addressed the problem with frequency dependence of the radiation efficiency (the eigenvalues) corresponding to the transformed modes by solving for a frequency independent transformed mode shape to give the minimum of the weighted radiation efficiency over some limited design frequency range. Though less difficult to implement than the system proposed by Snyder *et al.*, it would only work optimally over the limited design frequency range. Only control of the odd-odd grouping of modes was attempted using a single input/single output (SISO) controller. Although significant noise reductions were obtained at resonances, there were increased sound pressure levels at other frequencies, probably as a result of the presence of higher order uncontrolled transformed modes.

The sensitivity of transformed modes (now called *acoustic modes*) to the degrees of freedom (DOF) in the acoustic model (that is, the number of elements in the beam model for a discrete approach, which is equivalent to the number of normal modes considered in a continuous model) was studied for a beam by Cunefare and Currey (1994). It was shown that the transformed modes with high radiation efficiency (large eigenvalues) converged quickly to their final shape (ie. contained their complete contributions from the normal structural modes) compared to those with low radiation efficiency for increasing model DOF. For active control, this is a good result, as it is the first few high radiation efficiency transformed modes that are subject to minimisation.

1.3.5   MODAL SENSORS

The first discrete sensor systems (Meirovitch and Baruh, 1982/85; Morgan, 1991) required some form of sensor prefiltering to give the required modal output. This prompted Lee and Moon (1990) to adopt shaped PVDF film as a *distributed modal sensor*, with no requirement for explicit modal filtering. In this and in further work (Lee *et al.*, 1991; Collins *et al.*, 1992; Charette *et al.*, 1994; Guigou *et al.*, 1994) shaped PVDF film sensors were designed and implemented on beams to detect normal structural modes, with good results. Shaped PVDF sensors have also been implemented to measure normal modal velocity of cylindrical shells (Tzou *et al.*, 1991) and more recently, to measure acoustic properties in pipes (Royston, 1995; Fuller and Brevart, 1995; Brennan *et al.*, 1995). The only real problem reported with the use of the film was the difficulty of manufacture, resulting in shorting out and subsequent loss of signal (Collins *et al.*, 1992).

Modal sensors have not been proposed exclusively constructed from PVDF film. Rex and Elliott (1992) suggested a weighting scheme to allow the use of piezoelectric cables or optical fibre sensors, yet it appears that the difficulties in implementing these outweigh any difficulties of using PVDF film, leaving them only a theoretical consideration.

Distributed PVDF film sensors were used to control sound radiation (specifically via ASAC) from a simply supported rectangular panel by Clark and Fuller (1991). Minimising the signal from a pair of PVDF strips placed on the panel so as to detect a collective of odd-odd modes of vibration was shown to provide a similar, yet slightly less optimum, result to minimising the

pressure at an array of three microphones in the farfield. Continuing this same work, Clark and Fuller (1992) applied a wave-number analysis to the controlled and uncontrolled structural mode shapes to show that modal restructuring was occurring when control was applied using microphones as the error sensors. Implementing the modal restructuring control paradigm implies that the modal amplitudes are rearranged to produce an overall vibration field with a lower radiation efficiency without explicitly reducing all of the individual modal amplitudes. However as the PVDF film sensors did not exhibit the inherent radiation efficiency weighting of the microphone error sensors, they were not facilitating this control phenomenon but instead contributed mainly to the latter form, termed modal suppression. This problem was addressed by Snyder *et al.* (1993*b*) and Clark *et al.* (1993) by considering modal filtering techniques (see Section 1.3.4) when devising the shapes of the PVDF film sensors. Instead of sensing and minimising the structural modes, the transformed modes that contribute orthogonally to some farfield error criterion were controlled.

Clark *et al.* (1993) chose to implement the transformed modal sensors on a beam, with the error criterion simply the pressure at some point in the farfield (the same error criterion traditionally measured by a microphone; hence the sensor is metaphorically referred to as a *PVDF microphone*). Although theoretical predictions of attenuation did not closely match those observed experimentally due to nearfield effects (in particular the "notch" of increased attenuation at the error sensor elevation angle), the transformed modal sensors were shown to perform much better than the previous type that only sensed and allowed minimisation of normal structural modes. A theoretical study of ASAC on a simply supported panel again showed that

the transformed modal sensors could perform the same function as microphones in the farfield, but no experimental study was conducted because a two-dimensional transformed modal sensor was not believed to be practically realisable.

Snyder *et al.* (1993*b*) also theoretically examined the case of ASAC on a simply supported panel, though in this case the transformed mode sensors considered total acoustic power radiated from the panel as the error criterion. The importance of eigenvalue weighting the transformed mode sensors and the frequency dependence of the transformed mode shapes was also examined, with a view to practical implementation of the sensors. Experimental results with an *ad hoc* implementation of the transformed mode sensors showed much better power attenuation than that achieved with the normal structural mode sensors. A more detailed examination is presented in Snyder *et al.* (1995*b*) and a practical implementation of full two-dimensional PVDF film sensors in Snyder *et al.* (1995*a*).

Johnson and Elliott (1995) investigated the minimisation of volume velocity of a panel and compared that to minimisation of radiated acoustic power. It was shown numerically that at low frequencies minimising the volume velocity would provide levels of attenuation similar to those achievable when minimising radiated acoustic power, however regions existed where minimising this criterion would greatly increase the radiated acoustic power. The trade off for this lack of generality was a simplification to the sensing system, in particular that it would only require one distributed structural sensor independent from the material properties and excitation frequency. However, work by Snyder *et al.* (1993*b*) along with subsequent investigations (Snyder *et. al.*,

1995*b*) showed that measuring the radiated acoustic power with structural sensors was almost as straightforward without the disadvantage of increases at particular frequencies.

Charette *et al.* (1995) implemented a similar two dimensional structural sensor using orthogonal PVDF film strips on a clamped panel, shaped to sense the volume displacement. As such, it too could never provide as good a result as the acoustic power sensor implemented by Snyder *et al.* (1995*a*).

The PVDF film transformed mode power sensor appears to be almost ideal as a sensor design for ASAC, sensibly measuring the acoustic power radiation directly from the vibration levels of the source. However in the rush to develop ASAC systems coupled with the belief that measuring sound power would require large numbers of acoustic sensors (Johnson and Elliott, 1995), the application of the transformed modes of vibration and the corresponding sound radiation characteristics have been overlooked in cases where ASAC cannot readily be applied. The second part of this thesis will return to examine the use of traditional discrete *acoustic* sensors and appropriate modal filtering, such that acoustic power radiation can be accurately measured by a few acoustic sensors.

Chapter 2

CALCULATING RESONANCE FREQUENCIES OF PERFORATED PANELS

2.1   INTRODUCTION

To accurately calculate the sound pressure level radiated by a simply supported panel it is necessary to be able to accurately model the resonance frequencies. For a solid panel, these can be determined by solving the panel displacement equation with appropriate edge conditions, panel density, Young's Modulus and Poisson's Ratio. For a perforated panel, an analytical solution for the resonance frequencies has not been attempted, however as discussed in Section 1.3.3 many authors have determined ratios of the so called *effective material properties* of a perforate to the actual material properties of a corresponding solid material. The aim of this chapter is to determine whether these effective material properties, in particular the effective Young's Modulus (E^*), Poisson's Ratio (ν^*) and panel density (ρ^*), can be used in the place of the actual material properties in the classical solution for resonance frequencies of a solid panel, and so determine with sufficient accuracy the resonance frequencies of a perforated material.

In this chapter, Finite Element Analysis (F.E.A.) is used to computationally model the modal response of a range of panels with varying perforation geometries. These data are fit to a cubic expression to allow calculation of resonance frequencies of panels of any perforation geometry.

Secondly the effect of perforations in the panel on the density, Young's modulus' and Poisson's ratio are examined using past experimental measurements and F.E.A. of perforate material properties, with a view to being able to determine the resonance frequencies of perforates using classical analysis of solid panels with values of these material properties modified to account for the perforations.

Data from the classical analysis with effective material properties and F.E. analysis are compared to an experimental modal analysis of two simply supported perforated panels.

Few panel geometries fall into the range of applicability of all of the methods, and so it is necessary to estimate the accuracy of the cubic function model based on the error between the cubic function, the ANSYS analysis and measured data for different panel geometries.

2.2   DEFINITION OF PANEL GEOMETRY PARAMETERS

As discussed in Section 1.3.3, the pitch between holes in a perforated material and the diameter of the holes, are important panel geometry parameters.   These are useful only when the perforation array is regular; that is, that the distance between holes in each direction is the same. When this is not the case, two panel geometry parameters must be used, one for each axis of the perforation array. Forskitt *et al.* (1991) introduced the concept of a perpendicular and parallel ligament efficiency, *XLE* and *YLE* respectively, to allow for different spacing between layers of holes in an array of perforations.   For a diagonal array of circular holes of diameter *d*, perpendicular pitch p_x and parallel pitch p_y, as shown in Figure 2.1, the perpendicular and parallel ligament efficiencies, *XLE* and *YLE* are defined as

$$XLE = \frac{p_x - 2d}{p_x} \tag{2.1}$$

$$YLE = \frac{p_y - 2d}{p_y} \tag{2.2}$$

It should be noted that the position of point B in Figure 2 of Forskitt *et al.* is placed incorrectly and should be located at the lower right hand corner of the rectangular element, and not in the centre as shown.
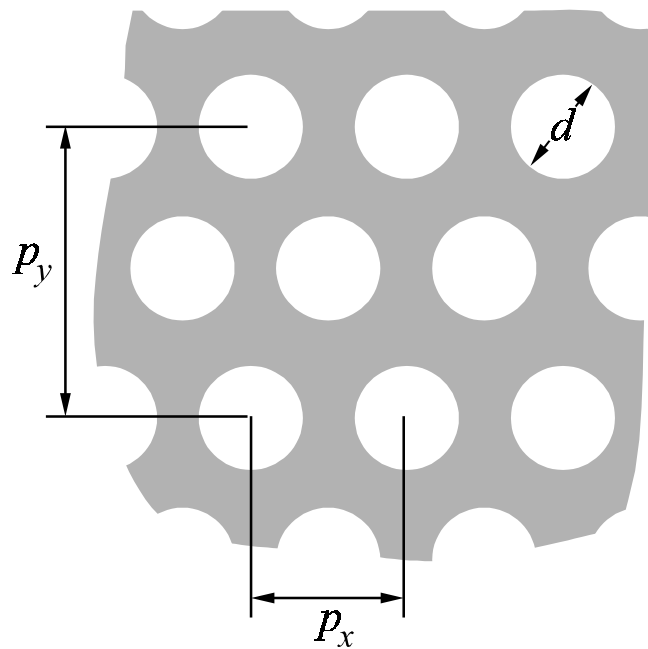
Figure 2.1   Perforated panel dimensions.

2.3   FINITE ELEMENT MODEL

A number of simply supported steel panels of dimensions L_x=0.38m by L_y=0.3m and thickness h=0.002m were modelled using 8-node shell elements in the ANSYS finite element analysis software on a DEC5000/240 workstation. Each panel was modelled as being perforated with a non-regular diagonal array of 8x5, 5x5, 8x3 and 5x3 holes. Three perforation sizes were used, d=6, 15 and 25mm, to give a range of 12 panels that were finely perforated, moderately perforated and highly perforated respectively. A further panel was considered with 5x3 holes and a perforation size of 40mm. The model used the material properties of mild steel, namely E=207GPa, ν=0.31 and ρ=7800kg m^{-1}. Figure 2.2 shows a scale diagram of the perforates, to give an indication of the density of the panels considered.

The 13 panels modelled using ANSYS were chosen so as to give panels with a spread of values of perpendicular and parallel ligament efficiencies. This spread is shown in Figure 2.3.

The Finite Element mesh density of the ANSYS models was constrained by the wavefront limit of the available software installation (500). The model parameters shown above were chosen such that a high number of perforations were considered, in an effort to ensure the homogeneity of their effect on the stiffness of the panel, while still being able to use a high enough mesh density to ensure good accuracy and convergence of the ANSYS model under the wavefront limit. Some ANSYS models, showing element shape and density for the 8x5 perforation geometry are shown in Figure 2.4. The computation was performed using the subspace iteration method for greater accuracy, and the resonance frequencies of the first 20 modes were determined.

Perforate 1
8x5 holes, 6mm diameter

Perforate 2
8x5 holes, 15mm diameter

Perforate 3
8x5 holes, 25mm diameter

Perforate 4
5x5 holes, 6mm diameter

Perforate 5
5x5 holes, 15mm diameter

Perforate 6
5x5 holes, 25mm diameter

Perforate 7
8x3 holes, 6mm diameter

Perforate 8
8x3 holes, 15mm diameter

Perforate 9
8x3 holes, 25mm diameter

Perforate 10
5x3 holes, 6mm diameter

Perforate 11
5x3 holes, 15mm diameter

Perforate 12
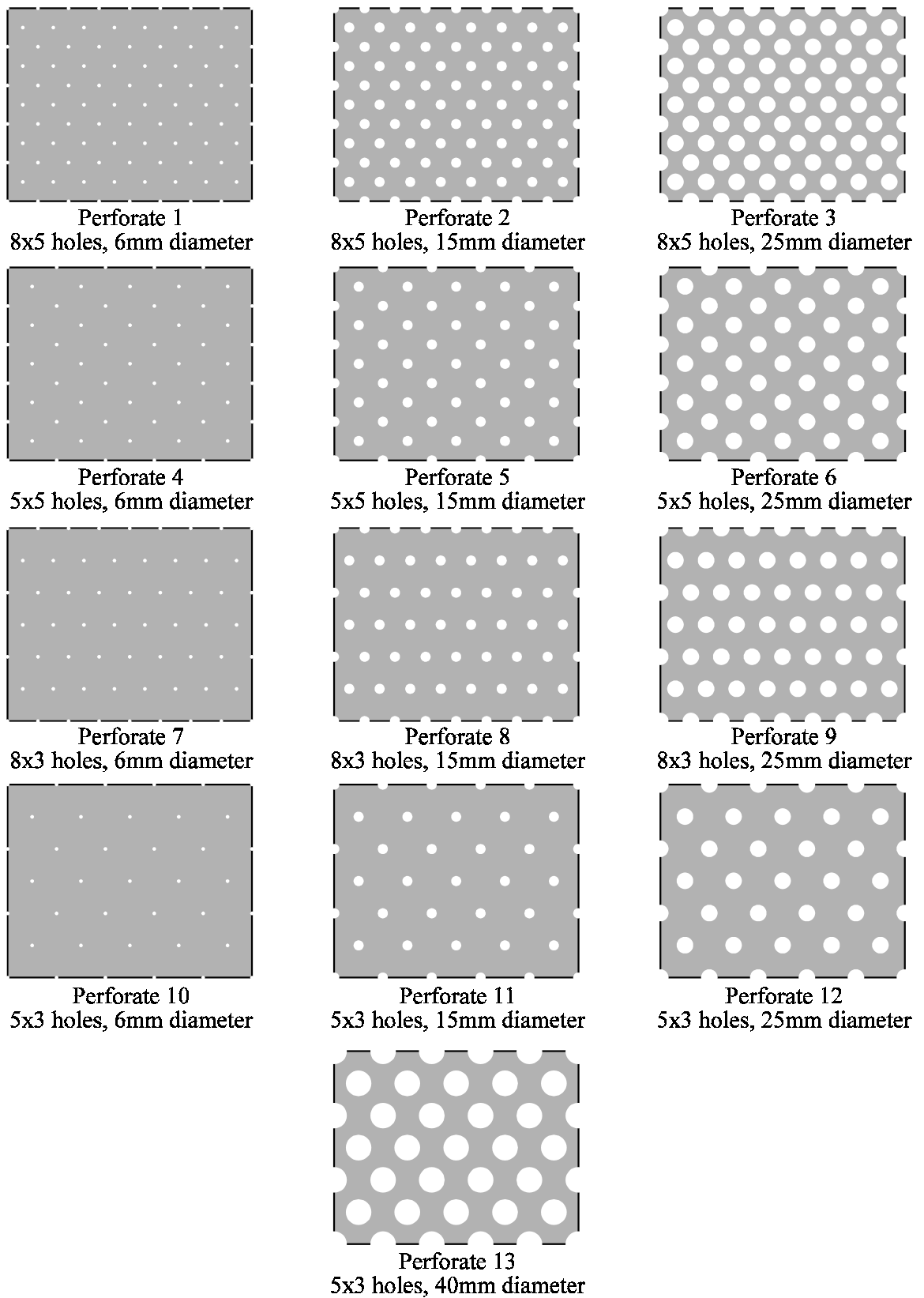5x3 holes, 25mm diameter

Perforate 13
5x3 holes, 40mm diameter
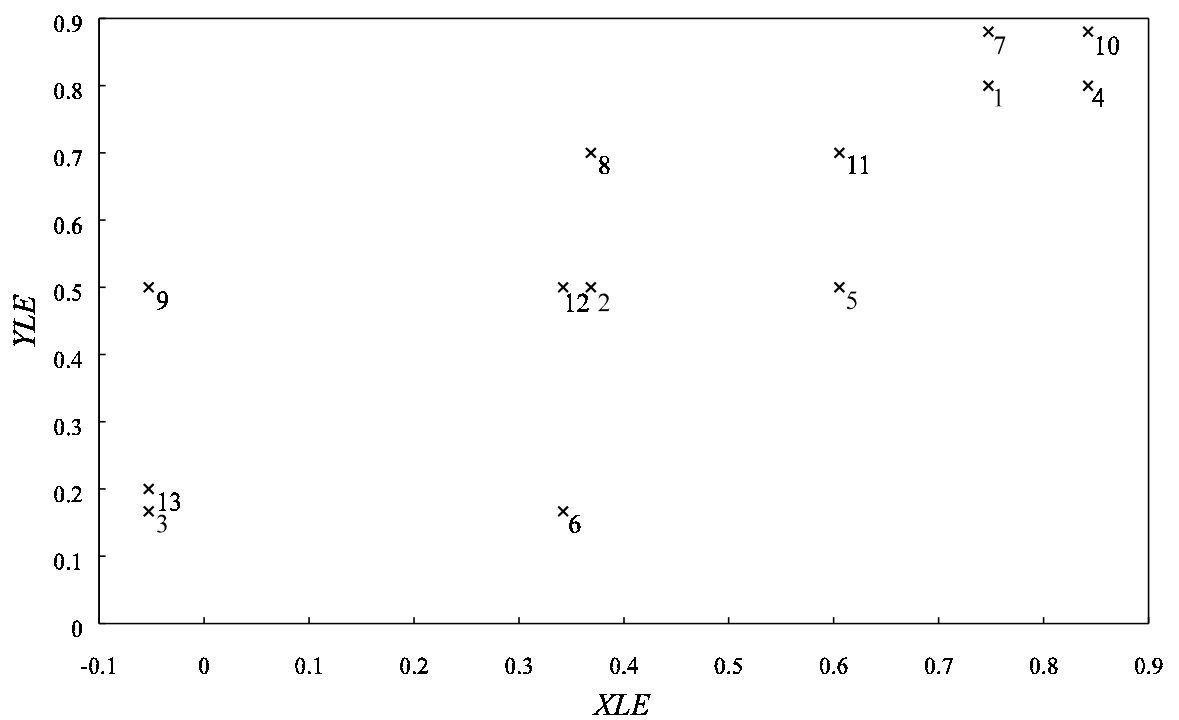
Figure 2.2   Perforated panels modelled using ANSYS.

Figure 2.3   Spread of panels over the range of ligament efficiencies, *XLE* and *YLE*.
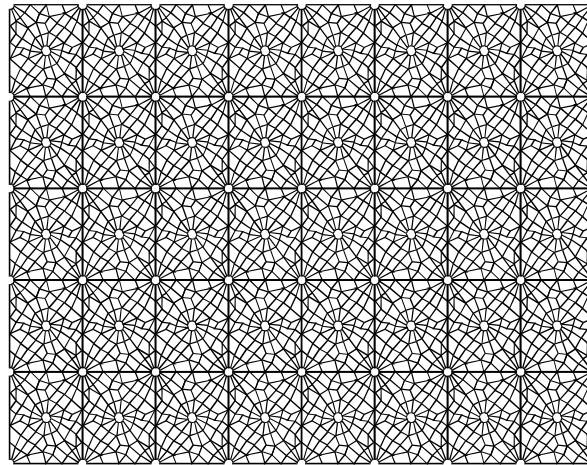
(a)
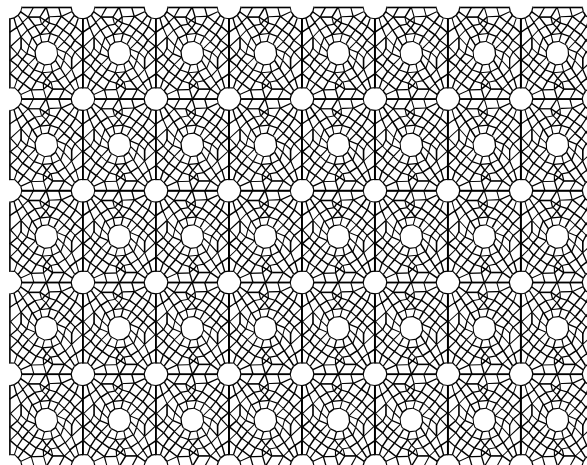
(b)
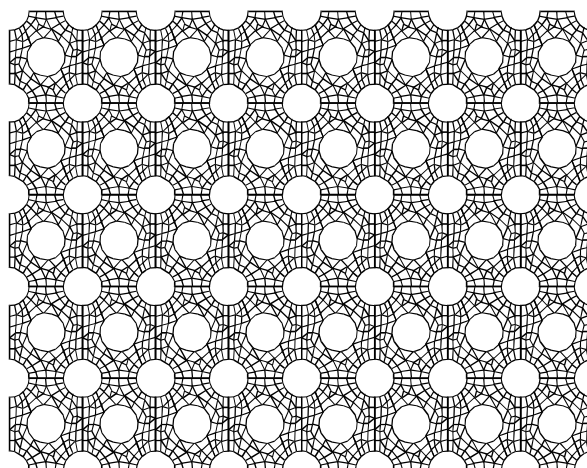
(c)

Figure 2.4   Ansys models of perforated panels with 8×5 hole geometry and holes of diameter (a) 6mm, (b) 15mm and (c) 25mm.

The individual modal resonance frequencies were compared to the modal resonance frequencies of a solid panel of the same overall dimensions to determine the effective modal resonance frequency ratio $\dfrac{f_{m,n}^{*}}{f_{m,n}}$, for each mode (m, n).

For a simply supported rectangular solid panel of dimensions L_x, L_y and thickness h the resonance frequency of the $(m,\ n)$ mode, $f_{m,n}$, is given by (Junger and Feit, 1986)

$$f_{m,n} \;=\; \frac{1}{2\pi}\left(\frac{Eh^2}{12\rho(1-\nu^2)}\right)^{1/2}\left(\left(\frac{m\pi}{L_x}\right)^2 + \left(\frac{n\pi}{L_y}\right)^2\right) \tag{2.3}$$

The form of the classical resonance frequency function suggests that the ratio $\dfrac{f_{m,n}^{*}}{f_{m,n}}$ should be independent of the mode order (m, n) for varying Young's modulus, Poisson's ratio and density, so that the individual effective modal resonance frequency ratios can be averaged over all of the modes to determine the overall resonance frequency ratio, $\dfrac{f^{*}}{f}$.

The data representing the overall resonance frequency ratio as a function of *XLE* and *YLE*, were curve fit in two dimensions using a cubic expression of the form

$$\frac{f^{*}}{f} \;=\; a\times XLE^3 + b\times XLE^2 + c\times XLE + d\times YLE^3 + e\times YLE^2 + f\times YLE + g \tag{2.4}$$

The coefficients a,b,c,d,e,f and the constant g were determined using MATLAB to solve the overdetermined system of equations for the 13 panels that were modelled. This function can be used to find the resonance frequency ratio for a large range of perforated panel geometries.

32

2.4   CLASSICAL ANALYSIS WITH EFFECTIVE MATERIAL PROPERTIES

The generality of the analysis of Forskitt *et al.* (1991) over a range of regular array geometries; that is where the ratio of ligament efficiency $\frac{XLE}{YLE} \neq 1$, makes it useful as a basis for the calculation of the effective material properties. Forskitt *et al.'s* analysis compares well with other results (Soler and Hill, 1977) when the array is regular, ie. $\frac{XLE}{YLE} \approx 1$. Although the method to determine the effective Young's modulus and Poisson's ratio can be applied to elliptical perforations in either diagonal or rectangular arrays, results are only considered here for the case of a perforated panel with a diagonal array of circular holes.

2.4.1   EFFECTIVE MATERIAL CONSTANTS AFTER FORSKITT *et al.*

Using ligament efficiencies it is possible to determine the ratio of effective Young's modulus to actual Young's modulus, *E*/E*, and the ratio of effective Poisson's ratio to actual Poisson's ratio, v^*/v for panel geometries of arbitrary *XLE* and *YLE* by interpolating in two dimensions between the data recorded by Forskitt *et al.* Further data were obtained from the authors of that paper to give a sufficient number of data points spread over a wide range of *XLE* and *YLE*.

An attempt was made to fit the data provided by Forskitt *et al.* to a polynomial function using multivariate interpolation; however, it was found that this method did not provide a suitably accurate polynomial approximation to Forskitt *et al's* data, even when fifteen terms were employed. To determine these effective material property ratios accurately, a bivariate quintic interpolation was performed on the data (Akima, 1978) for each panel's ligament efficiency by implementing the IMSL Math Library *SURF* function in FORTRAN (IMSL, 1990), the results of which are shown in Section 2.6.2 below.

According to Forskitt *et al.* the calculation of the effective density ρ^* is based on the solid area fraction of the panel, and can be expressed by a function of *XLE* and *YLE* as

$$\frac{\rho^*}{\rho} = 1 - \left(\frac{\pi}{8} (1 - XLE)(1 - YLE) \right) \tag{2.5}$$

For a simply supported rectangular perforated panel, with material properties the same as that of the solid panel it is proposed that the effective resonance frequency of the *m,n* mode will be given by

$$f_{m,n}^* = \frac{1}{2\pi} \left(\frac{E^* h^2}{12 \rho^* (1 - \nu^{*2})} \right)^{1/2} \left(\left(\frac{m\pi}{L_x} \right)^2 + \left(\frac{n\pi}{L_y} \right)^2 \right) \tag{2.6}$$

2.4.2   EFFECTIVE MATERIAL CONSTANTS AFTER SOLER AND HILL

Soler and Hill (1977) introduced a nondimensional thickness parameter ϕ, to account for the thickness of the material relative to the perforation geometry. The work expressed the effective bending stiffness ratio, D^*/D (which they referred to as the *deflection efficiency*), as a function of the thickness parameter ϕ and the perforation geometry, where the bending stiffness $D=Eh^3/12(1-\nu^2)$.

In the case of a regular diagonal array of circular perforations in a very thin panel (ie. $h<<p_x$) then $\phi = -1$ and Soler and Hill's analysis can be used. The effective resonance frequency of the *m, n* mode, $f_{m,n}^*$, can be expressed as

$$f_{m,n}^* = \frac{1}{2\pi} \left(\frac{Eh^2}{12\rho \left(1 - \frac{\pi d^2}{\sqrt{3}p_x^2}\right)(1-v^2)} \left(1 - \frac{\pi}{2\sqrt{3}}\left(1 - \frac{p_x - d}{p_x}\right)^2\right)^{\left(\frac{(2p_x - d)}{0.8 p_x}\right)} \right)^{1/2} \left(\left(\frac{m\pi}{L_x}\right)^2 + \left(\frac{n\pi}{L_y}\right)^2\right)$$

(2.7)

Results from this formulation are compared to those from Forskitt *et al.'s* analysis in Section

2.6.4.

2.5   MODAL ANALYSIS

Two perforated panels were constructed with the same overall dimensions as those modelled using ANSYS, with the exception of the thickness which was h=0.00205m. Spring steel shims were attached using set screws and epoxy resin adhesive to the edge of the panels to simulate simply supported edge conditions (Figure 2.5). The panels were securely mounted in a heavy steel frame. A Brüel and Kjær type 8202 Impact Hammer and type 2034 Dual Channel Signal Analyser were used to record frequency response data at various locations on the panels. These data were transferred to a PC running PC-MODAL analysis software (see Figure 2.6), where the resonant modes of vibration were determined and visualised, and their resonance frequencies recorded.
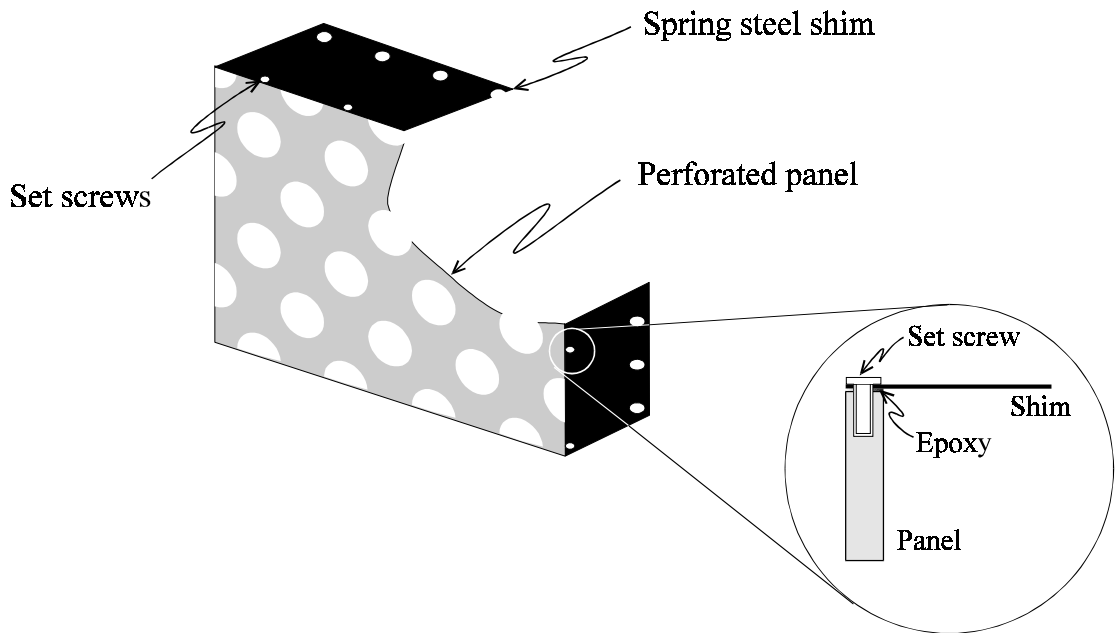
Figure 2.5   Spring steel shims secured by set screws, simulating simply supported edge conditions.
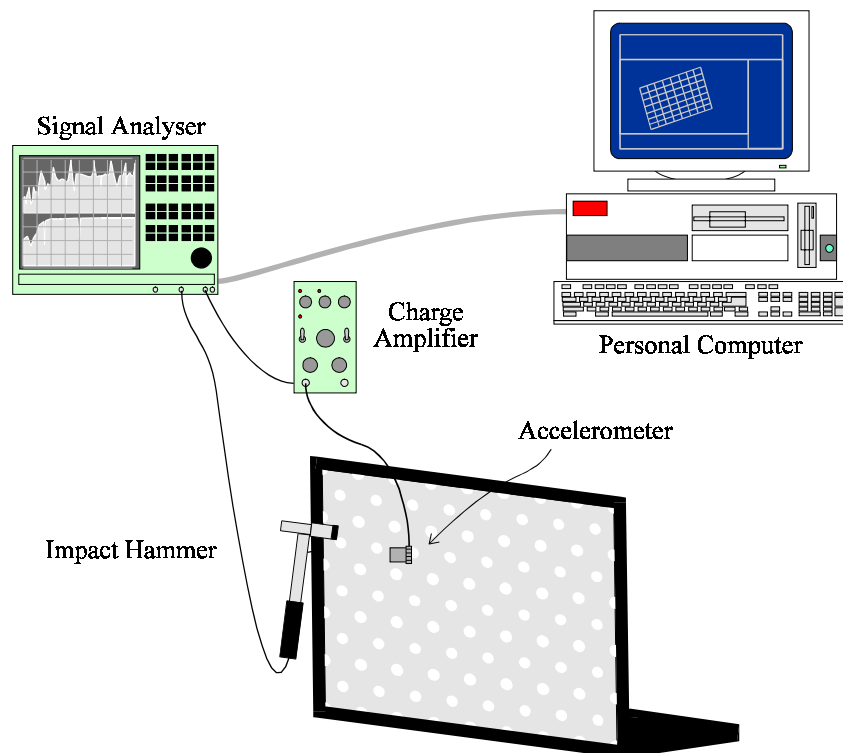
Figure 2.6   Experimental arrangement for the modal analysis of the perforates.

2.6 RESULTS AND DISCUSSION

2.6.1 FINITE ELEMENT ANALYSIS RESULTS

The first 20 modal resonance frequencies of each panel were compared to those of the corresponding solid panel, and averaged to give an overall effective frequency ratio independent of the modal indices, *m* and *n*. The effective resonance frequency value so calculated for all 13 panels modelled was used to calculate the values of the coefficients *a,b,c,d,e,f* and the constant *g* as shown in Table 2.1.

Table 2.1
Coefficients of the effective resonance frequency function, $f^*\!/f$ (Eqn. 2.4)

Coefficient	Value
a	0.0399
b	-0.0727
c	0.1161
d	-0.1295
e	0.1013
f	0.1096
g	0.8395

The function described by Equation 2.4 represents a surface, as shown in Figure 2.7, and is considered valid over a large range of $0 < XLE < 0.9$ and $0 < YLE < 0.9$. The validity of the function cannot, however, be assumed in the regions of $0.75 < XLE < 0.9$, $0 < YLE < 0.25$ and $0 < XLE < 0.25$, $0.75 < YLE < 0.9$, though panels with this physical geometry would be biased to having many holes in lines across the panel, possibly reducing the homogeneity of their effect, and would be rarely encountered in practice. The accuracy of this function is difficult to assess, and is discussed further in Section 2.6.4. It is interesting to note that this function is almost

linear, and can in fact almost be represented adequately by a plane.

2.6.2   RESULTS AFTER FORSKITT *et al.*

Data derived from the work of Forskitt *et al.* were interpolated for *XLE* and *YLE* with the region

of validity limited by the availability of that data to the range $0.1 < XLE < 0.9$, $0.1 < YLE < 0.9$.

The surfaces representing E^*/E and ν^*/ν are shown in Figures 2.8 and 2.9 respectively, and can

be seen to be generally smooth over the regions shown. The effective Young's modulus ratio is

observed to vary between 0.2 for dense arrays to 1.0, as expected for sparse arrays. There are

small regions where there is a predicted small *increase* in effective Young's modulus occurring

outside of the range of validity. The effective Poisson's ratio varies in a manner opposite to that

of the effective Young's modulus, with dense arrays experiencing an increase over that of a solid

panel. In sparsely populated arrays there is only a small change in the Poisson's ratio.

Introducing the effective density allows calculation of the effective resonance frequency ratio as

shown by the surface in Figure 2.10. It is clearly non-linear, as may be expected because it is

derived from the non-linear functions for effective Young's modulus and Poisson's ratio.

Comparing Figure 2.7 with 2.10 shows that the effective resonance frequencies determined using

ANSYS or effective material properties determined by Forskitt *et al.* will be quite different, more

so with small values of *XLE* and *YLE* (ie. larger holes in denser arrays) and where the values of

XLE and *YLE* differ from each other greatly (this will be confirmed in Section 2.6.4). The former

region is where the effective Poisson's ratio increases sharply and is greater than 1, and effective

Young's modulus is small, increasing the effect of small errors in these values. Furthermore it

is possible that the effective Young's modulus and Poisson's ratio determined by Forskitt *et al.*

for an element in tension does not correspond to the actual material properties of the plate undergoing bending.

2.6.3   MODAL ANALYSIS RESULTS

Two panels were chosen to validate the methods of calculation of the effective resonance frequency ratios outlined above. Modal resonance frequencies for panel 3 and panel 6, as determined from PC-MODAL and ANSYS are shown in Figures 2.11 and 2.12. Resonance frequencies determined by the analysis of Forskitt *et al.* are only shown in Figure 2.12 as the hole geometry of panel 3 is out of the range of the data contained therein. It can be observed that ANSYS predicts modal resonance frequencies that agree very closely (within 2%) with those determined with the experimental models. The Analysis of Forskitt *et al.*, however, does not allow accurate prediction of the resonance frequencies.
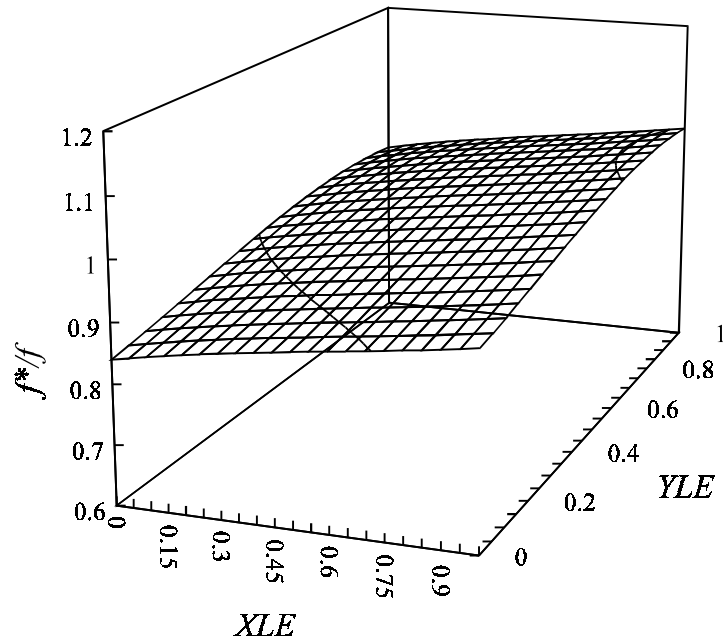
Figure 2.7   Ratio of effective resonance frequency of a perforated panel to resonance frequency of a solid determined by fitting ANSYS results (Eqn 2.4).
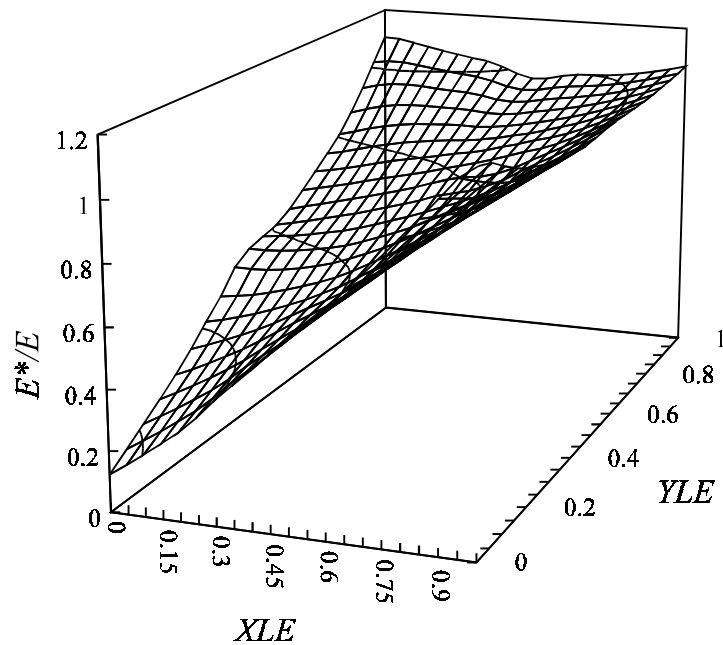
Figure 2.8   Ratio of effective Young's modulus of a perforated panel to actual Young's modulus of a solid panel. (from Forskitt *et al.* data)
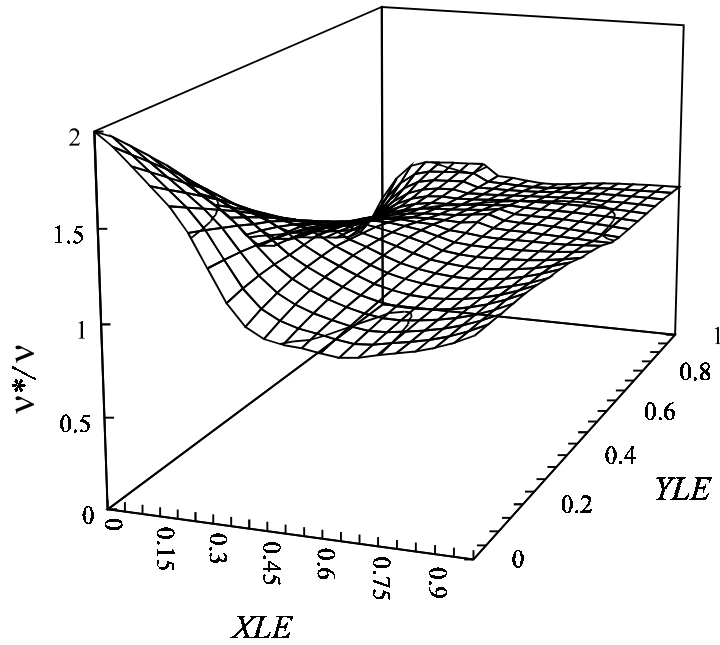
Figure 2.9   Ratio of effective Poisson's ratio of a perforated panel to actual Poisson's ratio of a solid panel. (from Forskitt *et al.* data)
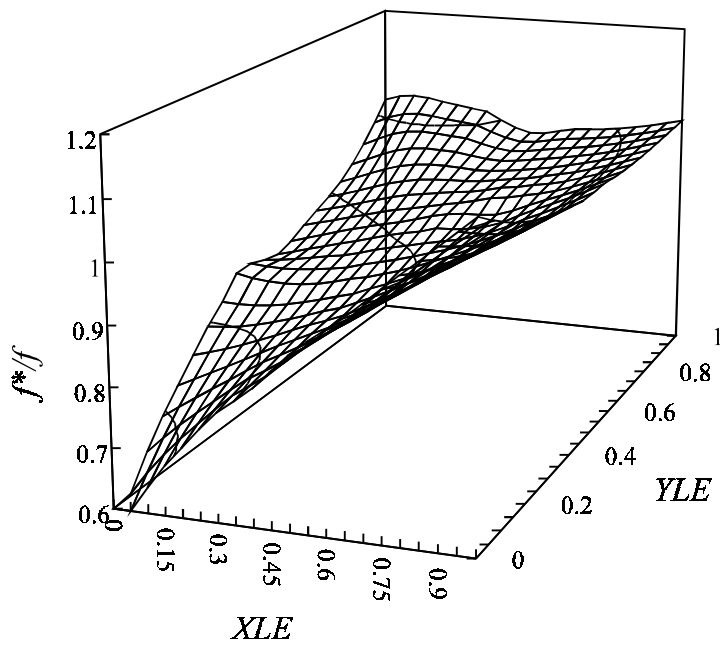
Figure 2.10   Ratio of effective resonance frequencies of a perforate to actual resonances of a solid panel. (from Forskitt *et al.* data)
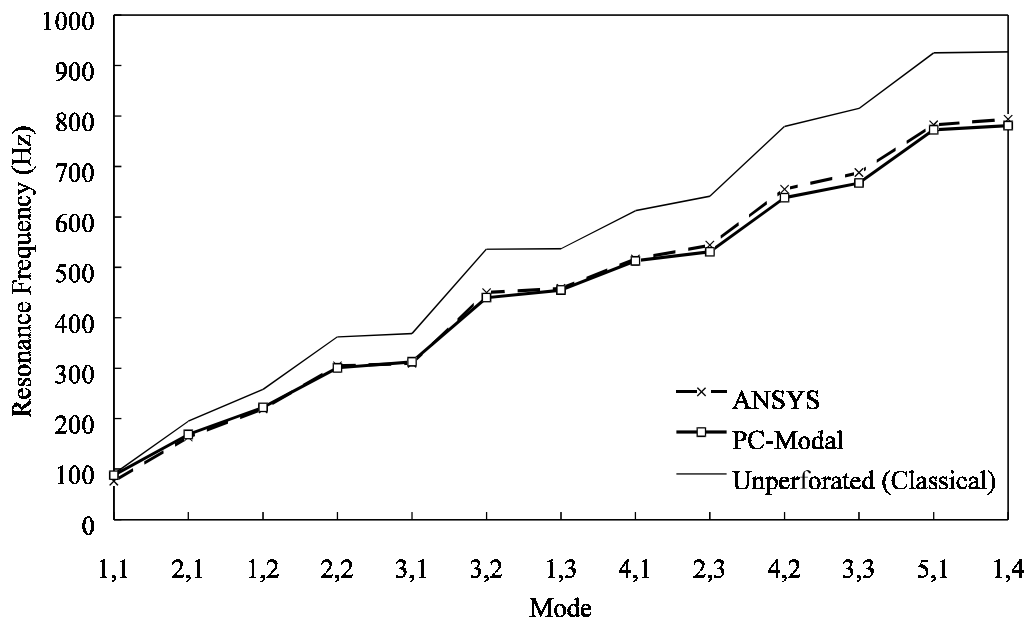
Figure 2.11   Comparison between measured modal resonance frequencies and those modelled using ANSYS for panel 3. Calculated resonance frequencies for a solid panel are shown for comparison.
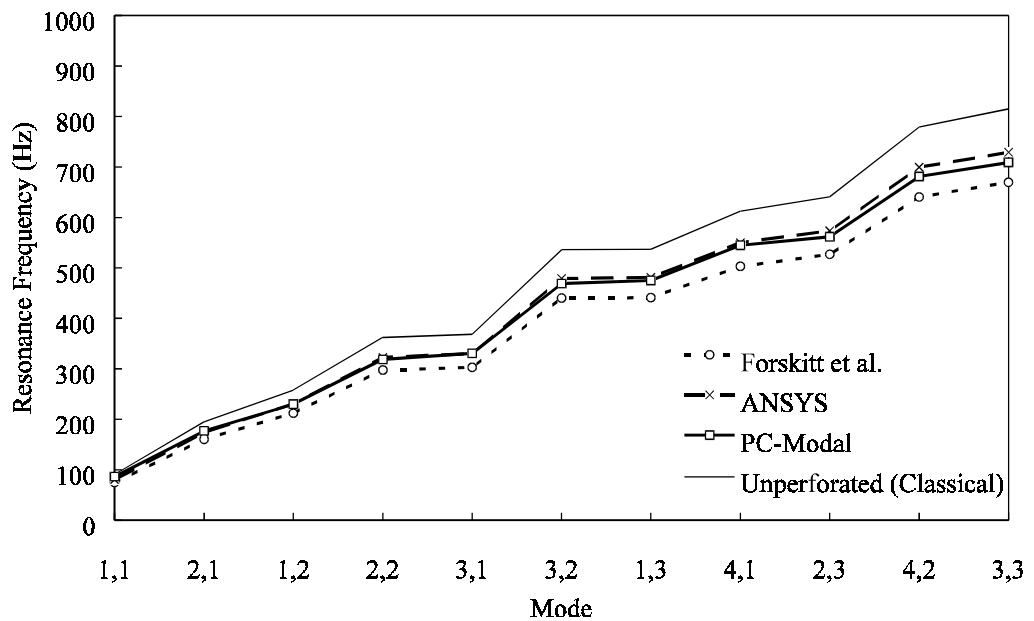
Figure 2.12   Comparison between measured modal resonance frequencies and those modelled using ANSYS for panel 6. Calculated resonance frequencies using the analysis of Forskitt *et al.* and for a solid panel are shown for comparison.

2.6.4 SUMMARY OF RESULTS

Table 2.2 summarises the results of the four analysis methods outlined above, comparing the ratio

of effective resonance frequency to resonance frequency of a solid panel, f^*/f.

Table 2.2
Summary of results of theoretical and experimental analysis.

Perf. No.	Panel Geom.	Hole Size (m)	*XLE*	*YLE*	Forskitt *et al.* f^*/f	Soler & Hill f^*/f	ANSYS f^*/f	Cubic f^*/f	Modal Analysis f^*/f
1		0.006	0.747	0.800	0.957	0.974	0.990	0.989	
2	8×5	0.015	0.368	0.500	0.795		0.932	0.938	
3	_____	0.025	-0.052	0.166			0.846	0.853	0.838
4		0.006	0.842	0.800	0.983	0.983	0.994	0.996	
5	5×5	0.015	0.605	0.5	0.847		0.958	0.956	
6	_____	0.025	0.342	0.166	0.678		0.898	0.892	0.885
7		0.006	0.747	0.880	0.972		0.987	0.989	
8	8×3	0.015	0.368	0.700	0.872		0.959	0.956	
9	_____	0.025	-0.052	0.500			0.901	0.897	
10		0.006	0.842	0.880	0.993	0.990	0.998	0.996	
11	5×3	0.0015	0.605	0.700	0.918	0.944	0.973	0.974	
12		0.025	0.342	0.500	0.788		0.935	0.936	
13		0.040	-0.052	0.200			0.861	0.858	

Gaps in the table correspond to where the hole geometry puts the values of *XLE* and *YLE* outside

the range of validity for each method. In particular, in the case of the data provided by Forskitt

et al., *XLE* cannot be negative and Soler and Hill's analysis can only be applied when *XLE* ≈

YLE. It is observed that the experimental results validate the ANSYS model of the resonance

frequencies of a perforate. The ANSYS model, in turn, does not agree with classical theory when

combined with modified material properties determined using Forskitt *et al.'s* results, except for

very lightly perforated materials (perforates 4,7 and 10), where, as expected, the modification is

only very small anyway. Both the moderately and highly perforated panels show a significant decrease in the frequency of their resonant modes because of their reduced effective stiffness. The cubic function fit to the ANSYS data is a convenient method for determining the effective resonance frequency ratio and has an error of less than ±1% of that predicted using ANSYS. Determining the accuracy of the results from ANSYS compared to those measured experimentally is perhaps a little ambitious; only two panels were tested in an attempt merely to verify the modelling methods; and the faithfulness of the panel supports in reproducing theoretical simply supported edge conditions, though considered excellent, is difficult to quantify. Nonetheless, as the ANSYS model was run with the most accurate (and hence time consuming) FEA method and large mesh density, it is reasonable to conclude that the error between these models will be less than ±2%. This implies that the error when using the cubic function (Equation 2.4) to determine the effective resonance frequencies of a perforate is less than ±3%.

The effective resonance frequency ratios determined using ANSYS for panels of similar geometry, namely panels 2 and 12 and panels 3 and 13, are similar. This is consistent with a large enough number of perforations being considered such that their effect does not appear macroscopically but rather is homogenous over the panel structure.

2.7   CONCLUSION

It has been shown that effective material constants cannot be used in classical equations to accurately predict the resonance frequencies of a simply supported perforated panel. Instead, it is much more accurate to fit the results from ANSYS over a range of *XLE* and *YLE* to a simple cubic function. This function can be used to determine the effective resonance frequency ratio for a large range of panel geometries in the range -0.1 < *XLE* < 1.0, -0.1 < *YLE* < 1.0 with an error of less than ±3%.

It does not appear intuitive that using effective material constants in classical analysis should produce such unacceptable results, particularly when it is observed that only these material constants and the overall panel geometry appear in Equation 2.3. Still, this points to the fact that the effective Young's modulus and Poisson's ratio determined by Forskitt *et al.* for a single perforated element in tension does not correspond to the actual material properties of the plate undergoing bending. It is plausible that in cases where the panel geometry is irregular, the holes in the perforation array may appear in somewhat linear groups across the panel and hence a different Young's Modulus may apply in different directions.

Chapter 3

COUPLED ANALYSIS OF A PERFORATED PANEL AS AN ACTIVE CONTROL SOURCE

3.1   INTRODUCTION

A previous paper (Pan *et al.*, 1992*a*) investigated analytically the feasibility of controlling low frequency sound radiated from a solid, simply supported rectangular panel with a second rectangular control panel containing a single large hole. Theoretical analysis of the system relied on the derivation of the equations of motion for the perforated front panel and for the air in the holes. These equations were derived by taking into account excitation by the internal pressure between the primary and control panel and by the point control force f_c, in the case of the perforated control panel, and by the internal pressure alone, in the case of the air in the holes. These equations were coupled to the displacement of the solid primary panel, due to its influence on the pressure in the cavity between the two panels. The control force required on the perforated control panel to optimally minimise the sound radiation for a particular harmonic excitation of the primary solid panel was then calculated.

As the theoretical work was limited to only one panel mode of vibration (the 1,1 mode) and one hole, the resultant coupled system of equations could be solved readily; however, for panels with many perforations the solution becomes more complex as additional equations are required to describe the motion of the air in each hole. In this chapter the work of Pan *et al.* is expanded to

47

a multi-mode, multi-hole analysis. It is shown that the analytical predictions so produced, do not

agree well with the experimental data, and suggestions are provided for improving the theoretical

model.

3.2   THEORETICAL ANALYSIS

The equations of motion for a perforated front control panel mounted in front of a solid radiating primary panel and a model describing the motion of the air in the holes of the perforate are derived for excitation by the sound field between the two panels and also by the point control force f_c. The resultant equations are coupled to the displacement of the primary panel via the pressure in the cavity between them, which is assumed to be constant throughout the cavity volume. An optimum control force is then derived to minimise the resulting sound radiation from the perforated control panel and the array of holes for a particular harmonic excitation of the primary solid panel. Using this optimum control force as well as the primary force, the resulting minimised sound field can be calculated and compared to the primary sound field, which is calculated with only the primary force acting on the panel.

3.2.1   PHYSICAL ARRANGEMENT

A vibrating rectangular panel (primary panel) of dimensions L_x, L_y, thickness h and point excitation f_p at $\sigma_p = (x_p, y_p)$ is located on the $z = -L_z$ plane. In front of the primary panel, a second simply supported perforated panel (the control panel) is installed on the $z = 0$ plane and is surrounded by an infinite rigid baffle. In the front panel there is an $H_x \times H_y$ array of rectangular holes, each of which has dimensions L_{xh} and L_{yh}, and the centre for the p, q^{th} hole is at

$$\left(\left(\frac{-L_x}{2} + \frac{L_x}{(H_x + 1)} p \right), \left(\frac{-L_y}{2} + \frac{L_y}{(H_y + 1)} q \right) \right). \tag{3.1}$$

A point force f_c is applied at $\sigma_c = (x_c, y_c)$ on the perforated panel surface to control the sound radiation into semi-infinite space (Figure 3.1).
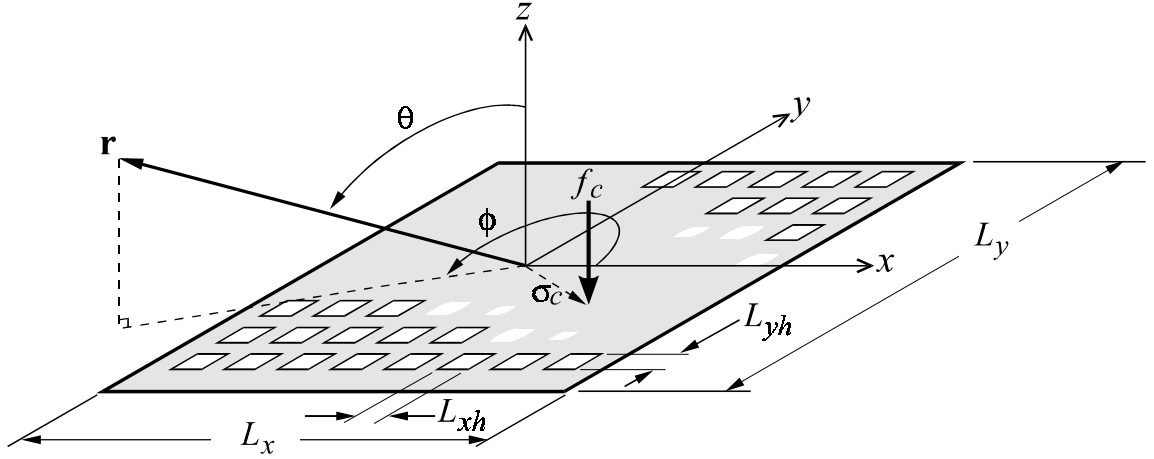
Figure 3.1   Perforated panel dimensions and coordinate system.

3.2.2   PERFORATED CONTROL PANEL RESPONSE

The displacement w of a thin panel containing an array of holes, numbering H_x in the x direction

and H_y in the y direction, can be described using the same mode shapes as for a solid panel

(Morse and Ingard, 1968) which (in the case of a solid panel) satisfies the following differential

equation of motion

$$\rho h \frac{\partial^2 w}{\partial t^2} + \frac{E h^3}{12(1 - \nu^2)} \nabla^4 w = p_{tot}, \tag{3.2}$$

where E, ρ and ν are Young's modulus, density and Poisson's ratio respectively. The quantity

p_{tot} is the total distributed sound pressure on both control panel surfaces given by

$$p_{tot} = p_{int} - p_{ext} + f_c \delta(\boldsymbol{\sigma} - \boldsymbol{\sigma}_c), \tag{3.3}$$

where p_{int} and p_{ext} are the internal (on the side closest to the solid primary panel) and external

sound pressures evaluated on the control panel surfaces. $\delta(\boldsymbol{\sigma} - \boldsymbol{\sigma}_c)$ is the Dirac delta function and f_c is a point control force applied at location $\boldsymbol{\sigma}_c = (x_c, y_c)$ on the control panel. The vector $\boldsymbol{\sigma} = (x, y)$ represents the coordinates of any location on the control panel surface.

Equations for the shape of the modes of a solid panel with no holes can be used to estimate the displacement of a panel with an array of small holes. In this case, the control panel displacement due to the (m,n) mode is given by

$$w_{m,n} \approx w_{c_{m,n}} \sin\left(\frac{m\pi x}{L_x} + \frac{m\pi}{2} \right) \sin\left(\frac{n\pi y}{L_y} + \frac{n\pi}{2} \right) e^{j\omega t}, \qquad (3.4)$$

where $w_{c_{m,n}}$ is the control panel modal displacement amplitude for mode (m,n). With the origin of the coordinate system at the centre of the panel, the normal mode shape function $\psi_{m,n}(\boldsymbol{\sigma})$ is given by

$$\psi_{m,n}(\boldsymbol{\sigma}) \approx \sin\left(\frac{m\pi x}{L_x} + \frac{m\pi}{2} \right) \sin\left(\frac{n\pi y}{L_y} + \frac{n\pi}{2} \right). \qquad (3.5)$$

The resonance frequency for the (m,n) panel mode can be approximated by using:

$$f_{m,n} \approx \frac{f^*}{f} \frac{1}{2\pi} \left(\frac{Eh^2}{12\rho(1 - v^2)} \right)^{1/2} \left(\left(\frac{m\pi}{L_x} \right)^2 + \left(\frac{n\pi}{L_y} \right)^2 \right). \qquad (3.6)$$

Where $\dfrac{f^*}{f}$ is the effective resonance frequency ratio, as defined in Chapter 2.

Substituting Equations (3.3), (3.4) and (3.6) into Equation (3.2), multiplying both sides of the resulting equation by $\sin(\pi x/L_x + \pi/2)\sin(\pi y/L_y + \pi/2)$, integrating over both sides of the front panel surface, and introducing panel modal damping, the system of equations describing the control

panel modal displacement as a function of the driving forces on the panel is obtained;

$$\mathbf{w}_c = \mathbf{Y}_c \mathbf{P}_c .$$

(3.7)

The control panel modal displacement amplitude matrix $\mathbf{w}_c$ is an $n_m \times 1$ matrix, where n_m is the total number of panel modes considered, defined by

$$\mathbf{w}_c = \begin{bmatrix} w_{c_1} \\ w_{c_2} \\ \vdots \\ w_{c_{n_m}} \end{bmatrix} .$$

(3.8)

The panel modal admittance matrix $\mathbf{Y}_c$ is an $n_m \times n_m$ diagonal matrix and the diagonal element corresponding to mode (m,n) is given by

$$y_{c_{m,n}} = \frac{1}{M_{c_{m,n}} (\omega_{c_{m,n}}^2 + j\eta_{m,n}\omega_{c_{m,n}}^2 - \omega^2)} ,$$

(3.9)

where ω is the angular frequency (rad/s) of excitation, $\omega_{c_{m,n}} = 2\pi f_{m,n}$ is the angular resonance frequency of the (m,n) panel mode, $\eta_{m,n}$ is the loss factor for the (m,n) mode, the quantity

$$M_{c_{m,n}} = \rho h \int_{A_c} \Psi_{m,n}^2(\boldsymbol{\sigma}) d\boldsymbol{\sigma}$$

(3.10)

is the modal mass of the control panel and A_c is the control panel area, excluding the area of the holes.

The quantity $\mathbf{P}_c$ is an $n_m \times 1$ matrix represented as follows

$$\mathbf{P}_c = \begin{bmatrix} P_{c_1} \\ P_{c_2} \\ \vdots \\ P_{c_{n_m}} \end{bmatrix}, \tag{3.11}$$

where the element corresponding to the (m,n) mode is the product of the total pressure p_{tot} and the mode shape function of the (m,n) panel mode, integrated over the panel surface

$$P_{c_{m,n}} = \frac{1}{A_c} \int_{A_c} \Psi_{m,n}(\sigma) p_{tot}(\sigma) d\sigma = P_{int_{m,n}} A_c - P_{ext_{m,n}} A_c + f_c \Psi_{m,n}(x_c, y_c) . \tag{3.12}$$

As it is assumed that the internal and external pressure fields acting on the control panel surface are uniform over the panel surface, the modal sound pressures $P_{int_{m,n}}$ and $P_{ext_{m,n}}$ can be expressed as the products of the pressures acting on the surfaces and a modal correction factor $\Delta_{m,n}$. For the control panel this is given by

$$\Delta_{c_{m,n}} = \frac{1}{A_c} \int_{A_c} \Psi_{m,n}(\sigma) d\sigma . \tag{3.13}$$

Thus,

$$P_{int_{m,n}} = p_{int} \Delta_{c_{m,n}} \tag{3.14}$$

and

$$P_{ext_{m,n}} = p_{ext} \Delta_{c_{m,n}} , \tag{3.15}$$

where

$$\psi_{m,n}(x_c, y_c) = \psi_{m,n}(\sigma_c) = \sin\left(\frac{m\pi x_c}{L_x} + \frac{m\pi}{2}\right) \sin\left(\frac{n\pi y_c}{L_y} + \frac{n\pi}{2}\right). \qquad (3.16)$$

3.2.3   PRIMARY PANEL RESPONSE

Similarly the panel modal displacement amplitude matrix for the solid primary panel is

$$\mathbf{w}_p = \begin{bmatrix} w_{p_1} \\ w_{p_2} \\ \vdots \\ w_{p_{n_m}} \end{bmatrix} \qquad (3.17)$$

which can be calculated (given the primary driving force vector f_p) as

$$\mathbf{w}_p = \mathbf{Y}_p \, \mathbf{f}_p. \qquad (3.18)$$

The primary panel modal admittance matrix, $\mathbf{Y}_p$, is an $n_m \times 1$ diagonal matrix with the diagonal element corresponding to the mode (m,n) given by

$$y_{p_{m,n}} = \frac{1}{M_{p_{m,n}} (\omega_{p_{m,n}}^2 + j\,\eta_{m,n}\,\omega_{p_{m,n}}^2 - \omega^2)} \qquad (3.19)$$

and modal force matrix is

$$\mathbf{f}_p = f_p \begin{bmatrix} \psi_1(x_p, y_p) \\ \psi_2(x_p, y_p) \\ \vdots \\ \psi_{n_m}(x_p, y_p) \end{bmatrix}, \qquad (3.20)$$

where f_p is the amplitude of the primary excitation force.

Chapter 3 Coupled analysis of a perforated control source

3.2.4   AIR PISTON RESPONSE

The air motion in the *p, q*[th] hole in the front panel can be modelled as the motion of an air piston

and is described by the following differential equation

$$M_{a_{p,q}} \frac{\partial^2 w_{a_{p,q}}}{\partial t^2} = P_{int} A_a - R_{a_{p,q}} \frac{\partial w_{a_{p,q}}}{\partial t} , \qquad (3.21)$$

where $w_{a_{p,q}}$ is the displacement of the fluid in the *p,q*[th] hole, $M_{a_{p,q}}$ is the mass reactance and

$R_{a_{p,q}}$ is the radiative and viscous resistance to the *p, q*[th] air piston's motion. The quantity $A_a =$

$L_{xh} L_{yh}$ is the opening area of each hole in the perforated front panel.

The total impedance `seen' by the *p, q*[th] air piston has components from self impedance and

mutual impedance from the array of pistons surrounding it. The interaction between the control

panel and the air piston array will also modify the mass reactance and radiation resistance

(Caldersmith, 1978). However, in calculating the overall levels of noise attenuation that can be

achieved by active control of the noise it makes little difference and so will be ignored with a

view to making the problem tractable.

The mass reactance $M_{a_{p,q}}$, and the acoustic resistance $R_{a_{p,q}}$ of the *p′, q′*[th] air piston can be

approximated as (Morse and Ingard, 1968; Pritchard, 1960)

$$M_{a_{p,q}} = \rho \left(h + \frac{2 \times 0.85}{\sqrt{\pi}} \sqrt{A_a} \right) A_a \left(1 + \sum_{p'=1}^{H_x} \sum_{q'=1}^{H_y} \frac{\cos(kd)}{kd} \right) \qquad (3.22)$$

and

$$R_{a_{p,q}} = \rho c k^2 \frac{A_a^2}{2\pi}\left(1 + \sum_{p'=1}^{H_x}\sum_{q'=1}^{H_y}\frac{\sin(kd)}{kd}\right),$$ (3.23)

where d is the distance between radiating pistons given by:

$$d = \left[\left(\left(\frac{L_x}{H_x+1}\right)(p-p')\right)^2 + \left(\left(\frac{L_y}{H_y+1}\right)(q-q')\right)^2\right]^{1/2}.$$ (3.24)

3.2.5 INTERNAL SOUND PRESSURE p_{int}

The low frequency internal sound pressure, p_{int}, between the front and back panels can be described by the volume compression relation in the cavity between the two panels as

$$p_{int} = -\gamma P_o\frac{\delta V}{V} = -\frac{\rho_o c_o^2}{V}(A_c\bar{w}_c + A_a\bar{w}_a - A_p\bar{w}_p),$$ (3.25)

where P_o is the atmospheric pressure, γ is the specific heat ratio and $c_o^2 = \gamma P_o/\rho_o$. The quantities $\bar{w}_c$, $\bar{w}_p$ and $\bar{w}_a$ are the space averaged displacements of the perforated control panel, solid primary panel and air pistons respectively.

The space averaged displacement of the control panel is given by

$$\bar{w}_c = \sum_{m,n} w_{c_{m,n}}\frac{1}{A_c}\int_{A_c}\psi_{m,n}(\sigma)\,d\sigma,$$ (3.26)

which by substituting Equation (3.13), reduces to

$$\bar{w}_c = \sum_{m,n} w_{c_{m,n}} \Delta_{c_{m,n}},$$ (3.27)

where $w_{c_{m,n}}$ is the modal displacement amplitude of the (m,n) mode.

Similarly then

$$\bar{w}_p = \sum_{m,n} w_{p_{m,n}} \Delta_{p_{m,n}},$$ (3.28)

where

$$\Delta_{p_{m,n}} = \frac{1}{A_p} \int_{A_p} \psi_{m,n}(\sigma) d\sigma .$$ (3.29)

The average displacement, $\bar{w}_a$, of the air pistons is given by

$$\bar{w}_a = \frac{\displaystyle\sum_{p=1}^{H_x} \sum_{q=1}^{H_y} w_{a_{p,q}}}{H_x H_y} .$$ (3.30)

3.2.6   EXTERNAL SOUND PRESSURE p_{ext}

The external sound pressure p_{ext} on the front control panel surface is determined by the equation of motion

$$p_{ext} A_c = M_c \frac{\partial^2 \bar{w}_c}{\partial t^2} + R_c \frac{\partial \bar{w}_c}{\partial t} .$$ (3.31)

M_c is the mass loading of the near acoustic field above the panel, and R_c is the acoustic resistance that the air provides to the panel motion, given by (Caldersmith, 1978)

$$M_c = \frac{0.85}{\sqrt{\pi}}\rho_o(A_c)^{\frac{3}{2}} \tag{3.32}$$

and

$$R_c = \rho_o c_o k^2 \frac{A_c^2}{2\pi}. \tag{3.33}$$

Again the interaction between the air piston array and the perforated control panel has been ignored for the sake of simplicity (see Section 3.2.4) with no loss of generality.

3.2.7   COUPLED SYSTEM RESPONSE

Using Equation (3.12) in Equation (3.7) for the (m', n') mode gives

$$y_{c_{m',n'}}^{-1} w_{c_{m',n'}} = P_{int_{m,n}} A_c - P_{ext_{m,n}} A_c + f_c \Psi_{m',n'}(x_c, y_c), \tag{3.34}$$

which upon substitution of Equations (3.14) and (3.15) yields

$$y_{c_{m',n'}}^{-1} w_{c_{m',n'}} = p_{int}\Delta_{c_{m',n'}} A_c - p_{ext}\Delta_{c_{m',n'}} A_c + f_c \Psi_{m',n'}(x_c, y_c). \tag{3.35}$$

Introducing Equation (3.25) for p_{int} and Equation (3.31) for p_{ext} yields

$$
\begin{aligned}
y_{c_{m',n'}}^{-1} w_{c_{m',n'}} = {}&- \frac{\rho_o c_o^2}{V}(A_c \bar{w}_c + A_a \bar{w}_a - A_p \bar{w}_p)\Delta_{m',n'} A_c \\[2mm]
&- M_c \frac{\partial^2 \bar{w}_c}{\partial t^2}\Delta_{c_{m',n'}} + R_c \frac{\partial \bar{w}_c}{\partial t}\Delta_{c_{m',n'}} + f_c \Psi_{m',n'}(x_c, y_c).
\end{aligned}
\tag{3.36}
$$

Chapter 3 Coupled analysis of a perforated control source

Rearranging, substituting for $\bar{w}_c$, $\bar{w}_p$ and $\bar{w}_a$ (Equations (3.27), (3.28) & (3.30)) and introducing the acoustical capacitance C_a (see Equation 3.44);

$$
y_{c_{m',n'}}^{-1} w_{c_{m',n'}} + \left(\frac{\Delta_{c_{m',n'}} A_c^2}{C_a} - \omega^2 M_c \Delta_{c_{m',n'}} + j\omega R_c \Delta_{c_{m',n'}} \right) \sum_{m,n} w_{c_{m,n}} \Delta_{c_{m,n}} +
$$

$$
\frac{\Delta_{c_{m',n'}} A_c A_a}{C_a H_x H_y} \sum_{p=0}^{H_x} \sum_{q=0}^{H_y} w_{a_{p,q}} = \frac{\Delta_{c_{m',n'}} A_c A_p}{C_a} \sum_{m,n} w_{p_{m,n}} \Delta_{p_{m,n}} + f_c \Psi_{m',n'}(x_c, y_c) .
$$

$$(3.37)$$

Coupling the internal pressure, by equating the internal pressure given in Equation (3.25) with Equation (3.21) for the hole p', q' gives

$$
M_{a_{p',q'}} \frac{\partial^2 w_{a_{p',q'}}}{\partial t^2} = -\frac{\rho_o c_o^2}{V} (A_c \bar{w}_c + A_a \bar{w}_a - A_p \bar{w}_p) A_c - R_{a_{p',q'}} \frac{\partial w_{a_{p',q'}}}{\partial t} .
$$

$$(3.38)$$

Rearranging and substituting for the space averaged displacements, $\bar{w}_c$, $\bar{w}_p$ and $\bar{w}_a$;

$$
\frac{A_a A_c}{C_a} \sum_{m,n} w_{c_{m,n}} \Delta_{c_{m,n}} + \left(-\omega^2 M_{a_{p',q'}} + j\omega R_{a_{p',q'}} \right) w_{a_{p',q'}} + \frac{A_a^2}{C_a H_x H_y} \sum_{p=0}^{H_x} \sum_{q=0}^{H_y} w_{a_{p,q}}
$$

$$
= \frac{A_a A_p}{C_a} \sum_{m,n} w_{p_{m,n}} \Delta_{p_{m,n}} .
$$

$$(3.39)$$

Using Equations (3.37) and (3.39), the coupled equations describing the overall displacements **w** of the perforated control panel and air pistons as a function of the displacement **w**$_p$ of the primary panel can be obtained as follows

$$
\mathbf{A} \, \mathbf{w} = \mathbf{B}_1 \, \mathbf{w}_p + \mathbf{B}_2 f_c ,
$$

$$(3.40)$$

where the overall displacement coefficient matrix **A** is a $(n_m + H_x \times H_y) \times (n_m + H_x \times H_y)$ matrix with the elements

$$\mathbf{A} = \begin{bmatrix}
y_1^{-1} + \Delta_1(\Delta_1 X_c) & \Delta_2(\Delta_1 X_c) & \cdots & \Delta_{n_m}(\Delta_1 X_c) \\
\Delta_1(\Delta_2 X_c) & y_2^{-1} + \Delta_2(\Delta_2 X_c) & & \Delta_{n_m}(\Delta_2 X_c) \\
\vdots & & \ddots & \vdots \\
\Delta_1(\Delta_{n_m-1} X_c) & & y_{n_m-1}^{-1} + \Delta_{n_m-1}(\Delta_{n_m-1} X_c) & \Delta_{n_m}(\Delta_{n_m-1} X_c) \\
\Delta_1(\Delta_{n_m} X_c) & \cdots & \Delta_{n_m-1}(\Delta_{n_m} X_c) & y_{n_m}^{-1} + \Delta_{n_m}(\Delta_{n_m} X_c) \\
\dfrac{A_a A_c}{C_a}\Delta_1 & \dfrac{A_a A_c}{C_a}\Delta_2 & \cdots & \dfrac{A_a A_c}{C_a}\Delta_{n_m} \\
\vdots & & \ddots & \vdots \\
\dfrac{A_a A_c}{C_a}\Delta_1 & \dfrac{A_a A_c}{C_a}\Delta_2 & \cdots & \dfrac{A_a A_c}{C_a}\Delta_{n_m}
\end{bmatrix}$$

$$\begin{bmatrix}
\dfrac{\Delta_1 A_c A_a}{C_a H_x H_y} & & \cdots & & \dfrac{\Delta_1 A_c A_a}{C_a H_x H_y} \\
\vdots & & \ddots & & \vdots \\
\dfrac{\Delta_{n_m} A_c A_a}{C_a H_x H_y} & & \cdots & & \dfrac{\Delta_{n_m} A_c A_a}{C_a H_x H_y} \\
X_{a_1} + \dfrac{A_a^2}{C_a H_x H_y} & \dfrac{A_a^2}{C_a H_x H_y} & \cdots & & \dfrac{A_a^2}{C_a H_x H_y} \\
\dfrac{A_a^2}{C_a H_x H_y} & X_{a_2} + \dfrac{A_a^2}{C_a H_x H_y} & & & \dfrac{A_a^2}{C_a H_x H_y} \\
\vdots & & \ddots & & \vdots \\
& & & & \dfrac{A_a^2}{C_a H_x H_y} \\
\dfrac{A_a^2}{C_a H_x H_y} & & \cdots & \dfrac{A_a^2}{C_a H_x H_y} & X_{a_{H_x+H_y}} + \dfrac{A_a^2}{C_a H_x H_y}
\end{bmatrix},$$

$$(3.41)$$

where

$$X_c = (A_c^2 / C_a) - \omega^2 M_c + j\omega R_c ,$$
(3.42)

$$X_{a_{p,q}} = -\omega^2 M_{a_{p,q}} + j\omega R_{a_{p,q}}$$
(3.43)

and the acoustical capacitance, C_a of the volume V is given by

$$C_a = V / \rho_o c_o^2 .$$
(3.44)

The overall system displacement amplitude matrix is

$$\mathbf{w} = \begin{bmatrix} w_{c_1} \\ w_{c_2} \\ \vdots \\ w_{c_{n_m}} \\ w_{a_1} \\ w_{a_2} \\ \vdots \\ w_{a_{H_x \times H_y}} \end{bmatrix}.$$
(3.45)

The $(n_m + H_x \times H_y) \times n_m$ matrix $\mathbf{B}_1$ is

$$\mathbf{B}_1 = \begin{bmatrix} \dfrac{\Delta_{c_1} A_c A_p}{C_a}\Delta_{p_1} & \cdots & \dfrac{\Delta_{c_1} A_c A_p}{C_a}\Delta_{p_{n_m}} \\ \vdots & \ddots & \vdots \\ \dfrac{\Delta_{c_{n_m}} A_c A_p}{C_a}\Delta_{p_1} & \cdots & \dfrac{\Delta_{c_{n_m}} A_c A_p}{C_a}\Delta_{p_{n_m}} \\ \dfrac{A_a A_p}{C_a}\Delta_{p_1} & \cdots & \dfrac{A_a A_p}{C_a}\Delta_{p_{n_m}} \\ \vdots & \ddots & \vdots \\ \dfrac{A_a A_p}{C_a}\Delta_{p_1} & \cdots & \dfrac{A_a A_p}{C_a}\Delta_{p_{n_m}} \end{bmatrix}. \tag{3.46}$$

The $(n_m + H_x \times H_y) \times 1$ force coefficient matrix $\mathbf{B}_2$ is

$$\mathbf{B}_2 = \begin{bmatrix} \psi_1(x_c, y_c) \\ \psi_2(x_c, y_c) \\ \vdots \\ \psi_{n_m}(x_c, y_c) \\ 0 \\ \vdots \\ 0 \end{bmatrix}. \tag{3.47}$$

By inverting the coefficient matrix $\mathbf{A}$ of the system displacement amplitude matrix in Equation (3.40), the vector $\mathbf{w}$ containing the modal displacement amplitudes of the front panel and the air piston displacement amplitudes is obtained in terms of the modal displacement of the primary panel and the control force, as follows

$$\mathbf{w} = \mathbf{A}^{-1}\mathbf{B}_1\mathbf{w}_p + \mathbf{A}^{-1}\mathbf{B}_2 f_c. \tag{3.48}$$

With vibration control sources only, the overall farfield sound pressure is generated entirely by

the vibration response of the control panel and the air pistons, as their response also accounts for radiation from the solid primary panel. Thus the radiated sound pressure at angular frequency ω and location vector $\mathbf{r}$ in the far field may be described by the Rayleigh Integral (Morse, 1986);

$$p_t(\mathbf{r},\omega) = \sum_{m,n} -\frac{\rho\omega^2}{2\pi} \int_{A_c} \frac{w_{c_{m,n}}(\boldsymbol{\sigma})e^{-jkr_c}}{|\mathbf{r}|} d\boldsymbol{\sigma}$$

$$+ \sum_{p=1}^{H_x}\sum_{q=1}^{H_y} -\frac{\rho\omega^2}{2\pi} \int_{A_a} \frac{w_{a_{p,q}}e^{-jkr_a}}{r_a} d\boldsymbol{\sigma},$$

(3.49)

where $|\mathbf{r}|$ is the distance from the centre of the panel to the observation location $\mathbf{r}$.

If it is assumed that the size of the air pistons are small compared to the observation distance, Equation (3.49) can be simplified to

$$p_t(\mathbf{r},\omega) = \sum_{m,n} -\frac{\rho\omega^2}{2\pi} \int_{A_c} \frac{w_{c_{m,n}}(\boldsymbol{\sigma})e^{-jkr_c}}{|\mathbf{r}|} d\boldsymbol{\sigma}$$

$$-\frac{\rho\omega^2 A_a}{2\pi} \sum_{p=1}^{H_x}\sum_{q=1}^{H_y} w_{a_{p,q}} \left(\frac{e^{-jkr_a}}{r_a} \right),$$

(3.50)

where r_c is the distance from the element $d\boldsymbol{\sigma}$ on the panel surface to the observation point and r_a is the distance from the element $d\boldsymbol{\sigma}$ on the p, q^{th} air piston to the observation point in the case of Equation (3.49) or the distance from the centre of the p, q^{th} air piston to the observation point in the case of Equation (3.50). These can be approximated as (Wallace, 1972)

$$r_c \approx |\mathbf{r}| - \frac{1}{k}\left[\left(\frac{\alpha x}{L_x} \right) + \left(\frac{\beta y}{L_y} \right) \right]$$

(3.51)

and

$$r_a \approx |\mathbf{r}| - \frac{1}{k} \left[\left(\frac{\alpha \left(\frac{-L_x}{2} + \frac{L_x}{H_x+1} p \right)}{L_x} \right) + \left(\frac{\beta \left(\frac{-L_y}{2} + \frac{L_y}{H_y+1} q \right)}{L_y} \right) \right],$$

(3.52)

where

$$\alpha = kL_x \sin\theta \cos\phi$$

(3.53)

and

$$\beta = kL_y \sin\theta \sin\phi .$$

(3.54)

As shown in Figure 3.1, θ and ϕ are the elevation and azimuth angles of the observation vector **r**.

As

$$w_c(\mathbf{\sigma}) = \sum_{m,n} w_{c_{m,n}} \psi_{m,n}(\mathbf{\sigma})$$

(3.55)

the acoustic radiation transfer matrix **Z** can be defined such that

$$\mathbf{Z} = \begin{bmatrix} -\frac{\rho\omega^2}{2\pi} \int_{A_c} \psi_1(\mathbf{\sigma}) \frac{e^{-jkr_c}}{|\mathbf{r}|} d\mathbf{\sigma} \\ \vdots \\ -\frac{\rho\omega^2}{2\pi} \int_{A_c} \psi_{n_m}(\mathbf{\sigma}) \frac{e^{-jkr_c}}{|\mathbf{r}|} d\mathbf{\sigma} \\ -\frac{\rho\omega^2 A_a}{2\pi} \left(\frac{e^{-jkr_{a_1}}}{r_{a_1}} \right) \\ \vdots \\ -\frac{\rho\omega^2 A_a}{2\pi} \left(\frac{e^{-jkr_{a_{H_x+H_y}}}}{r_{a_{H_x+H_y}}} \right) \end{bmatrix}^{\mathrm{T}}$$

(3.56)

and so the radiated sound pressure will be

$$p_t(\mathbf{r}, \omega) = \mathbf{Z}\mathbf{A}^{-1}\mathbf{B}_1\mathbf{w}_p + \mathbf{Z}\mathbf{A}^{-1}\mathbf{B}_2 f_c \tag{3.57}$$

or

$$p_t(\mathbf{r}, \omega) = \mathbf{\Pi}_1\mathbf{w}_p + \mathbf{\Pi}_2 f_c, \tag{3.58}$$

where

$$\mathbf{\Pi}_1 = \mathbf{Z}\mathbf{A}^{-1}\mathbf{B}_1 \tag{3.59}$$

and

$$\mathbf{\Pi}_2 = \mathbf{Z}\mathbf{A}^{-1}\mathbf{B}_2. \tag{3.60}$$

The sound pressure at location $\mathbf{r}$ due to the back panel alone may also be calculated for comparison as,

$$p_p = \sum_{m,n} -\frac{\rho\omega^2}{2\pi} \int_{A_p} \frac{w_{p_{m,n}} e^{-jkr_p}}{|\mathbf{r}|} d\boldsymbol{\sigma}, \tag{3.61}$$

where r_p is the distance from the element $d\boldsymbol{\sigma}$ on the primary panel surface to the observation point and can be approximated as

$$r_p \approx |\mathbf{r}| + L_z - \frac{1}{k}\left[\left(\frac{\alpha x}{L_x}\right) + \left(\frac{\beta y}{L_y}\right)\right]. \tag{3.62}$$

The magnitude of the sound pressure calculated using Equation (3.57) can be re-expressed as a quadratic function of the complex control force f_c

$$|p_t(\mathbf{r}, \omega)|^2 = f_c^* a f_c + f_c^* b + b^* f_c + c, \tag{3.63}$$

where * represents the complex conjugate,

$$a = \mathbf{\Pi}_2{}^H \mathbf{\Pi}_2 , \tag{3.64}$$

$$b = \mathbf{\Pi}_2{}^H \mathbf{\Pi}_1 \mathbf{w}_p \tag{3.65}$$

and

$$c = \mathbf{w}_p{}^* \mathbf{\Pi}_1{}^H \mathbf{\Pi}_1 \mathbf{w}_p . \tag{3.66}$$

The Hermitian transpose of the matrix (the complex conjugate and transpose of a matrix) is represented by ^{H}. This quadratic equation has a unique (global) minimum, which is the optimum control force required to produce a minimum sound pressure at an error microphone located at some observation point $\mathbf{r}$. The optimum value of the control force obtained by differentiating Equation (3.63) with respect to f_c is

$$f_c^{opt} = -a^{-1} b . \tag{3.67}$$

The resulting minimum sound pressure (Nelson *et al.*, 1987) is

$$\left| p(\mathbf{r}, \omega) \right|_{min}^2 = c - b^* a^{-1} b . \tag{3.68}$$

3.2.8   COMPUTATION METHOD

The computation of the theoretical model outlined above is straightforward, but nonetheless demanding, due to the excessive size of the matrix **A**, and the computationally expensive action of calculating it's inverse for any practically sized perforated panel (say with two thousand holes). Hence it was necessary to perform the calculations on a 32 Node CM-5 Massively Parallel Processor, which reduced the processing time by two orders of magnitude. The system of equations was programmed in CM-FORTRAN (A subset of FORTRAN 90), and computations performed in approximately 40 CPU hours for each physical arrangement.

3.3   EXPERIMENTAL VERIFICATION

3.3.1   PROCEDURE

A rectangular steel panel (primary panel) of dimensions 380mm x 300mm, and thickness 1.98mm was mounted in a heavy steel frame using spring steel shims to approximate simply supported boundary conditions. The panel was placed in the centre of a large wooden baffle and excited using a Brüel & Kjær 4809 electrodynamic shaker at its centre. In front of the primary panel, a second simply supported panel (control panel) of the same dimensions (as the primary panel) was installed. Three different control panels were tested, positioned 30mm in front of the primary panel (ie. L_z = -30mm). The first panel was constructed to match the panel used by Pan *et al.* in their theoretical analysis (1992). It had one 47.5mm square hole, offset 95mm from the centre of the panel. It's vibration was controlled by using a pair of thin piezoceramic actuators, one on each side of the panel, offset 70mm from the centre of the panel, as shown in Figure 3.2.
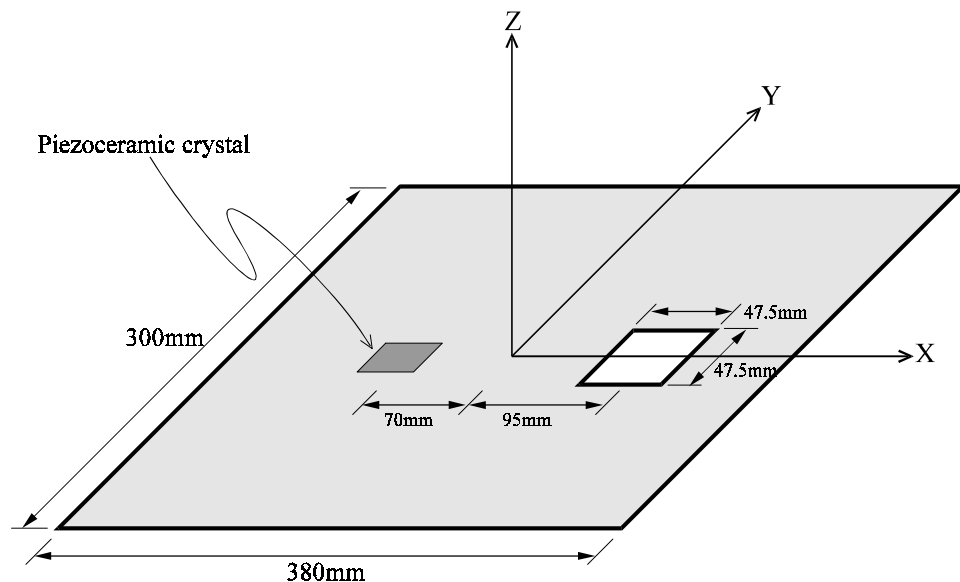

Figure 3.2   Panel dimensions for the panel considered by Pan *et al.*

The remaining two panels were uniformly perforated with arrays of 22x10, 6mm diameter holes and 56x41, 3.25mm diameter holes. Both were controlled using a pair of piezoceramic actuators, one on each side of the panel, at it's centre. These panels were mounted in a frame with spring steel edges to approximate simply supported boundary conditions (see Figure 2.5).

The radiated sound field was measured in an anechoic chamber using a Brüel & Kjær type 4131 one inch microphone connected to Brüel & Kjær type 2604 Microphone Amplifier and filter set. The microphone was mounted on a Brüel & Kjær type 3921 turntable which rotated through $180°$ so that the microphone traversed a horizontal arc of radius 1.8m around the panel centre, perpendicular to the plane of the panel (see Figure 3.3). A Brüel & Kjær type 2307 level recorder was used to record the measurements on a polar plot.

Control was achieved using an adaptive multichannel controller based on INMOS Transputer digital signal processing hardware, using a filtered-x LMS algorithm. The traversing microphone was set to either of the two control angles considered, and the output used as the error criterion for the control system to minimise. Once minimisation had occurred, the controller adaptation was stopped, and a constant optimised control output was used to drive the control source while the polar plots were recorded.
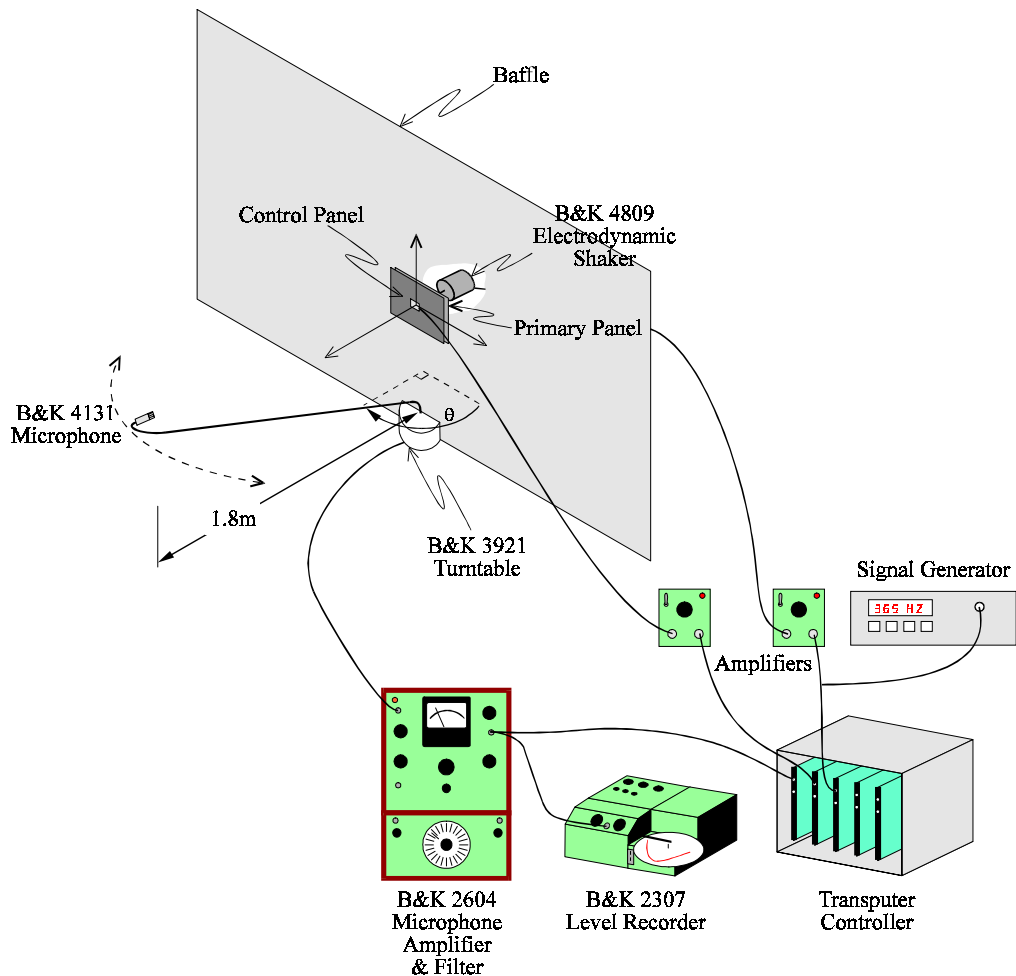
Figure 3.3   Experimental arrangement for Active Noise Control experiments.

3.3.2   RESULTS AND DISCUSSION

A comparison between the radiated sound fields calculated using Equation (3.58), to the measured radiated sound field for the case of the panel with a single offset hole is shown in Figures 3.4 to 3.7. The polar plots show the relative sound pressure level for a given elevation angle, θ, an azimuth of $\phi = 0°$ at a radius of $r = 1.8$m. The measurements were taken at 335Hz (Figures 3.4 and 3.5) and 365Hz (Figures 3.6 and 3.7), which are slightly above and slightly below the resonance frequency of the primary radiating mode (the 3,1) of the primary panel

respectively. The error sensor location is at $\theta = 40°$ and $\theta = 90°$ so that the symmetry of the experimental setup can be properly appraised. The predicted and measured sound fields for the primary panel without the perforated control panel in place is also shown for comparison, and were used to normalise the results for the case of the controlled sound fields.

The theoretical results presented have been limited in the amount of control that is achievable by introducing a control efficiency factor η. The calculated optimum control force was multiplied by this factor so that it more closely models the physical system where the controller is unlikely to converge to the exact value of the optimum control output. An efficiency factor of $\eta = 0.99$ was used, which limited the theoretical achievable attenuation to about 40dB.

All figures indicate that prediction of the sound field from the primary panel alone is in good agreement with that measured. Small perturbations are evident, more so at 365Hz, and are due to diffraction around the edges of the baffle. This effect is more pronounced near the baffle (ie. $\theta \approx 0°$ and $\theta \approx 180°$). The predicted attenuation however is vastly more than that achieved in practice in all cases.

The errors between the measured and calculated resonance frequencies were small enough to ensure that the effect on the calculated sound pressure levels off resonance, was negligible.

Figure 3.4   Comparison between the theoretical and measured data at 335Hz, with the error sensor at 40°. (calculated using Equation 3.49)
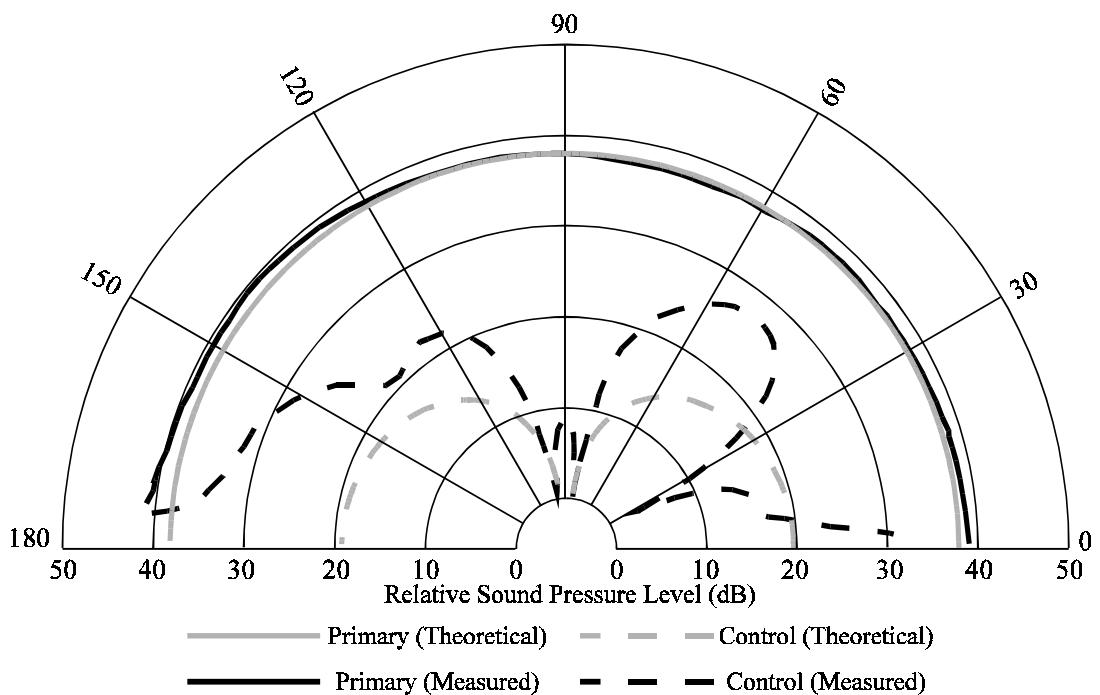
Figure 3.5   Comparison between the theoretical and measured data at 335Hz, with the error sensor at 90°. (calculated using Equation 3.49)
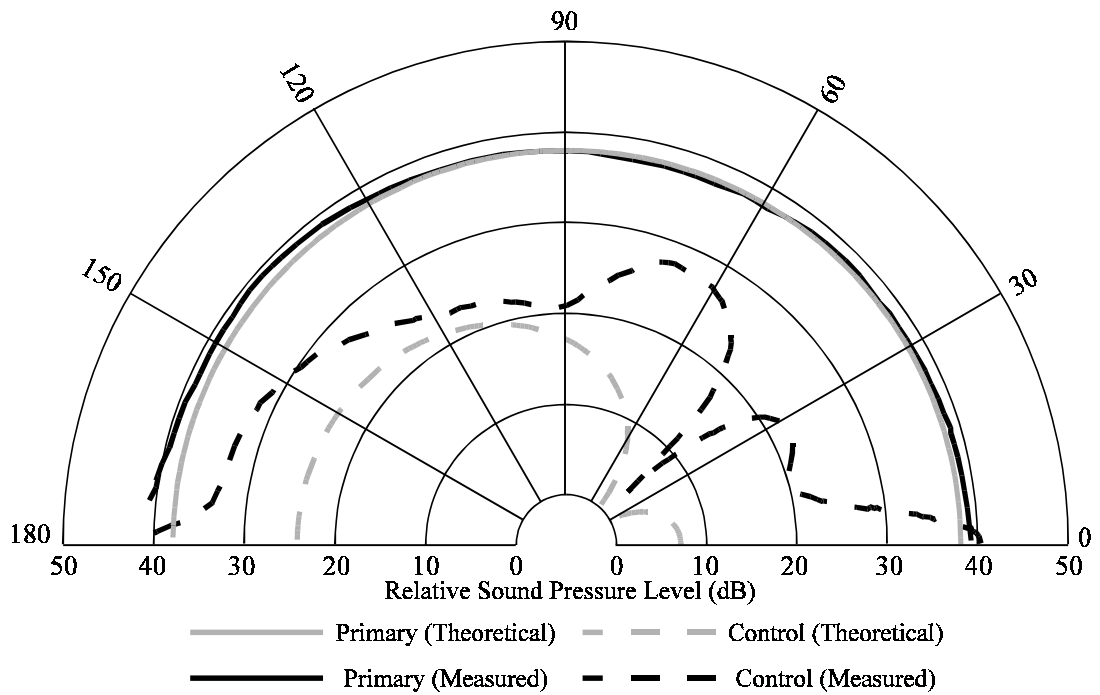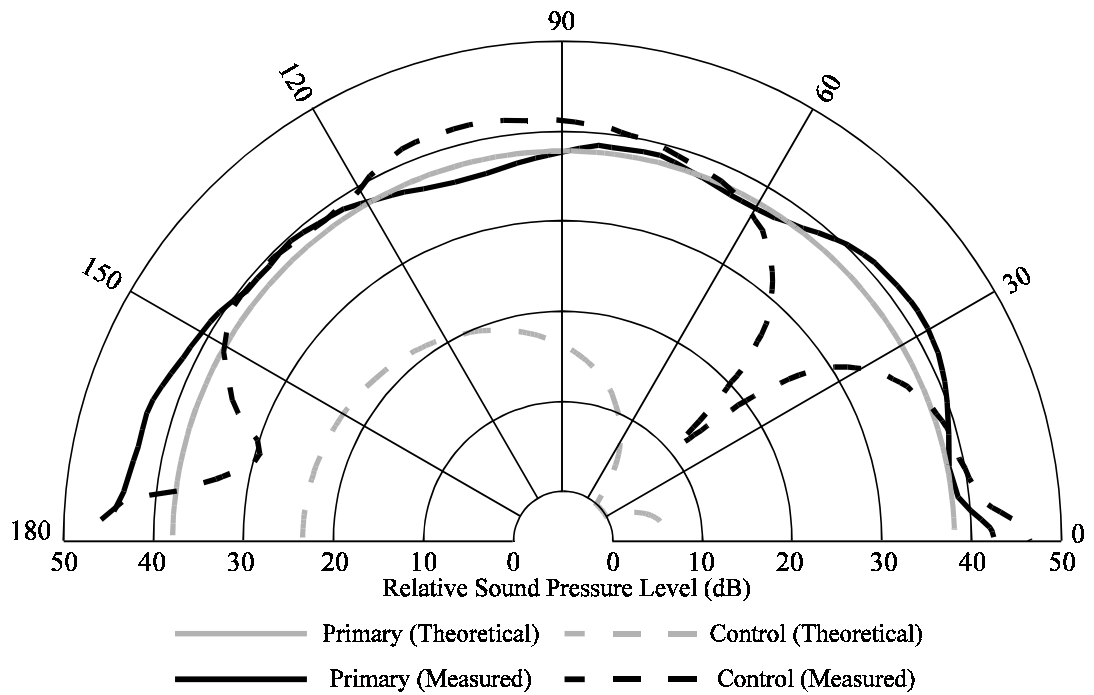
Figure 3.6   Comparison between the theoretical and measured data at 365Hz, with the error sensor at 40°. (calculated using Equation 3.49)
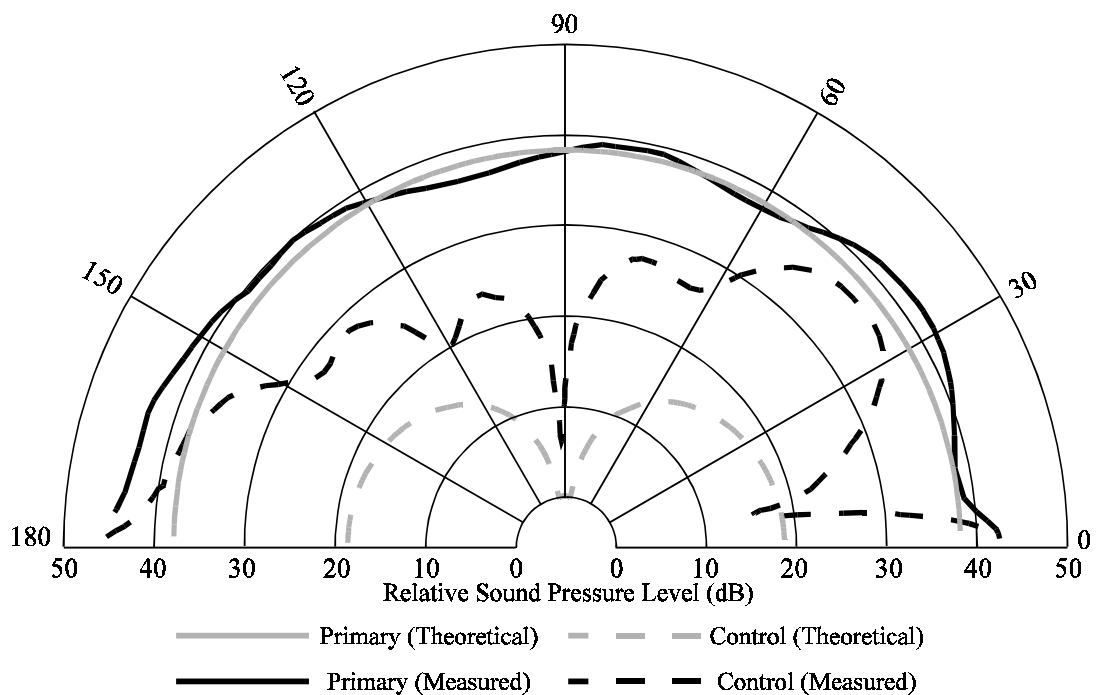
Figure 3.7   Comparison between the theoretical and measured data at 365Hz, with the error sensor at 90°. (calculated using Equation 3.49)

The reason for this overprediction is clear, when the amount of noise control achievable by placing the control panels in front of the primary panel *without* applying any control force, is considered. This passive control is shown for the single offset hole panel, the 22x10 perforate and the 56x41 perforate in Figures 3.8 to 3.10 respectively, over a frequency range from 0Hz to 800Hz . The microphone was placed directly in front of the panels (ie. $\theta = 0°$ and $\phi = 0°$) and the frequency response between the sound pressure and a 1N primary force measured.
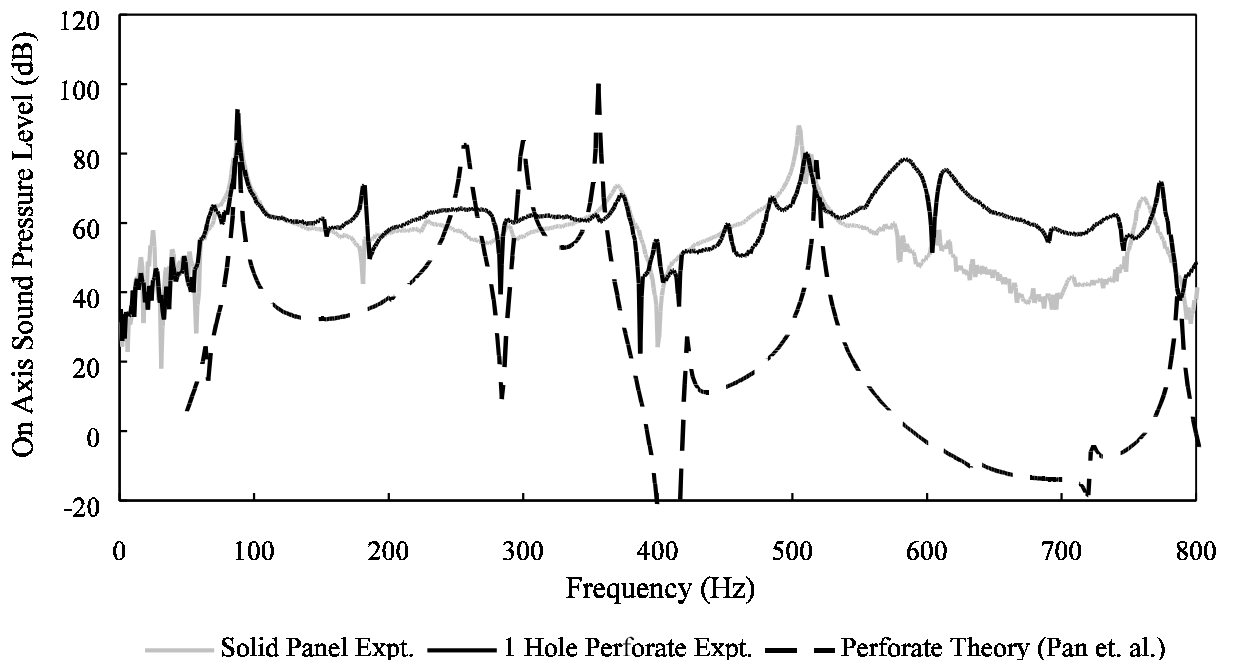
Figure 3.8   The effect of an uncontrolled panel with a single 47.5mm square hole on the sound radiation from a solid panel mounted behind it.

——— Solid Panel Expt.   ———22 x 10 Perforate Expt. — — 22 x 10 Perforate Theory
(extended Pan et al.)
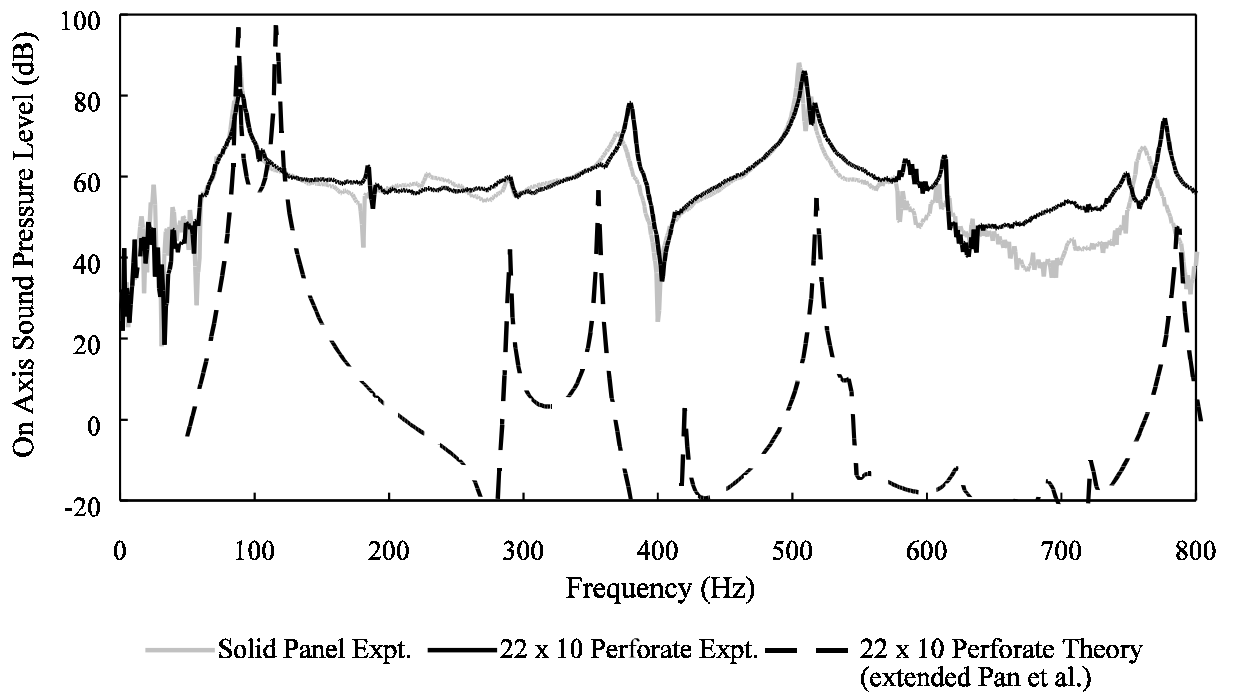
Figure 3.9   The effect of an uncontrolled panel with an array of 22 × 10, φ = 6mm holes on the sound radiation from a solid panel mounted behind it.

——— Solid Panel Expt.   ———56 x 41 Perforate Expt. — — 56 x 41 Perforate Theory
(extended Pan et al.)

Figure 3.10   The effect of an uncontrolled panel with an array of 22 × 10, φ = 6mm holes on the sound radiation from a solid panel mounted behind it.

It can be seen that the theory generally massively overpredicts the passive control that is achieved. At some frequencies system resonances are predicted to increase the sound radiated by the overall panel system.
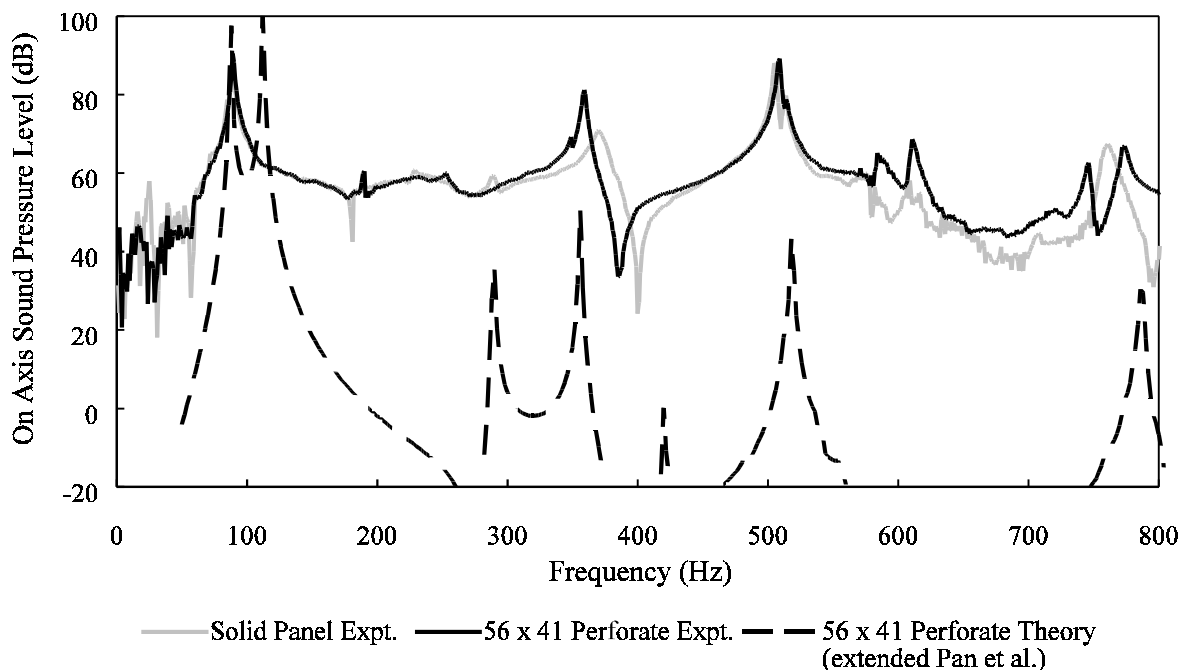
In an attempt to explain the large discrepancy between the theory and experimental work, it was decided to investigate the assumption that the acoustic pressure in the air cavity between the solid primary panel and the perforated control panel is constant. Measurement of the pressure between the two panels using a Brüel and Kjær microphone with a probe attachment, directed through the holes in the perforated panel, confirmed that the acoustic pressure (with the solid primary panel excited by a low frequency pure tone (335Hz)) was definitely non-uniform. As this pressure is not uniform, the driving force on the perforated control panel cannot be calculated by the distributed force that this pressure is assumed to exert on the perforated panel (Section 3.2.2). Instead, the pressure field varies significantly over the panel area. The lack of uniformity of the measured acoustic pressure in the space between the two panels is probably a result of the space being in the near field of the radiating panel or that the lateral dimensions of the panels are not really small, relative to the wavelength. This property of the sound field incident on the perforated panel has to be taken into account if the theoretical analysis is to be useful. This may be possible by reformulating the nearfield radiation of the primary panel in terms of evanescent duct modes in the cavity. This type of model would be extremely complex, and is not considered further in this thesis. Fortunately however, the analysis is not as complex as it might be because Figures 3.8, 3.9 and 3.10 show that the vibration of the perforated panel forced by the acoustic field contributes little to the far field sound radiation when compared to the radiation from the

primary panel transmitted through the holes in the perforated panel. This is because the part of the sound field reflected by the perforated panel back towards the solid panel eventually escapes to the far field. The only significant effect of the perforated panel is to change the phase of the radiated field with no corresponding change in amplitude. Thus, it would seem valid to assume, that in the absence of control forces acting on the perforated panel, the radiated sound field may be approximated by the sound field radiated by the solid primary panel alone. This is the assumption made in the next chapter when calculating the contribution of the solid panel to the radiated field when the perforated panel is driven by active control forces. This result is in agreement with investigations which show that below 1000Hz, thin perforated sheets provide negligible transmission loss (Schultz, 1986).

Because the theoretical model described here was clearly inadequate (for the reasons given), theoretical and experimental results for the array of perforated control sources have not been shown. Theoretical active control was in general 15-30dB greater than that afforded passively by the perforated panels alone, and amounted to some 80-100dB total attenuation globally. Physically, this could be considered absolute control, and not surprisingly, was not observed in practice.

3.4   CONCLUSIONS

A coupled system of equations have been developed to predict the level of active noise attenuation achievable using a perforated control source. The model overpredicts the amount of passive attenuation that the perforate provides when no control force is applied to it because the assumption of a uniform pressure in the cavity between them does not appear to be valid. This contributes to the vast overprediction that the model calculates when an optimised control force is also applied. Measurements show that the passive attenuation is in fact, very small, and can probably be neglected, to simplify the analysis.

Chapter 4

DISTRIBUTED SOURCE ANALYSIS OF A PERFORATED PANEL AS AN ACTIVE CONTROL SOURCE

4.1   INTRODUCTION

Experimental results presented in Chapter 3 suggest that the coupled analysis of the solid primary - perforated control panel system is inadequate for describing the passive effects that the control panel has on the radiation from the primary. It is therefore also inadequate for predicting the amount of *active* attenuation that may be achieved.

In this chapter the assumption of a constant pressure in the cavity between the solid primary panel and the perforated control panel is examined with a view to simplifying the theoretical analysis of the primary-control panel system.

Instead of coupling the motion of the two panels motion via the internal pressure, a distributed source model is examined where the radiation from each panel is considered separately, and the panels are considered to be uncoupled acoustically. Though a similar analysis to that in Chapter 3 is undertaken, here any number of primary forces, control forces and error sensors are considered. The theoretical study is extended to consider minimising the total acoustic power output of the two panel system.

Chapter 4 Distributed source analysis of a perforated control source

The model is used to predict the maximum noise reduction which is achievable when actively minmising the sound pressure at a single error sensor by controlling the vibration of a perforated control panel placed in front of a primary radiating panel. The analytical results are supported by experimental data for a solid rectangular primary panel and a perforated control panel of similar size.

4.2   THEORETICAL ANALYSIS

As demonstrated in the previous chapter, the assumption used in the model, that the sound field between the two panels is uniform is not valid. Based on the experimental results shown in Figures 3.8, 3.9 and 3.10, it may be assumed that the effect of the front perforated panel on the sound radiation at the solid panel is negligible, allowing for significant simplification of the theory. Instead of some complex coupling between each panels' radiation, it can be assumed that the panels radiate independently of each other. That is, the sound field generated by the solid panel does not affect the response of the solid part of the perforated panel and the sound field radiated by the perforated panel does not affect the response of the solid panel. Hence a simple addition of the far field sound pressure levels resulting from each source (including sound from the rear of the perforated panel reflected from the solid panel and back through perforated panel) can be made.

The equations of motion for the perforated front panel are derived for excitation by a number of point control forces, f_{c_i}. As no coupling between the primary panel and the control panel is considered, optimum control forces are derived for each control position to minimise the sum of the primary and control panel sound radiation at some point in the radiated field, or to minimise the total acoustic power output of the system.

4.2.1   PHYSICAL ARRANGEMENT

The physical model to be analysed is similar to that given in Section 3.2.1, however here the analysis is generalised to consider n_p primary forces and n_c control sources, minimised at n_e error sensors. It consists of a vibrating rectangular panel of dimensions L_x, L_y, thickness h and point

excitations f_{p_i} at $\boldsymbol{\sigma}_{p_i} = (x_{p_i}, y_{p_i})$, located on the $z = -L_z$ plane. In front of the primary panel, a second simply supported panel (the control panel) is installed on the $z = 0$ plane and is surrounded by an infinite rigid baffle. In the control panel there is an $H_x \times H_y$ array of rectangular holes, each of which has dimensions L_{xh} by L_{yh}. The location of the centre of the p, q^{th} hole is given by Equation 3.1.

A number of point control forces, f_{c_i}, are applied at locations $\boldsymbol{\sigma}_{c_i} = (x_{c_i}, y_{c_i})$ on the perforated panel surface to minimise the sound radiated into a semi-infinite space.

4.2.2   PERFORATED CONTROL PANEL RESPONSE

The displacement w_c of the control panel is described by the differential equation of motion in Equation (3.2); however, in this case for n_c control forces, the quantity p_{tot} is given by

$$p_{tot} = p_{int} - p_{ext} + \sum_{i=1}^{n_c} f_{c_i} \delta(\boldsymbol{\sigma} - \boldsymbol{\sigma}_{c_i}), \qquad (4.1)$$

where p_{int} and p_{ext} are the internal and external sound pressures evaluated on the front perforated panel surfaces. Based on the results described in Section 3.3.2, they are assumed to be negligible compared to the control force. The quantity $\delta(\boldsymbol{\sigma} - \boldsymbol{\sigma}_{c_i})$ is the Dirac delta function and f_{c_i} is the ith point control force applied at the ith control force location $\boldsymbol{\sigma}_{c_i}$ on the perforated control panel. The quantity $\boldsymbol{\sigma} = (x, y)$ represents the coordinates of any location on the front panel surface.

Solving the differential equation of motion (Equation (3.2)) by substituting in Equations (4.1), (3.4) and (3.6) and integrating over the control panel surface the following system of equations is obtained;

$$\mathbf{w}_c = \mathbf{Y}_c \mathbf{P}_c.$$

(4.2)

The control panel modal displacement amplitude matrix $\mathbf{w}_c$ is an $n_m \times 1$ matrix defined by Equation (3.8), the panel modal admittance matrix $\mathbf{Y}_c$ is an $n_m \times n_m$ diagonal matrix given by Equation (3.9)

The quantity $\mathbf{P}_c$ is an $n_m \times 1$ matrix represented as shown in Equation (3.11), however here the element corresponding to the *m,n* mode is

$$P_{c_{m,n}} = \frac{1}{A_c} \int_{A_c} \psi_{m,n}(\sigma) p_{tot}(\sigma) d\sigma = \sum_{i=1}^{n_c} \psi_{m,n}(x_{c_i}, y_{c_i}) f_{c_i},$$

(4.3)

so that

$$\mathbf{P}_c = \mathbf{\Psi}_c \mathbf{f}_c.$$

(4.4)

$\mathbf{\Psi}_c$ is a $n_m \times n_c$ matrix of the form

$$\mathbf{\Psi}_c = \begin{bmatrix} \psi_1(\sigma_{c_1}) & \cdots & \psi_1(\sigma_{c_{n_c}}) \\ \vdots & \ddots & \vdots \\ \psi_{n_m}(\sigma_{c_1}) & \cdots & \psi_{n_m}(\sigma_{c_{n_c}}) \end{bmatrix}$$

(4.5)

and $\mathbf{f}_c$ is the column vector representing the n_c control forces.

4.2.3   PRIMARY PANEL RESPONSE

Similarly the primary panel modal displacement amplitude $\mathbf{w}_p$ (Equation (3.17)) may be calculated as

$$\mathbf{w}_p = \mathbf{Y}_p \mathbf{P}_p.$$

(4.6)

The panel modal admittance matrix $\mathbf{Y}_p$ is an $n_m \times n_m$ diagonal matrix with the diagonal element corresponding to the mode m,n given by Equation (3.19) and the $n_m \times 1$ modal force vector is

$$\mathbf{P}_p = \mathbf{\Psi}_p \mathbf{f}_p, \tag{4.7}$$

where $\mathbf{\Psi}_p$ is a $n_m \times n_p$ matrix of the form

$$\mathbf{\Psi}_p = \begin{bmatrix} \psi_1(\sigma_{p_1}) & \cdots & \psi_1(\sigma_{p_{n_p}}) \\ \vdots & \ddots & \vdots \\ \psi_{n_m}(\sigma_{p_1}) & \cdots & \psi_{n_m}(\sigma_{p_{n_p}}) \end{bmatrix} \tag{4.8}$$

and $\mathbf{f}_p$ is the column vector representing the n_p primary forces.

4.2.4   FARFIELD SOUND PRESSURE

The farfield sound pressure is generated by superposition of the fields radiated by the solid primary panel and the perforated control panel. Reflections of the field radiated by the control panel from the primary panel are incorporated by calculating the pressure from a virtual control panel located behind the primary panel.

It is appreciated that the sound field radiated by the solid panel and that radiated by the back of the perforated panel will suffer multiple reflections between the two panels before finally escaping to the far field. However, at each reflection from the perforated panel, some of the sound will escape through the holes. It can be shown easily that for a single frequency source, the sound emanating from the perforated panel as a result of all the reflections can be represented as a single harmonic wave. Thus the assumption made in this analysis that all of the energy from the primary panel and the back side of the control panel escapes through the perforated panel with no reflection results only in an error in the phase of the resulting calculated control force for

maximum noise reduction. However, the amount of sound level reduction calculated is not affected.

Making the previously discussed assumption that the perforated panel has a negligible effect on the sound field radiated by the solid panel, the acoustic pressure in the farfield at the ith error sensor as a result of mode m,n on the primary solid panel may be calculated as follows;

$$p_{p_{m,n_i}} = -\frac{\rho \omega^2}{2\pi} \int_{A_p} w_{p_{m,n}}(\sigma) \frac{e^{-jkr_{p_i}}}{|\mathbf{r}|_i} d\sigma \ , \tag{4.9}$$

where r_{p_i} is the distance from the element $d\sigma$ on the primary panel surface to the ith error sensor, defined later in Equation (4.15a), and $|\mathbf{r}|_i$ is the distance from the centre of the control panel to the ith error sensor.

Because

$$w_{p_{m,n}}(\sigma) = w_{p_{m,n}} \psi_{m,n}(\sigma) \ , \tag{4.10}$$

the $n_e \times 1$ column vector representing the contribution of the primary panel to the acoustic pressure at the n_e error sensors due to all modes is given by

$$\mathbf{p}_p = \mathbf{Z}_p \mathbf{w}_p \ , \tag{4.11}$$

where $\mathbf{Z}_p$ is the $n_e \times n_m$ modal radiation transfer function matrix given by

$$\mathbf{Z}_p = -\frac{\rho\omega^2}{2\pi}\begin{bmatrix} \displaystyle\int_{A_p}\psi_1(\boldsymbol{\sigma})\frac{e^{-jkr_{p_1}}}{|\mathbf{r}|_1}\,d\boldsymbol{\sigma} & \cdots & \displaystyle\int_{A_p}\psi_{n_m}(\boldsymbol{\sigma})\frac{e^{-jkr_{p_1}}}{|\mathbf{r}|_1}\,d\boldsymbol{\sigma} \\[4pt] \vdots & \ddots & \vdots \\[4pt] \displaystyle\int_{A_p}\psi_1(\boldsymbol{\sigma})\frac{e^{-jkr_{p_{n_e}}}}{|\mathbf{r}|_{n_e}}\,d\boldsymbol{\sigma} & \cdots & \displaystyle\int_{A_p}\psi_{n_m}(\boldsymbol{\sigma})\frac{e^{-jkr_{p_{n_e}}}}{|\mathbf{r}|_{n_e}}\,d\boldsymbol{\sigma} \end{bmatrix}. \tag{4.12}$$

Similarly, for the perforated control panel

$$\mathbf{p}_c = \mathbf{Z}_c\,\mathbf{w}_c, \tag{4.13}$$

where $\mathbf{Z}_c$ is the $n_e \times n_m$ modal radiation transfer function matrix, given by

$$\mathbf{Z}_c = -\frac{\rho\omega^2}{2\pi}\begin{bmatrix} \displaystyle\int_{A_c}\psi_1\frac{e^{-jkr_{c_1}}}{|\mathbf{r}|_1}\,d\boldsymbol{\sigma} + \int_{A_c}\psi_1\frac{e^{-jkr_{v_1}}}{|\mathbf{r}|_1}\,d\boldsymbol{\sigma} & \cdots & \displaystyle\int_{A_c}\psi_{n_m}\frac{e^{-jkr_{c_1}}}{|\mathbf{r}|_1}\,d\boldsymbol{\sigma} + \int_{A_c}\psi_{n_m}\frac{e^{-jkr_{v_1}}}{|\mathbf{r}|_1}\,d\boldsymbol{\sigma} \\[4pt] \vdots & \ddots & \vdots \\[4pt] \displaystyle\int_{A_c}\psi_1\frac{e^{-jkr_{c_{n_e}}}}{|\mathbf{r}|_{n_e}}\,d\boldsymbol{\sigma} + \int_{A_c}\psi_1\frac{e^{-jkr_{v_{n_e}}}}{|\mathbf{r}|_{n_e}}\,d\boldsymbol{\sigma} & \cdots & \displaystyle\int_{A_c}\psi_{n_m}\frac{e^{-jkr_{c_{n_e}}}}{|\mathbf{r}|_{n_e}}\,d\boldsymbol{\sigma} + \int_{A_c}\psi_{n_m}\frac{e^{-jkr_{v_{n_e}}}}{|\mathbf{r}|_{n_e}}\,d\boldsymbol{\sigma} \end{bmatrix}. $$

$$\tag{4.14}$$

It may be observed here that any computational implementation of this analysis requires the evaluation of the Rayleigh integral for a large number of cases, particularly when integrating over the surface of the control panel, A_c. Computationally this is not difficult, but it is extremely time consuming due to the iterative procedures that must be used. As an alternative Appendix A suggests some of the practical methods of calculation of the radiation transfer function matrices.

The distances r_{c_i} and r_{v_i} are the distances to the ith error sensor from the elements $d\boldsymbol{\sigma}$ on the control panel surface and a *virtual* control panel surface (corresponding to the radiation from the rear of the control panel, reflected by the primary panel) respectively.

The distances r_{p_i}, r_{c_i} and r_{v_i} from the corresponding panels to the ith error sensor at elevation θ_i and azimuth ϕ_i, may be approximated by

$$r_{p_i} \approx |\mathbf{r}|_i + L_z - \frac{1}{k}\left[\left(\frac{\alpha_{p_i} x}{L_x}\right) + \left(\frac{\beta_{p_i} y}{L_y}\right)\right], \tag{4.15a}$$

$$r_{c_i} \approx |\mathbf{r}|_i - \frac{1}{k}\left[\left(\frac{\alpha_{c_i} x}{L_x}\right) + \left(\frac{\beta_{c_i} y}{L_y}\right)\right] \tag{4.15b}$$

and

$$r_{v_i} \approx |\mathbf{r}|_i + 2L_z - \frac{1}{k}\left[\left(\frac{\alpha_{v_i} x}{L_x}\right) + \left(\frac{\beta_{v_i} y}{L_y}\right)\right]. \tag{4.15c}$$

Here

$$\alpha_{p_i} = kL_x \sin\theta_{p_i}\cos\phi_{p_i}, \quad \beta_{p_i} = kL_y \sin\theta_{p_i}\sin\phi_{p_i},$$

$$\alpha_{c_i} = kL_x \sin\theta_i\cos\phi_i, \quad \beta_{c_i} = kL_y \sin\theta_i\sin\phi_i, \tag{4.16a,b,c}$$

$$\alpha_{v_i} = kL_x \sin\theta_{v_i}\cos\phi_{v_i}, \quad \beta_{v_i} = kL_y \sin\theta_{v_i}\sin\phi_{v_i},$$

$$\theta_{p_i} = \arctan\left(\frac{|\mathbf{r}|_i \tan\theta_i}{|\mathbf{r}|_i + L_z}\right), \quad \phi_{p_i} = \arctan\left(\frac{|\mathbf{r}|_i \tan\phi_i}{|\mathbf{r}|_i + L_z}\right) \tag{4.17a,b}$$

and

$$\theta_{v_i} = \arctan\left(\frac{|\mathbf{r}|_i \tan\theta_i}{|\mathbf{r}|_i + 2L_z}\right), \quad \phi_{v_i} = \arctan\left(\frac{|\mathbf{r}|_i \tan\phi_i}{|\mathbf{r}|_i + 2L_z}\right). \tag{4.17c,d}$$

So the total farfield sound pressure is

$$\mathbf{p}_{tot} = \mathbf{p}_p + \mathbf{p}_c \tag{4.18}$$

and therefore the pressure amplitude squared is:

$$\sum_{i=1}^{ne} |\mathbf{p}_{tot}|^2 = \mathbf{p}_p \mathbf{p}_p^{H} + \mathbf{p}_p \mathbf{p}_c^{H} + \mathbf{p}_c \mathbf{p}_p^{H} + \mathbf{p}_c \mathbf{p}_c^{H} , \tag{4.19}$$

where ^{H} represents the Hermitian transpose of the matrix (the complex conjugate and transpose of a matrix).

From Equations (4.6) and (4.11);

$$\mathbf{p}_p = \mathbf{Z}_p \mathbf{Y}_p \mathbf{P}_p = \mathbf{Z}_p \mathbf{Y}_p \boldsymbol{\Psi}_p \mathbf{f}_p \tag{4.20}$$

and similarly from Equations (4.2) and (4.13)

$$\mathbf{p}_c = \mathbf{Z}_c \mathbf{Y}_c \mathbf{P}_c = \mathbf{Z}_c \mathbf{Y}_c \boldsymbol{\Psi}_c \mathbf{f}_c . \tag{4.21}$$

4.2.5   QUADRATIC OPTIMISATION OF THE FARFIELD SOUND PRESSURE

The magnitude of the sound pressure calculated using Equation (4.19) can be re-expressed as a quadratic function of the complex control forces $\mathbf{f}_c$;

$$\sum_{i=1}^{ne} |\mathbf{p}_{tot}|^2 = \mathbf{f}_c^{H} \mathbf{A} \mathbf{f}_c + \mathbf{f}_c^{H} \mathbf{b} + \mathbf{b}^{H} \mathbf{f}_c + c \tag{4.22}$$

where

$$\mathbf{A} = \boldsymbol{\Psi}_c^{H} \mathbf{Y}_c^{H} \mathbf{Z}_c^{H} \mathbf{Z}_c \mathbf{Y}_c \boldsymbol{\Psi}_c , \tag{4.23}$$

$$\mathbf{b} = \boldsymbol{\Psi}_c^{H} \mathbf{Y}_c^{H} \mathbf{Z}_c^{H} \mathbf{Z}_p \mathbf{Y}_p \boldsymbol{\Psi}_p \mathbf{f}_p \tag{4.24}$$

and

$$c = \mathbf{f}_p^{\text{H}} \, \mathbf{\Psi}_p^{\text{H}} \, \mathbf{Y}_p^{\text{H}} \, \mathbf{Z}_p^{\text{H}} \, \mathbf{Z}_p \, \mathbf{Y}_p \, \mathbf{\Psi}_p \, \mathbf{f}_p.$$

(4.25)

Equation (4.22) has a unique (global) minimum, which is the optimum control force required to produce a minimum mean square sound pressure averaged over n_e error microphones located at some observation points $\mathbf{r}_i$. The optimum value of the control force vector is (Nelson et. al., 1987)

$$\mathbf{f}_c^{opt} = -\mathbf{A}^{-1}\mathbf{b} \ .$$

(4.26)

The resulting minimum mean square sound pressure is (Nelson et. al., 1987)

$$\sum_{i=1}^{ne} |\mathbf{p}_{tot}|_{\min}^2 = c - \mathbf{b}^{\text{H}} \mathbf{A}^{-1} \mathbf{b} \ .$$

(4.27)

4.2.6 QUADRATIC OPTIMISATION OF THE TOTAL ACOUSTIC POWER

Alternatively, it is advantageous to express the error criteria as the total acoustic power output of the system, and to minimise this. The total acoustic power output W_{tot} is the sum of both the primary source power output W_p and the control source power output W_c where these may be determined either by a near field measure, integrating over the surface of each panel (Snyder and Tanaka, 1993*a*) of the form

$$W_{tot} = \frac{1}{2} Re \left\{ j\omega \int_{A_p} w_p(\boldsymbol{\sigma}_p) \, p_{tot}^*(\boldsymbol{\sigma}_p) \, d(\boldsymbol{\sigma}_p) + j\omega \int_{A_c} w_c(\boldsymbol{\sigma}_c) \, p_{tot}^*(\boldsymbol{\sigma}_c) \, d(\boldsymbol{\sigma}_c) \right\} ,$$

(4.28)

or by a far field measure, integrating over a hemisphere enclosing the radiating surfaces as

$$W_{tot} = \int\limits_{\phi=0}^{2\pi} \int\limits_{\theta=0}^{\pi/2} \frac{|p_{tot}(\mathbf{r})|^2}{2\rho c} r^2 \sin\theta \, d\theta \, d\phi .$$

(4.29)

In this case it is much more convenient to consider the latter case which can be re-expressed as

$$W_{tot} = \frac{r^2}{2\rho c} \int\limits_{0}^{2\pi} \int\limits_{0}^{\pi/2} p_{tot}^*(\mathbf{r}) \, p_{tot}(\mathbf{r}) \sin\theta \, d\theta \, d\phi .$$

(4.30)

Expressing the total pressure in the farfield as the sum of contributions from the primary and control panels the following is obtained

$$W_{tot} = \frac{r^2}{2\rho c} \int\limits_{0}^{2\pi} \int\limits_{0}^{\pi/2} \left[(p_p(\mathbf{r}) + p_c(\mathbf{r}))^* (p_p(\mathbf{r}) + p_c(\mathbf{r})) \right] \sin\theta \, d\theta \, d\phi .$$

(4.31)

The acoustic pressure $p(\mathbf{r})$ at the observer location $\mathbf{r}$ can be written in terms of the Rayleigh integral (Equation (4.9)) so that the primary and control pressures can be expressed as the product of the modal radiation transfer function $\mathbf{z}(\mathbf{r})$ and the modal displacement vectors as

$$p_p(\mathbf{r}) = \mathbf{z}_p(\mathbf{r}) \mathbf{w}_p$$

(4.32)

and

$$p_c(\mathbf{r}) = \mathbf{z}_c(\mathbf{r}) \mathbf{w}_c ,$$

(4.33)

where

$$\mathbf{z}_p(\mathbf{r}) = -\frac{\rho \omega^2}{2\pi} \left[\int\limits_{A_p} \psi_1 \frac{e^{-jkr_{p\mathbf{r}}}}{|\mathbf{r}|_{\mathbf{r}}} dA \quad \cdots \quad \int\limits_{A_p} \psi_{n_m} \frac{e^{-jkr_{p\mathbf{r}}}}{|\mathbf{r}|_{\mathbf{r}}} dA \right]$$

(4.34)

and

$$\mathbf{z}_c(\mathbf{r}) = -\frac{\rho\,\omega^2}{2\,\pi}\left[\int\limits_{A_c}\psi_1\frac{e^{-jkr_{c_\mathbf{r}}}}{|\mathbf{r}|_\mathbf{r}}\,dA + \int\limits_{A_c}\psi_1\frac{e^{-jkr_{v_\mathbf{r}}}}{|\mathbf{r}|_\mathbf{r}}\,dA \;\cdots\; \int\limits_{A_c}\psi_{n_m}\frac{e^{-jkr_{c_\mathbf{r}}}}{|\mathbf{r}|_\mathbf{r}}\,dA + \int\limits_{A_c}\psi_{n_m}\frac{e^{-jkr_{v_\mathbf{r}}}}{|\mathbf{r}|_\mathbf{r}}\,dA\right].$$

(4.35)

Again, appendix A, offers a practical method for the implementation of the Rayleigh integral for the efficient computational evaluation of the radiation transfer function matrices.

Using Equations (4.32) and (4.33), Equation (4.31) can be re-written in terms of the primary and control panel modal displacement vectors as

$$W_{tot} = \begin{bmatrix}\mathbf{w}_p\\\mathbf{w}_c\end{bmatrix}^{\mathrm{H}}\begin{bmatrix}\mathbf{\Pi}_{pp} & \mathbf{\Pi}_{cp}^{\mathrm{H}}\\\mathbf{\Pi}_{cp} & \mathbf{\Pi}_{cc}\end{bmatrix}\begin{bmatrix}\mathbf{w}_p\\\mathbf{w}_c\end{bmatrix},$$

(4.36)

where

$$\mathbf{\Pi}_{pp} = \frac{r^2}{2\rho c}\int\limits_0^{2\pi}\int\limits_0^{\pi/2}\mathbf{z}_p^{\mathrm{H}}(\mathbf{r})\,\mathbf{z}_p(\mathbf{r})\,\sin\theta\,d\theta\,d\phi\,,$$

(4.37)

$$\mathbf{\Pi}_{cp} = \frac{r^2}{2\rho c}\int\limits_0^{2\pi}\int\limits_0^{\pi/2}\mathbf{z}_c^{\mathrm{H}}(\mathbf{r})\,\mathbf{z}_p(\mathbf{r})\,\sin\theta\,d\theta\,d\phi$$

(4.38)

and

$$\mathbf{\Pi}_{cc} = \frac{r^2}{2\rho c}\int\limits_0^{2\pi}\int\limits_0^{\pi/2}\mathbf{z}_c^{\mathrm{H}}(\mathbf{r})\,\mathbf{z}_c(\mathbf{r})\,\sin\theta\,d\theta\,d\phi\,.$$

(4.39)

In this case the error criterion W can also be expressed as a quadratic function of the complex control forces $\mathbf{f}_c$;

$$W_{tot} = \mathbf{f}_c^H \mathbf{A}_W \mathbf{f}_c + \mathbf{f}_c^H \mathbf{b}_W + \mathbf{b}_W^H \mathbf{f}_c + c_W \tag{4.40}$$

where

$$\mathbf{A}_W = \mathbf{\Psi}_c^H \mathbf{Y}_c^H \mathbf{\Pi}_{cc} \mathbf{Y}_c \mathbf{\Psi}_c , \tag{4.41}$$

$$\mathbf{b}_W = \mathbf{\Psi}_c^H \mathbf{Y}_c^H \mathbf{\Pi}_{cp} \mathbf{Y}_p \mathbf{\Psi}_p \mathbf{f}_p \tag{4.42}$$

and

$$c_W = \mathbf{f}_p^H \mathbf{\Psi}_p^H \mathbf{Y}_p^H \mathbf{\Pi}_{pp} \mathbf{Y}_p \mathbf{\Psi}_p \mathbf{f}_p . \tag{4.43}$$

Again, the optimum control forces are given by an equation of the form

$$\mathbf{f}_c^{opt} = -\mathbf{A}_W^{-1} \mathbf{b}_W . \tag{4.44}$$

The resulting minimum sound power is (Nelson et. al., 1987)

$$W_{min} = c_W - \mathbf{b}_W^H \mathbf{A}_W^{-1} \mathbf{b}_W . \tag{4.45}$$

4.3   NUMERICAL RESULTS

Both the quadratic optimisation of the farfield sound pressure and the total system sound power

output were programmed in double precision FORTRAN and run on a SUNSPARC10 computer.

For the experimental results shown in Section 4.4 below, the farfield sound pressure at a single

point was used as the error criterion, and the resulting radiation pattern calculated, as it was

uncomplicated to measure experimentally.   The numerical results presented in this section

however, concentrate on minimising the radiated sound power, a global measurement of

controllability, although a measure beyond the scope of the experimental work presented in this

chapter (instead see Chapter 5).

The primary numerical difficulty arises when implementing Equations (4.37)-(4.39) to determine

the submatrices $\mathbf{\Pi}_{pp}$, $\mathbf{\Pi}_{cp}$ and $\mathbf{\Pi}_{cc}$ for the sound power weighting matrix. The primary panel self-

weighting matrix, $\mathbf{\Pi}_{pp}$, is clearly necessarily real and symmetric, as is $\mathbf{\Pi}_{cc}$, the control panel self-

weighting matrix. Both these matrices contain diagonal terms representing the self-impedance

of the structural mode and off-diagonal terms representing the modifications in radiation

efficiency due to the co-existence of the other structural modes. It has been shown that for a

simply supported panel, only modes with like index pairs (ie. pairs of (odd,odd) and (even,even)

modes and the combinations of (odd,even) (odd,even) and (even,odd) (even,odd) modes) will

exert a mutual influence on each other (Snyder and Tanaka, 1993*b*). The cross-weighting matrix

$\mathbf{\Pi}_{cp}$, is dense, complex and hermitian, such that the overall weighting matrix is also hermitian.

Chapter 4 Distributed source analysis of a perforated control source

Secondly the evaluation of the weighting submatrices $\mathbf{\Pi}_{cp}$ and $\mathbf{\Pi}_{cc}$ is numerically demanding due to the huge number of sub-calculations to account for the holes in the control panel required *inside* the numerical integration used to evaluate Equations (4.38) & (4.39).

The sound power radiation submatrix calculations required over 100CPU hours for the variations undertaken here.   Due to the large number of calculations required, the numerical results presented in this chapter consider only the first 20 modes of vibration.

To observe the effect of varying the solid area of the panel on the maximum attenuation achievable, four perforated panels with a 22x10 array of holes were modelled and mounted a distance L_z=0.03m in front of the primary panel. The perforation diameters of the control panels were d = 6, 10, 12 and 15mm, such that the panels had perforation geometry factors and solid areas as shown in Table 4.1. Note that the ligament efficiencies for the panels with the largest holes fall out of the range of applicability of the theory developed in Chapter 2. Though a concern, the results for the modal resonance frequencies of these perforates (Table 4.2) are considered to be of sufficient accuracy to enable at least a qualitative comparison between the control performance of the perforates. The theoretical resonance frequency of the first 14 significant modes of perforated panels (up to 1000Hz) are shown in Table 4.2.

Additionally the effect of the spacing between the solid primary panel and the perforated control panel is assessed by performing theoretical calculations with L_z=0.01, 0.03 and 0.05m for a single perforation diameter of d=10mm.

Table 4.1
Perforated control panel geometry parameters.

Perforation Diameter (mm)	*XLE*	*YLE*	Solid Area
6	0.305	0.560	88%
10	-0.158	0.267	67%
12	-0.389	0.120	52%
15	-0.736	-0.100	25%

In all cases a single point primary force was located on the solid panel at (35mm,103.3mm) and one control force at (35mm,0mm) on the perforated panel. This arrangement resulted in matrices that were close to singular and consideration of further primary or control sources would require a quad-precision FORTRAN implementation to maintain accuracy.

Finally the amount of noise control provided by perforated control panels is compared to that achievable by application of a secondary point control force applied directly to the primary panel (commonly called Active Structural Acoustic Control (ASAC)) with the control source located at (35mm,0mm) on the *primary* panel.

Table 4.2

Theoretical panel resonance frequencies of perforated panels
with varying perforation diameter

Mode	Resonance Frequency (Hz) Solid	Resonance Frequency (Hz) d=6mm	Resonance Frequency (Hz) d=10mm	Resonance Frequency (Hz) d=12mm	Resonance Frequency (Hz) d=15mm
1,1	88.3	83.0	75.36	70.3	60.8
2,1	190.1	178.6	162.2	151.2	130.9
1,2	251.6	236.4	214.6	200.1	173.3
2,2	353.3	332.0	301.5	281.0	243.3
3,1	359.7	338.0	306.9	286.0	247.7
3,2	522.9	491.4	446.1	415.9	360.1
1,3	523.7	492.1	446.8	416.5	360.7
4,1	597.1	561.1	509.4	474.9	411.2
2,3	625.4	587.7	533.6	497.4	430.7
4,2	760.3	714.5	648.7	604.7	523.6
3,3	795.0	747.1	678.3	632.3	547.5
5,1	902.3	847.9	769.8	717.6	621.4
1,4	901.6	850.0	771.8	719.4	623.0
2,4	1006	945	859	800	693

4.3.1   EFFECT OF PERFORATE OPEN AREA

The effect of the open area of the perforated control panels on the controlled radiation levels and corresponding attenuation and relative control force is shown in Figures 4.1-4.4. It can be observed in Figures 4.1 & 4.2 that all of the perforated panels provide a similar level of attenuation, except near their second resonance. Here the location of the control source enables the (2,1) mode to be driven easily, shown by a drop in the relative control force magnitude at the resonance frequencies associated with this mode in Figure 4.3. In general the levels of sound power attenuation below the second resonant mode are well over 15dB, however they soon drop to between 0-4dB over a wide range. The next (even,odd) mode is the (4,1) which also shows some (slight) increase in the achievable attenuation.

The control force magnitudes (shown in Figure 4.3) show that in general the perforates with a very low solid area require a much higher control force, as may be expected given the relative area of their radiating surfaces. The (1,1) resonance of the primary panel at around 90Hz requires a large control force on all of the perforated control panels, of which the small (perforation induced) drop in corresponding resonance frequency leaves them deficient in power radiation ability.

An interesting effect occurs at around 360Hz, where the second (odd,odd) radiation mode of the primary panel conveniently has a resonance frequency similar to that of the *third* (odd,odd) radiation mode of the perforate with d=15mm. The control force required on this control panel is therefore much lower than that demanded by the other perforates. Thus it appears that if the

perforated panel is properly tuned to resonate at the frequencies at which sound is radiated by the primary source, it may be an effective control source.

4.3.2   EFFECT OF PANEL SPACING

The effect of the spacing (for $d = 10$mm) between the primary panel and the perforated control panels on the controlled levels and corresponding attenuation is shown in Figures 4.5 & 4.6. It is shown that there is little discernible difference between the amount of attenuation that can be achieved. This is not surprising, since the spacing between the two panels is very much less than the wavelength in all cases.

As may be expected given these results, the corresponding relative control force magnitude and phase are also so close to each other as to be indistinguishable when graphed, and have therefore not been shown.
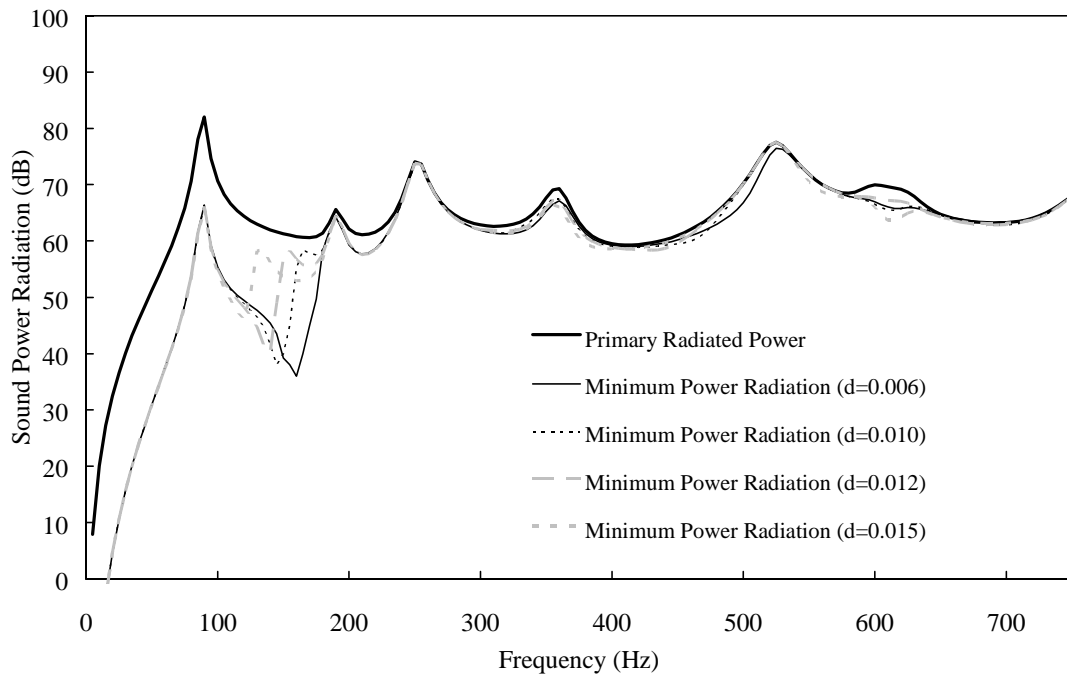
Figure 4.1   Primary and controlled radiated sound power using perforated control panels with perforation diameters d=6, 10, 12 and 15mm and L_z=0.03m.
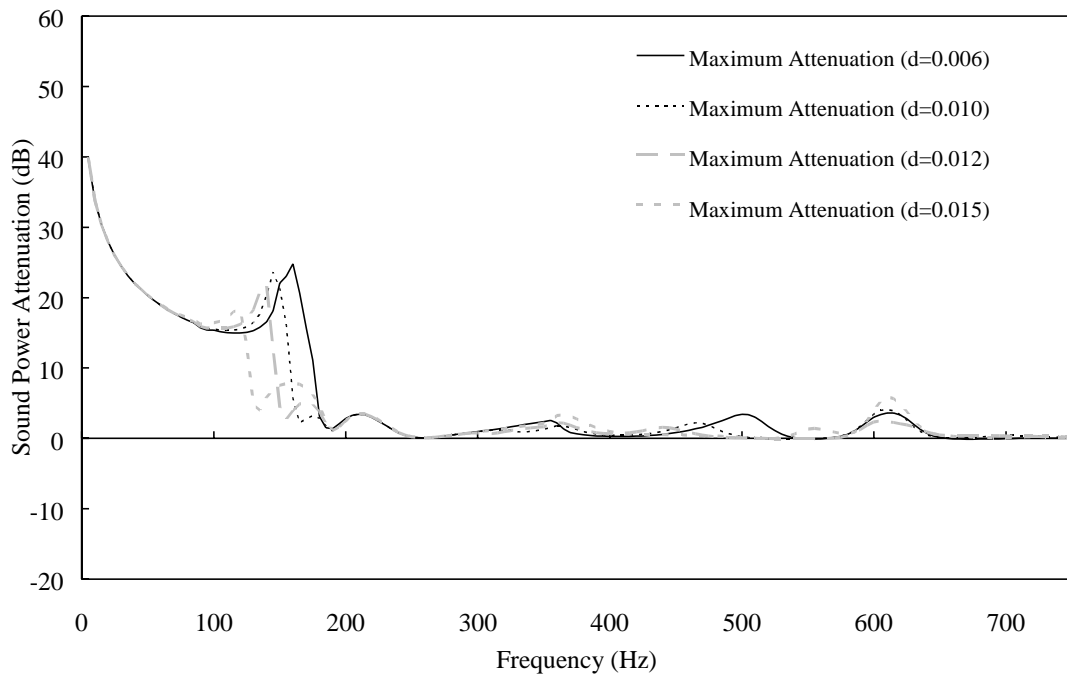

Figure 4.2   Attenuation using perforated control panels with perforation diameters d=6, 10, 12 and 15mm and L_z=0.03m.
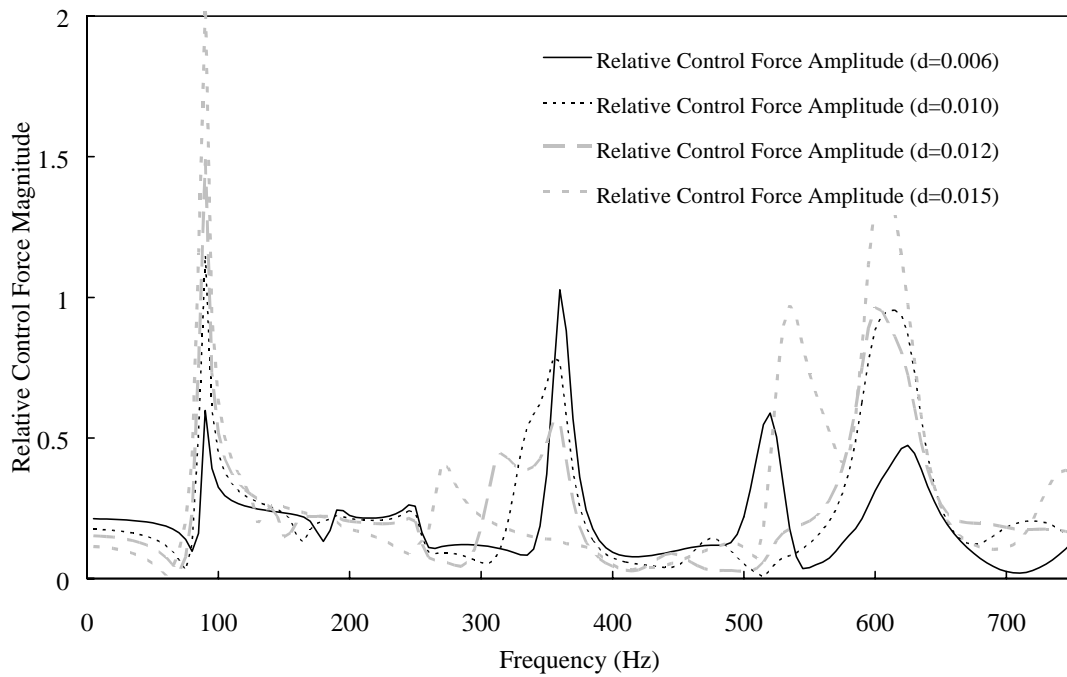
Figure 4.3 Optimum control force magnitude relative to a 1N input force using perforated control panels with perforation diameters d=6, 10, 12 and 15mm.
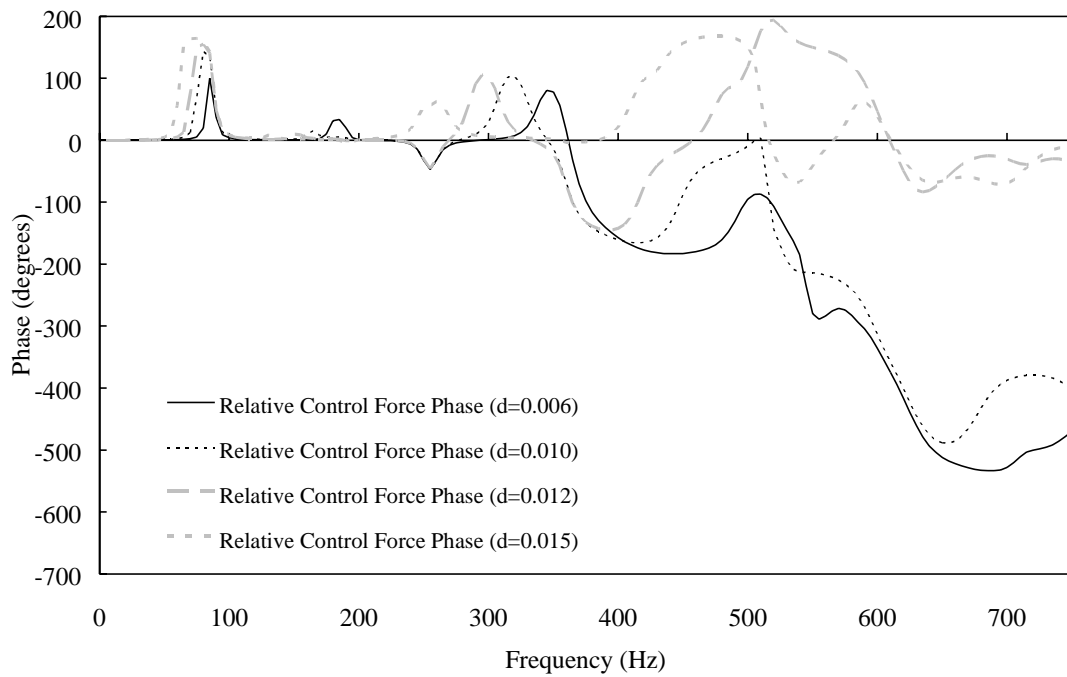

Figure 4.4 Optimum control force phase (unwrapped) relative to a 1N input force using perforated control panels with perforation diameters d=6, 10, 12 and 15mm.
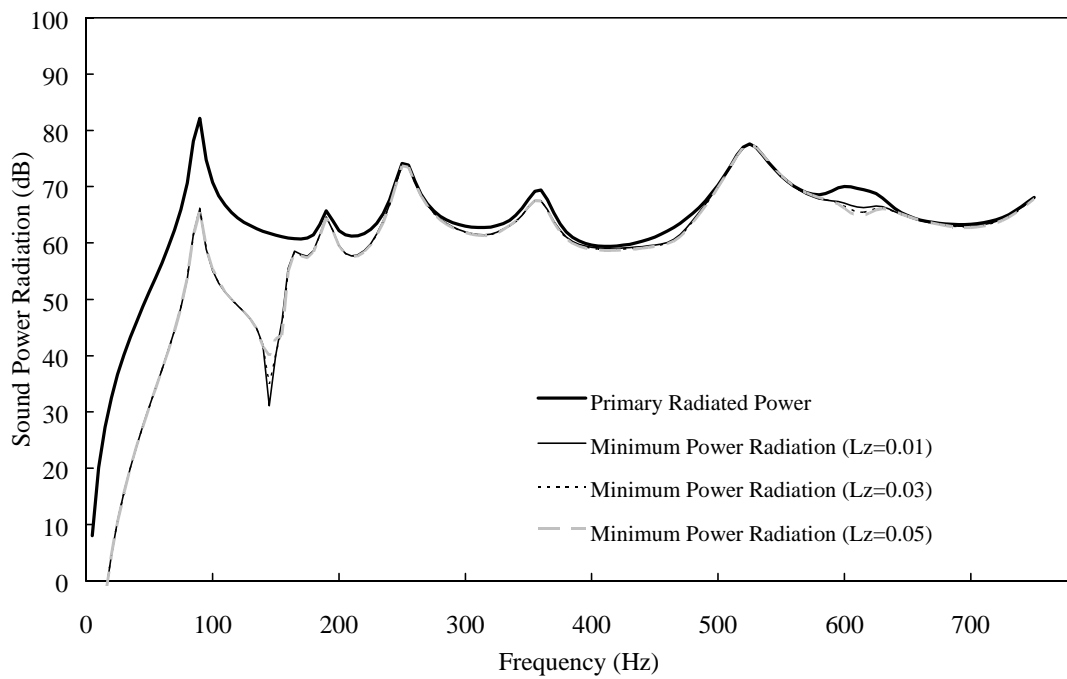
Figure 4.5   Primary and controlled radiated sound power using a perforated control panel with d=10mm and spacing L_z=0.01, 0.03 and 0.05m.
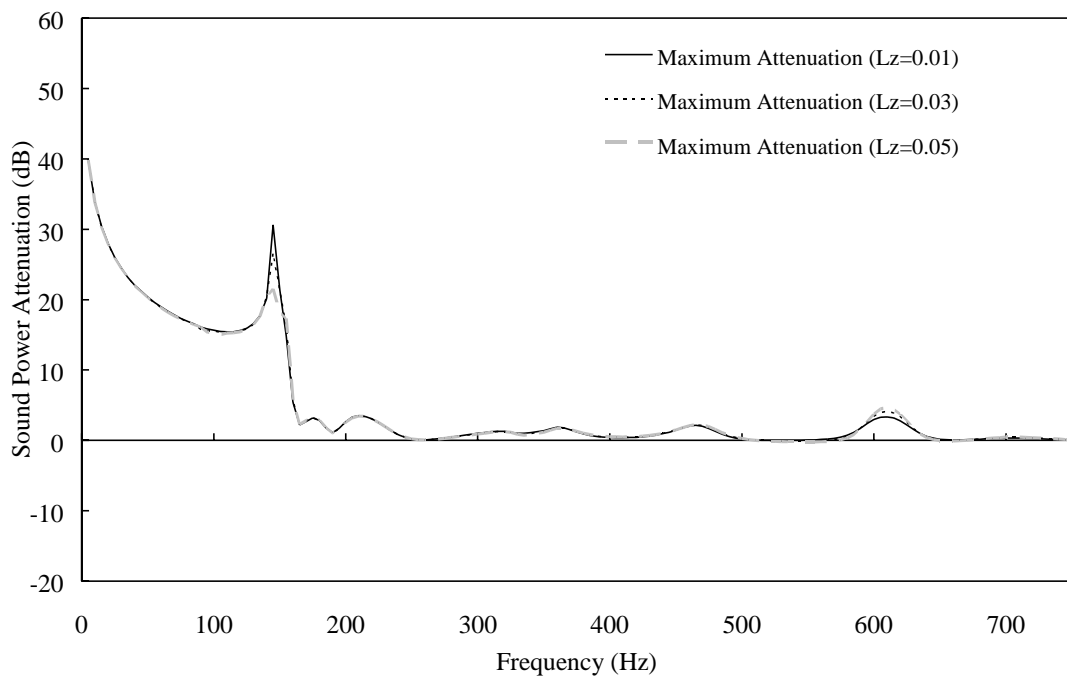

Figure 4.6   Attenuation using a perforated control panel with d=10mm and spacing L_z=0.01, 0.03 and 0.05m.

4.3.3 PERFORATED CONTROL SOURCE COMPARED TO ASAC

The controlled radiated sound power and corresponding attenuation and relative control force for control by a secondary perforated panel is compared to control by direct Active Structural Acoustic Control (ASAC) in Figures 4.7-4.10.

The low frequency attenuation is clearly much better with ASAC (Figure 4.7 & 4.8), particularly at the first resonance of the primary panel. Note that in regions where control is difficult (or impossible) such as around 250Hz and 410Hz *both* control methods fail to provide any attenuation. This is due to the poor coupling of the control source on the panels to the modes operating at these frequencies.

The control force acting on the perforated panel is generally lower than that required for ASAC (Figure 4.9). There are however several large peaks in the perforated panel control force, due to the matching (and mismatching) of its resonance frequency with those of the solid primary panel. These large, sudden changes in control force are not apparent when applying ASAC, as the resonances of the control source, of course, exactly match those of the primary source. Given that in this analysis the thickness of the primary and perforated control panels is the same (h=0.002m), it appears that if the primary structure were much thicker, requiring a correspondingly higher control force, then the control force on a perforated control panel could be very much less than that required for ASAC.
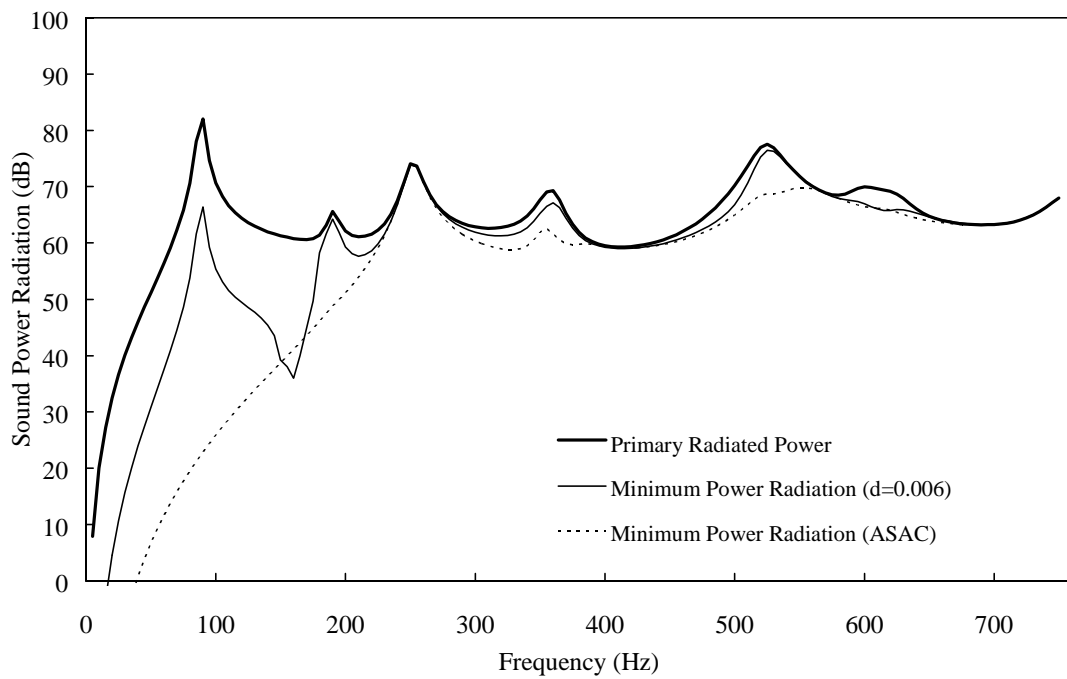
Figure 4.7　　Primary and controlled radiated sound power using a perforated control panel (d=10mm, L_z=0.03) compared to ASAC.
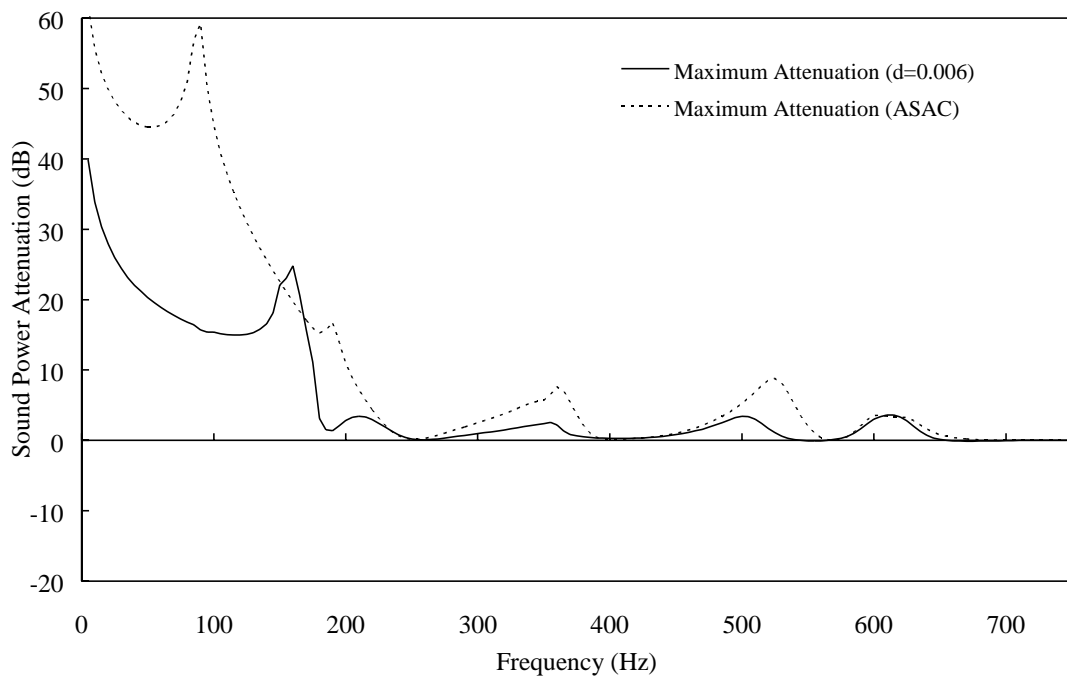

Figure 4.8　　Attenuation using a perforated control panel (d=10mm, L_z=0.03) compared to ASAC.

103

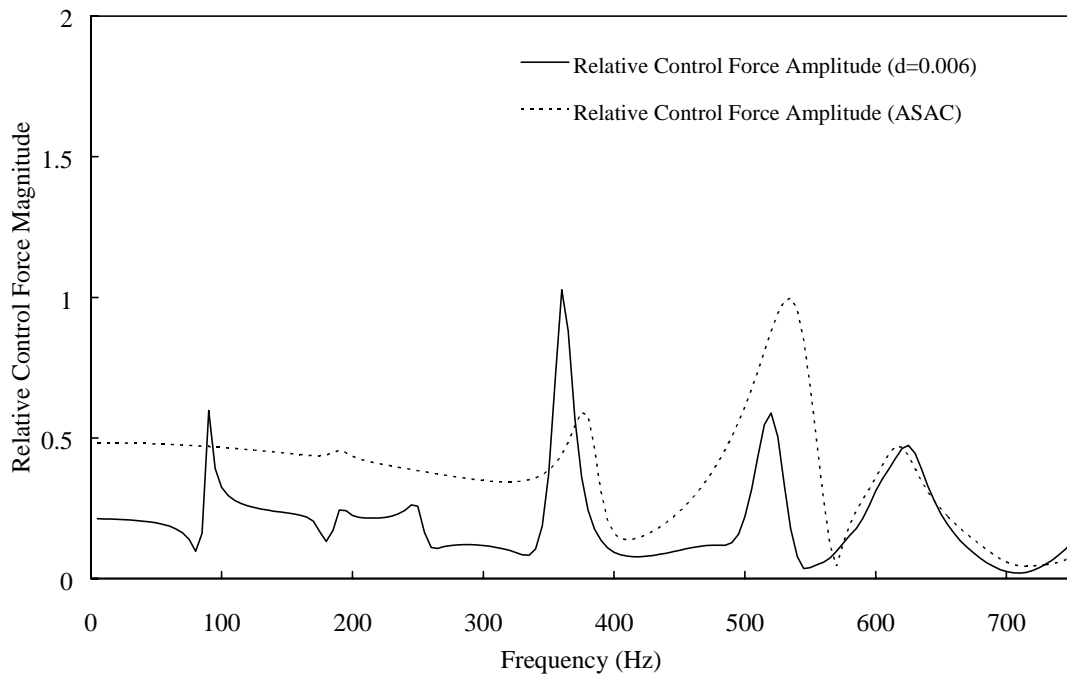**Figure 4.9**   Optimum control force magnitude relative to a 1N input force using a perforated control panel (*d*=6mm, L_z=0.03m) compared to ASAC.
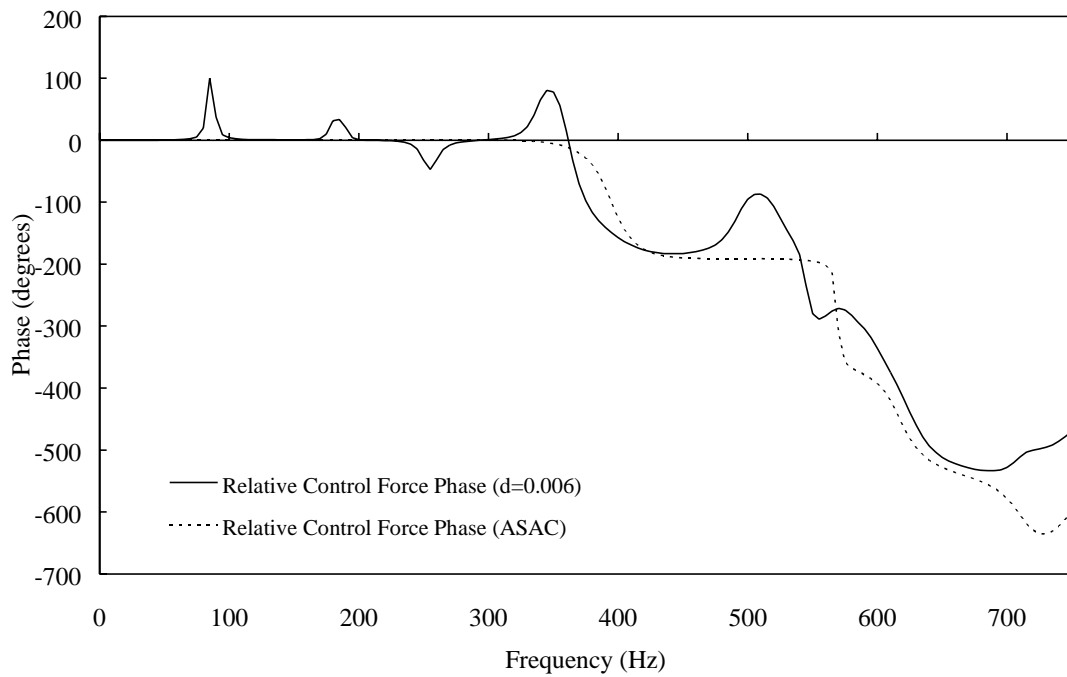

Figure 4.10   Optimum control force phase relative to a 1N input force using a perforated control panel (*d*=6mm, L_z=0.03m) compared to ASAC.

104

4.4 EXPERIMENTAL VERIFICATION

4.4.1 PROCEDURE

The same experimental arrangement as used in Section 3.3.1 was used. Two different control panels were tested, located a distance of 20mm from the primary panel. The first control panel was perforated with a diagonal array of 22x10, 6mm diameter holes and the second with an array of 56x41, 3.25mm diameter holes. Both were controlled using a pair of piezoceramic actuators, one on each side of the panel, at its centre. These panels were mounted in a frame with spring steel edges to approximate simply supported boundary conditions.

The radiated sound field was measured in an anechoic chamber using a Brüel & Kjær one inch microphone mounted on a turntable. The turntable rotated through 180° so that the microphone traversed a horizontal arc of radius 1.8m around the panel centre, perpendicular to the plane of the panel (see Figure 3.3). A Brüel & Kjær level recorder was used to record the measurements on a polar plot.

4.4.2 RESULTS AND DISCUSSION

Theoretical and measured levels of active noise control achieved by the perforated panels can be seen in Figures 4.11 to 4.16. The theoretical results were calculated by minimising the sound pressure level at the error sensor location, in this case at $\mathbf{r} = 1.7$m, $\phi = 0°$ and $\theta = 90°$ or $40°$. In Figures 4.11 and 4.12 it can be seen that the theory closely predicts the level of noise control that can be achieved at 335Hz using the 22x10 perforated control. High levels of attenuation over relatively wide azimuthal angles can be observed with the error sensor at both $\theta = 40°$ and 90°. Close to the baffle, at $\theta = 0°$ and 180°, both the primary and controlled levels differ from

that predicted by the theory due to diffraction around the baffle edges. In Figures 4.13 & 4.14, results are presented for a primary driving force at 365Hz, and again the levels of noise control predicted by the theory show a strong resemblance to the experimental results; however, the measured level of control at $\theta = 40°$ (with the error sensor at $\theta = 40°$, Figure 4.13) is clearly not sufficiently close to the theoretical optimum to give good measured control at $\theta = 140°$ as well. In Figure 4.14 it can be seen that the error sensor was misaligned by approximately 5°, with the symmetry of the experimental setup leading to two minimisations at $\theta = 85°$ and 95°.

Theoretical and experimental results using a 56x41 perforated panel are shown in Figures 4.15 & 4.16, and agreement between the two is generally good. Again diffraction around the edges of the baffle has produced spurious results near $\theta = 0°$ and 180° in both the primary and controlled sound field. Even though the 56x41 perforate has a far smaller solid surface area than the 22x10 perforate, high levels of control are predicted and measured at the error sensor.

In each case, reductions of the order of 25-35dB were achieved at the error sensor, and in the case with the error sensor at $\theta = 40°$, a second minimisation generally occurred at $\theta = 140°$ as predicted by the theory, and as would be expected due to the symmetry of the experimental setup. Generally the theory overpredicted the amount of control that can be achieved, and given the limitations on the accuracy of phase and amplitude of the signal output from the electronic controller it is understandable that these predicted levels were not reached in practice.

Unfortunately, even though the levels of attenuation are high at the error sensor, noise levels are often increased in other regions (generally closer to the baffle), thus reducing the global

effectiveness of the control. Employing more error sensors and control actuators on the perforate, or implementing a sound power sensor, would produce better overall control and thus would be necessary in an implementation to control noise radiated by electric power transformers.

Figure 4.11   Comparison between theory for a 22x10 perforate and measured data at 335Hz with the error sensor at 40°.

Figure 4.12   Comparison between theory for a 22x10 perforate and measured data at 335Hz with the error sensor at 90°.

Figure 4.13 Comparison between theory for a 22x10 perforate and measured data at 365Hz with the error sensor at 40°.
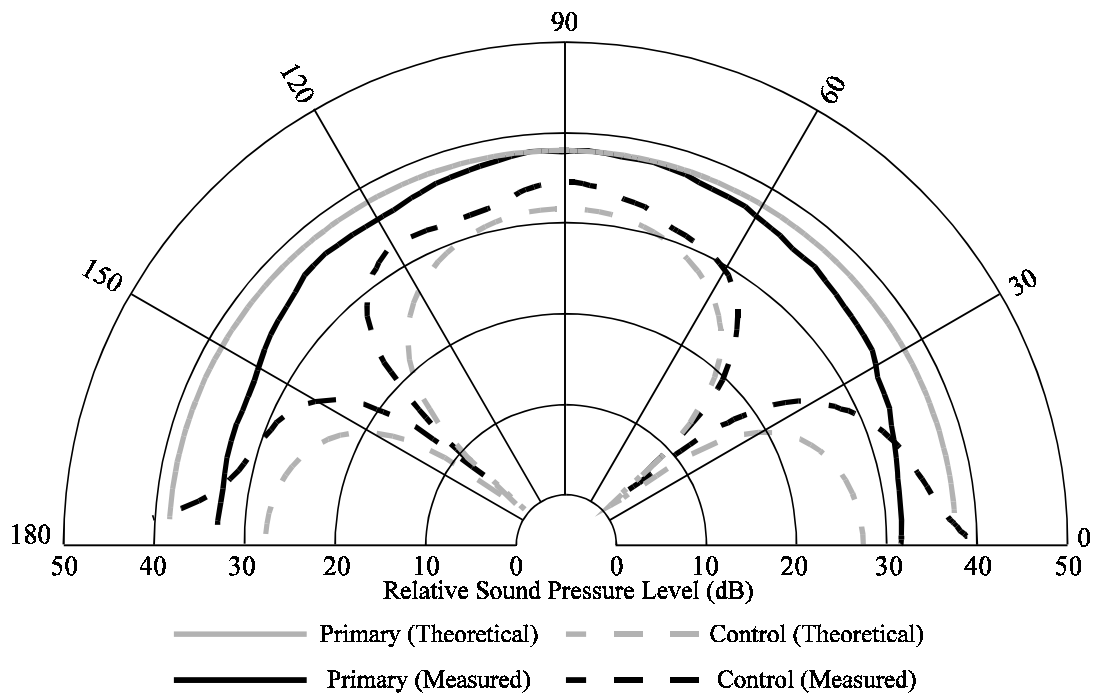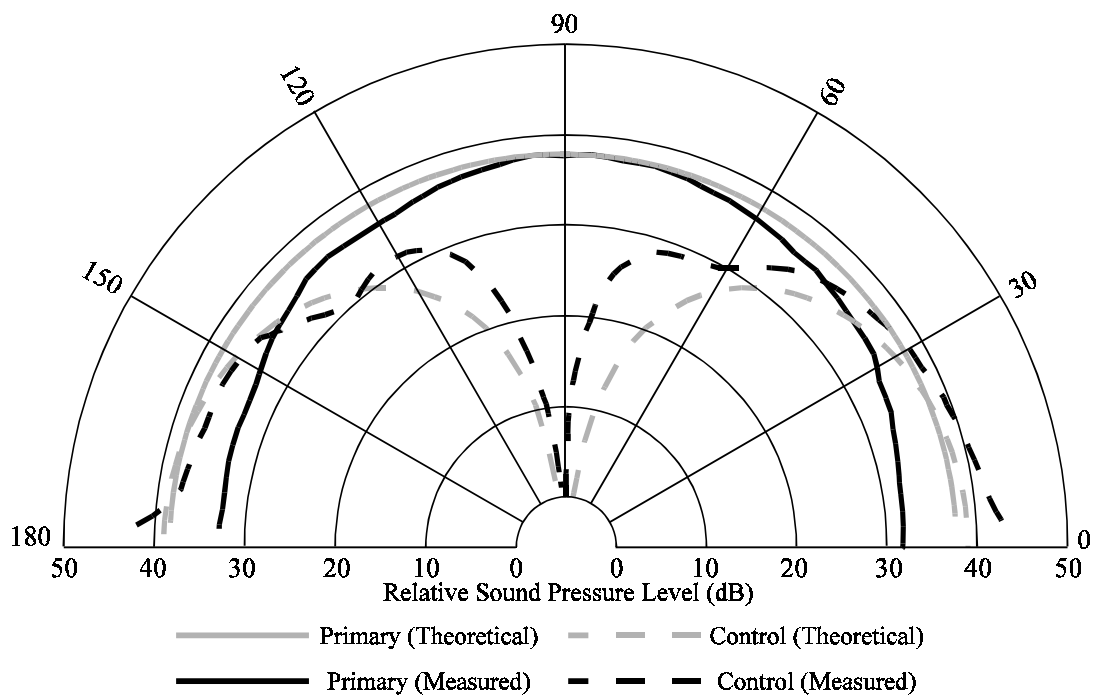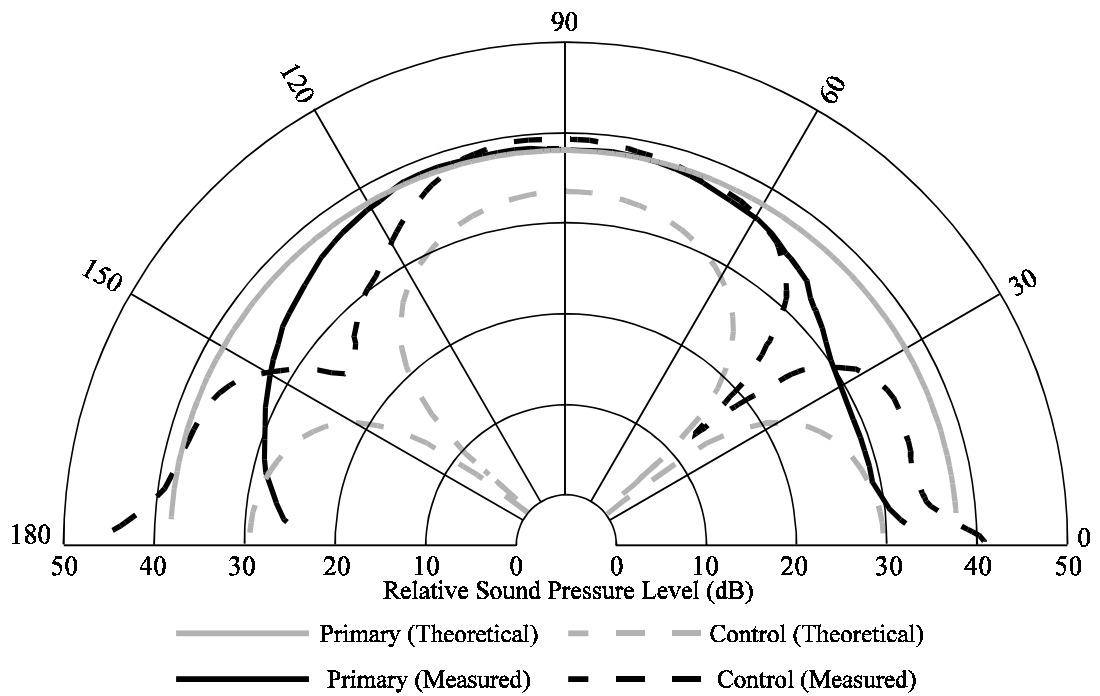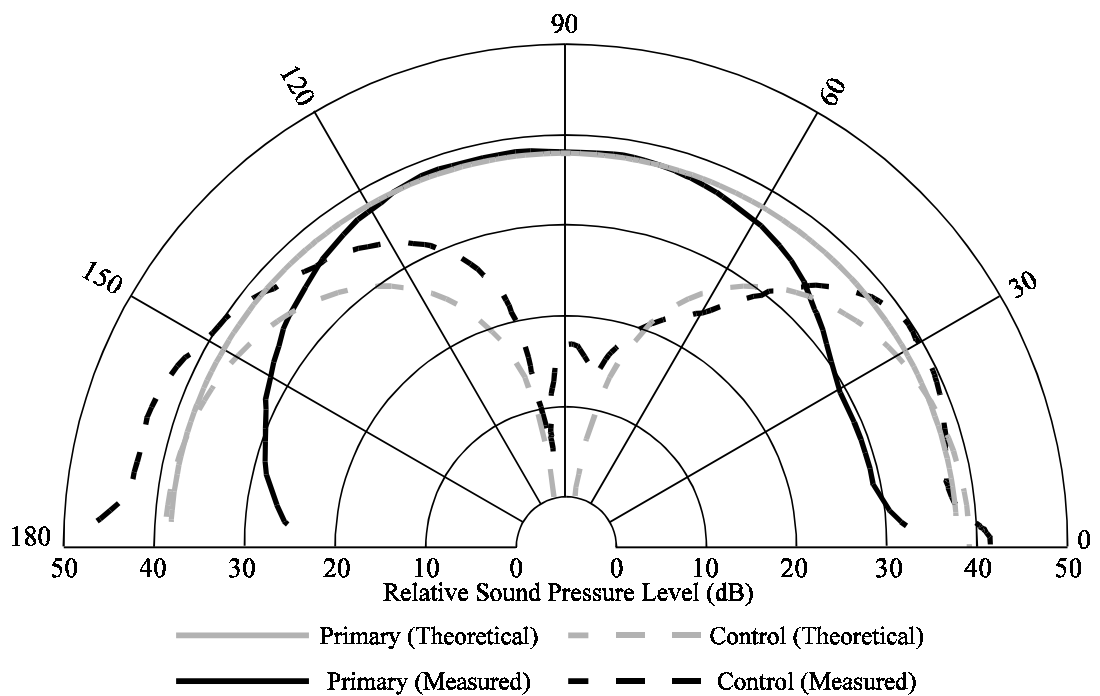

Figure 4.14 Comparison between theory for a 22x10 perforate and measured data at 365Hz with the error sensor at 90°.
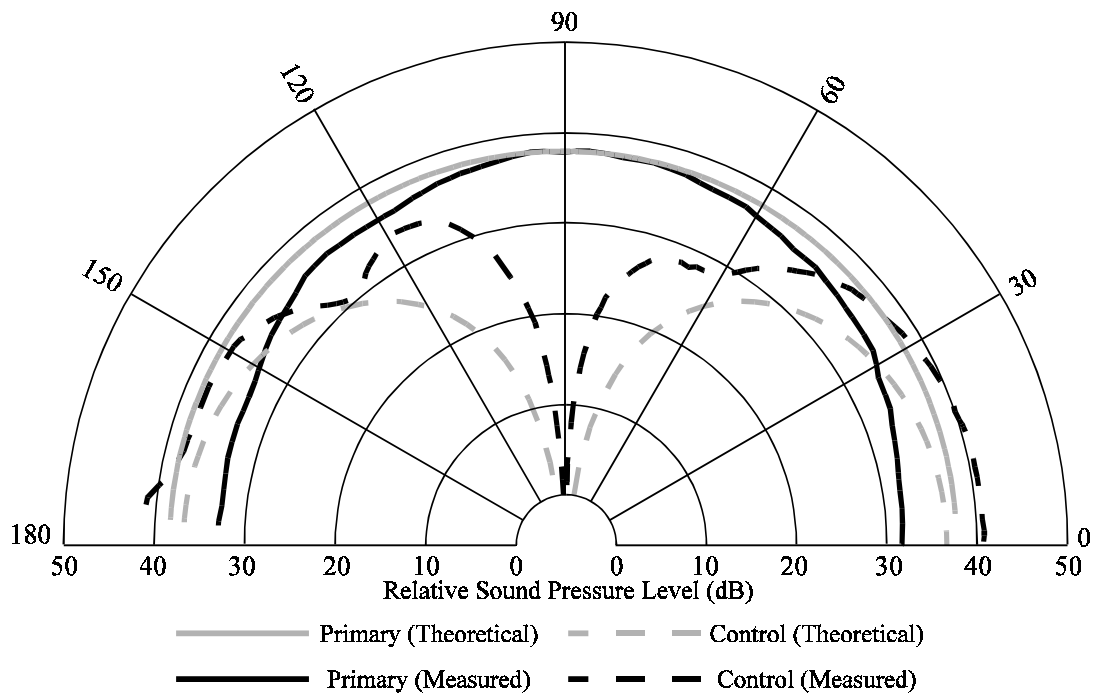
Figure 4.15   Comparison between theory for a 56x41 perforate and measured data at 335Hz with the error sensor at 90°.
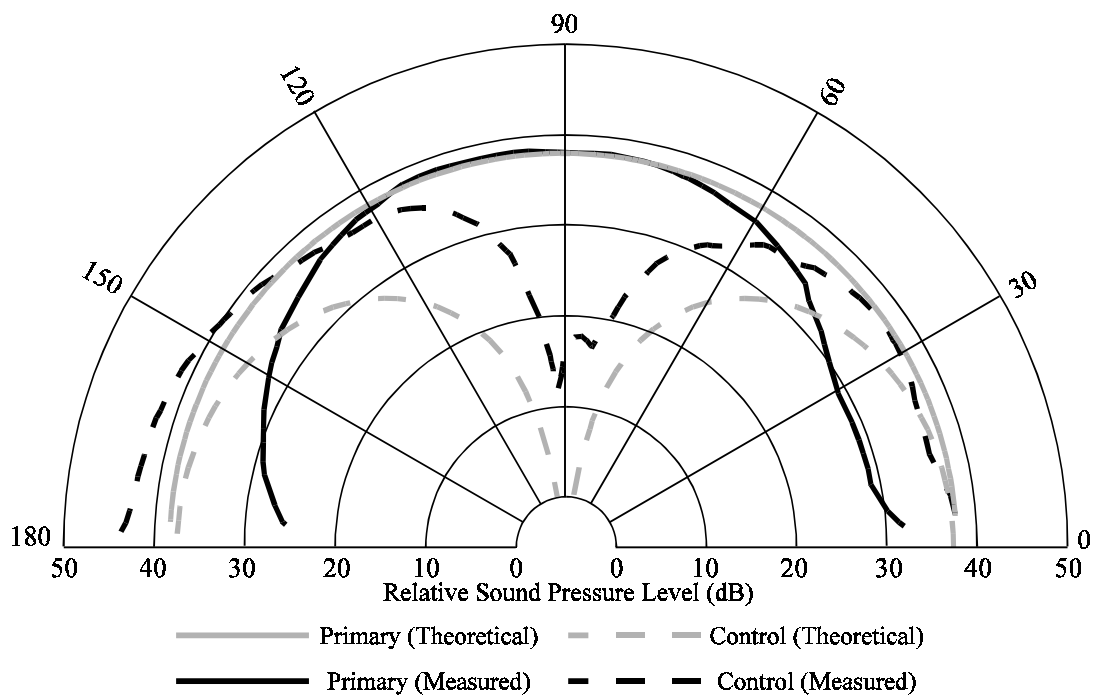

Figure 4.16   Comparison between theory for a 56x41 perforate and measured data at 365Hz with the error sensor at 90°.

4.5   CONCLUSIONS

A new model for predicting the level of active control achievable by placing a perforated control panel in front of a solid noise radiating panel has been presented. This model is more accurate and easier to implement computationally than previous models. It has been applied not only to the prediction of the sound pressure level reductions but to sound power level reductions achievable using a number of perforated control panels driven by a single centrally located actuator.

Numerical results, calculated when minimising the radiated sound power, showed that panels with a low solid area required a higher relative control force than those with a high solid area. The overall levels of control that could be achieved, however, were similar. The attenuation levels were shown to be independent of the spacing of the perforated control panel from the primary panel provided that this was much less than an acoustic wavelength.

It was shown that using perforated control panels would not produce global attenuation levels as high as could be expected using ASAC, but that the control force required to drive the perforated control panel could often be much less than the control force required for ASAC.

Experimental results verified the numerical model when the sound pressure level at a point in the farfield was minimised. It was found that in general, the model over-predicted the experimental data, and noise reductions in the vicinity of the error sensor were often achieved at the expense of increased noise levels elsewhere. Better global levels of noise control could be expected if more error sensors and control actuators were used, or if the overall acoustic power level were

minimised rather than the acoustic pressure at one point in the farfield.

Chapter 5

ACOUSTIC SENSING OF GLOBAL ERROR CRITERIA

5.1   INTRODUCTION

The total sound power radiating from a vibrating structure is often preferred to acoustic pressure at a point (or points) as an error function for an active noise control system (Borgiotti, 1990; Elliott *et al.*, 1991; Snyder *et al.*, 1993*a*). It provides a measure that, when minimised, guarantees the best global result, however it should be noted that radiation or acoustic intensity may still increase in some directions (Cunefare and Koopmann, 1991). One way of achieving a measure of sound power for the control system to minimise is to use a combination of modal filtering and distributed structural vibration sensors (Snyder *et al.* 1995*a*). This is acceptable when the control source is a secondary vibration source on the structure as used in applications of ASAC. However on some structures it is inconvenient to apply ASAC due to factors such as their physical size, large internal impedances presented to the vibration control actuators or susceptibility to stress related failure. For these structures, acoustic control sources may provide the only option; either traditional loudspeakers, or some distributed perforated control structure as detailed in the first part of this thesis. In this case, the *structural measure* of acoustic power provided by distributed PVDF film sensors no longer represents the total farfield sound power. This chapter examines the use of appropriately pre-filtered microphone signals to provide a simple and instantaneous *acoustic measure* of the farfield sound power for use as the error criterion for active control of radiated noise.

5.2   THEORETICAL ANALYSIS

The sound power radiated from a single simply supported rectangular panel is considered as the error criterion. Note that this case does not restrict the application of structural sensors to provide a measure of the radiated sound power; however it will provide a useful theoretical base onto which a *multiple source* model can be constructed. This will be done in the following chapter which will expand the theoretical analysis presented here to consider the case when the primary and control source are two separate radiating entities.

Here, an appropriate weighting matrix is calculated so that the farfield power can be determined from the normal modal displacement. This matrix contains off diagonal terms representing coupling between the various structural vibration modes.   Applying an orthonormal transformation to this weighting matrix results in a matrix of eigenvectors representing *structural transformed modes* that contribute *independently* to the radiated sound power.   It is the amplitudes of these transformed modes that have been sensed directly on the structure in previous work (Snyder *et al.*, 1995*a/b*). Here however, the farfield acoustic pressure associated with each transformed mode is related to the normal modal amplitudes via the inverse of the normal mode radiation transfer function matrix, thus allowing acoustic sensors to be used to sense the transformed mode contributions to the radiated sound power. In other words, a modal filter is defined, which decomposes a measure of the transformed modal amplitudes from the measured acoustic field. The frequency dependence of both the radiation efficiency and the shape of the transformed modes is examined. Further reductions are applied to the model to simplify the practical implementation of the modal filters, while only slightly compromising the effective

bandwidth of the transformed mode acoustic power sensors.

5.2.1 PHYSICAL ARRANGEMENT

A vibrating rectangular panel of dimensions $L_x \times L_y$, thickness h and with n_p point excitations $\mathbf{f}_p$ is located on the $z = 0$ plane as shown in Figure 5.1. In this analysis direct vibration control of the panel by n_c point control forces, given by the vector $\mathbf{f}_c$, is considered.

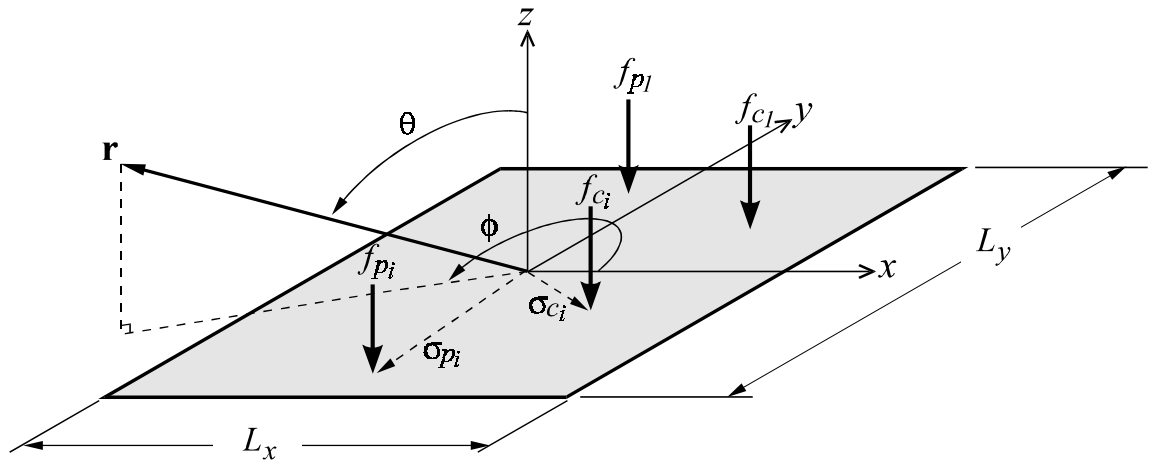**Figure 5.1**   Theoretical arrangement.

5.2.2 GLOBAL ERROR CRITERION

The general form of the error criterion is

$$J = \mathbf{w}^H \mathbf{\Pi} \mathbf{w} ,\qquad\qquad(5.1)$$

where J is the global error criterion, $\mathbf{w}$ is the modal displacement amplitude vector and $\mathbf{\Pi}$ is a $n_m \times n_m$ weighting matrix. Again, the Hermitian transpose is represented by ^{H}.

If the radiated sound power is used as the error criterion then, for a single radiating panel, the weighting matrix is similar to Equation (4.37) and can be expressed

$$\mathbf{\Pi} \ = \ \frac{r^2}{2\rho c} \int\limits_{\phi=0}^{2\pi} \int\limits_{\theta=0}^{\pi/2} \mathbf{z}^H(\mathbf{r}) \, \mathbf{z}(\mathbf{r}) \, \sin\theta \, d\theta \, d\phi \, , \qquad (5.2)$$

where the modal radiation transfer function vector $\mathbf{z}(\mathbf{r})$ is the same as $\mathbf{z}_p(\mathbf{r})$ given in Equation (4.34). The weighting matrix so produced is real and symmetric, with the diagonal terms representing the *self impedance* of the structural mode and the off-diagonal terms representing the modifications in radiation efficiency due to the co-existence of the other structural modes. The matrix is also sparse, with only the modes with like index pairs exerting a mutual influence on each other (see Section 4.3).

As the weighting matrix is real and symmetric it can be diagonalised by the orthonormal transformation;

$$\mathbf{\Pi} \ = \ \mathbf{Q} \, \mathbf{\Lambda} \, \mathbf{Q}^T \, , \qquad (5.3)$$

where $\mathbf{Q}$ is the orthonormal transformation matrix with columns representing the eigenvectors of the weighting matrix. This matrix has the property

$$\mathbf{Q}^{-1} \ = \ \mathbf{Q}^T \, . \qquad (5.4)$$

$\mathbf{\Lambda}$ is the diagonal matrix of the n_m associated eigenvalues, λ_i of $\mathbf{\Pi}$;

$$\mathbf{\Lambda} \ = \ \begin{bmatrix} \lambda_1 & 0 & \cdots & 0 \\ 0 & \lambda_2 & \cdots & 0 \\ \vdots & & \ddots & \vdots \\ 0 & 0 & \cdots & \lambda_{n_m} \end{bmatrix} . \qquad (5.5)$$

Substituting the transformation of the weighting matrix (Equation (5.3)) into Equation (5.1) shows that the total system sound power can be expressed as (Snyder *et al.*, 1993*b*)

$$W = \mathbf{w}^H \mathbf{Q} \, \boldsymbol{\Lambda} \, \mathbf{Q}^T \mathbf{w} = \mathbf{u}^H \boldsymbol{\Lambda} \, \mathbf{u} , \qquad (5.6)$$

where **u** is the transformed modal displacement amplitude vector defined by

$$\mathbf{u} = \mathbf{Q}^T \mathbf{w} . \qquad (5.7)$$

Equation (5.7) shows that each transformed mode is made up of some combination of the normal structural modes, the proportion defined by the associated eigenvector contained in **Q**.

Each transformed mode is an orthogonal contributor to the error criterion, in this case the total sound power, and so can be added linearly as

$$W = \sum_{i=1}^{n_m} \lambda_i \, |u_i|^2 . \qquad (5.8)$$

Two important properties of the transformed modes can be exploited. The first is that the eigenvalues (representing the radiation efficiency of the transformed modes) quickly become very small, so in practice it is only necessary to include the first few transformed modes to account for most of the power radiated from the panel (Borgiotti, 1990; Elliott and Johnson, 1993). The second is that the low order transformed modes (with the highest radiation efficiency) *also* converge very quickly to their correct shape by considering a limited number of structural modes (Cunefare and Currey, 1994). In practice then, it is possible to use the $n_m \times n_{tm}$ submatrix of the $n_m \times n_m$ orthonormal transformation **Q** where n_{tm} is the number of transformed modes

considered analytically. Similarly the $n_{tm} \times n_{tm}$ submatrix of the eigenvalue matrix $\mathbf{\Lambda}$ can be used with no appreciable loss of accuracy in calculating the sound power.

5.2.3 ACOUSTIC SENSING OF TRANSFORMED MODES

PVDF film sensors have been implemented to detect the transformed modal displacement amplitudes, $\mathbf{u}$, directly on the structure (Snyder *et al.*, 1993*b*/95*a*/95*b*). The farfield sound pressure radiation patterns can also be decomposed to determine the contributions from the transformed modes.

The farfield sound pressure at n_e microphone error sensors resulting from all of the *normal* structural modes is given by the $n_e \times 1$ vector

$$\mathbf{p} = \mathbf{Z}_n \mathbf{w},$$
(5.9)

where $\mathbf{Z}_n$ is the $n_e \times n_m$ normal mode radiation transfer function matrix given by

$$\mathbf{Z}_n = -\frac{\rho \omega^2}{2\pi} \begin{bmatrix} \int_A \psi_1(\boldsymbol{\sigma}) \dfrac{e^{-jkr_1}}{|\mathbf{r}_1|} d\boldsymbol{\sigma} & \cdots & \int_A \psi_{n_m}(\boldsymbol{\sigma}) \dfrac{e^{-jkr_1}}{|\mathbf{r}_1|} d\boldsymbol{\sigma} \\ \vdots & \ddots & \vdots \\ \int_A \psi_1(\boldsymbol{\sigma}) \dfrac{e^{-jkr_{n_e}}}{|\mathbf{r}_{n_e}|} d\boldsymbol{\sigma} & \cdots & \int_A \psi_{n_m}(\boldsymbol{\sigma}) \dfrac{e^{-jkr_{n_e}}}{|\mathbf{r}_{n_e}|} d\boldsymbol{\sigma} \end{bmatrix}.$$
(5.10)

In this case the distance r_i is similar to that for r_{c_i} given in Equation (4.15b).

Rearranging Equation (5.9) to decompose the normal modal displacement amplitude, $\mathbf{w}$, from the pressure field and substituting into Equation (5.6) gives

$$W = \mathbf{w}^{\mathrm{H}} \mathbf{Q} \boldsymbol{\Lambda} \mathbf{Q}^{\mathrm{T}} \mathbf{w} = \mathbf{p}^{\mathrm{H}} (\mathbf{Z}_n^{-1})^{\mathrm{H}} \mathbf{Q} \boldsymbol{\Lambda} \mathbf{Q}^{\mathrm{T}} \mathbf{Z}_n^{-1} \mathbf{p} \qquad (5.11)$$

or

$$W = \mathbf{p}^{\mathrm{H}} \mathbf{Z}_t^{\mathrm{H}} \boldsymbol{\Lambda} \mathbf{Z}_t \mathbf{p} \qquad (5.12)$$

where $\mathbf{Z}_t$ is the $n_{tm} \times n_e$ transformed mode radiation transfer function matrix (or *modal filter matrix*) which relates the pressure in the far field to each transformed modal amplitude, given by

$$\mathbf{Z}_t = \mathbf{Q}^{\mathrm{T}} \mathbf{Z}_n^{-1} . \qquad (5.13)$$

The elements of each row of this modal filter matrix represent a weighting value that, when applied to the signal from the corresponding pressure sensor and the result summed over all of the sensors, will give a measure of the transformed modal amplitude. In practice the number of error sensors (n_e) will be much less than the number of normal modes considered (n_m) and so the normal mode radiation transfer function matrix, $\mathbf{Z}_n$, will be rectangular and underdetermined. It is therefore necessary to apply the Moore-Penrose pseudoinverse of a matrix to determine $\mathbf{Z}_n^{-1}$.

The error criterion can then be expressed as a quadratic function of the complex control forces $\mathbf{f}_c$ as

$$W = \mathbf{f}_c^{\mathrm{H}} \mathbf{A} \mathbf{f}_c + \mathbf{f}_c^{\mathrm{H}} \mathbf{b} + \mathbf{b}^{\mathrm{H}} \mathbf{f}_c + c \qquad (5.14)$$

where

$$\mathbf{A} = \boldsymbol{\Psi}^{\mathrm{H}} \mathbf{Y}^{\mathrm{H}} \mathbf{Z}_n^{\mathrm{H}} \mathbf{Z}_t^{\mathrm{H}} \boldsymbol{\Lambda} \mathbf{Z}_t \mathbf{Z}_n \mathbf{Y} \boldsymbol{\Psi} , \qquad (5.15)$$

$$\mathbf{b} = \boldsymbol{\Psi}^{\mathrm{H}} \mathbf{Y}^{\mathrm{H}} \mathbf{Z}_n^{\mathrm{H}} \mathbf{Z}_t^{\mathrm{H}} \boldsymbol{\Lambda} \mathbf{Z}_t \mathbf{Z}_n \mathbf{Y} \boldsymbol{\Psi} \mathbf{f}_p \qquad (5.16)$$

and

$$c = \mathbf{f}_p^{\text{H}} \, \boldsymbol{\Psi}^{\text{H}} \, \mathbf{Y}^{\text{H}} \, \mathbf{Z}_n^{\ \text{H}} \, \mathbf{Z}_t^{\ \text{H}} \, \boldsymbol{\Lambda} \, \mathbf{Z}_t \, \mathbf{Z}_n \, \mathbf{Y} \, \boldsymbol{\Psi} \, \mathbf{f}_p. \tag{5.17}$$

Here $\boldsymbol{\Psi}$ is the mode shape matrix, similar in form to $\boldsymbol{\Psi}_p$ (given by Equation (4.8)), and $\mathbf{Y}$ is the panel modal admittance matrix, similar to $\mathbf{Y}_p$ and given by Equation (3.19). The optimum control force is given by Equation (4.44).

The eigenvalue matrix $\boldsymbol{\Lambda}$ is highly frequency dependent, and frequency weighting each transformed mode sensor output to account for the different radiation efficiency of the transformed modes has been suggested using appropriately shaped *eigenvalue filters* (Snyder *et al.*, 1993*b*). The transformed mode radiation transfer function matrix, $\mathbf{Z}_t$, is a direct function of the transformed mode shapes which, although dependent on frequency, have been shown to change by only a small amount over *small* ranges for a simply supported rectangular panel (Snyder *et al.,* 1993*b*; Naghshineh and Koopmann, 1993). This is fortunate as in a practical *frequency correct* modal filter system such as that shown in Figure 5.2, it may not be practical to store filters representing the matrix for a wide range of frequencies. Even so, for broadband control over a wide frequency range it would be much better to incorporate the frequency dependence of the radiation transfer function matrix into a single meta-filter representing the frequency dependence of both the transformed mode radiation efficiency (eigenvalues), $\boldsymbol{\Lambda}$, *and* the radiation transfer function matrix $\mathbf{Z}_t$.
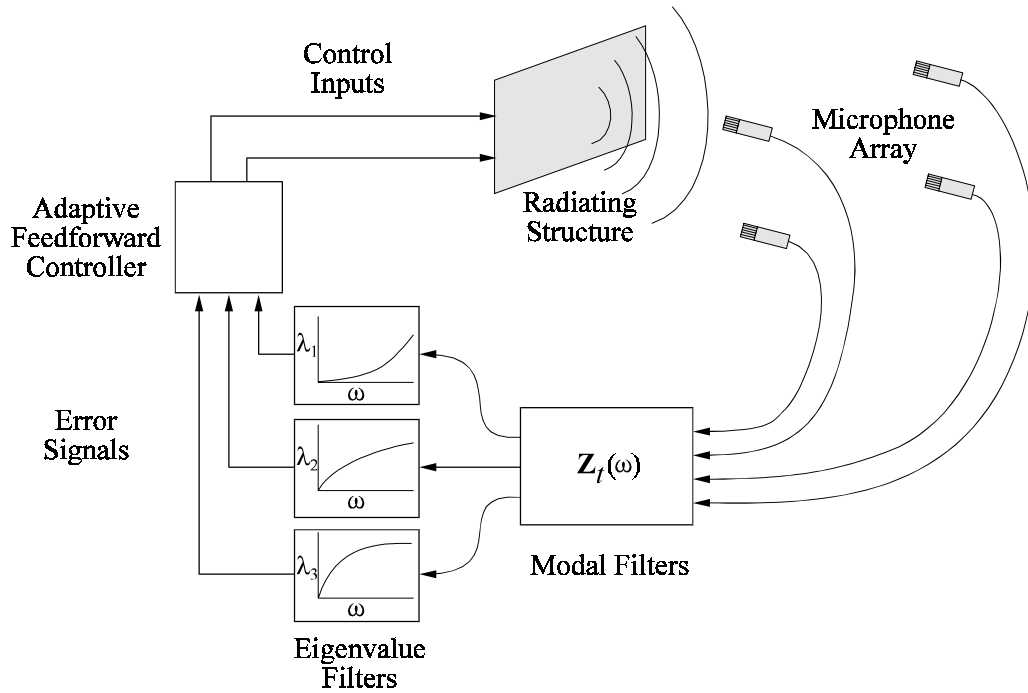
Figure 5.2   Modal filter and eigenvalue filter arrangement.

This can be achieved by normalising the radiation transfer function matrix to that at some fixed

frequency ω_f such that

$$\mathbf{Z}_t = \mathbf{K}\,\mathbf{Z}_{t|\omega_f} \tag{5.18}$$

to give the $n_{tm} \times n_{tm}$ correction matrix

$$\mathbf{K} = \mathbf{Z}_t\,\mathbf{Z}_{t|\omega_f}^{-1}. \tag{5.19}$$

If ω_f is chosen such that the transformed mode shapes at that frequency are representative of the

mode shapes over the frequency range of interest then the off diagonal terms in $\mathbf{K}$ can be ignored

with little loss in accuracy.   All of the frequency dependence of both the eigenvalue and

transformed mode radiation transfer function matrices can then be grouped into one *real $n_{tm} \times$*

n_{tm} diagonal frequency weighting matrix $\mathbf{X}$ with elements

$$\chi_{ij} = \begin{cases} k_{ij}^{*}\, \lambda_{ij}\, k_{ij}, & i = j \\ 0, & i \neq j \end{cases}. \tag{5.20}$$

Practically, this *corrected fixed frequency* modal filter system can be implemented by a simpler system such as that shown in Figure 5.3, where the modal filter $\mathbf{Z}_{t}$, isn't implemented explicitly, but is replaced by a single frequency independent weighting value $\mathbf{Z}_{t|\omega_f}$, for each transformed mode. It is also possible to implement an *uncorrected fixed frequency* filter system by not correcting the eigenvalue filter to account for the frequency dependence of the transformed mode radiation transfer function matrix (ie. $\mathbf{X} = \mathbf{\Lambda}$ rather than $\mathbf{X} = \mathbf{K}^{H}\mathbf{\Lambda}\mathbf{K}$), but still replacing the modal filter with a single weighting value from a fixed frequency ω_f. In practice this would appear to be an unnecessary complication, considering the eigenvalue filter would still need to be implemented (in fact it will be shown later that in this case, because the frequency weighting factor $\mathbf{X}$ is so flat, it can be more complicated than the accurate filter).

If these modifications are required to enable wideband control then Equation (5.12) becomes

$$W = \mathbf{p}_{n}^{\ H}\, \mathbf{Z}_{t|\omega_f}^{H}\, \mathbf{X}\ \mathbf{Z}_{t|\omega_f}\, \mathbf{p}\,. \tag{5.21}$$

Note that the only difference between this approach and the exact solution of Equation (5.12) is the small loss of accuracy introduced by ignoring the off diagonal terms of the correction matrix $\mathbf{K}$.
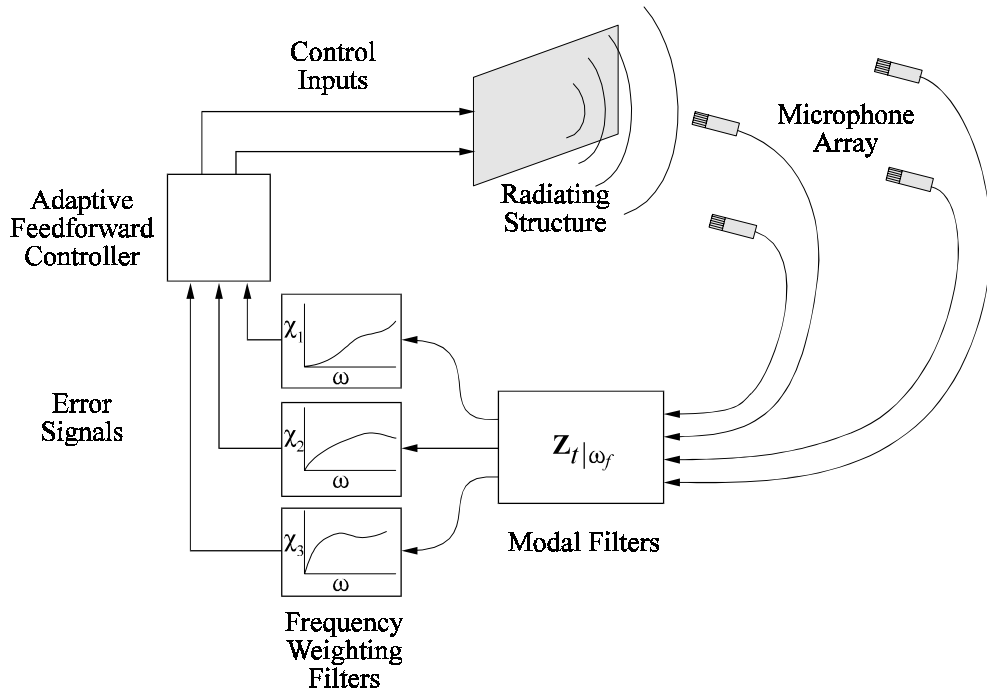
Figure 5.3   Modal filter and frequency weighting filter arrangement.

The quadratic function of the control force given by Equation (5.14) can be applied to minimise the error criterion with

$$\mathbf{A} \; = \; \mathbf{\Psi}^{H}\,\mathbf{Y}^{H}\,\mathbf{Z}_{n}{}^{H}\,\mathbf{Z}_{t|\omega_{f}}^{H}\,\mathbf{X}\,\mathbf{Z}_{t|\omega_{f}}\,\mathbf{Z}_{n}\;\mathbf{Y}\;\mathbf{\Psi}\,, \tag{5.22}$$

$$\mathbf{b} \; = \; \mathbf{\Psi}^{H}\,\mathbf{Y}^{H}\,\mathbf{Z}_{n}{}^{H}\,\mathbf{Z}_{t|\omega_{f}}^{H}\,\mathbf{X}\,\mathbf{Z}_{t|\omega_{f}}\,\mathbf{Z}_{n}\;\mathbf{Y}\;\mathbf{\Psi}\;\mathbf{f}_{p} \tag{5.23}$$

and

$$c \; = \; \mathbf{f}_{p}{}^{H}\,\mathbf{\Psi}^{H}\,\mathbf{Y}^{H}\,\mathbf{Z}_{n}{}^{H}\,\mathbf{Z}_{t|\omega_{f}}^{H}\,\mathbf{X}\,\mathbf{Z}_{t|\omega_{f}}\,\mathbf{Z}_{n}\;\mathbf{Y}\;\mathbf{\Psi}\;\mathbf{f}_{p}\,. \tag{5.24}$$

5.2.4   TRANSFORMED MODE ACOUSTIC RADIATION PATTERNS

It is of interest to examine the radiation patterns of the transformed modes contributing to the farfield sound power of a simply supported rectangular steel panel. For the purpose of this discussion the dimensions will be set to L_x = 0.38m, L_y = 0.30m and thickness h = 0.002m. Below 1000Hz there are 13 panel resonances as shown in Table 5.1.

Table 5.1
Theoretical panel resonance frequencies.

Mode	Theoretical Resonance Frequency (Hz)
1,1	88
2,1	190
1,2	252
2,2	353
3,1	360
3,2	523
1,3	524
4,1	597
2,3	625
4,2	760
3,3	795
5,1	902
1,4	905

The transformed modes (contributing to the farfield sound power) can then be found using the method outlined above operating on the first 100 structural modes. The constituents of the first

five transformed modes are defined by the eigenvectors of the weighting matrix $\mathbf{\Pi}$, as contained in the columns of $\mathbf{Q}$. These eigenvectors are frequency dependent and representative values are shown in Table 5.2 evaluated at 100Hz.

Table 5.2
Structural mode constituents of the first five transformed modes at 100Hz.

Transformed Mode No. 1		Transformed Mode No. 2		Transformed Mode No. 3		Transformed Mode No. 4		Transformed Mode No. 5	
Struct. Mode	Value	Struct. Mode	Value	Struct. Mode	Value	Struct. Mode	Value	Struct. Mode	Value
(1,1)	0.8435	(2,1)	0.7554	(1,2)	0.7587	(2,2)	0.6810	(3,1)	0.6033
(1,3)	0.2786	(4,1)	0.3756	(1,4)	0.3781	(2,4)	0.3397	(5,1)	0.3930
(3,1)	0.2771	(2,3)	0.2505	(1,6)	0.2519	(4,2)	0.3392	(1,3)	-0.3457
(1,5)	0.1671	(6,1)	0.2502	(3,2)	0.2507	(2,6)	0.2264	(7,1)	0.2868
(5,1)	0.1661	(8,1)	0.1876	(1,8)	0.1889	(6,2)	0.2260	(9,1)	0.2250
(1,7)	0.1193	(2,5)	0.1502	(1,10)	0.1511	(2,8)	0.1697	(1,5)	-0.2204
(7,1)	0.1186	(10,1)	0.1500	(5,2)	0.1503	(8,2)	0.1694	(1,1)	-0.2093
(1,9)	0.0928	(12,1)	0.1250	(3,4)	0.1249	(4,4)	0.1692	(11,1)	0.1845
(9,1)	0.0922	(4,3)	0.1245	(7,2)	0.1074	(2,10)	0.1358	(1,7)	-0.1599
(3,3)	0.0915	(2,7)	0.1073	(2,3)	0.0835	(10,2)	0.1355	(13,1)	0.1568

It can be observed that the first five transformed modes consist of orthogonal groupings of (odd,odd), (even,odd), (odd,even), (even,even) and a second (odd,odd) grouping of structural modes respectively. The three dimensional acoustic pressure fields of each of these transformed modes, measured at a distance of $r = 2.0$m and frequency $f = 100$Hz and 500Hz are shown in Figures 5.4 and 5.5 respectively. In each case the farfield pressure magnitude has been normalised to the largest acoustic response so that the overall shape can be examined.
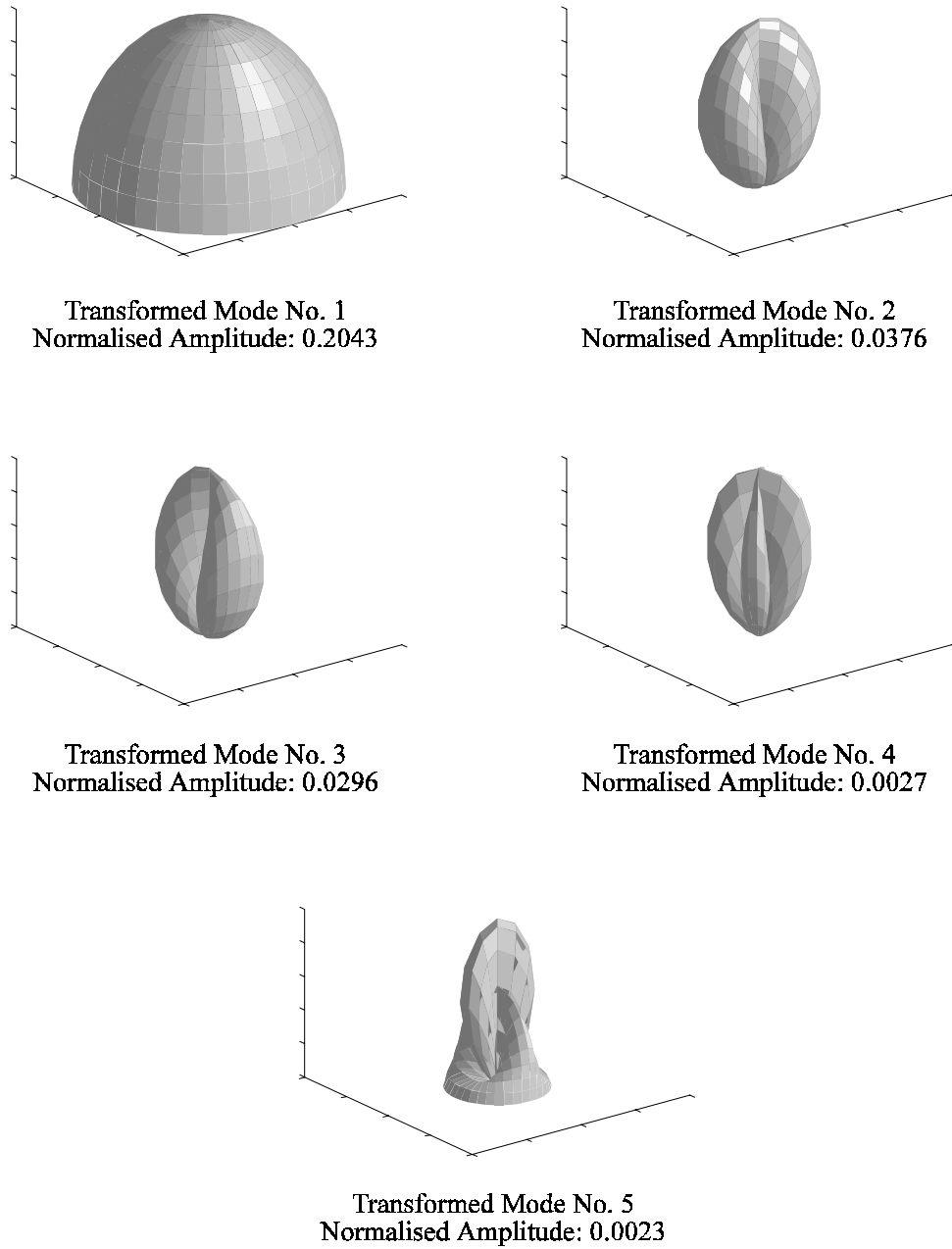
Transformed Mode No. 1
Normalised Amplitude: 0.2043

Transformed Mode No. 2
Normalised Amplitude: 0.0376

Transformed Mode No. 3
Normalised Amplitude: 0.0296

Transformed Mode No. 4
Normalised Amplitude: 0.0027

Transformed Mode No. 5
Normalised Amplitude: 0.0023

Figure 5.4   Normalised acoustic response of the first five transformed modes at $r = 2.0$m, 100Hz.

Transformed Mode No. 1
Normalised Amplitude: 1.0

Transformed Mode No. 2
Normalised Amplitude: 0.7306

Transformed Mode No. 3
Normalised Amplitude: 0.6285

Transformed Mode No. 4
Normalised Amplitude: 0.2796

Transformed Mode No. 5
Normalised Amplitude: 0.2597
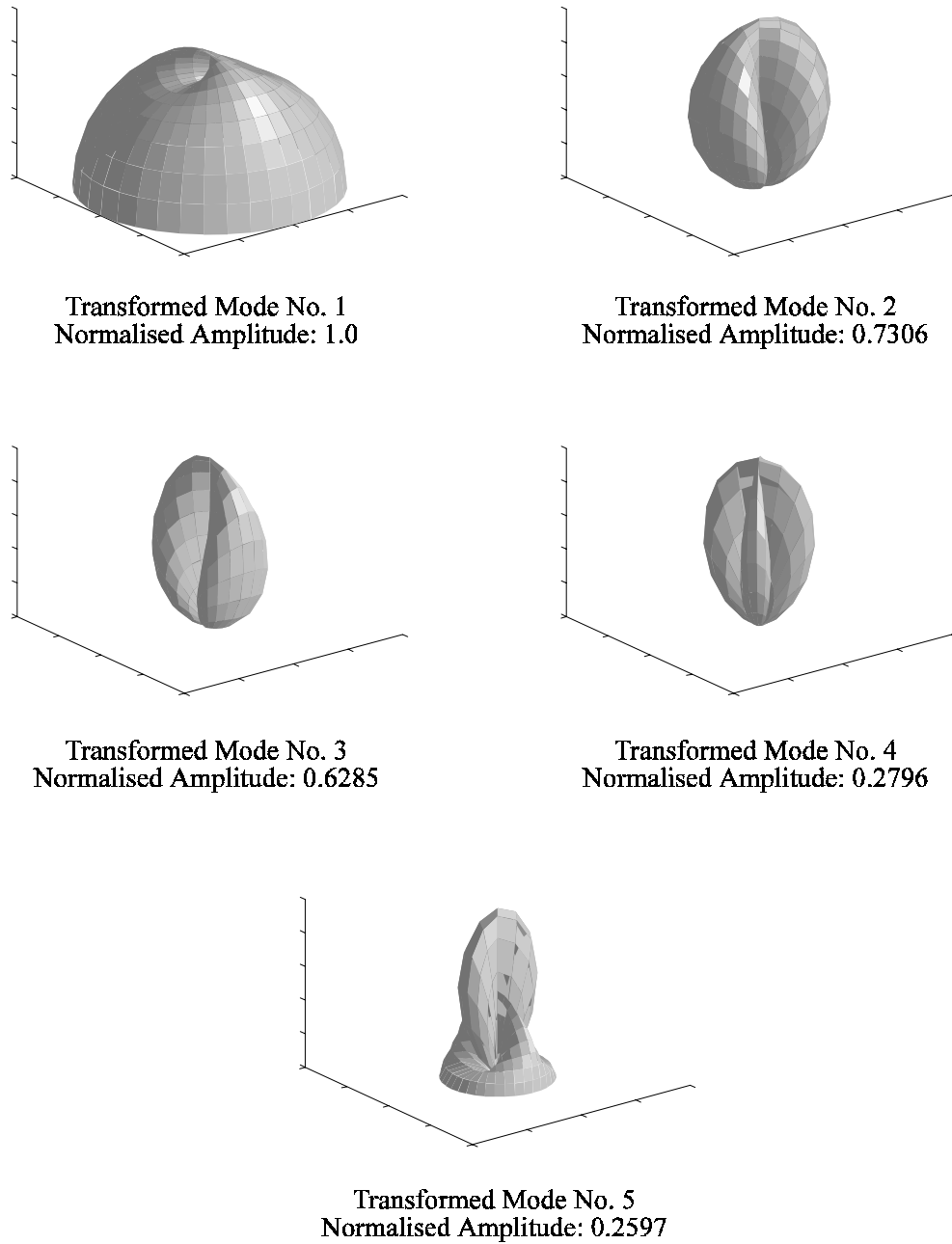
Figure 5.5   Normalised acoustic response of the first five transformed modes at $r = 2.0$m, 500Hz.

It is not surprising that the first transformed acoustic mode shape, corresponding to the (odd,odd) structural mode grouping, is comparable to the radiation pattern of a monopole source. Similarly the second and third transformed acoustic mode shapes are comparable to the radiation patterns of two orthogonal dipole radiators respectively. The fourth transformed acoustic mode shape is comparable to that of a quadrupole radiator, while the fifth is some more complex shape based on another orthogonal grouping of (odd,odd) modes. These acoustic radiation patterns may be decomposed from a microphone array sensor by the modal filter specified by $\mathbf{Z}_t$. It is also interesting to note the small change in shape between the acoustic response at 100Hz and 500Hz. The shapes are generally very similar, with the higher order acoustic responses having slightly plumper lobes at 500Hz than at 100Hz. The main difference is evident when comparing the relative magnitude of the modes at each frequency, with all modes being of much greater amplitude at 500Hz. It is because of this small change in overall shape that the frequency dependence of the amplitude of each transformed mode apparent in these figures can be incorporated into the meta-filter described by Equation (5.20).

The transformed modes do not contribute equally to the overall sound power; instead the eigenvalues λ_i, defined in the diagonal matrix $\boldsymbol{\Lambda}$, are representative of the acoustic radiation efficiency of these transformed modes. The variation of the eigenvalues as a function of frequency is shown in Figure 5.6. It can be observed that at low frequencies only the first transformed mode contributes significantly to the overall sound power, at higher frequencies the second and third transformed modes catch up and also contribute significantly, while the fourth and fifth transformed modes continue to be trivial. Higher order transformed modes contribute
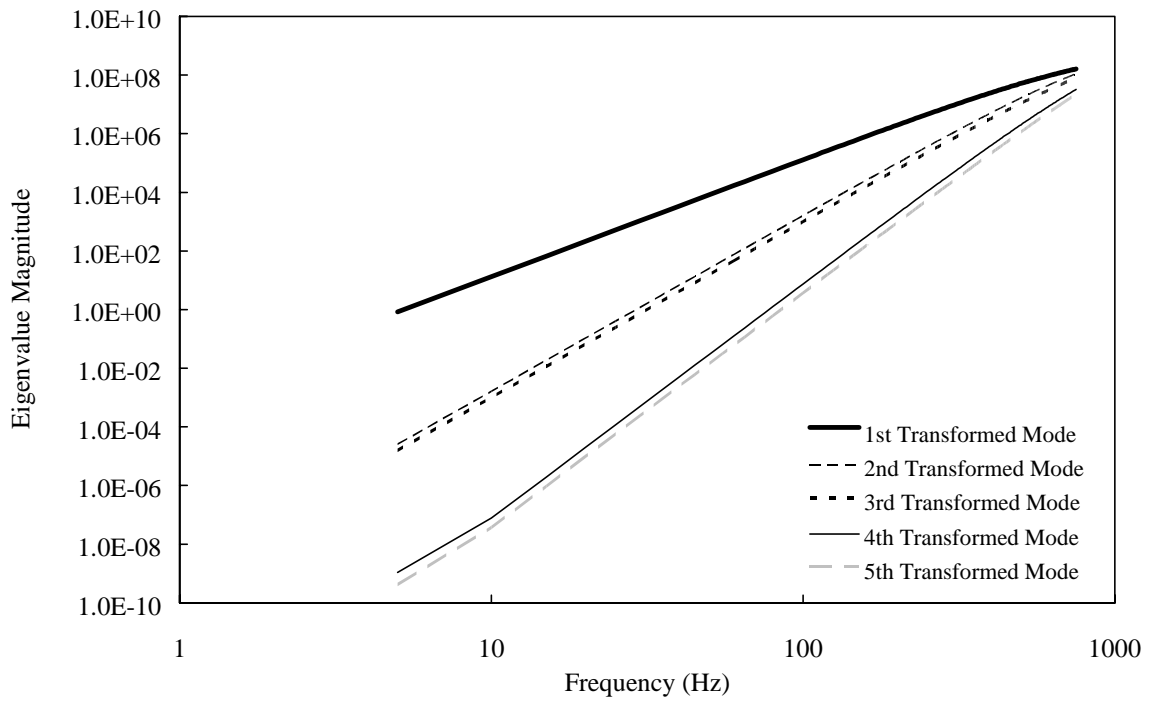
insignificantly and have not been shown.

Figure 5.6   Eigenvalues of the first five transformed (*power radiation*) modes of a simply supported rectangular plate as a function of frequency.

5.3   NUMERICAL RESULTS

A simply supported panel of the dimensions specified in Section 5.2.4 is assumed. The form of

the transformed mode radiation transfer function matrix is dependent on the position of the error

sensors in the farfield. The symmetrical nature of the transformed mode radiation patterns shown

in Figures 5.4 and 5.5 imply that symmetrical positioning of these error sensors can result in

some degree of duplication within the modal filter. While this could be capitalised on to simplify

a practical system, the more general case of a non-symmetrical sensor array is considered here.

The three dimensional locations of five farfield error sensors used for both the following

numerical and experimental (Section 5.4) results are given in Table 5.3. In cases considering less

than five error sensors, the lowest order error sensor locations are used (eg. when three error

sensor locations are considered, they are locations 1-3).

Table 5.3
Error sensor locations.

Error Sensor Location No.	θ	ϕ	r (m)
1	60°	40°	2.0
2	60°	130°	2.0
3	30°	220°	2.0
4	80°	300°	2.0
5	45°	90°	2.0

A single point primary source is located at (35mm,103.3mm) and one control source at

(35mm,0mm).

The theoretical model discussed above was programmed in double precision FORTRAN using

IMSL Eigenanalysis, matrix inverse and singular value decomposition mathematical routines. Implementing Equation (5.2) to calculate the sound power weighting matrix over a frequency range between 0 and 750Hz proved to be most time consuming requiring approximately 10 hours CPU time on a DEC5000/240 server when the first 100 modes of vibration were considered. Fortunately this calculation is independent of the error sensor, primary and control source locations and so was performed once and saved to a file which was subsequently read when examining different control system arrangements.

5.3.1   CONTROLLING TRANSFORMED MODES COMPARED TO TRADITIONAL ERROR CRITERIA

Figures 5.7-5.12 compare the radiated sound power and sound power attenuation achieved by minimising the least mean square pressure at some error sensors, to that achieved by minimising the first (Figures 5.7 & 5.8) and both first and second transformed modes (Figures 5.9-5.12) using a single point primary and control force acting on the panel. Note that these radiated power and attenuation levels are those achievable given the error sensor locations listed in Table 5.3 above. Using different error sensor locations could lead to controlled levels better or worse than those shown here, though these levels will be indicative of those that may be obtained in practice (particularly as a greater number of error sensors are used). In Figures 5.7 & 5.8, only one error signal is minimised to provide control. In the case of the least mean square pressure it is simply the pressure at a single farfield sensor. As only one error signal is considered, only the first transformed mode is minimised, however it is decomposed from three sensors in the farfield. Below 300 Hz, minimising the first transformed mode amplitude is shown to provide the maximum possible sound power attenuation, given the control force location. Minimising the

pressure at a single point provides surprisingly good global control, only about 3-4dB below the maximum achievable attenuation. At frequencies where the control force position is not conducive to good global control (250Hz and 400Hz) minimising the sound pressure is observed to *increase* the overall sound power radiation by as much as 5dB.

Around 360Hz, minimising the sound pressure also leads to poor global control compared to that achievable when minimising the transformed mode amplitude. At this frequency the radiation from the dominant (3,1) and (2,2) normal modes of vibration may combine such that a large minimisation of LMS pressure occurs at the single error sensor, however the analysis above shows that these two (odd,odd) and (even,even) modes cannot affect the power radiation from each other. The first transformed mode does not have any contribution from the (2,2) mode, and so minimising it, though not producing as large a minimisation at the first error sensor, does provide a much better global result. This is not to say that controlling the first transformed mode is always ideal, as demonstrated at frequencies just below 400Hz and around 600Hz where controlling the transformed mode greatly increases the overall sound power radiation. In these regions it is apparent that the sound power radiation is dominated by higher order transformed modes.

Introducing a second error signal input; that is, two pressure sensor inputs in the case of minimising the LMS pressure and the first and second transformed modes for the case of minimising power, the problems of poor global attenuation when minimising LMS pressure at 360Hz and when minimising power at frequencies above 550Hz is observed to be arrested (Figures 5.9 & 5.10). As might be expected, the global attenuation achievable by minimising the

LMS pressure at two sensors rather than just one is generally better, especially around 350Hz; however, minimising amplitudes of just two transformed modes is seen to produce overall levels comparable to the maximum achievable attenuation. It appears that deficiencies in the error sensor locations make detection of the transformed modes difficult around 350Hz, though without increasing the controller dimensionality it is possible to produce the result shown in Figures 5.11 & 5.12, where five sensors are decomposed into just two transformed modes to provide near-optimal control over a wide frequency range. It is evident from Figures 5.13 & 5.14 that minimising the least mean square pressure at three or five distributed error sensors in the farfield will result in sound power attenuation becoming progressively more optimal, and that no advantage would be gained by decomposing this many power modes from an even larger number of error sensors for this arrangement. However, the advantage of using the transformed modes is that fewer controller error inputs are needed, although a similar number of sensors is needed to obtain similar results as obtained using minimisation of LMS pressure.
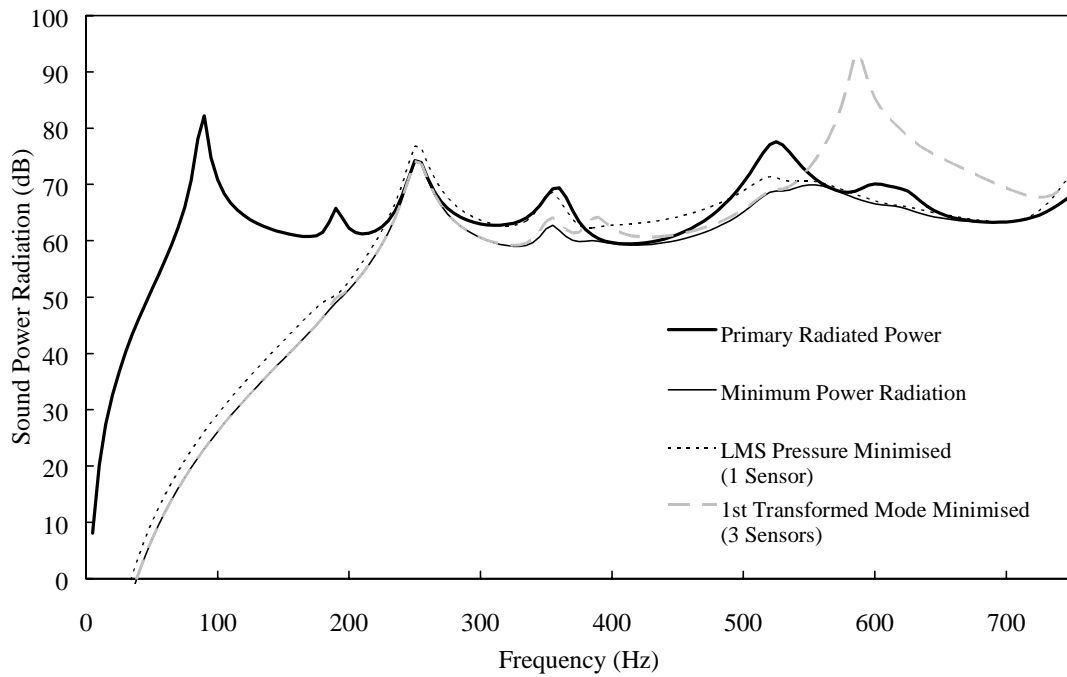
Figure 5.7 Primary and controlled radiated sound power, minimising pressure at 1 sensor and by minimising the 1st transformed mode decomposed from 3 sensors.
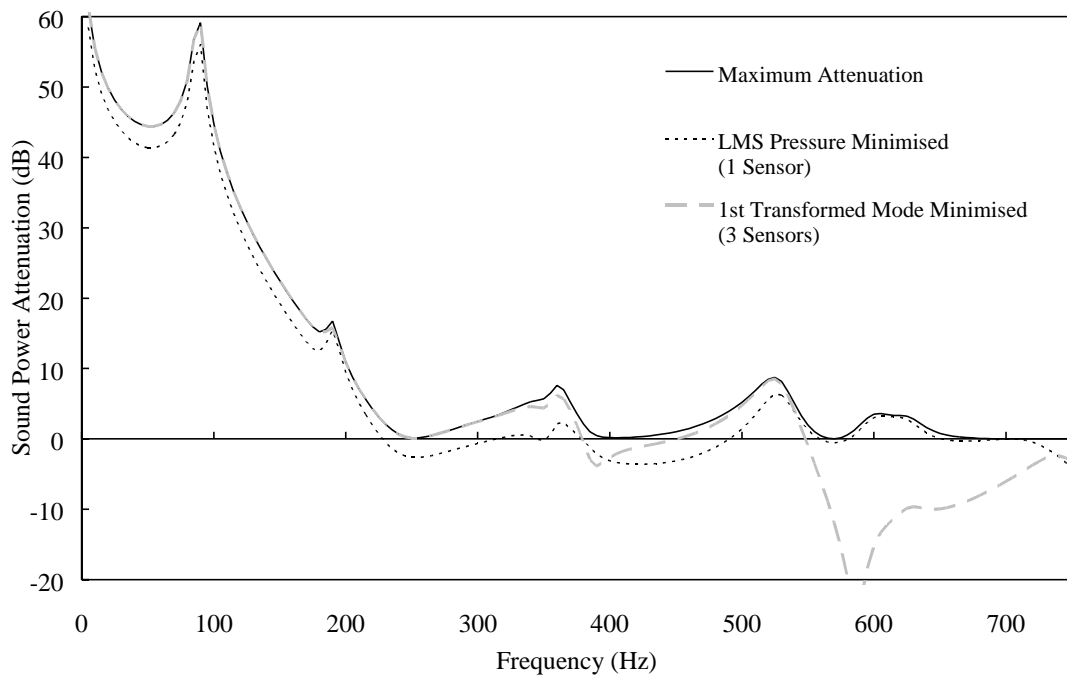

Figure 5.8   Maximum attenuation, attenuation achieved by minimising pressure at 1 sensor and by minimising the 1st transformed mode decomposed from 3 sensors.
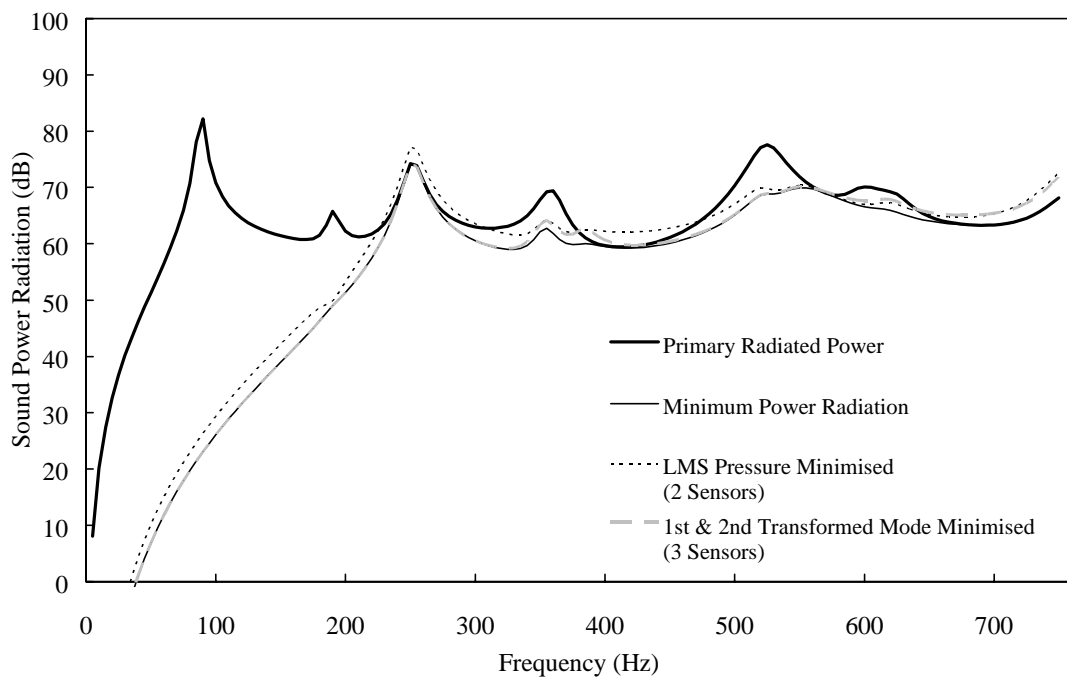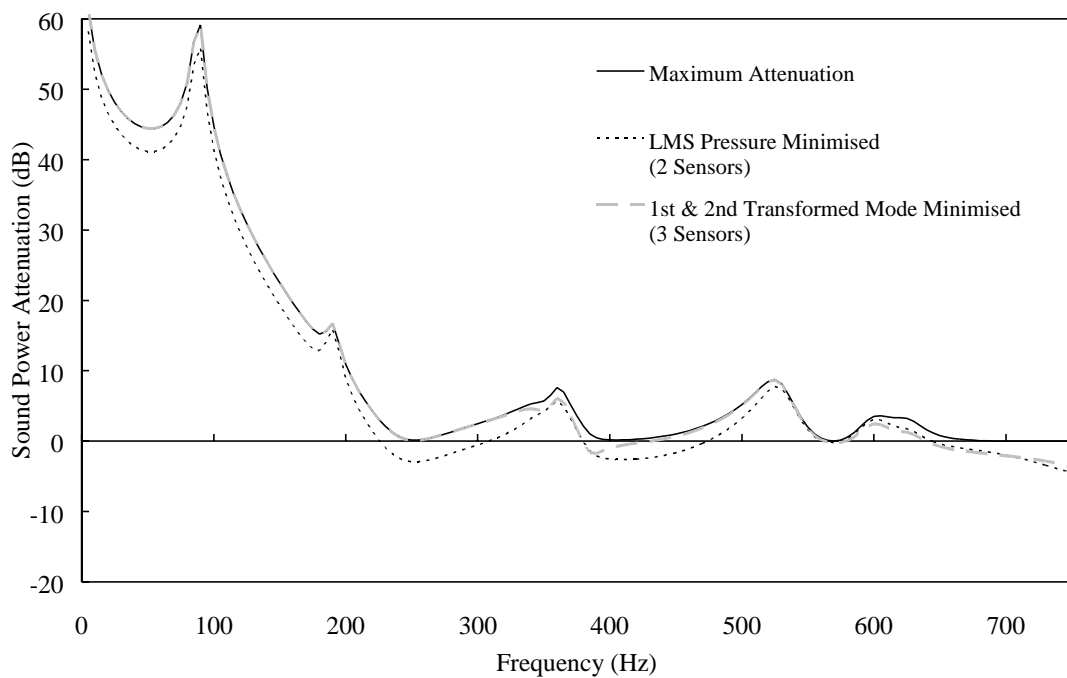
Figure 5.9 Primary and controlled radiated sound power, minimising pressure at 2 sensors and minimising the 1st & 2nd transformed modes decomposed from 3 sensors.

Figure 5.10   Maximum attenuation, attenuation achieved by minimising pressure at 2 sensors and minimising the 1st & 2nd transformed modes decomposed from 3 sensors.
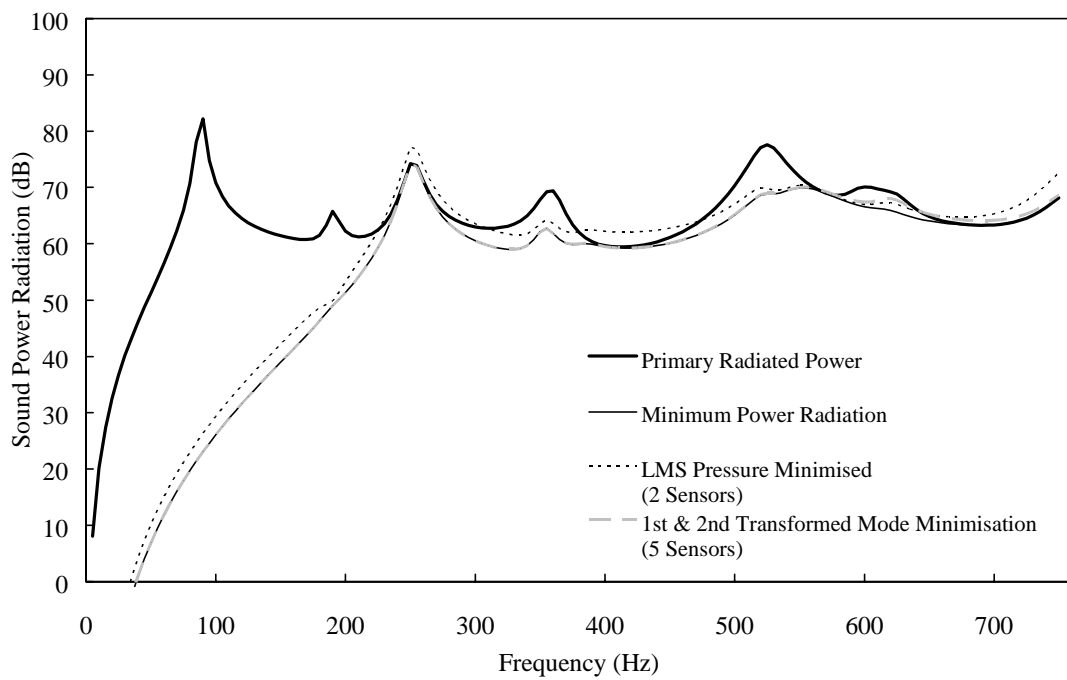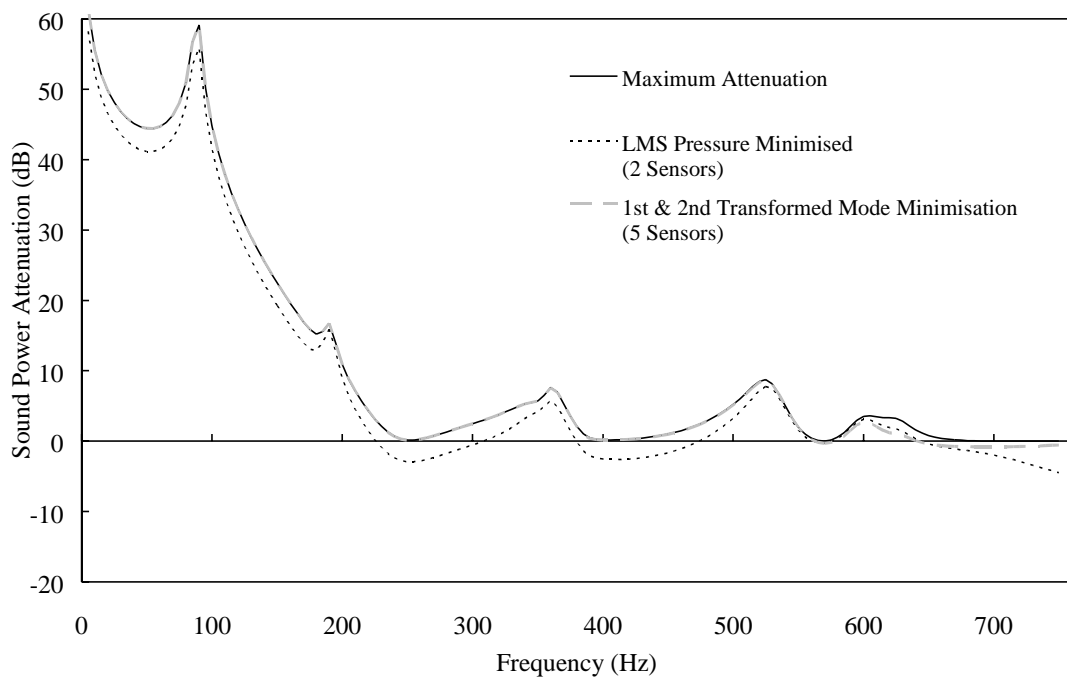
135

Figure 5.11   Primary and controlled radiated sound power, minimising pressure at 2 sensors and minimising the 1st & 2nd transformed mode decomposed from 5 sensors.

Figure 5.12   Maximum attenuation, attenuation achieved by minimising pressure at 2 sensors and by minimising the 1st & 2nd transformed modes decomposed from 5 sensors.
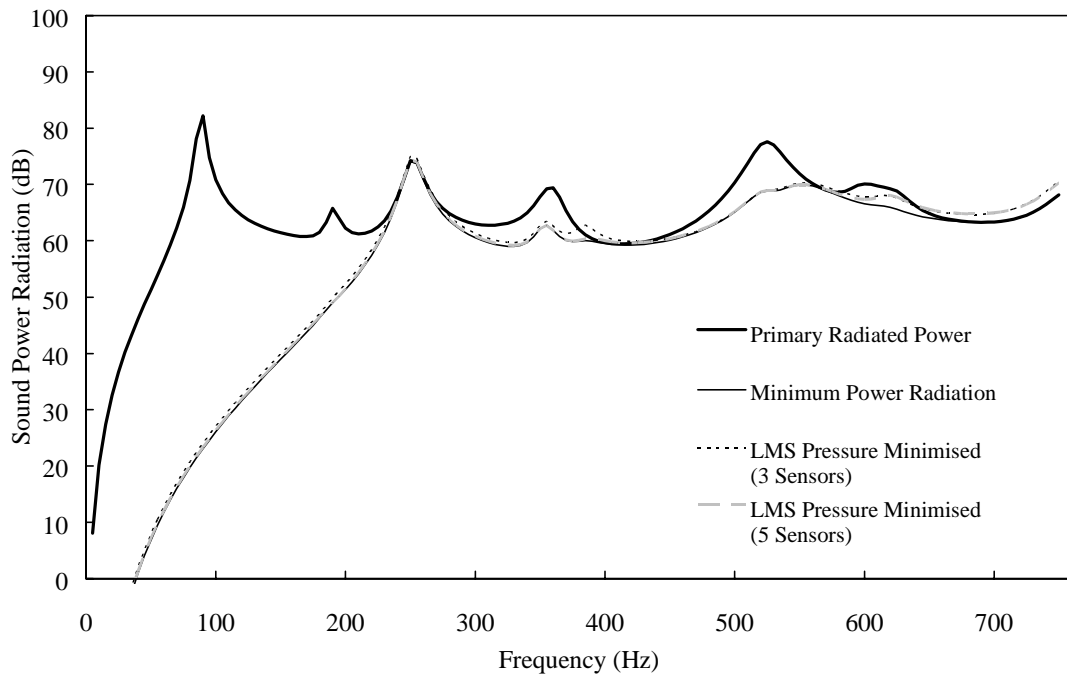
Figure 5.13   Primary and controlled sound power radiation, minimising the LMS pressure at 3 & 5 farfield sensors.
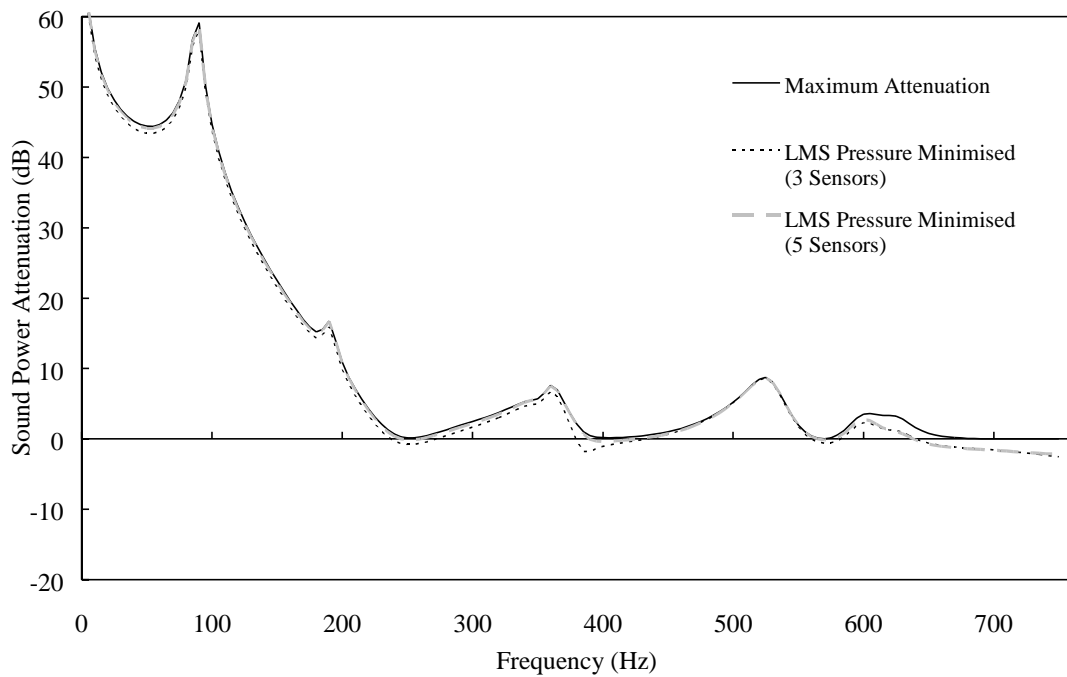

Figure 5.14   Maximum attenuation and attenuation achieved by minimising the LMS pressure at 3 & 5 farfield sensors.

5.3.2 MODAL FILTER RESPONSE

The complex elements of the transformed mode radiation transfer function matrix, $\mathbf{Z}_t$, make up the modal filters (which is coupled with the eigenvalue filter to make up the complete modal filter system). In particular, each row of the matrix represents the overall filter required for each transformed mode, and each column within that row the filter for the corresponding sensors contribution to that mode. For the case considered above where three error sensors are decomposed into the first and second transformed modes the transformed mode radiation transfer function is a 2 x 3 matrix, with the phase and amplitude response of each element of the first row corresponding to the filters for the first transformed mode and shown in Figures 5.15 and 5.16 respectively. The filter set for the second transformed mode is shown in Figures 5.17 and 5.18. Again, it should be recognised that the form of these filters depends entirely on the position of the error sensors and as such the results presented here show only what may be expected for a typical arrangement. In particular the form of the amplitude filters shown in Figure 5.16 indicate that the second error sensor contributes very little to the detection of the first transformed mode. Similarly in Figure 5.18 it can be seen that the first two error sensors contribute similarly to the detection of the second transformed mode. In this case it is apparent that these sensors are almost symmetrically located when compared to the acoustic radiation pattern of the second transformed mode shown in Figure 5.4.

The phase response of the filters would be implemented in practice by introducing a group delay (corresponding to the slope of the phase response) between the signal paths of the individual sensors. What is not immediately evident is that the required group delay is *the same* for a particular sensor for both transformed modes. In the case of the second transformed mode it

would also be necessary to introduce a 180° phase shift to the signal from the first error sensor as shown in Figure 5.17. The group delay for each error sensor location determined from Figures 5.15 & 5.17 is shown in Table 5.4

Table 5.4
Error sensor group delay.

Error Location	Group Delay
1	6.423ms
2	5.796ms
3	5.462ms

In practice it would only be necessary to implement the relative (net) delay of 0.334ms between sensors 3 and 2, and 0.961ms between sensors 3 and 1. The electronic control system would compensate for the gross delay (and corresponding phase shift).
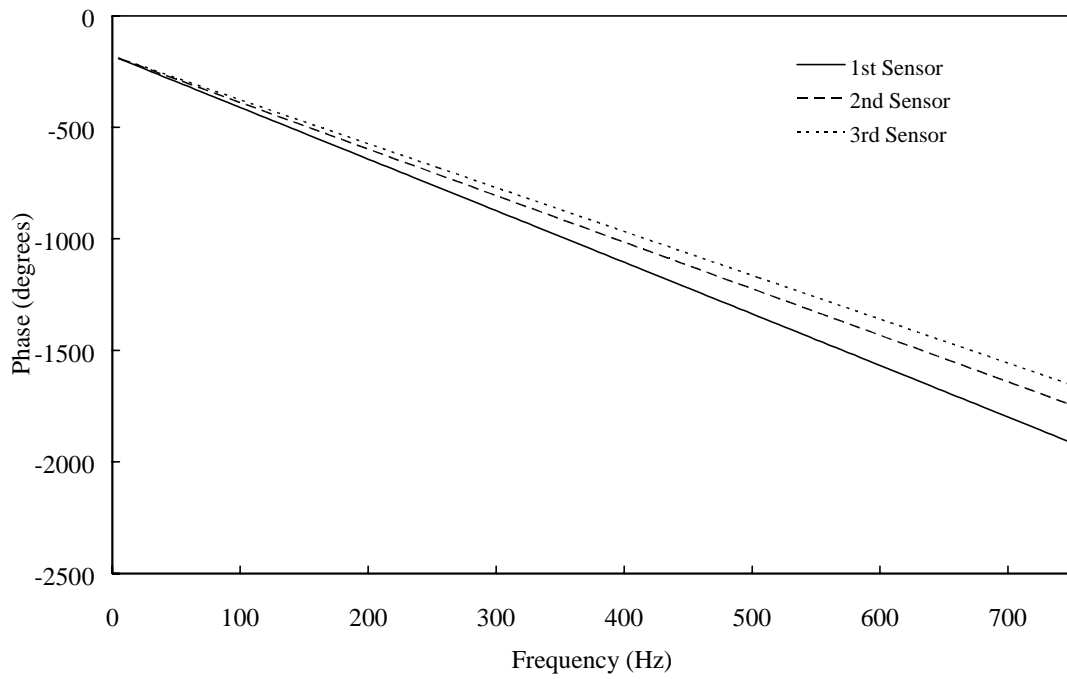
Figure 5.15   Phase response of the modal filter required to decompose the 1st transformed mode from 3 farfield sensors.
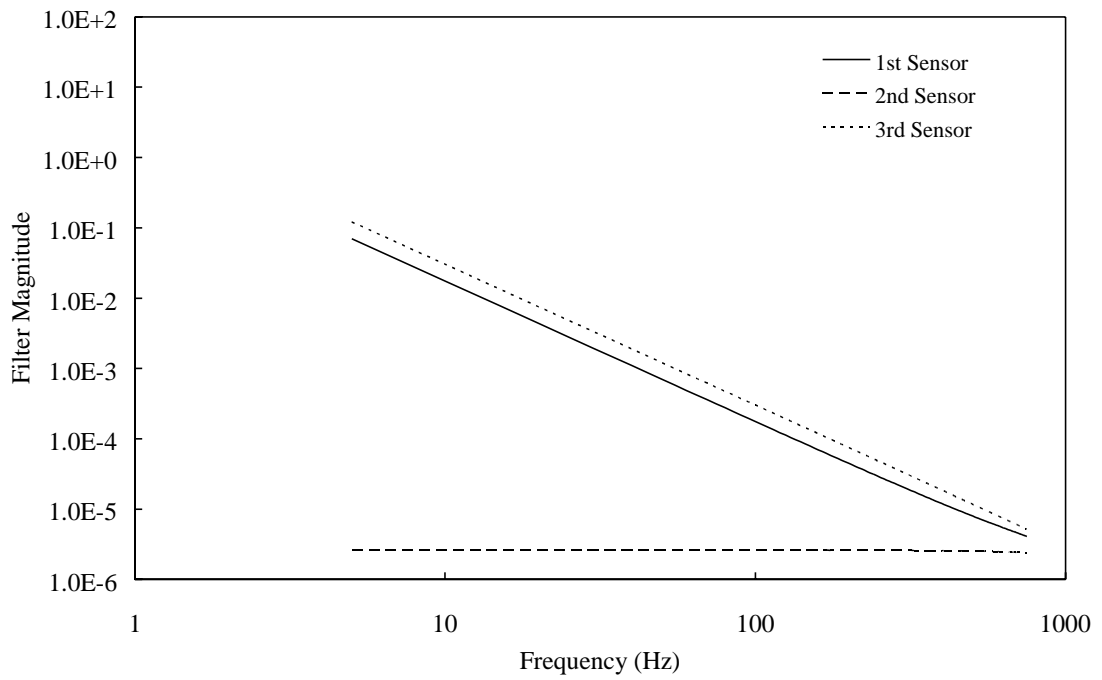

Figure 5.16   Amplitude response of the modal filter required to decompose the 1st transformed mode from 3 farfield sensors.
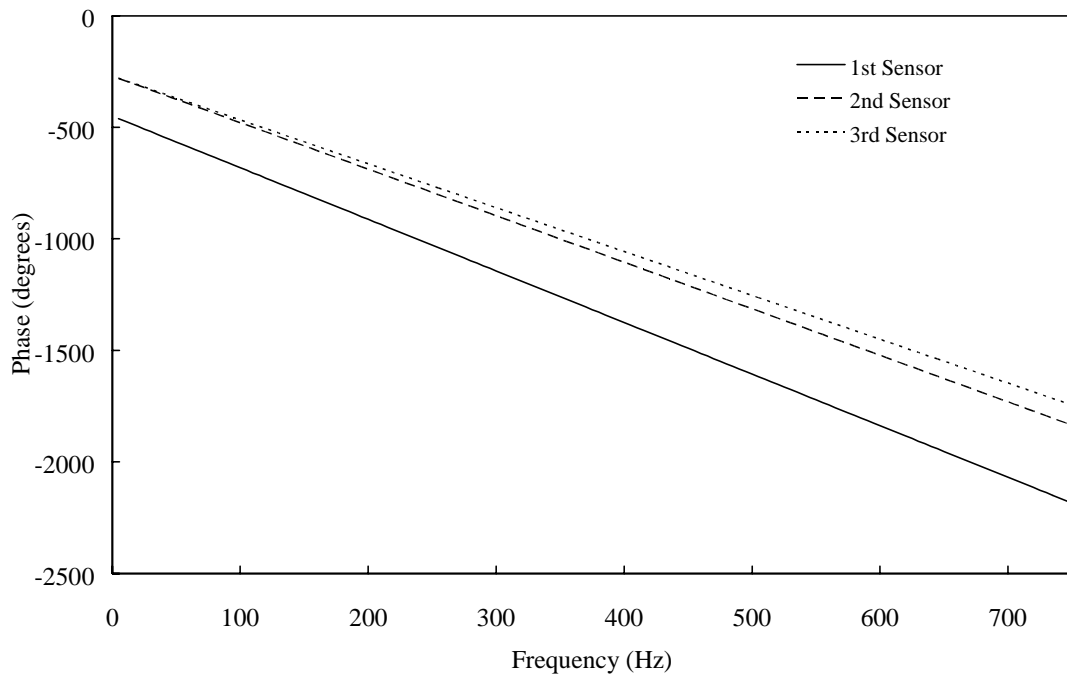
Figure 5.17   Phase response of the modal filter required to decompose the 2nd transformed mode from 3 farfield sensors.
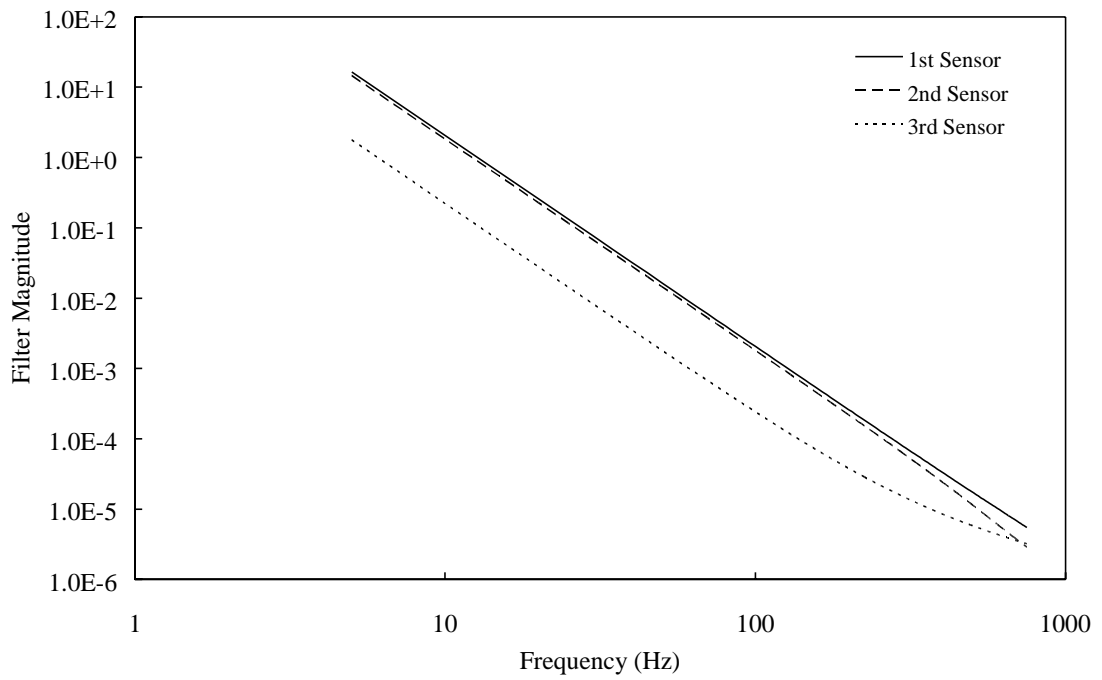

Figure 5.18   Amplitude response of the modal filter required to decompose the 2nd transformed mode from 3 farfield sensors.

5.3.3   TRANSFORMED MODE FREQUENCY CORRECTION

Further simplifications can be made in the physical realisation of the modal filter by fixing the transfer function to that at a single frequency and then lumping the frequency dependence together with the eigenvalue filter as defined in Equation (5.20) above (see Figure 5.3), to create a *corrected fixed frequency* filter system, where the modal filter is not frequency dependant at all, and is replaced by a frequency independent weighting value. The meta-filter response for each transformed mode, as contained in the diagonal of **X**, is shown in Figure 5.19 for a transfer function fixed at 100Hz. The sound power attenuation achieved by minimising two transformed modes determined from a *frequency correct* modal filter system (which varies optimally with frequency) is compared to that from a *corrected fixed frequency* filter system and an *uncorrected fixed frequency* filter system in Figures 5.20 and 5.21 (see Section 5.2.3). It is observed that the corrected fixed frequency filter performs as well as the frequency correct filter over a wide frequency range, with a few slight deviations of both *better* and worse control. The uncorrected fixed frequency modal filter causes severe lapses in control at some frequencies, particularly above 350Hz, though below this it performs as well as the frequency correct filter. This suggests that a fixed frequency modal filter could be used *without correction*, if control were limited to a small frequency range around that of the filter.

Moreover, it is of interest that the magnitude of the correction filter, **X**, is itself relatively constant over a large frequency range (Figure 5.19). This indicates that it should be possible to select a single *correction factor*, say the value of the correction filter at 100Hz, which when combined with the frequency independent weighting values of the modal filter at some fixed frequency, will produce a single weighting value for each sensor that will perform as well as a

fully implemented frequency correct filter system up to between 500 and 600Hz. In other words the corrected fixed frequency filter *value* and correction *factor* could be combined to give a single gain factor to be applied to each sensor input (see Equation (5.21)), independent of the operating frequency. In this way a "modal filter" implementation, albeit with somewhat limited performance, could be constructed by simply delaying and weighting each sensor input, without the need for any explicit "filtering" at all.
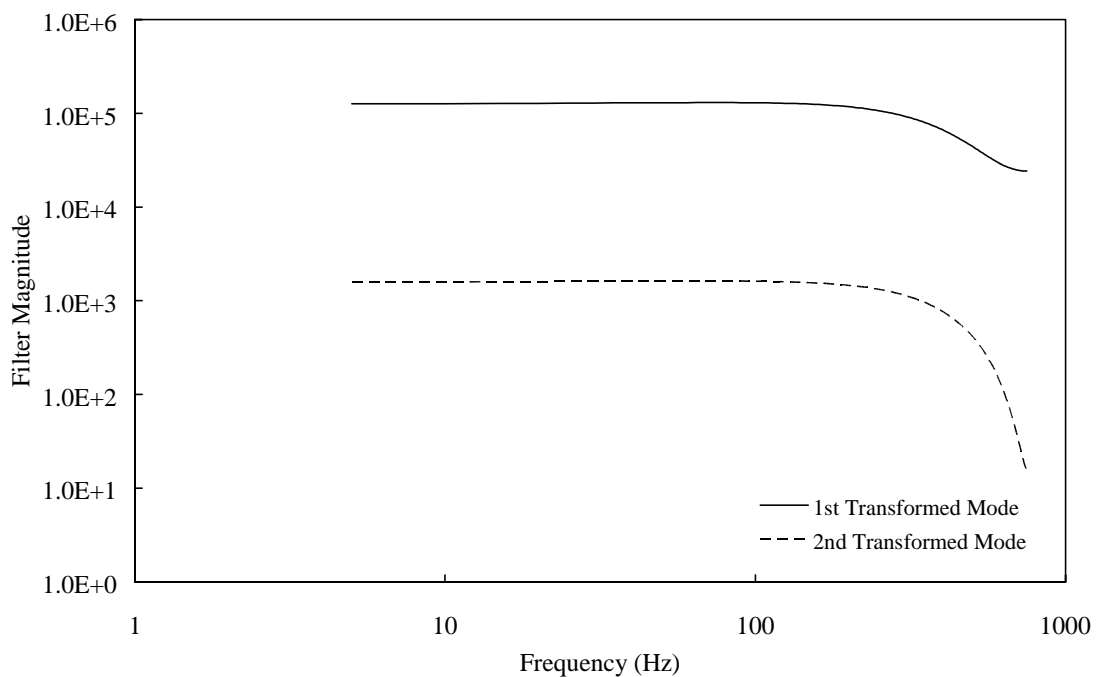

Figure 5.19   Amplitude response of the correction filter, **X**, for the 1st and 2nd transformed modes decomposed from 3 sensors.
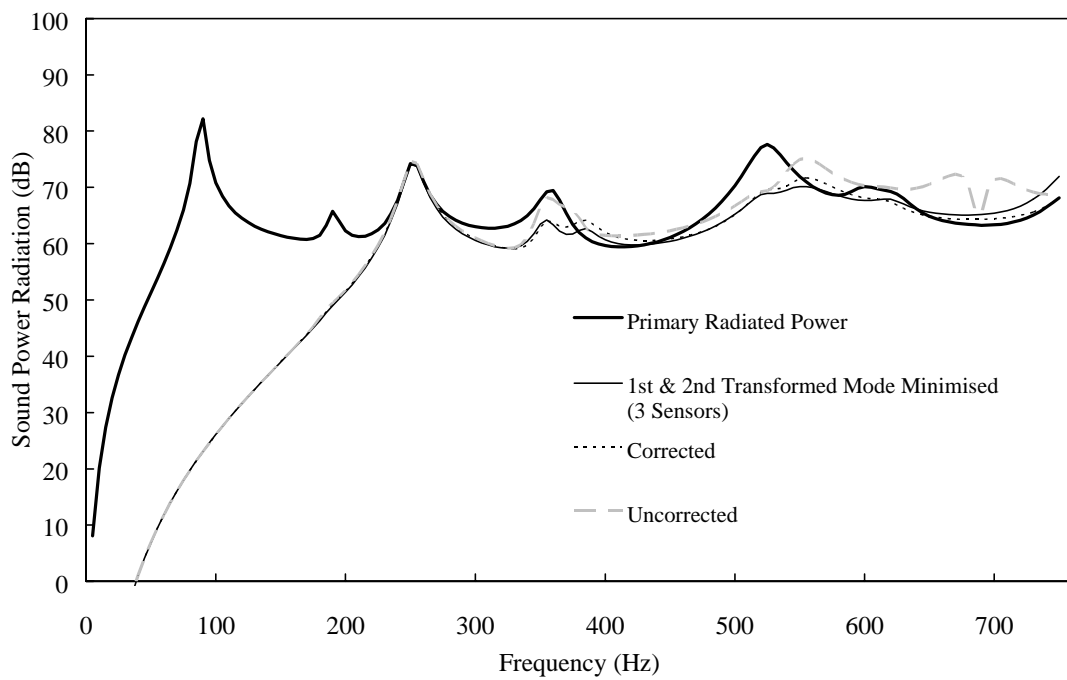
Figure 5.20   Primary and controlled radiated sound power, minimising the 1st & 2nd transformed modes decomposed with corrected and fixed frequency (100Hz) modal filters.
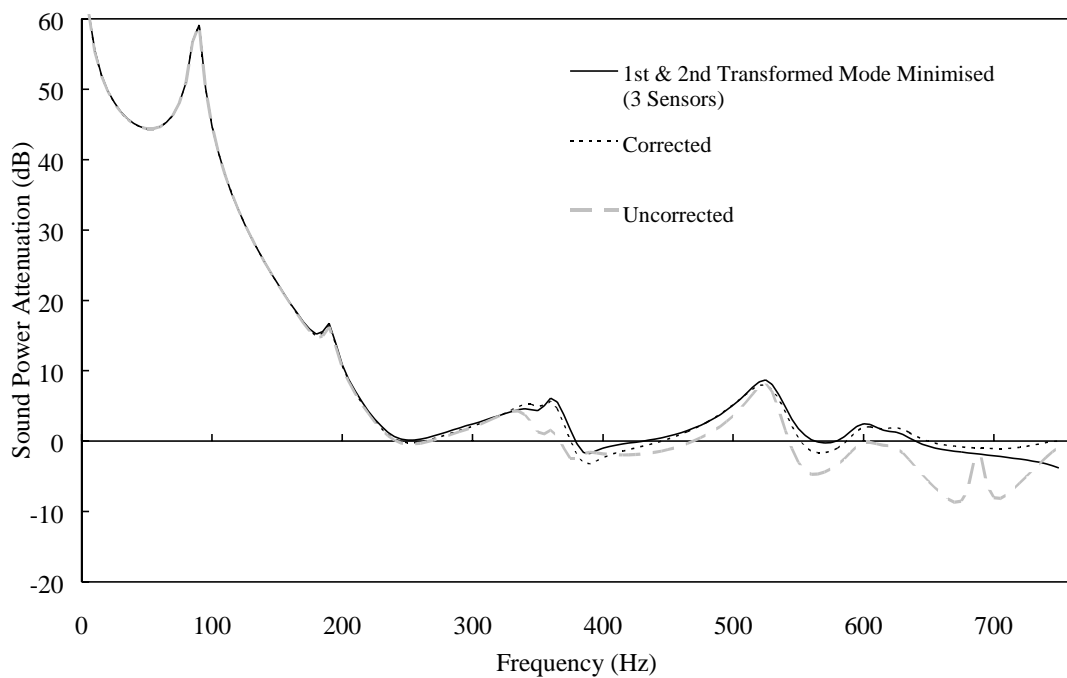

Figure 5.21   Attenuation by minimising the 1st and 2nd transformed modes decomposed with corrected and fixed frequency (100Hz) modal filters.

5.4   EXPERIMENTAL VERIFICATION

5.4.1   PROCEDURE

A rectangular steel panel of dimensions 380mm x 300mm, and thickness h=1.942mm was mounted in a heavy steel frame using spring steel shims to approximate simply supported boundary conditions. The panel was placed in the centre of a large wooden baffle in an anechoic chamber (see Figure 5.22). A Brüel and Kjær 4810 electrodynamic minishaker was used to excite the panel at (35mm,103.3mm) through a thin spring steel stinger and ball joint to eliminate any bending moment that may have been present due to misalignment. A Brüel and Kjær 8200 force transducer was attached to the panel between the stinger and the panel and connected to a Brüel and Kjær 2635 charge amplifier and a Brüel and Kjær 2034 signal analyser to measure the input force. A pair of 25mm square piezoceramic crystals were placed one on each side of the panel at (35mm,0mm) and connected with opposite phases so as to provide a control moment onto the panel. Both the primary and control sources were driven from a pair of power amplifiers, with the piezoceramic crystals requiring a small step up transformer to supply the high voltage required for their operation.

The acoustic intensity at a distance of 70mm away from the panel was measured using a Brüel and Kjær 3519 intensity probe powered by a Brüel and Kjær 2804 microphone power supply and connected to a second Brüel and Kjær 2034 signal analyser. The intensity probe was mounted in an X-Y traverse such that it could be remotely positioned at any location in front of the panel with an accuracy of approximately ±0.5mm. Custom software was written in TURBOPASCAL 5 to control the X-Y traverse via a PCL Traverse Controller. The input force and acoustic intensity

data were recorded via a GPIB interface to the pair of Brüel and Kjær spectrum analysers. The software also controlled the signal generator on the second analyser to provide the primary and reference signals. The software performed the necessary calculations to determine the sound power radiated by the panel by measuring the acoustic intensity at a large number of points in front of the panel. The primary force magnitude was used to normalise the measured sound power radiation to that produced by 1N. A number of preliminary power measurements were performed to determine the optimum density of intensity measurements that were required to perform the radiated power calculation accurately, while not requiring obscene amounts of time to conduct the experiment. It was determined that seventy intensity measurement points (an array of ten points in the x direction and seven points in the y direction) provided sufficient repeatability (± 0.5 dB) with an associated measurement time of approximately ten minutes per single frequency tone.

An array of five inexpensive electret microphones were used as error sensors and mounted at a radius of 2.0m from the centre of the panel in the positions shown in Table 5.3 above. The microphones were powered by a proprietary electret microphone amplifier and power supply, and adjusted with the use of in-line attenuators to a consistent sensitivity.

The modal filter was implemented with custom software on a modified CAUSAL SYSTEMS EZ-ANC digital signal processing board (see Section 5.4.1.1 below). In the cases where direct acoustic pressure signals were used as the error criterion this board was bypassed (not shown).

At each measurement frequency the measurement software paused to allow control to be achieved and optimised using a CAUSAL SYSTEMS EZ-ANC Active Noise Control System. A pair of Hewlett Packard four channel digital oscilloscopes (not shown) and a further dual channel spectrum analyser (not shown) were used to monitor the error signals both before and after the modal filter to provide some visual evidence that the control parameters had in fact been set to *allow* the controller to reach an optimum level of attenuation. Once minimisation of the error signals had occurred the controller adaptation was stopped. The measurement software was restarted to measure the resulting controlled sound power radiation while a constant output was used to drive the control source.

Four different control scenarios were tested; control of one, two or five pressure signals (with the modal filter bypassed) and control of the first and second transformed mode decomposed from three pressure signals using the modal filter.
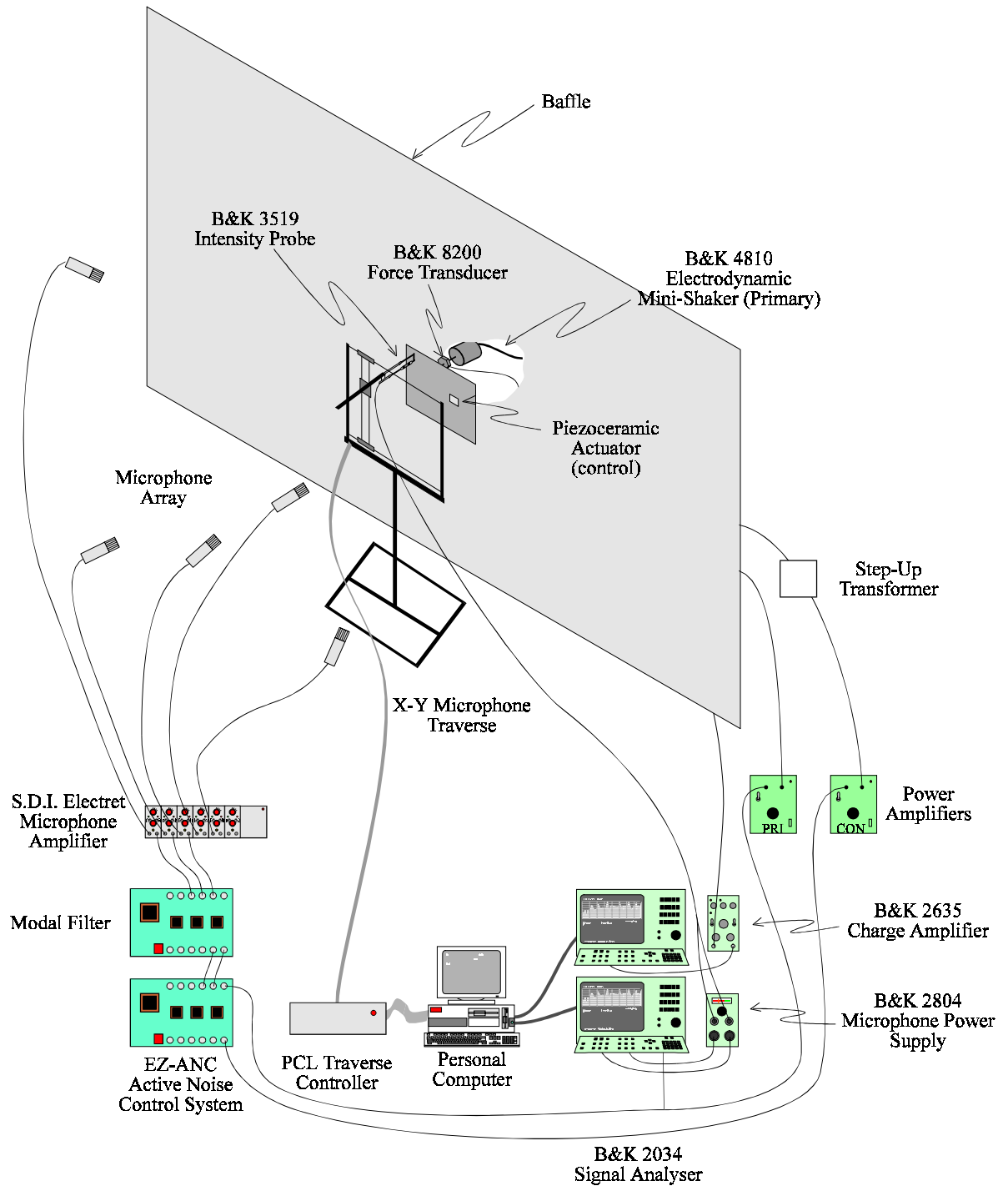
Figure 5.22 Experimental arrangement to measure and actively control radiated sound power.

5.4.1.1 Modal filter implementation

The modal filters were implemented on a modified Causal Systems EZ-ANC digital signal processing board. In this case a *corrected fixed frequency* filter was implemented with the transfer function frequency fixed at 100Hz. The correction factor was also assumed to be a constant, using the value at 100Hz, and multiplied by the modal filter magnitudes to give a single overall gain for each sensor input as discussed in Section 5.3.3 above.

Custom software was written to provide the group delay, appropriate relative gains and signal summation to produce output signals representing the magnitude of the first and second transformed modes as shown in Figure 5.23. The group delay was implemented by using short FIFO buffers on the first and second input signal channels, sampled at a rate of 6.25kHz.
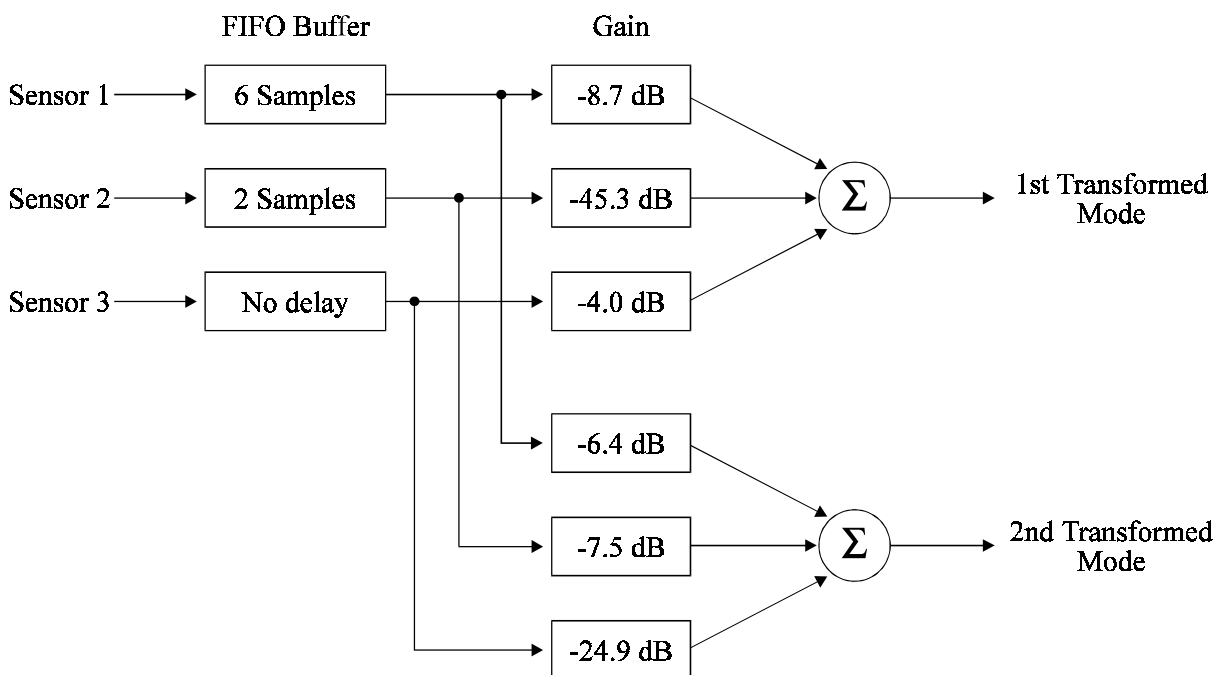
Figure 5.23   Modal filter implementation.

5.4.1.2 Panel loss factors

To enable the accurate theoretical calculation of the primary (and hence controlled) radiated sound power of the simply supported panel, the loss factors of the first nine modes of vibration of the panels were measured with only the primary electrodynamic minishaker attached and used to excite the structure. An accelerometer was fastened at five random locations on the panel with a lightweight high field strength magnet and the transfer function between the input force (measured with the force transducer) and the acceleration at the measurement location was recorded using a Brüel and Kjær 2034 dual channel signal analyser. Each resonant peak was examined with a high resolution Zoom FFT analysis over a range of 12.5Hz, such that the 3dB bandwidth of the peaks could be accurately measured and the loss factor calculated by use of the relation

$$\eta \; = \; \frac{1}{Q} \; = \; \frac{\Delta f_{3dB}}{f} \; .$$

(5.24)

The average of the modal loss factors are presented in Table 5.6 below. The loss factor for modes above the ninth were assumed to be $\eta = 0.01$.

5.4.1.3 A comparison of control sources

Initially it was envisioned that a second Brüel and Kjær 4810 electrodynamic minishaker would be used as the control source as it would closely approximate a point source on the panel and could produce comparable input levels to the primary source. An initial assessment of the primary radiated power was conducted with a second minishaker attached to the structure at (35mm,0mm) but not operating. This is compared to the theoretically calculated primary radiated

Table 5.6

Panel loss factors

Mode	Measured panel loss factor
1,1	0.0296
2,1	0.0137
1,2	0.0062
2,2	0.0094
3,1	0.0058
3,2	0.0038
1,3	0.0044
4,1	0.0086
2,3	0.0102

power in Figure 5.24. It can be seen that the measured radiated power corresponds poorly with that predicted theoretically, particularly between 400 and 500Hz, where a large increase in radiated power was observed.

A modal analysis was carried out on the panel using the same procedure as that described in Section 2.5 for two cases; with only the primary minishaker attached, and with both the primary and control minishakers attached. The theoretical and measured resonance frequencies of the modes of vibration of the panel are shown in Table 5.7 below. With only the primary source and no control sources attached, the measured resonance frequencies agree closely with those predicted theoretically, as may be expected given the low additional mass and stiffness of the
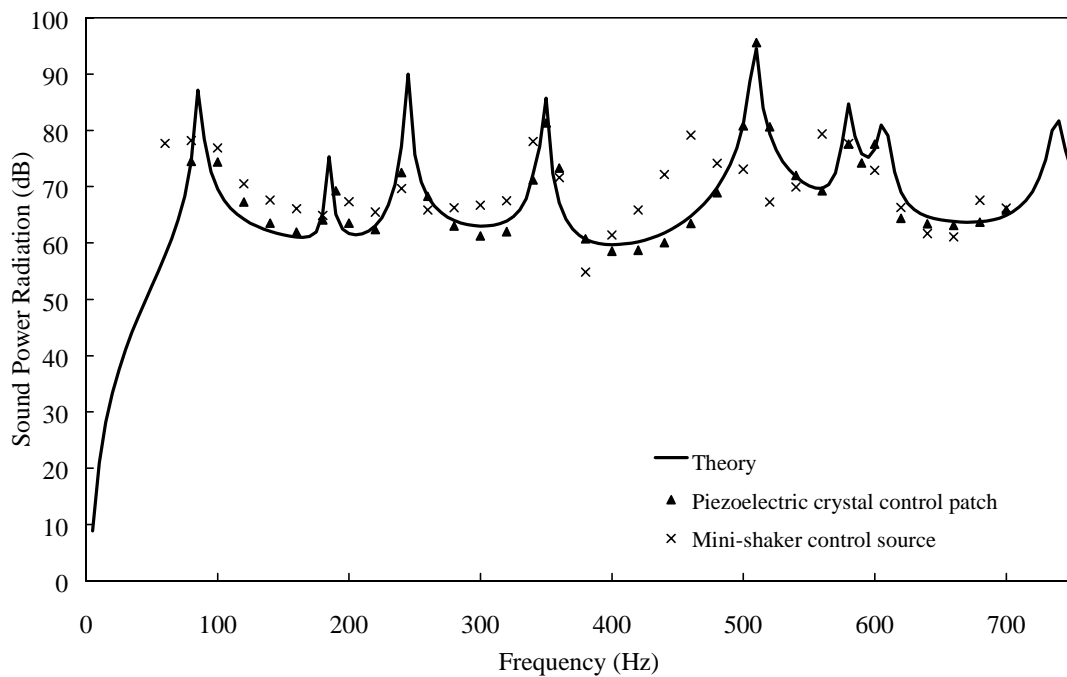
Figure 5.24   Theoretical and measured primary radiated power from a panel with a mini-shaker control source or a piezoelectric crystal control patch attached.

shaker armature. However, when a control minishaker was attached, it was observed that the (3,1) mode of vibration underwent a massive shift in its resonance frequency to 480Hz, corresponding to the increase in power radiation observed at that frequency. In this case the (1,3) mode of vibration could not be identified by the modal analysis. It is believed that a system resonance was produced at this frequency either due to the additional mass and stiffness of the control shaker mechanism or corresponding to a resonance of the aluminium stinger connecting it to the panel. Both minishakers were hung by rubber strips in an effort to alleviate this problem, but negligible change in the resonance frequencies or primary radiated power was observed.

Table 5.7

Panel resonance frequencies

with and without control sources attached

Mode	Theoretical resonance frequency (Hz) $h = 1.942$mm	Measured resonance frequency without control sources (Hz)	Measured resonance frequency with minishaker control source (Hz)	Measured resonance frequency with piezocrystal control patch (Hz)
1,1	86	88	86	89
2,1	185	186	184	188
1,2	244	247	248	246
2,2	343	343	345	343
3,1	349	354	480	354
3,2	507	503	505	503
1,3	508	510		509
4,1	580	584	565	584
2,3	607	602	600	601
4,2	738	746	747	745
3,3	772	772	769	767

As an alternative a pair of 25mm square piezoelectric crystals were bonded with epoxy, one to each side of the panel centred at (35mm, 0mm). The piezoelectric crystals were connected with opposite phases to provide a control moment onto the panel. Again a modal analysis was performed to assess the influence of the control source on the resonance properties of the panel, and as shown in Table 5.7, the piezoelectric crystals had little measurable effect on the resonance frequencies of the structure. Furthermore the measured primary sound power radiation now

closely matched that predicted theoretically, as shown in Figure 5.24. Although using the piezoceramic crystals avoided problems with altering the dynamics of the vibrating structure, a number of associated complications were introduced. Primarily, the control source was now distributed over a finite area, rather than a point force, although the size of the crystals was kept small to curb this effect. Secondly, the primary input levels to the panel may have been compromised (ie. reduced to such an extent as to put the maximum achievable attenuation below the noise floor of the instruments) to allow for the lower control force possible with the piezoceramic crystals. Fortunately these concerns caused no observable effect throughout the experimental work, and it was left for the third and most unexpected complication, discussed in the following section, to reduce the preliminary experimental results to nonsense.

5.4.1.4 Piezoelectric crystal electro-magnetic radiation effects

As demonstrated in the previous section, the use of piezoceramic crystals as the control source (albeit inoperational) allowed excellent agreement between theoretical and measured primary sound power radiation levels. When the crystals were first used to control the sound radiation from the panel however, the resulting measured net intensity always proved to be negative. A surface plot of the raw intensity levels measured over the panel during active control is shown in Figure 5.25. It can be seen in this figure that the intensity has the greatest negative magnitude in the region of the piezoceramic crystal actuator, and drops off sharply on every side. This was calculated by the Brüel and Kjær 2034 signal analyser by measuring the gradient of the pressure between two closely spaced microphones on the intensity probe. The probe was positioned only 70mm from the surface of the panel so that radiation from the edges of the panel would not

"leak" past the intensity probe. The close proximity of the microphone pair, in particular the front microphone, to the high voltages driving the piezoelectric crystal indicated that electromagnetic interference from the crystal was producing spurious electric signals from the probe. The problem was solved by screening the entire panel with a fine wiremesh screen placed 15mm away from the panel and connected to ground, similar in effect to a Faraday Cage. The screen had no effect on the primary sound power radiation from the panel. Figure 5.26 shows the raw intensity field in front of the shielded panel, where it is observed that the intensity field is now relatively even across the surface of the panel with no apparent interference effect near the piezoelectric crystal.
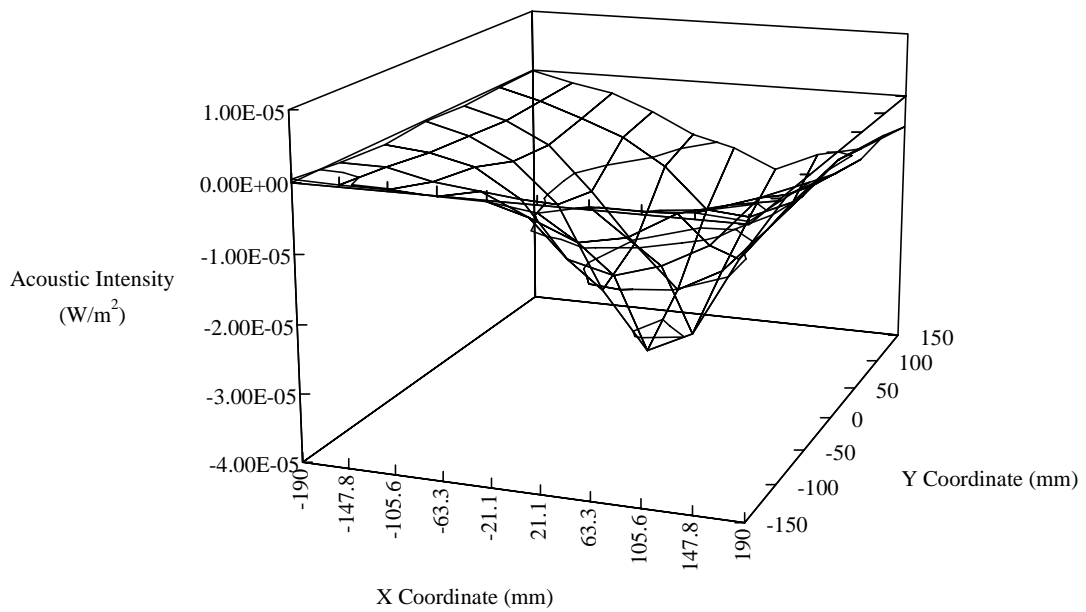
Figure 5.25   Intensity at 100Hz over the panel surface without shielding mesh.
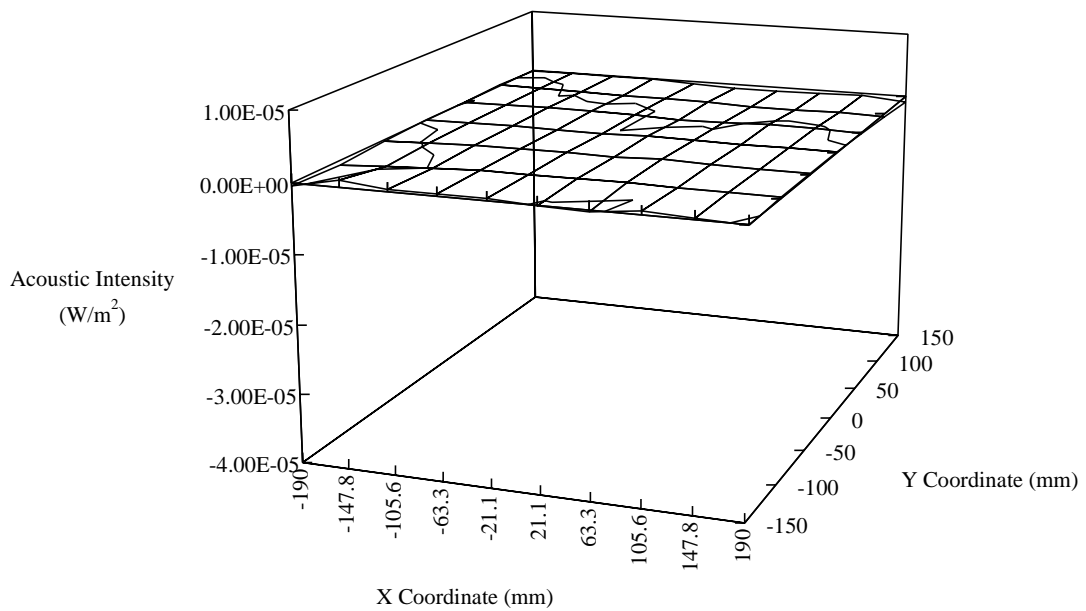

Figure 5.26   Intensity at 100Hz over the panel surface with shielding mesh.

5.4.2 RESULTS AND DISCUSSION

Figures 5.27-5.34 show theoretical and measured power radiation paired with the corresponding sound power attenuation when active control was applied for cases where the least mean square pressure was minimised using one, two and five error sensors and the 1st and 2nd transformed mode. The theoretical predictions are made in 5Hz increments from 5Hz to 750Hz while the experimental measurements were recorded in 20Hz increments from 100Hz to 700Hz. Extra experimental measurements were taken at points of interest, namely; 190Hz, 350Hz, 510Hz and 590Hz, corresponding to the (2,1), (3,1), (1,3) and (4,1) modal resonances respectively.

Below 100Hz the amount of control achieved in each case was so large, and consequently the controlled level so small, so as to make their measurement unreliable due to the noise floor of the instruments. Between 100Hz and 200Hz controlled levels were still relatively low and reduced the repeatability of the experiment to approximately ±3dB. Above 200Hz the repeatability of the experiment was as low as ±0.5dB, assuming that the electronic controller had converged to a "similarly" optimum control output. Therein lay a major difficulty: ensuring that the convergence, gain, filter length, sample rate and other parameters governing the adaptation of the control filter were set to produce the optimum control output to minimise the error signals. Small changes in the setup of the control algorithm could produce as much as 10dB difference in the amount of attenuation provided at the error sensors, though fortunately measuring the sound power radiated by the panel effectively diluted the effect of having a particularly low radiation in the direction of the error sensor, as levels remained (relatively) stable elsewhere.

Figures 5.27 and 5.28 show the theoretical and measured power radiation and corresponding sound power attenuation with only one error sensor in the farfield. Agreement between the two is generally very good, with the measured power attenuation slightly lower than that predicted theoretically, due to the finite precision of the controller. The measured resonance of the (1,3) mode at 509Hz allows a very large attenuation which is not shown by the theoretical predictions because they are made at 505Hz and 510Hz with the theoretical resonance frequency lying between them at 507Hz. This large attenuation at 510Hz is evident for all of the error criteria.

Figures 5.29 and 5.30 show the theoretical and measured power radiation and corresponding sound power attenuation with two error sensors in the farfield. Again the agreement is good, however at 120Hz and 140Hz it proved difficult to achieve good control. Similarly with five error sensors (Figures 5.31 and 5.32) control at 120Hz was difficult to optimise and measure, whilst elsewhere agreement is good.

When minimising the 1st and 2nd transformed modes (Figures 5.33 and 5.34) there is good agreement between theoretical predictions and measured data. Spurious results occur here at 480Hz, where applying even a small control force resulted in a large change of input impedance seen by the primary source. In practice this produced large changes of input force and correspondingly large changes in the observed sound field, which often led to overloading of the inputs of the modal filter, the EZ-ANC and even overdriving of the primary minishaker. This led to difficulties in achieving either stable or optimum control at this frequency.

Before comparing between error criteria a few general observations need to be made. In general it was aimed to achieve between 35-40dB attenuation *at the sensor* for the single error sensor, 10-20dB attenuation at each sensor with two or five sensors and 15-25dB attenuation when minimising the transformed modes. In particular with the single sensor, the amount of control achieved at the error sensor was always high and did not correspond well to the overall power attenuation. With two or five error sensors it was more apparent that good control could not be achieved at some frequencies, and when minimising the transformed modes it was clear that at some frequencies no control could be achieved at all, with no corresponding reduction of the error signals. Furthermore with fewer sensors it was easier to ensure that the controller parameters were set to *allow* the optimum control output to be reached, by observing the reduction in error signal levels on the oscilloscopes and signal analyser. When five sensors were implemented it proved to be very difficult task to visually assess the "optimality" of one set of parameters as compared to another. As an adjunct to this it should be noted that having more error sensors acted to increase the stability of the system, and in some small way compensated for this problem.

A theoretical comparison between minimising one and five pressure sensors and the 1st and 2nd transformed modes are shown in Figures 5.35 and 5.36. There it can be seen that minimising pressure at five sensors and the transformed modes guarantees that the maximum attenuation capable with the given control source location is achieved. Minimising only one pressure sensor in the farfield is between 3dB and 5dB worse. Above 650Hz all error criteria afford little overall control, and one sensor performs comparably with the "better" error criterion. It is also clear that

no control is achievable with any error criterion at 245Hz, as the control source lies on a node of the (1,2) modal resonance. Corresponding experimental results are shown in Figures 5.37 and 5.38 and, though cluttered due to the small differences in levels expected between error criteria, a number of trends are clearly evident. Except for a few spurious results discussed previously the sound power attenuation achievable when using five sensors or the transformed modes is clearly greater than using a single sensor. At frequencies above 550Hz controlling the transformed modes does not perform well, as expected. Additionally, the attenuation levels achieved by controlling five sensors and the transformed modes are of a similar level. This is of interest because although the levels are comparable, the latter were achieved using only two channels on the electronic controller.

With this in mind Figures 5.39 and 5.40 show theoretical results for the two cases where only two error channels are minimised by the control system, specifically either two farfield pressure signals or the first and second transformed modes. These results show that an increase in attenuation of between 3dB and 4dB can be expected when minimising the transformed modes at frequencies less than 500Hz. Corresponding experimental results are shown in Figures 5.41 and 5.42, and show that the expected gains in attenuation are achievable.
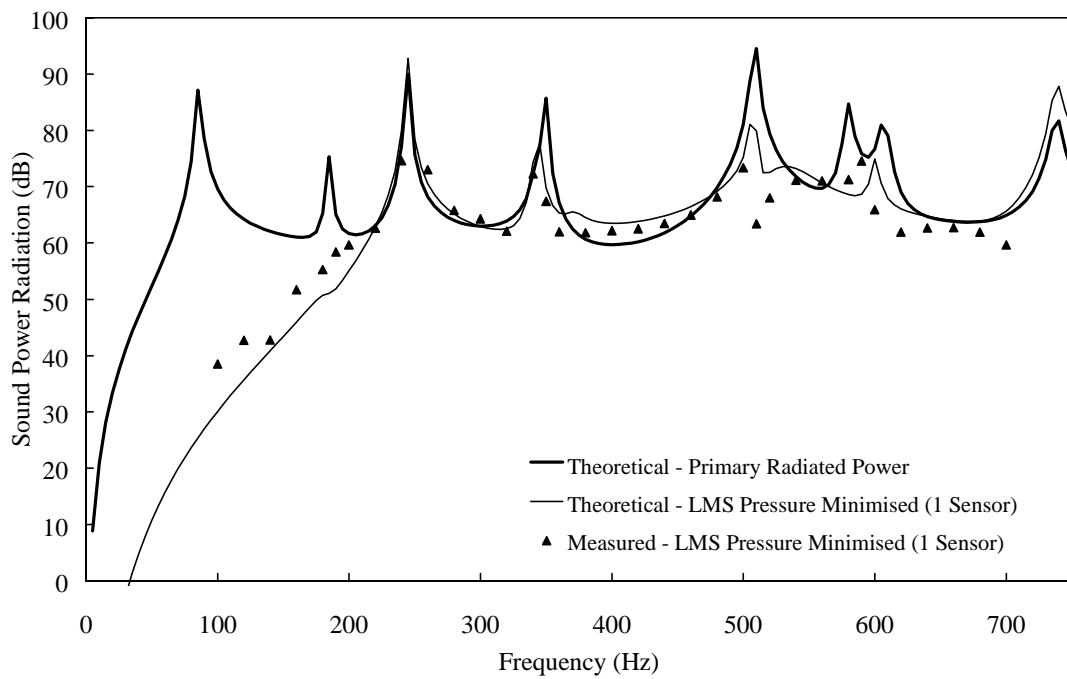
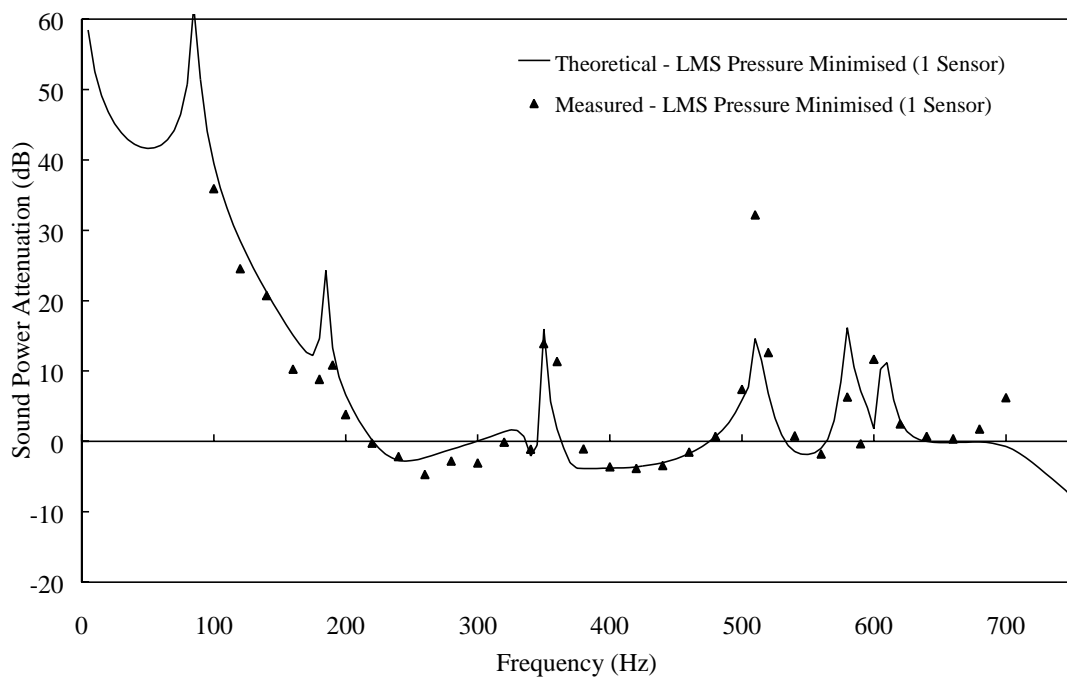**Figure 5.27**   Theoretical and measured controlled radiated sound power, minimising pressure at 1 sensor.

Figure 5.28   Theoretical and measured radiated sound power attenuation, minimising pressure at 1 sensor.

Figure 5.29   Theoretical and measured controlled radiated sound power, minimising pressure at 2 sensors.

Figure 5.30   Theoretical and measured radiated sound power attenuation, minimising pressure at 2 sensors.

Figure 5.31   Theoretical and measured controlled radiated sound power, minimising pressure at 5 sensors.

Figure 5.32   Theoretical and measured radiated sound power attenuation, minimising pressure at 5 sensors.
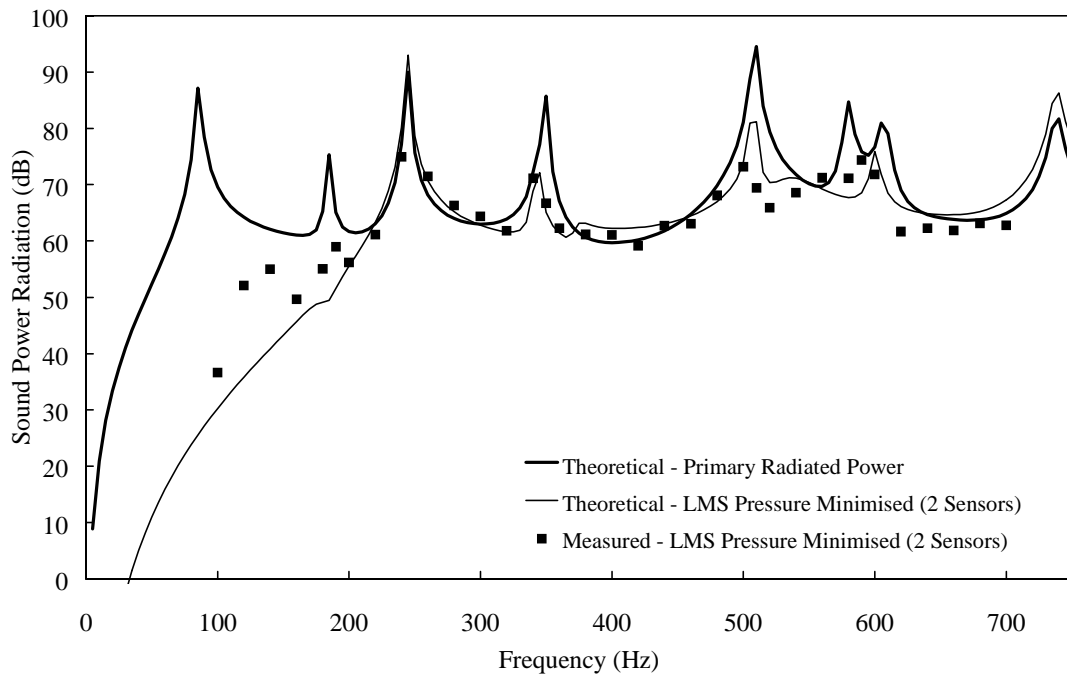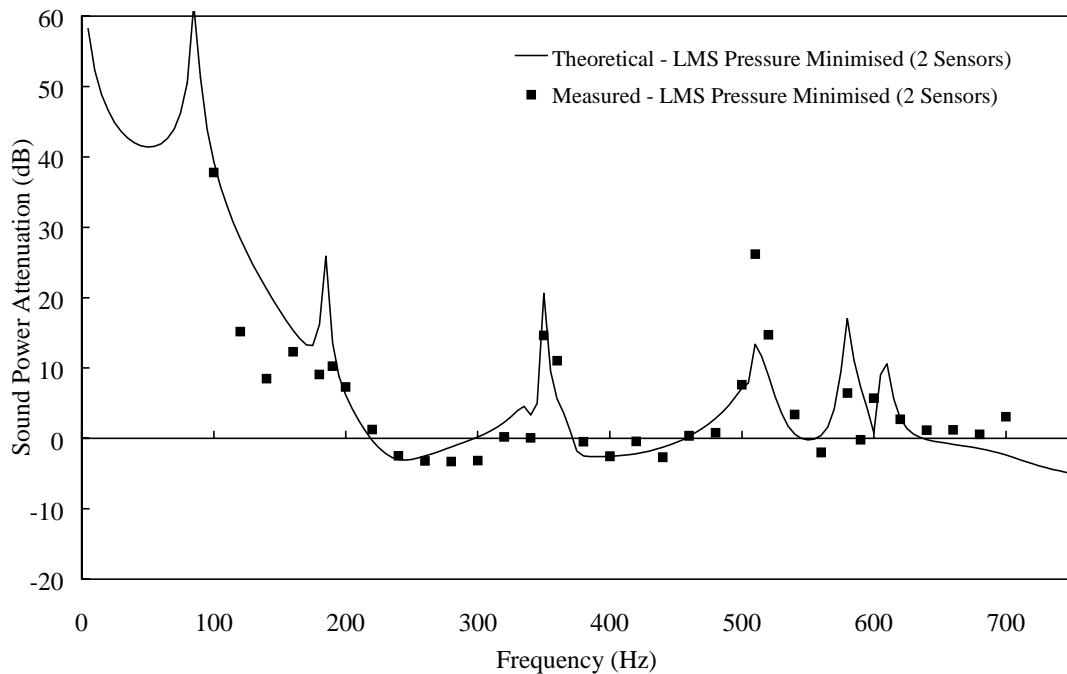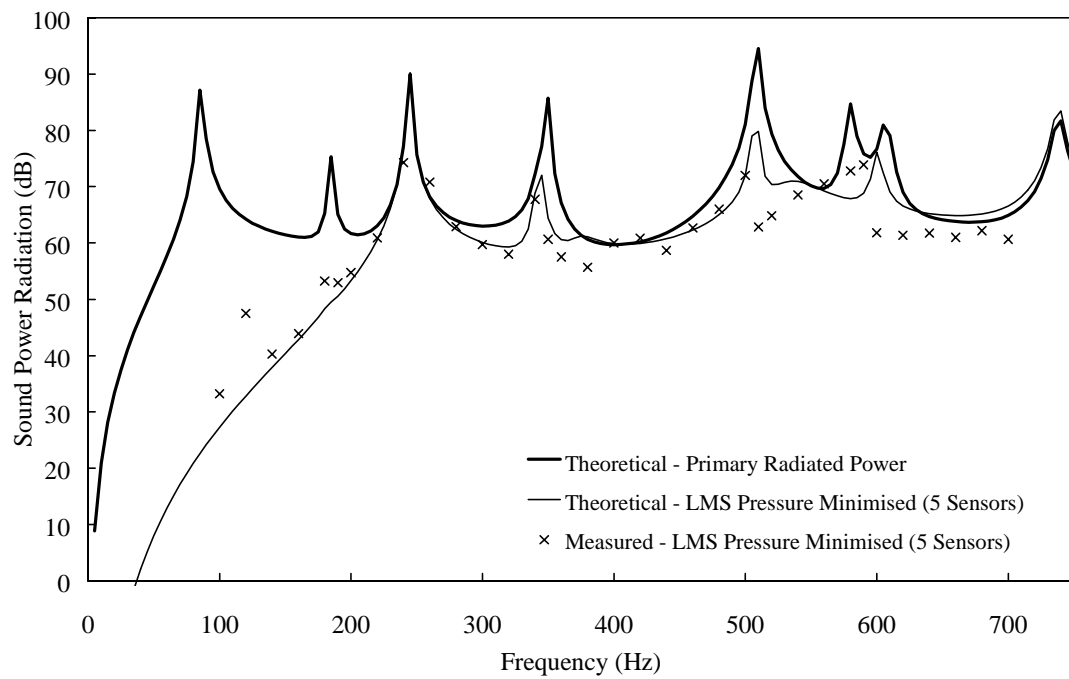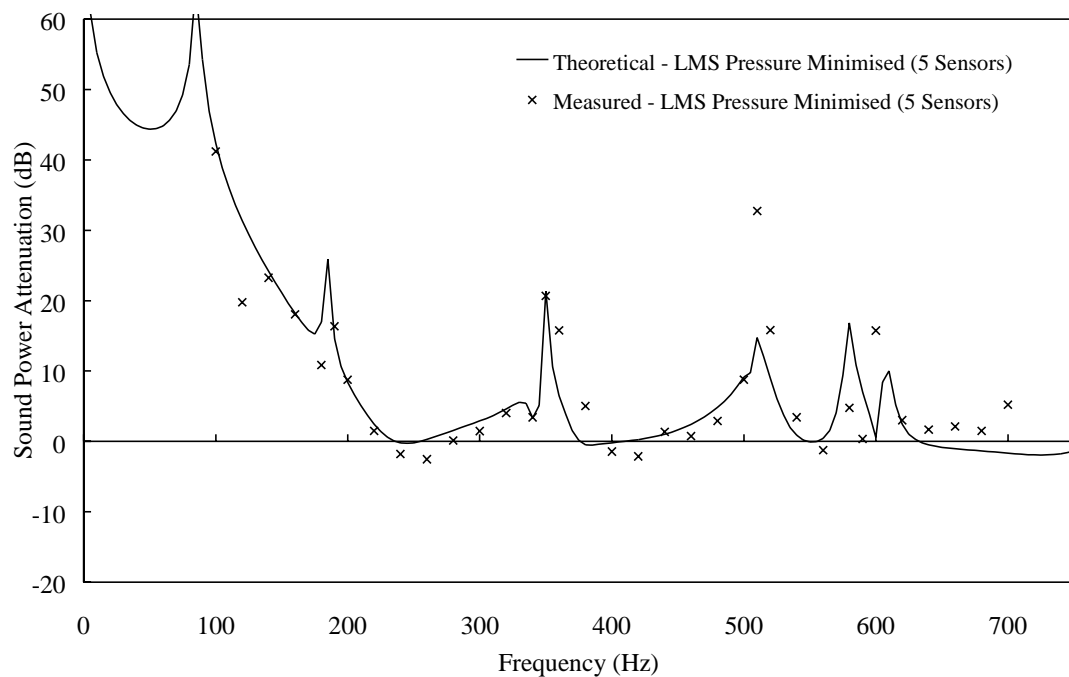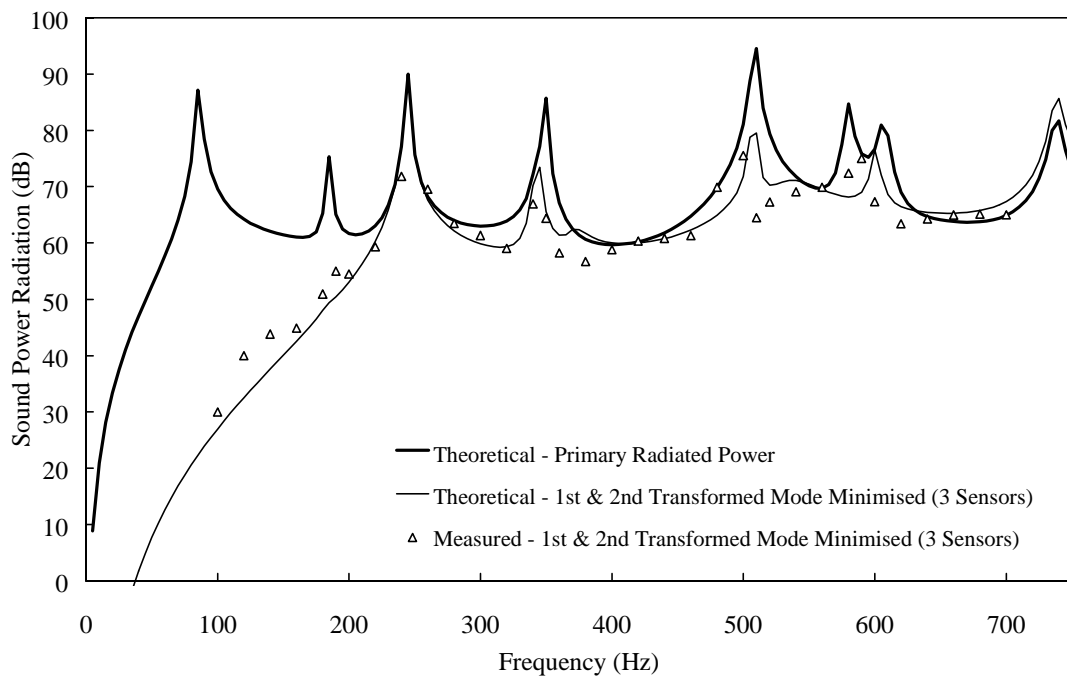
Figure 5.33   Theoretical and measured controlled radiated sound power, minimising the 1st & 2nd transformed modes decomposed from 3 sensors.
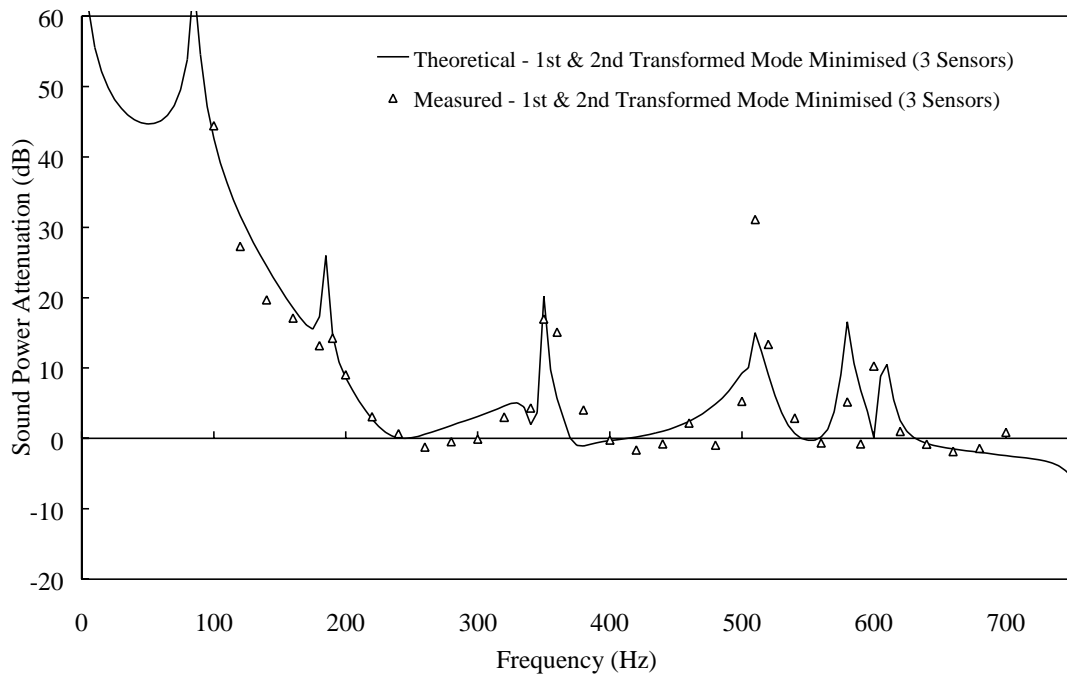
Figure 5.34   Theoretical and measured radiated sound power attenuation, minimising the 1st and 2nd transformed mode decomposed from 3 sensors.

Figure 5.35   Theoretical controlled radiated sound power, minimising pressure at 1 and 5 sensors and minimising the 1st and 2nd transformed modes.

Figure 5.36   Theoretical radiated sound power attenuation, minimising pressure at 1 and 5 sensors and minimising the 1st and 2nd transformed modes.

Figure 5.37   Experimental controlled radiated sound power, minimising pressure at 1 and 5 sensors and minimising the 1st and 2nd transformed modes.

Figure 5.38   Experimental radiated sound power attenuation, minimising pressure at 1 and 5 sensors and minimising the 1st and 2nd transformed modes.

Figure 5.39   Theoretical controlled radiated sound power, minimising pressure at 2 sensors and minimising the 1st and 2nd transformed modes.
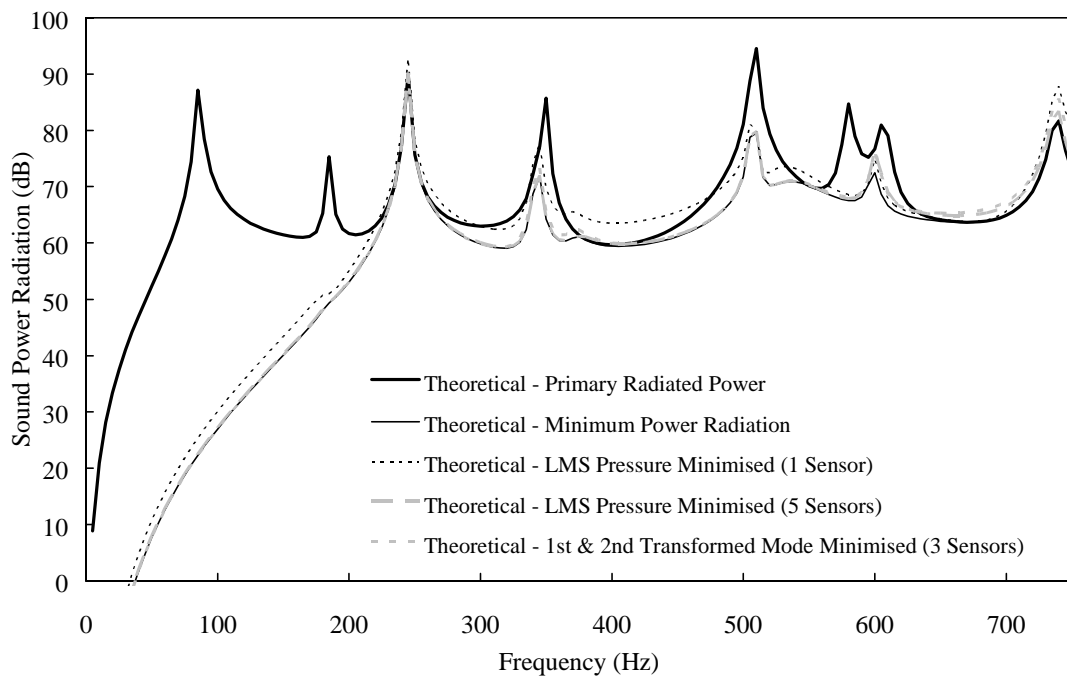

Figure 5.40   Theoretical radiated sound power attenuation, minimising pressure at 2 sensors and minimising the 1st and 2nd transformed modes.
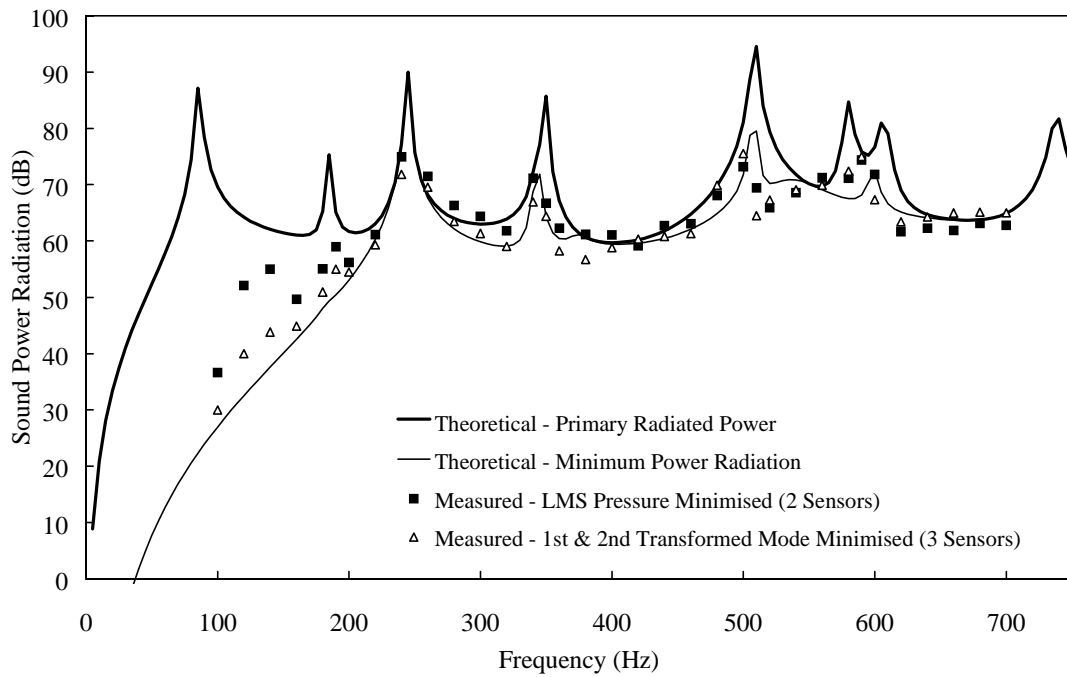
Figure 5.41   Experimental controlled radiated sound power, minimising pressure at 2 sensors and minimising the 1st and 2nd transformed modes.
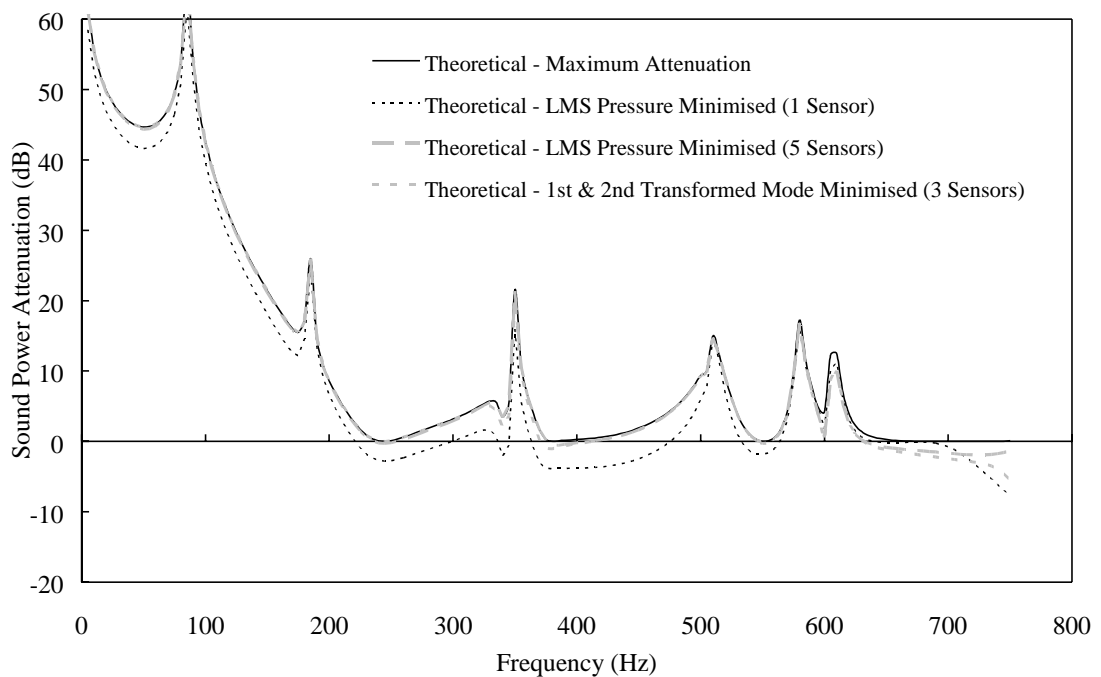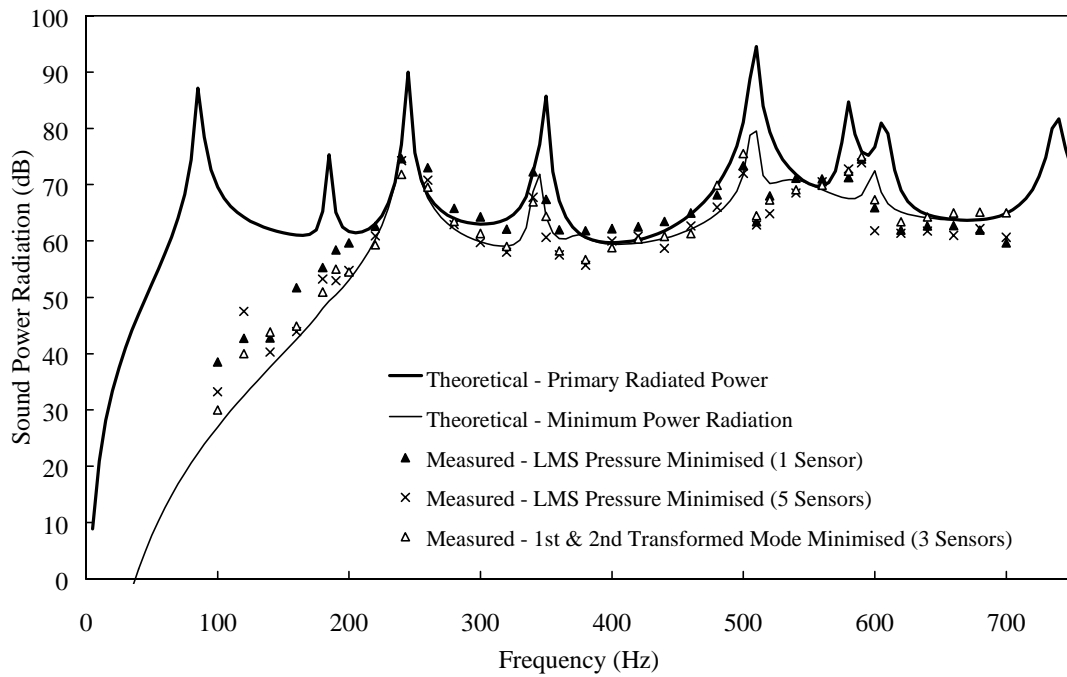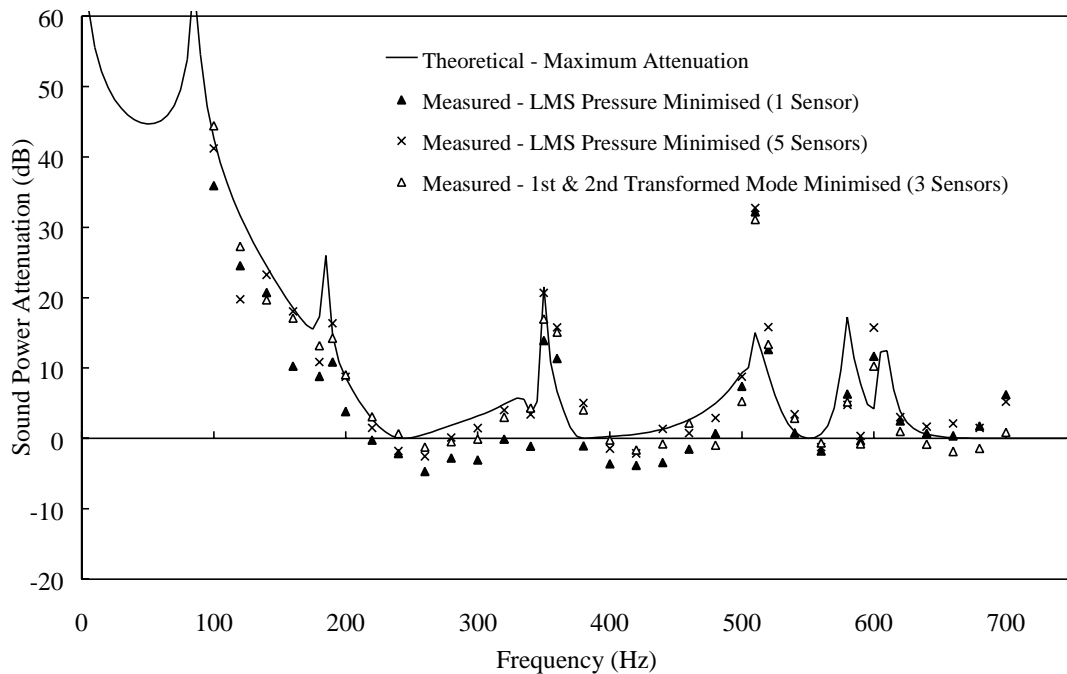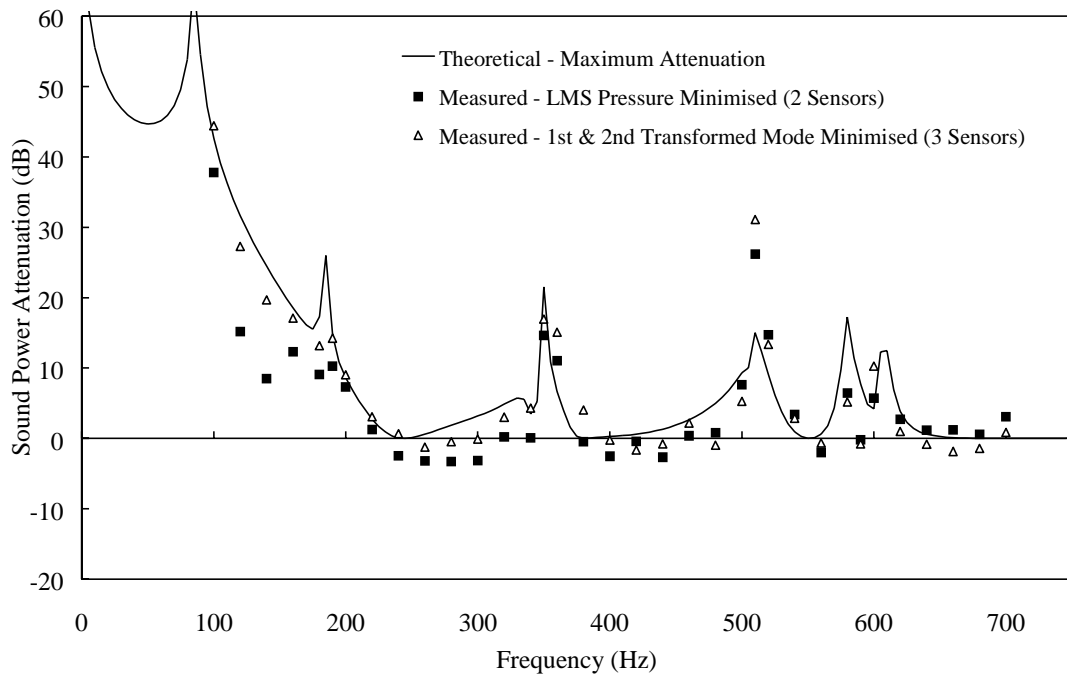

Figure 5.42   Experimental radiated sound power attenuation, minimising pressure at 2 sensors and minimising the 1st and 2nd transformed modes.
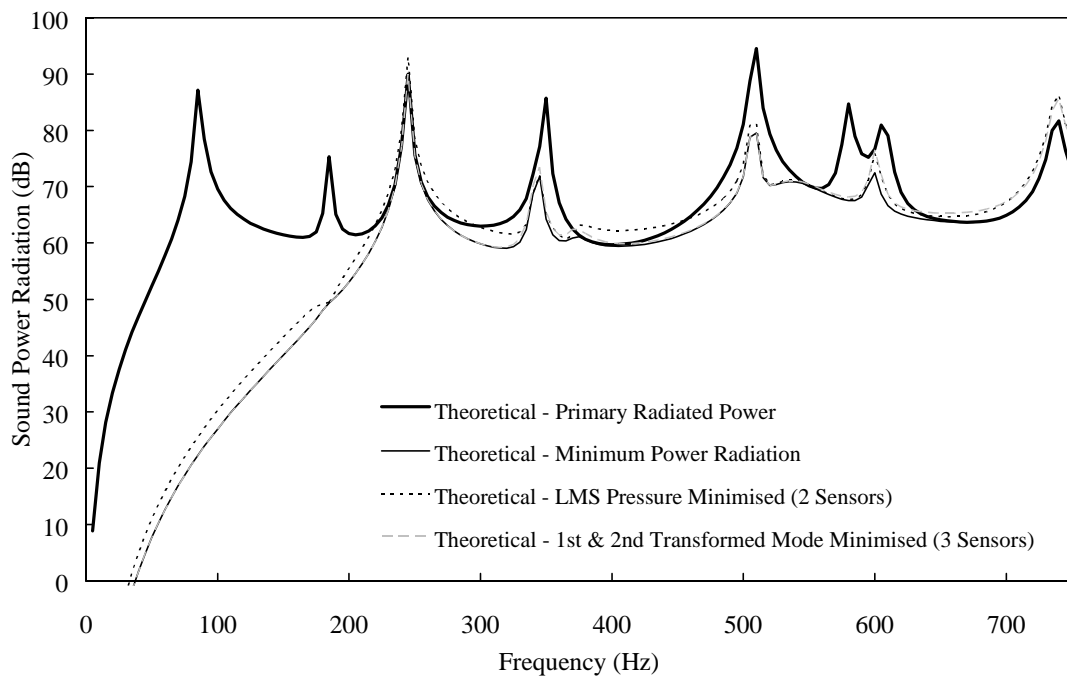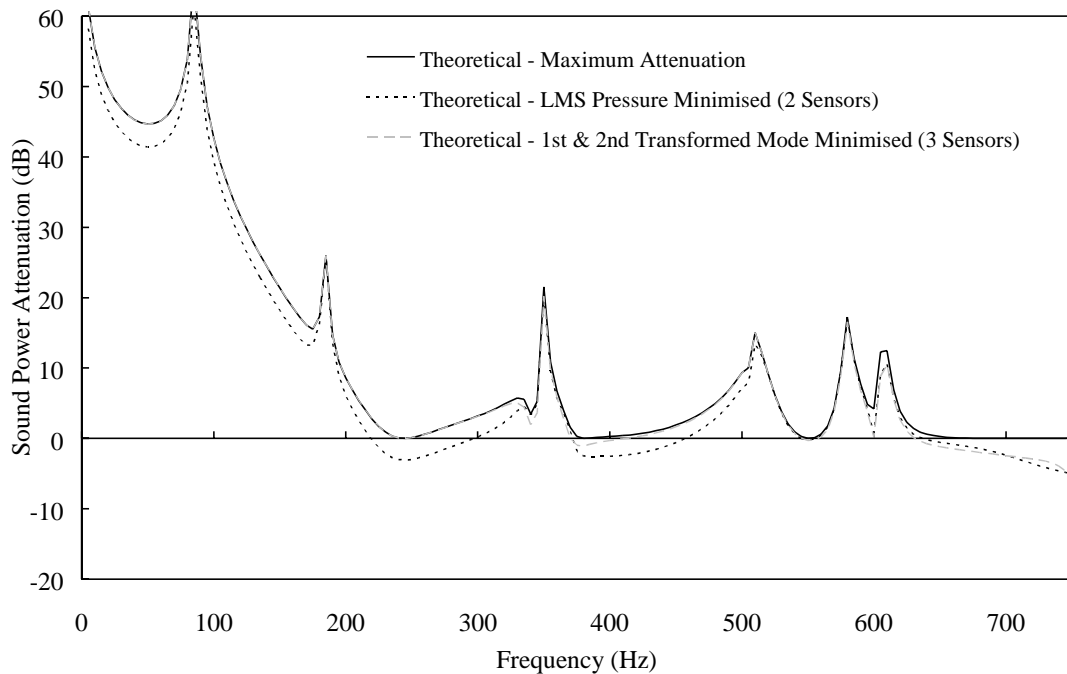
5.5   CONCLUSIONS

The concept of the *transformed modes* of vibration which contribute independently to radiated sound power have been introduced. Their relation to normal structural modes of vibration and their acoustic radiation patterns have been examined. Theoretical definitions of modal filters were developed such that the transformed modal amplitudes (and indirectly the radiated sound power) could be measured by using a small number of acoustic sensors in the farfield. Due to the consistency of the acoustic radiation patterns of the transformed modes over a wide range of frequencies, the model was extended to enable simpler implementation of the filters.

Theoretical results indicated that, by using a measure of the transformed modes as error criteria for an active noise control system and by minimising only a small number of the transformed modes, maximum achievable power reduction could be realised over a wide frequency range. It was found that if the modal filters were constructed simply by a constant weighting and time delay applied to the error sensor outputs, rather than by a full frequency dependent implementation, then good control could be maintained with only a small reduction in effective bandwidth.

Experimental measurements of actively controlled radiated sound power were performed for four different error criteria. The results of the experimental work validated the predictions made theoretically, and showed that construction of an acoustic sensor to measure sound power radiation using a small number of filtered pressure sensors is practical.

For the physical system that was modelled, gains in attenuation of the overall sound power radiation were not significant when minimising the transformed modes as compared to minimising five pressure signals. For this system both were close to the maximum achievable attenuation given the primary and control actuator locations. What was achieved however was a marked reduction in the number of error channels required on the control system to produce similar levels of attenuation.

The accuracy of the detection of the transformed modes was very good and is primarily governed by the accuracy of the calculation of the inverse of the normal mode transfer function $\mathbf{Z}_n^{-1}$ (used in Equation 5.13). Generally the number of error sensors n_e is less than the number of normal modes considered n_m, in which case the inverse of the normal mode transfer function matrix is underdetermined and needs to be found by a pseudoinverse technique. The accuracy of this procedure depends not only on the ratio of the number of error sensors to the number of contributing normal modes, but on the linear independence of the contributions from the error sensors. Mathematically this corresponds to the measurement of the linear independence of the rows in matrix $\mathbf{Z}_m$, commonly called the condition number of the matrix. Physically this will depend on the locations of the microphone sensors in the farfield. As such it does not seem practical to generalise a criterion for the minimum number of microphones for the accurate detection of the transformed modes.

Chapter 6

TRANSFORMED MODES OF MULTIPLE SOURCE SYSTEMS

6.1   INTRODUCTION

In the previous chapter theory was developed to model the acoustic sensing of transformed modes of vibration, which could be used as an error function to actively minimise the sound power radiation from a single vibrating panel. In that case distributed PVDF structural sensors have been implemented previously to sense the transformed modes (Snyder *et al.*, 1995*a*), although it is not apparent that these structural sensors are any more easily constructed (for use on a 2D structure) than sensors implemented acoustically. Furthermore the analysis of Chapter 5 allows a fundamental understanding to be obtained of the mechanisms of the acoustic sensing system and allows a more direct physical comparison of the results obtained with the structural transformed modes.

In this chapter the theoretical work presented previously is extended to account for cases where the control source is physically separate from the primary radiating structure (ie. a loudspeaker or perforated control panel). A number of modifications are introduced to the theory to account for the changes to the physical system.

6.2   THEORETICAL ANALYSIS

The theoretical analysis developed here closely follows that presented in Chapter 5. The overall sound power radiated from a multiple panel system is considered as the error criterion. A weighting matrix is calculated so that the farfield power can be determined as a function of the displacement of each normal structural mode contributing to the vibration response of each panel. The radiated sound power weighting matrix is constructed from the self and cross-weighting functions of the two panels. This matrix contains off diagonal terms representing coupling between the various normal modes. An orthonormal transformation is applied to the weighting matrix to diagonalise it so that the resulting matrix can be used to calculate the power contribution of each transformed mode, which is independent of the contribution of all other transformed modes. The measured acoustic field is decomposed by a modal filter to give an acoustic measure of each of the transformed modes.

6.2.1   PHYSICAL ARRANGEMENT

A vibrating rectangular panel (primary panel) of dimensions $L_x \times L_y$, thickness h and with n_p point excitations $\mathbf{f}_p$ is located on the $z = -L_z$ plane. In front of the primary panel, a second simply supported perforated panel (the control panel) is installed on the $z = 0$ plane and is surrounded by an infinite rigid baffle. This is identical to the arrangement described in Section 3.2.1 and shown in Figure 3.1.

6.2.2   GLOBAL ERROR CRITERION

The radiated sound power given by Equation (4.36) can be re-expressed for this multiple source

system as

$$W = \mathbf{w}_t^{\text{H}} \, \mathbf{\Pi}_m \, \mathbf{w}_t , \tag{6.1}$$

where $\mathbf{w}_t$ is the total modal displacement amplitude vector incorporating both the primary and control panels given by

$$\mathbf{w}_t = \begin{bmatrix} \mathbf{w}_p \\ \mathbf{w}_c \end{bmatrix} . \tag{6.2}$$

In this case the $(n_m + n_m) \times (n_m + n_m)$ *multiple source* sound power weighting matrix is

$$\mathbf{\Pi}_m = \begin{bmatrix} \mathbf{\Pi}_{pp} & \mathbf{\Pi}_{cp}^{\text{H}} \\ \mathbf{\Pi}_{cp} & \mathbf{\Pi}_{cc} \end{bmatrix} \tag{6.3}$$

where the $n_m \times n_m$ submatrices $\mathbf{\Pi}_{pp}$, $\mathbf{\Pi}_{cp}$ and $\mathbf{\Pi}_{cc}$ are given by Equations (4.37-4.39). Note that $\mathbf{\Pi}_{pp}$, the primary panel self-weighting matrix is identical to $\mathbf{\Pi}$ defined by Equation (5.2), and is therefore necessarily real and symmetric, as is $\mathbf{\Pi}_{cc}$ the control panel self-weighting matrix. Both these matrices are also sparse, with only the modes with like index pairs exerting a mutual influence on each other. The cross-weighting matrix $\mathbf{\Pi}_{cp}$, however is dense, complex and hermitian, such that the multiple source weighting matrix is also hermitian.

Diagonalising this hermitian weighting matrix by the orthonormal transformation;

$$\mathbf{\Pi}_m = \mathbf{Q}_m \mathbf{\Lambda}_m \mathbf{Q}_m^{\text{T}} , \tag{6.4}$$

produces the *complex* orthonormal transformation matrix, $\mathbf{Q}_m$, with columns representing the *complex* eigenvectors of the weighting matrix. The diagonal matrix of associated eigenvalues,

173

$\mathbf{\Lambda}_m$, remains totally *real*. Alternatively, it can be determined from the form of Equation (6.1), where W is real, and noting that $\mathbf{\Pi}_m$ is a hermitian matrix that the imaginary components of $\mathbf{\Pi}_m$ can be ignored with no loss of generality, and in this case that the orthonormal transformation matrix, $\mathbf{Q}_m$, also remains completely *real*.

The farfield sound pressure at n_e microphone error sensors positioned at $\mathbf{e}_i$ ($i = 1, n_e$), resulting from all of the *normal* structural modes on both the primary and control panels is given by the $n_e \times 1$ vector

$$\mathbf{p} = \mathbf{Z}_n^m \mathbf{w}_t, \tag{6.5}$$

where $\mathbf{Z}_n^m$ is the $n_e \times (n_m + n_m)$ normal mode radiation transfer function matrix given by

$$\mathbf{Z}_n^m = \begin{bmatrix} \mathbf{z}_p(\mathbf{e}_1) & \mathbf{z}_c(\mathbf{e}_1) \\ \vdots & \vdots \\ \mathbf{z}_p(\mathbf{e}_{n_e}) & \mathbf{z}_c(\mathbf{e}_{n_e}) \end{bmatrix}. \tag{6.6}$$

The modal radiation transfer functions $\mathbf{z}_p$ and $\mathbf{z}_c$ are defined in Equations (4.34) and (4.35) respectively.

Rearranging Equation (6.5) and substituting with Equation (6.4) into Equation (6.1) gives

$$W = \mathbf{w}_t^H \mathbf{Q}_m \mathbf{\Lambda}_m \mathbf{Q}_m^T \mathbf{w}_t = \mathbf{p}^H \left((\mathbf{Z}_n^m)^{-1} \right)^H \mathbf{Q}_m \mathbf{\Lambda} \mathbf{Q}_m^T (\mathbf{Z}_n^m)^{-1} \mathbf{p} \tag{6.7}$$

or

$$W = \mathbf{p}^H (\mathbf{Z}_t^m)^H \mathbf{\Lambda} \mathbf{Z}_t^m \mathbf{p}. \tag{6.8}$$

If $\mathbf{Q}_m$ is truncated as discussed in Section 5.2.2, then $\mathbf{Z}_t^m$ is the $n_e \times n_{tm}$ multiple source transformed mode radiation transfer function matrix given by

$$\mathbf{Z}_t^m \;=\; \mathbf{Q}_m^{\mathrm{T}}(\mathbf{Z}_n^m)^{-1}\,. \tag{6.9}$$

The error criterion can then be expressed as a quadratic function of the complex control forces $\mathbf{f}_c$ as shown in Equation (5.14), with corresponding coefficients;

$$\mathbf{A} \;=\; \boldsymbol{\Psi}_c^{\mathrm{H}}\,\mathbf{Y}_c^{\mathrm{H}}\,\mathbf{Z}_c^{\mathrm{H}}\,(\mathbf{Z}_t^m)^{\mathrm{H}}\,\boldsymbol{\Lambda}_m\,\mathbf{Z}_t^m\,\mathbf{Z}_c\,\mathbf{Y}_c\,\boldsymbol{\Psi}_c\,, \tag{6.10}$$

$$\mathbf{b} \;=\; \boldsymbol{\Psi}_c^{\mathrm{H}}\,\mathbf{Y}_c^{\mathrm{H}}\,\mathbf{Z}_c^{\mathrm{H}}\,(\mathbf{Z}_t^m)^{\mathrm{H}}\,\boldsymbol{\Lambda}_m\,\mathbf{Z}_t^m\,\mathbf{Z}_p\,\mathbf{Y}_p\,\boldsymbol{\Psi}_p\,\mathbf{f}_p \tag{6.11}$$

and

$$c \;=\; \mathbf{f}_p^{\mathrm{H}}\,\boldsymbol{\Psi}_p^{\mathrm{H}}\,\mathbf{Y}_p^{\mathrm{H}}\,\mathbf{Z}_p^{\mathrm{H}}\,(\mathbf{Z}_t^m)^{\mathrm{H}}\,\boldsymbol{\Lambda}_m\,\mathbf{Z}_t^m\,\mathbf{Z}_p\,\mathbf{Y}_p\,\boldsymbol{\Psi}_p\,\mathbf{f}_p\,. \tag{6.12}$$

6.3   NUMERICAL RESULTS

The numerical analysis undertaken here considers a perforated control panel with a 22x10 array of holes of diameter d=10mm and spaced a distance L_z=0.03m away from the primary panel. A single point primary source is located at (35mm,103.3mm) on the primary panel and one control source is located at (35mm,0mm) on the perforated control panel. Three error sensors are positioned in three dimensions as given by Error Sensor Locations No. 1-3 in Table 5.3.

Changing the solid area of the perforates can be expected to have a marked effect on the form of the modal filters due to their differing radiation properties, making an examination of the differences here, mostly worthless. The spacing of the control panel from the primary panel has been shown in Section 4.3.2 to have a negligible effect on the attenuation levels; however it is not clear what effect, if any, this may have on the form of the modal filters. Therefore an analysis is also undertaken with the control panel spacing set at L_z=0.01 and 0.05m, to observe the effect of the panel spacing on the form of the modal filters.

The theoretical work outlined above was programmed in double precision FORTRAN and run on a SUNSPARC10 computer. As mentioned in Section 4.3, the calculation of the weighting submatrices $\mathbf{\Pi}_{pp}$, $\mathbf{\Pi}_{cp}$ and $\mathbf{\Pi}_{cc}$ was computationally intensive, and so because of computational restraints only the first 20 modes of vibration are considered here. Theoretical modal resonance frequencies below 1000Hz of the primary panel and the perforated control panel are shown in Table 4.2.

6.3.1   TRANSFORMED MODE RADIATION EFFICIENCY

Of primary interest is the relative magnitude of the eigenvalues of the transformed modes, which represent their corresponding radiation efficiency. These are shown, for the first five transformed modes, in Figure 6.1. When compared to the eigenvalues of the transformed modes of a single radiating panel (Figure 5.6) it is observed that the 4th and 5th transformed modes of the two panel system have a much larger influence on the overall radiation levels. Whereas with a single panel the high power radiating *normal* modes (generally the (odd,odd) modes) were limited *exclusively* to the 1st or 2nd transformed modes (see Table 5.2), due to the cross-weighting functions inherent with multiple panels, they now make small contributions to these higher order transformed modes, increasing their relative radiation efficiency.
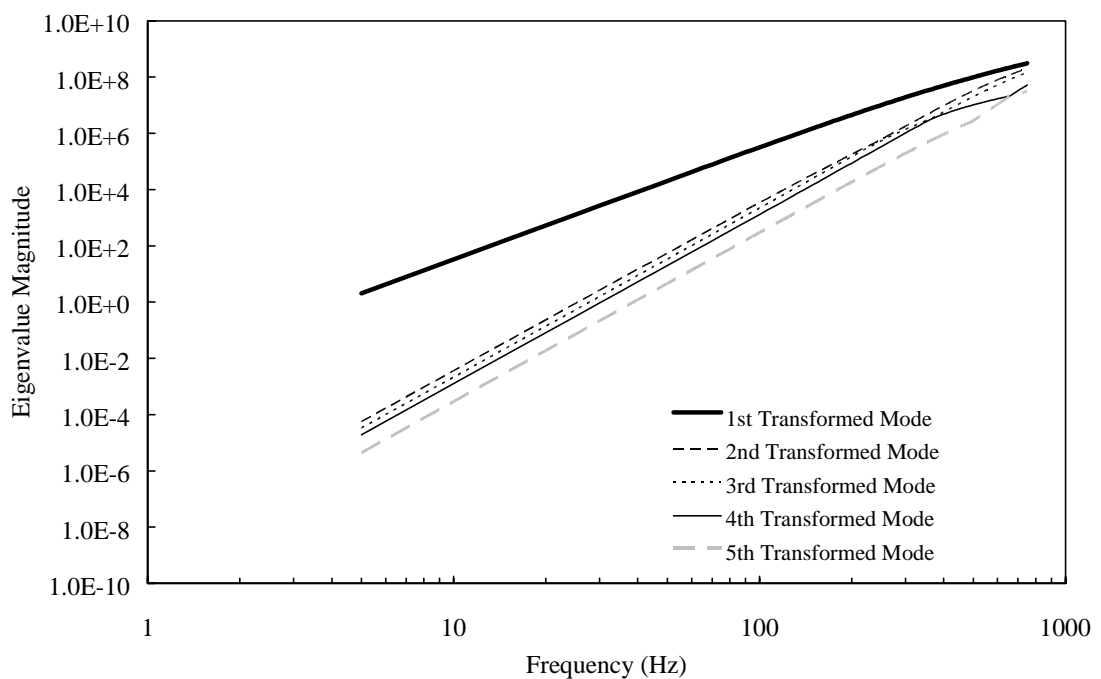

Figure 6.1   Eigenvalues of the first five transformed modes of a multiple source arrangement radiating into free space as a function of frequency.

6.3.2   CONTROLLING TRANSFORMED MODES COMPARED TO TRADITIONAL ERROR CRITERIA

Figures 6.2 & 6.3 show the controlled sound radiation levels and corresponding attenuation levels when the radiated sound power and the 1st and 2nd Transformed Modes (decomposed from three farfield error sensors) are minimised. As was evident in the previous chapter, controlling the transformed modes is highly effective at low frequencies and produces attenuation within 1dB of the maximum that can be expected given the control force location. At higher frequencies however, there are a few lapses in control, until at about 500Hz and beyond it can be seen that minimising the transformed modes mostly serves to increase the overall radiated power.

Given the increased importance of the 4th and 5th transformed modes demonstrated in Section 6.3.1, it appears that more transformed modes need to be considered to allow the minimisation of radiated sound power from multiple sources over a wide frequency range.
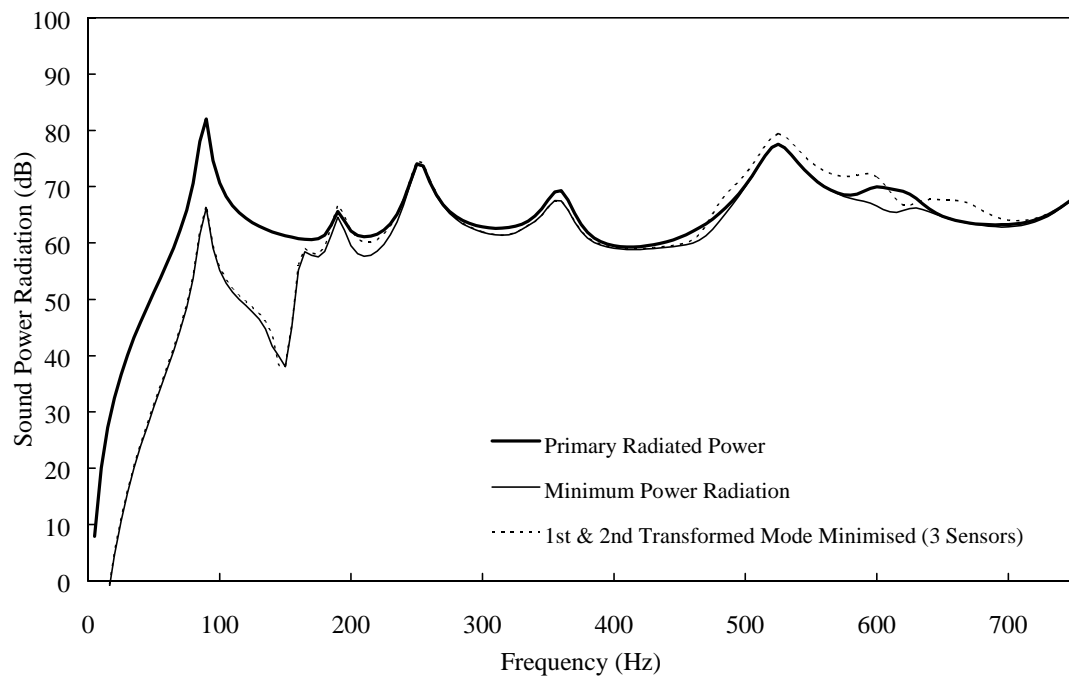
Figure 6.2 Primary and controlled radiated sound power by minimising the 1st and 2nd transformed modes decomposed from 3 sensors.
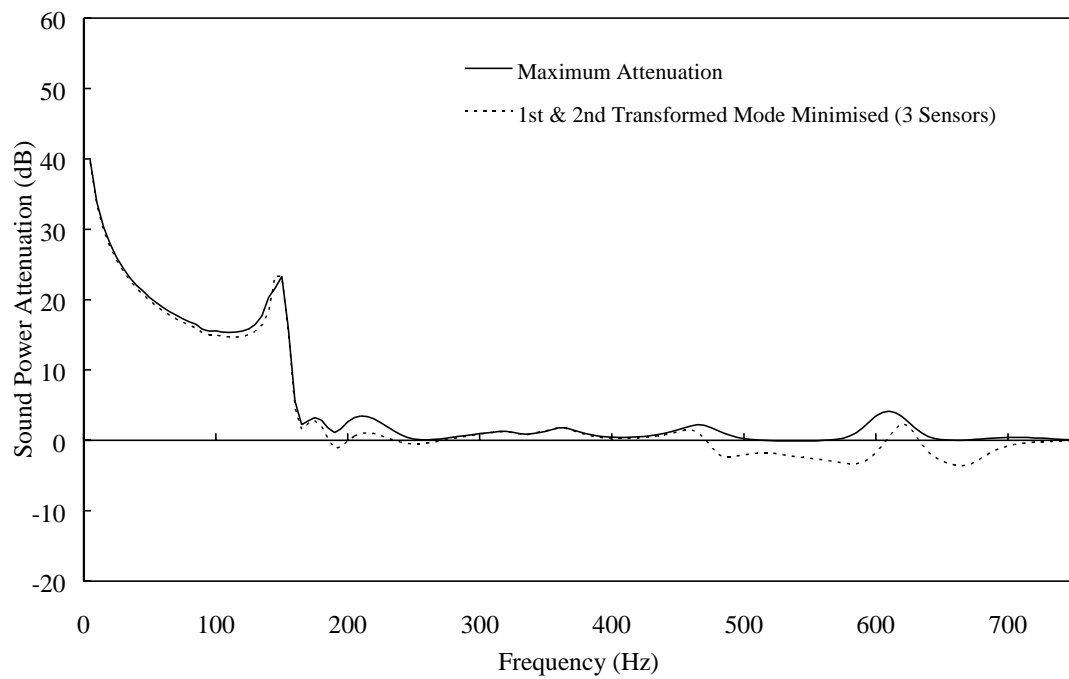
Figure 6.3 Maximum attenuation and attenuation achieved by minimising the 1st and 2nd transformed modes decomposed from 3 sensors.

6.3.3   MULTIPLE SOURCE MODAL FILTER RESPONSE

The response of the modal filter required to decompose the 1st and 2nd transformed mode from three farfield error sensors is shown in Figures 6.4-6.7. There are a number of important differences between these modal filters and those of a single radiating panel (shown in Figures 5.15-5.18) discussed below. These are caused by the addition of the cross coupling between the two panels.

For the 1st transformed mode there is a much increased contribution from the second error sensor (Figure 6.5). Coupled with this is a marked variation in the relative amplitudes at higher frequencies that was not apparent with only a single panel. The relative phase shift between the three sensors is also no longer linear, but incorporates a slight nonlinearity. Moreover, the relative phase shift is *not* the same for both transformed modes, and would require separate time delays to be implemented for each transformed mode.

The 2nd transformed modal filter magnitude is also clearly a nonlinear function of frequency, with the second sensor contributing very little to the detection of the mode at around 250Hz. This has been caused by changes in positions of the nodes in the radiation patterns of the transformed modes, and has also resulted in a sudden change in importance of the contribution of the 1st and 3rd sensors to the detection of the transformed mode at that frequency.

Figure 6.4 Phase response of the modal filter required to decompose the 1st transformed mode from 3 farfield sensors.
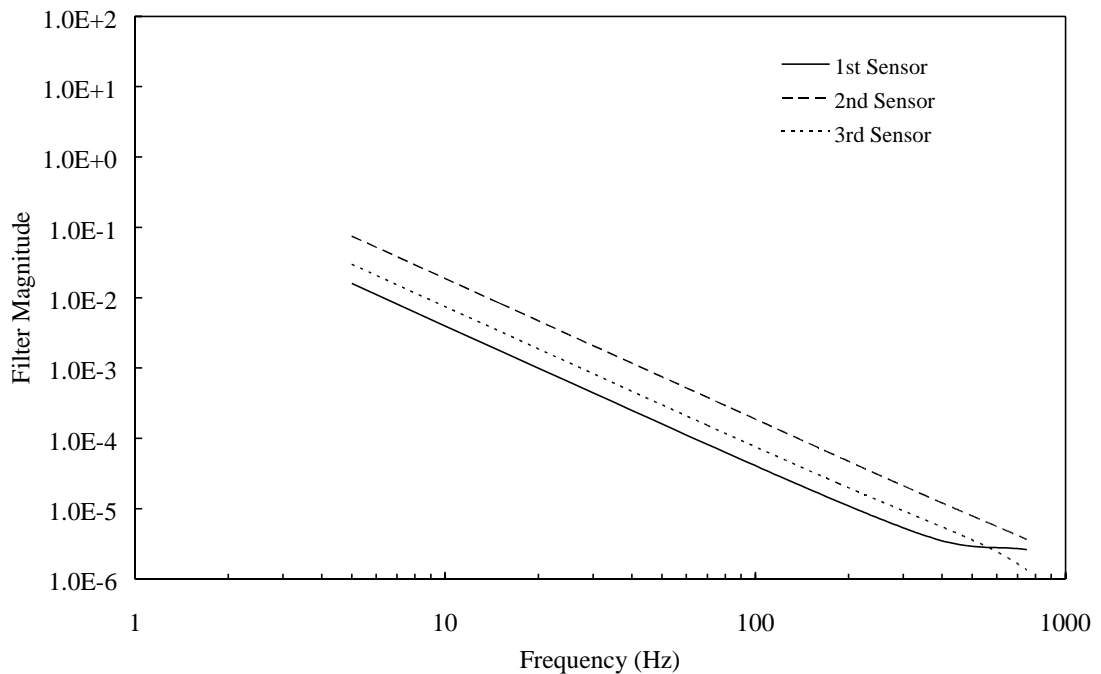
Figure 6.5 Amplitude response of the modal filter required to decompose the 1st transformed mode from 3 farfield sensors.
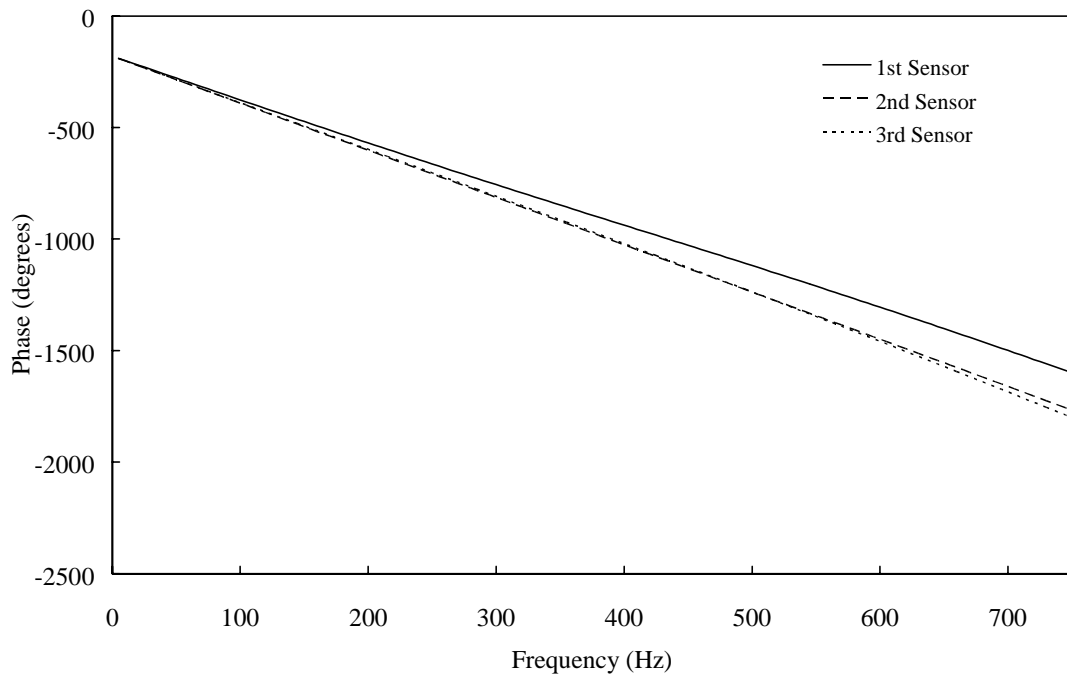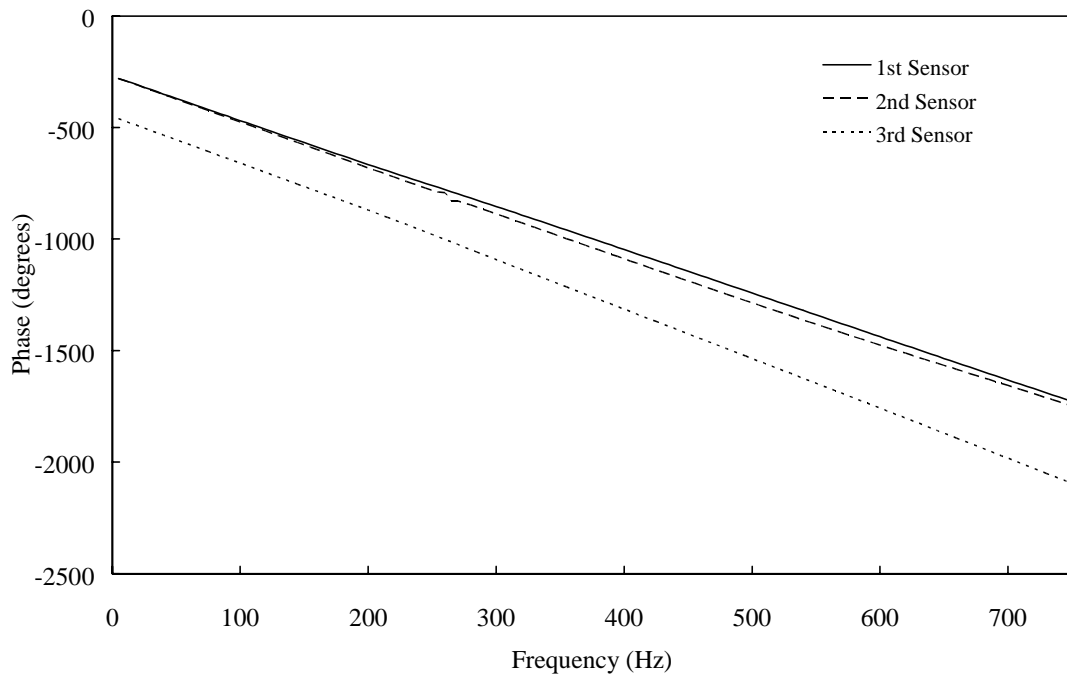
Figure 6.6 Phase response of the modal filter required to decompose the 2nd transformed mode from 3 farfield sensors.
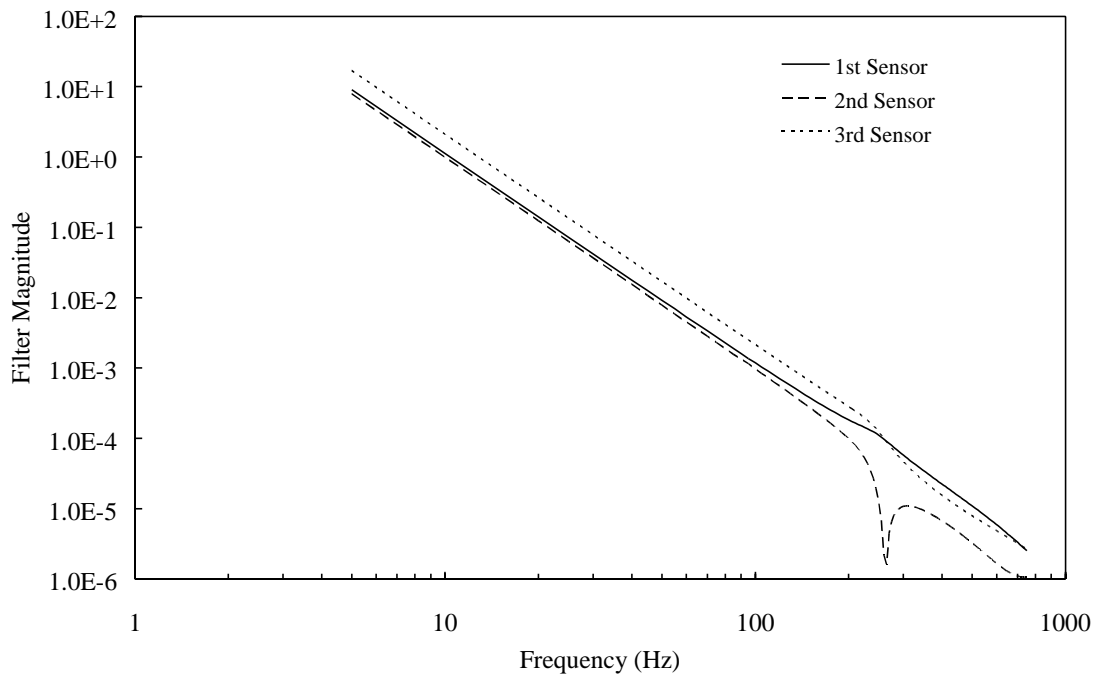
Figure 6.7 Amplitude response of the modal filter required to decompose the 2nd transformed mode from 3 farfield sensors.

6.3.4 MULTIPLE SOURCE TRANSFORMED MODE FREQUENCY CORRECTION

It is also possible, in the case of multiple sources, to implement a corrected fixed frequency modal filter by applying a correction filter, $\mathbf{X}_m$, following the analysis of Section 5.2.3. In this case the correction filters for each transformed mode are of the form shown in Figure 6.8. Although both are nearly linear up to 250Hz, the 2nd transformed mode's filter is not nearly as well behaved above 250Hz as the correction filter for a single panel (shown in Figure 5.19), though this may limit its effective bandwidth, it is worthwhile recognising that the second transformed mode's contribution to the radiated sound power here is shown to be nearly two orders of magnitude lower than that by the 1st transformed mode.
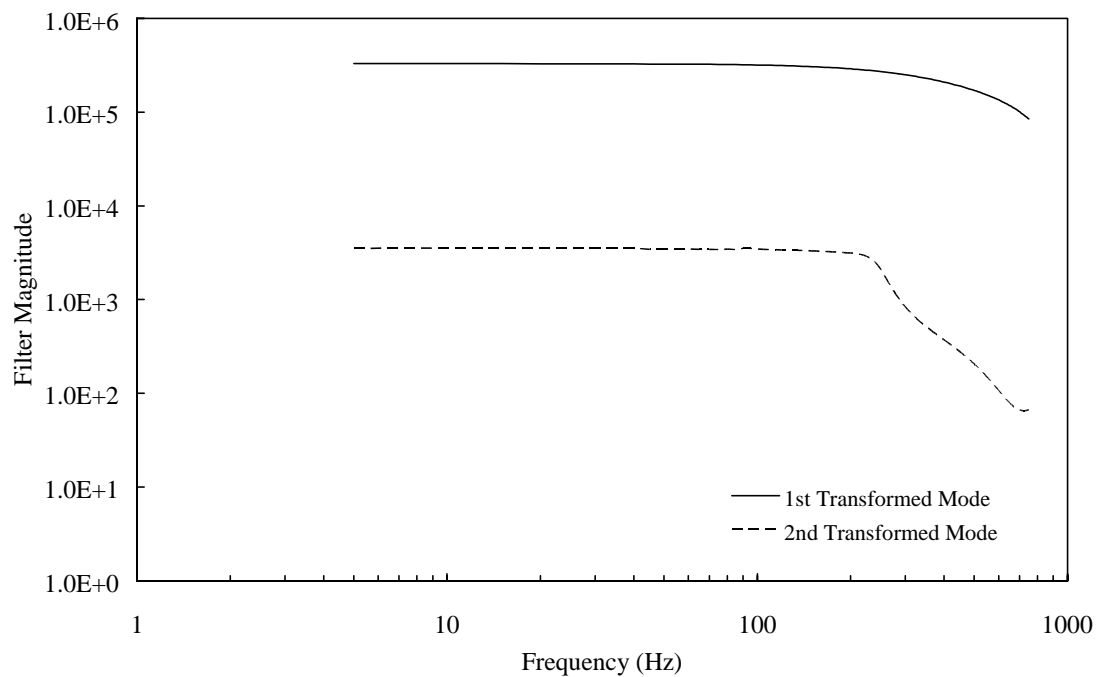
Figure 6.8 Amplitude response of the correction filter, $\mathbf{X}_m$, for the 1st and 2nd transformed modes decomposed from 3 farfield sensors.

183

6.3.5   EFFECT OF PANEL SPACING ON THE MODAL FILTER RESPONSE

The effect of the spacing, L_z, between the perforated control source and the primary panel on the modal filters is shown in Figures 6.9-6.12. The effect at low frequency is observed to be negligible, however at frequencies above 300Hz large deviations in the both the phase and magnitude of the filters can occur. In particular, the position of the sharp drop in influence of the 2nd sensor on the detection of the 2nd transformed mode changes by about 30Hz, shown in Figure 6.12. This is likely due to small changes in the position of the nodes in the acoustic radiation pattern of the 2nd transformed mode.
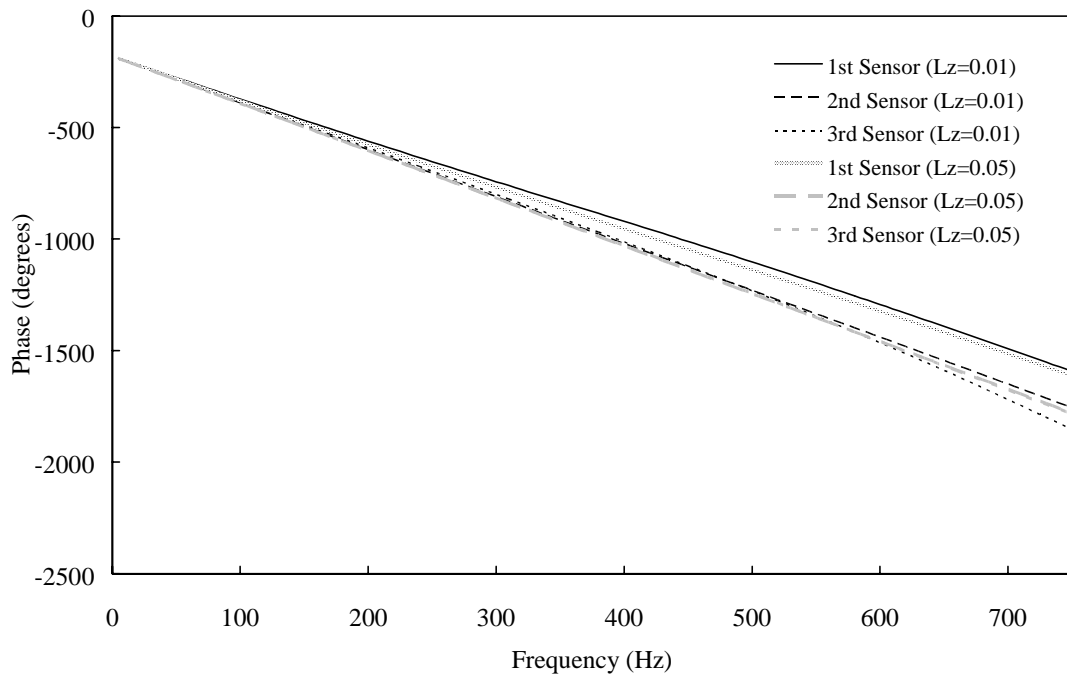
Figure 6.9   Phase response of the modal filter (to decompose the 1st transformed mode) with perforated control panels spaced at L_z=0.01 and 0.05m.
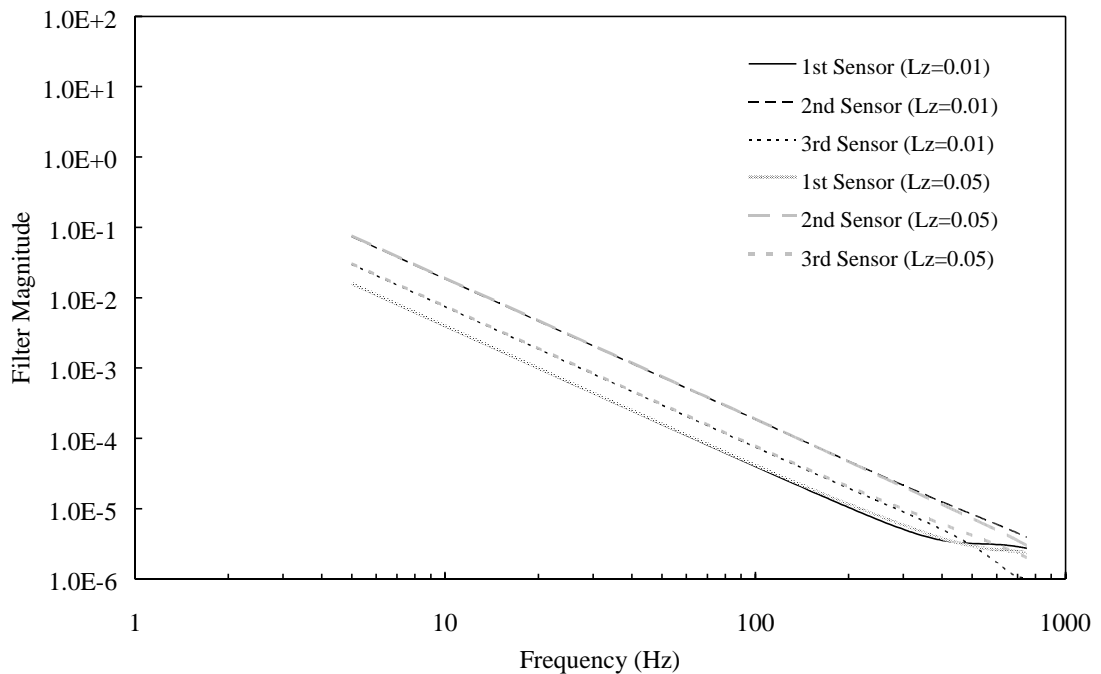
Figure 6.10   Amplitude response of the modal filter (to decompose the 1st transformed mode) with perforated control panels spaced at L_z=0.01 and 0.05m.
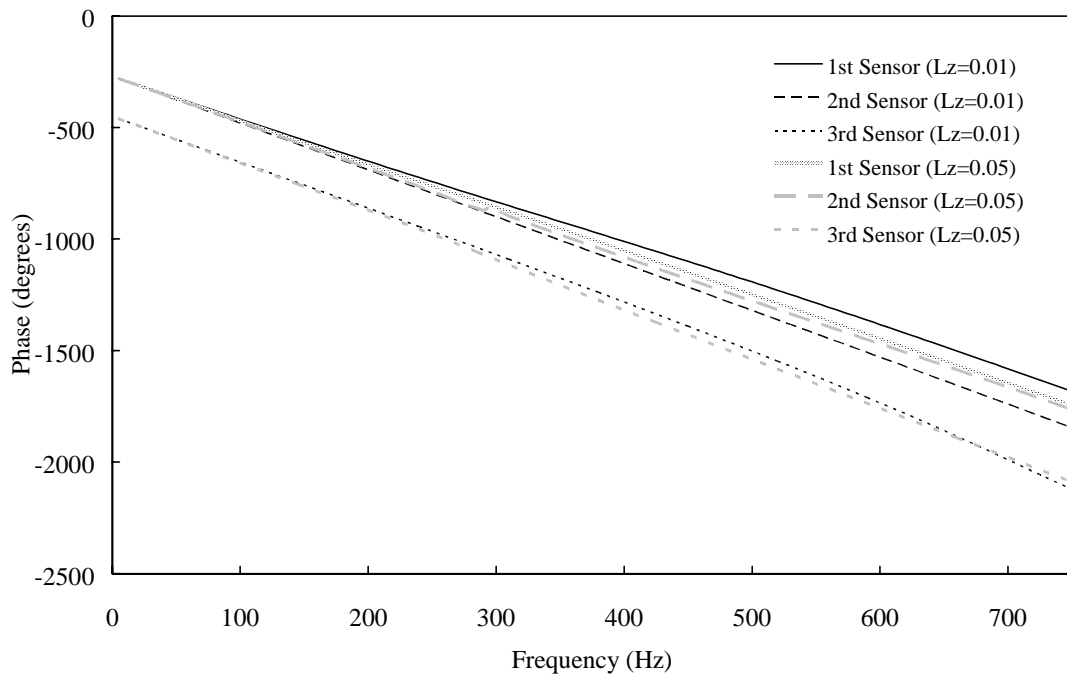
Figure 6.11   Phase response of the modal filter (to decompose the 2nd transformed mode) with perforated control panels spaced at L_z=0.01 and 0.05m.
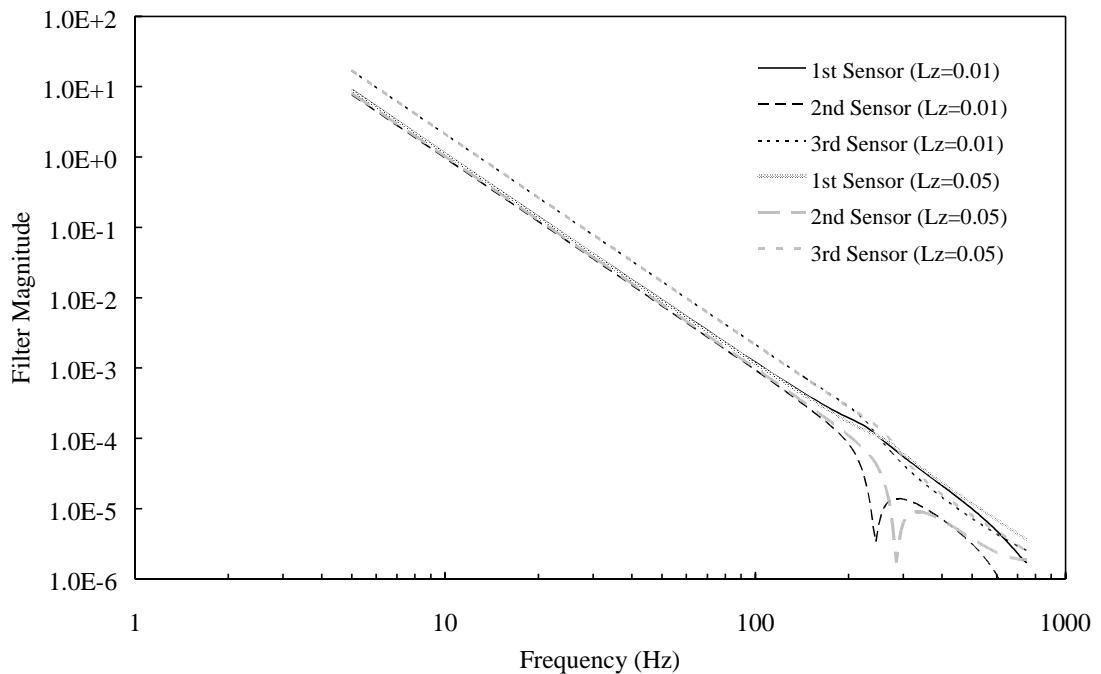
Figure 6.12   Amplitude response of the modal filter (to decompose the 2nd transformed mode) with perforated control panels spaced at L_z=0.01 and 0.05m.

186

6.4   CONCLUSIONS

The transformed modes of vibration of a multiple source system that contribute orthogonally to the overall radiated sound power have been examined for the case of a pair of closely placed rectangular panels. Modal filters were developed to enable the measurement of the transformed modes, and therefore the radiated sound power, by using a small number of acoustic sensors in the farfield.

A number of important differences were observed between the transformed modes and hence the modal filters used for a multi-source system as compared to radiation from a single source system (analysed in Chapter 5). In particular, a larger number of transformed modes were identified as being significant contributors to the radiated sound power, manifest by a larger number of important eigenvalues of the transformed modes. This had implications upon the amount of attenuation that could be achieved by minimising only the first two transformed modes, which while excellent at low frequencies, proved non-optimal at higher frequencies, when more higher order transformed modes needed to be considered.

The form of the modal filter's amplitude and phase response was more nonlinear than those for a single radiating panel. In particular the phase response of the filters were not only nonlinear, but different for each of the transformed modes.

A corrected fixed filter implementation was also shown to be viable, over a reduced frequency range compared with that for a single radiating panel.

Finally, the spacing between the control panel and the primary radiating panel was observed to

have a significant effect on the form of the modal filter at higher frequencies.

Chapter 7

CONCLUSIONS

7.1   CONCLUSIONS

The application of a perforated panel as an acoustic control source for use in actively controlling the noise radiated by structures has been examined. Initially the relationship between the resonance frequencies of a perforate and a solid panel of corresponding thickness and size were determined. This provided an *effective resonance frequency ratio* so that the acoustic radiation properties of the perforate could be modelled accurately.

A number of modified classical analyses were applied to calculate effective material properties for perforates that fell within certain geometric bounds, and then to predict their resonance frequencies. A F.E.A. was also used to theoretically predict resonance frequencies. It was found that these two different methods did not agree well, except when the panel perforation geometry was regular, and the size and number of perforations was small. An experimental modal analysis on a small number of panels validated the numerical results of the F.E. Analysis rather than either of the modified classical analyses. A two dimensional cubic function was fit to the F.E.A. results so that the effective resonance frequency ratio of a perforate could be calculated for a wide range of perforation geometries. The effective resonance frequency function so determined was only slightly non-linear, as opposed to that predicted by modified classical analyses which were clearly

nonlinear.

A theoretical model was developed to investigate the feasibility of controlling low frequency sound radiated from a vibrating panel with a perforated control panel placed closely in front of it. Each hole in the perforate was assumed to radiate as an air-piston, driven by the pressure in the cavity behind it and therefore coupled to the displacement of the primary panel. This work was complex, computationally demanding and did not prove to model the achievable sound pressure reductions at all well. This was believed to be because the assumption that a constant pressure was acting throughout the cavity between the two panels did not hold, a view supported by experimental measurements.

In view of the poor performance of this coupled model, a simpler analysis was undertaken, where it was assumed that the primary and control panel's radiation were acoustically uncoupled. This proved to be much more satisfactory in predicting attenuation levels that could be attained experimentally. Theory was developed to predict the resulting pressure field when the least mean square pressure was minimised in the farfield, and to predict the overall radiated sound power when it was used as an error function.

This analysis was used to show numerically that perforates could provide good levels of global noise attenuation at low frequencies, though they were not as effective as Active Structural Acoustic Control applied directly to the radiating panel's surface. The spacing of the control panel (provided that it was much less than a wavelength) from the primary panel was shown have

negligible effect on the amount of control that could be achieved or the magnitude of the control forces required.

The fact that the perforated panel has proved effective at controlling the radiation of the primary panel is partly attributable to the fact that the modal densities of the primary and perforated control panels are roughly comparable. If the modal densities of the primary structure and the control panel were very different it would require much more careful thought as to the design of the control panel (in terms of its thickness, hole density and size) so that the resonance frequencies were in some respect aligned with the primary radiating modes of the primary structure.

The control forces required to attain the attenuation were in general, much lower than required for direct structural control, and for large heavy structures controlled by (relatively) lightweight control panels, the difference in control force magnitude would be considerable. The precise control force magnitude is difficult to quantify and is highly dependent on the physical design of the perforate, and its corresponding acoustic radiation properties. It is clear that perforates with a high solid area in general require a much lower control effort than low solid area perforates. The control effort is however, also closely related to the perforates resonance properties, which can be somewhat controlled by the size, thickness and perforation geometry. This leads to interesting situations where highly perforated (low solid area) panels may require a smaller control effort than lightly perforated (high solid area) panels, due to the matching of different modal resonance frequencies between the control and primary panel, coupled with a

corresponding mismatching of resonance frequencies between the lightly perforated control panel and primary panel.

In designing perforated control panels then, it will be necessary to optimise the physical structure to provide a high level response and radiation efficiency at the frequencies of interest, whilst still allowing ventilation of the controlled structure.

An added advantage of the perforated panel control sources is that they are environmentally robust, compared to traditional loudspeaker sources, which in most cases require regular attention to prevent mould growth, weather damage or other deterioration.

The level of attenuation that may be achieved is often limited, not by the control source, but by the measure of the error criterion. The use of modal filtering of traditional acoustic signals to provide a direct measurement of the total radiated acoustic power, for use as the error criterion for the control system to minimise, was investigated for a single radiating panel with direct structural control. The transformed modes of vibration of the structure were defined, and shown to represent a set of independent contributors to the radiated sound power. Decomposing the sound field radiated by these transformed modes allowed the construction of a modal filter that could be used to measure the transformed modes directly from the acoustic field. Due to the high radiation efficiency of the first few transformed modes, their measurement could be used directly as an estimate of the radiated sound power with little error.

It was shown numerically that minimising the first transformed mode was identical to minimising the radiated sound power at low frequencies. To achieve similar levels of control above 300Hz, both the first and second transformed mode needed to be minimised. For the physical arrangement described, there was little advantage in decomposing the transformed modes from five, rather than three error sensors.

Notwithstanding this, there are still advantages to be gained using more sensors in the farfield, as the estimate of the transformed modal amplitude, and hence the radiated sound power, will be improved. This points to what has appeared as the main advantage of minimising the transformed modes rather than the LMS minimisation of pressure; a reduction in the number of error channels required by the control systems signal processing hardware. Apart from reducing the cost of the control system, this reduction in the number of control channels leads to gains in the speed and stability of convergence to an optimum control signal.

Furthermore, it may be possible that there is a reduced sensitivity of the controlled sound power levels to the position of the error sensors in the farfield when compared to the minimisation of LMS pressure. This could lead to an advantage of this type of error sensing scheme whereby the sensors could be positioned in convenient locations with little degradation of performance, rather than those demanded by the requirements of the control system to achieve acceptable control.

The advantages of controlling the radiated sound power rather minimising the LMS pressure were disappointingly meagre, particularly for the cases of between three and five error sensors

for which minimising the two different error functions produced a similar result. It is expected however, that for the case of radiated sound power minimisation the controlled sound field would be much more uniform, without the large local minima at the positions of the error sensors which is a characteristic of pressure squared minimisation.

The form of the modal filter for sound power minimisation by way of transformed modes was such that it could be implemented over a wide frequency range without any explicit frequency dependent filtering at all. By taking the values of the filter at single frequency and then applying a correction factor, a single weighting and time delay were determined for each error sensor signal. The error signals were then summed together to give a measure of each transformed mode. This produced attenuation levels that were as good as a fully implemented modal filter system around the selected frequency and deviated by only a few dB at other frequencies.

Experimental results were obtained by implementing a modal filter system and measuring the primary and controlled sound power radiation levels from a single rectangular panel using an intensity probe. These results showed excellent agreement between the controlled levels predicted by the theory and attained by controlling the panel with ASAC while minimising the LMS pressure at a number of sensors, and minimising the radiated sound power (by minimising the 1st and 2nd transformed modes).

The theoretical work was then extended to define the transformed modes of a multiple radiator arrangement consisting of a solid panel primary source and a perforated panel control source.

Modal filters were derived to decompose the amplitude of the transformed modes from acoustic measurements in the farfield. While similar in form to the modal filters required for a single radiating panel a number of differences were apparent. The number of transformed modes that needed to be considered to accurately measure the radiated sound power was increased. An increased nonlinearity in both the magnitude and phase response of the filters was observed, particularly at higher frequencies. The spacing between the control panel and the primary panel was shown to have significant effects on the magnitude response of the modal filters. This was somewhat unexpected as the spacing had little effect on the overall levels of control that could be achieved, or the magnitude of the optimum control force.

To calculate the transformed modes of vibration of a structure the normal structural mode shape functions must be known. For structures used in practice, where these cannot be determined analytically, methods such as Finite Element Analysis can used.

The two techniques described in this thesis have been independently shown to allow improvement of the performance of active noise control systems, compared to using traditional acoustic sources or error criteria. Practically, the improvements offered would manifest themselves not only by greater levels of control, but by better *global* control and a greater robustness of both the physical and signal processing components of the control system.

7.2   RECOMMENDATIONS FOR FUTURE WORK

It appears that the magnitude of the modal filter (used to decompose the acoustic radiation pattern of the transformed modes of vibration) may be exploited in such a way to provide a measure of the ability of any particular error sensor location to represent a measure of the sound power radiation from a structure. This may lead to a method for optimising the positions of farfield error sensors, such that little or no explicit filtering is required to determine an acceptable measure of radiated sound power. For example, the second transformed mode of a rectangular panel may be adequately measured by a small number of symmetrically placed sensors, with no relative gain shift and a simple 180° phase shift. Alternatively, an analysis of the sensitivity of the amount of control achievable to the error sensor locations could indicate that minimising the transformed modes allows for a system where sensors could be located in 'convenient' locations with little degradation of the performance of the system.

The ongoing problem of an acoustical sensing systems' susceptibility to environmental conditions, in particular with outdoor applications like substation transformers which are subject to wind and traffic noise, remains here. It is not apparent, however, that an acoustic power mode sensor would be affected more adversely than a traditional pressure sensor. Practical applications may require that the acoustic sensor be used in conjunction with appropriately weighted structural sensor measurements, though it has yet to be shown that even PVDF film sensors themselves are suitably robust for field applications (particularly on very hot or cold surfaces). Clearly more work is required on this.

While considering a practical implementation of sound power measurement and control systems it is recognised that there will be situations when minimising the radiated sound power may *not* be desired. This may occur when it is desired to provide high levels of noise reduction in a single direction, namely a particular complainant's location, without regard for increased overall radiation. The use of a different type of transformed mode may prove useful in this case.

APPENDIX A

For a solid rectangular panel of dimensions $L_x \times L_y$ and displacement w, the farfield pressure at angular frequency ω is described by the Rayleigh integral

$$p(\mathbf{r}) = -\frac{\rho\,\omega^2}{2\pi} \int_{-\frac{L_x}{2}}^{\frac{L_x}{2}} \int_{-\frac{L_y}{2}}^{\frac{L_y}{2}} w(x,y) \frac{e^{-jkr_p}}{r_p}\, dy\, dx .$$

(A.1)

Equation (A.1) can be rewritten as

$$p(\mathbf{r}) = \mathbf{z}(\mathbf{r})^{\mathrm{T}} \mathbf{w},$$

(A.2)

where $\mathbf{z}$ is the pressure transfer function matrix given by

$$\mathbf{z}(\mathbf{r}) = -\frac{\rho\,\omega^2}{2\pi} \int_{-\frac{L_x}{2}}^{\frac{L_x}{2}} \int_{-\frac{L_y}{2}}^{\frac{L_y}{2}} \mathbf{\Psi}(x,y) \frac{e^{-jkr_p}}{r_p}\, dy\, dx$$

(A.3)

where $\mathbf{\Psi}(x,y)$ is the mode shape function of the panel evaluated at position $\boldsymbol{\sigma} = (x,y)$ on the panel surface and r_p is the distance of element $dy\, dx$ to the observer location $\mathbf{r} = (r, \theta, \phi)$ with elevation θ, and azimuth ϕ. The distance r_p is given by

$$r_p = |\mathbf{r}| - \frac{1}{k}\left[\left(\frac{\alpha x}{L_x}\right) + \left(\frac{\beta y}{L_y}\right)\right],$$

(A.4)

where

$$\alpha = kL_x \sin\theta \cos\phi$$

(A.5)

and

$$\beta = kL_y \sin\theta \sin\phi .$$

(A.6)

Replacing r_p in the denominator of Equation (A.3) by $|\mathbf{r}|$ gives negligible error in the result and enables evaluation of this transfer function over the total area of the panel as (Wallace, 1972; Snyder and Tanaka, 1993*b*)

$$z_{m,n}(\mathbf{r}) = -\frac{\rho\omega^2 e^{-jk|\mathbf{r}|}}{2\pi|\mathbf{r}|} \frac{L_x L_y}{mn\pi^2} \left[\frac{(-1)^m e^{j\alpha}-1}{\left(\frac{\alpha}{m\pi}\right)^2 - 1} \right]\left[\frac{(-1)^n e^{j\beta}-1}{\left(\frac{\beta}{n\pi}\right)^2 - 1} \right].$$

(A.7)

In the case of the perforated panel, in order to perform the integration over the area of the solid part of the panel the transfer function needs to be evaluated over the total area of the panel and then have the contributions corresponding to each hole subtracted. Wallace's result (Equation (A.7)) cannot be used to determine these hole contributions; instead, it is necessary to evaluate the integral numerically over the range of values of x and y which describe the position of the holes on the panel. Thus, if the radiation transfer function vector for a small region of the panel $x_1 \le x \le x_2, y_1 \le y \le y_2$ is re-expressed as

$$z_{m,n}(\mathbf{r}) = -\frac{\rho\omega^2}{2\pi} \int_{x_1}^{x_2}\int_{y_1}^{y_2} \psi_{m,n}(x,y)\frac{e^{-jkr_p}}{|\mathbf{r}|}\,dy\,dx ,$$

(A.8)

then $z(\mathbf{r})$ can be found analytically as

$$z_{m,n}(\mathbf{r}) = -\rho\omega^2 \frac{e^{-jk|\mathbf{r}|}}{2\pi|\mathbf{r}|} \frac{1}{(\beta_y^2 + d_y^2)(\alpha_x^2 + d_x^2)}$$
$$\times \left[\left(\beta_y\cos(d_y y_1) + d_y\sin(d_y y_1)\right)e^{\beta_y y_1} - \left(\beta_y\cos(d_y y_2) + d_y\sin(d_y y_2)\right)e^{\beta_y y_2} \right]$$
$$\times \left[\left(\alpha_x\cos(d_x x_1) + d_x\sin(d_x x_1)\right)e^{\alpha_x x_1} - \left(\alpha_x\cos(d_x x_2) + d_x\sin(d_x x_2)\right)e^{\alpha_x x_2} \right],$$

(A.9)

with the coefficients;

$$d_x = \frac{m\pi}{L_x},$$ (A.10)

$$d_y = \frac{n\pi}{L_y},$$ (A.11)

$$\alpha_x = j\frac{\alpha}{L_x}$$ (A.12)

and

$$\beta_y = j\frac{\beta}{L_y}.$$ (A.13)

REFERENCES

Akima, H. (1978) "A method of bivariate interpolation and smooth surface fitting for irregularly distributed data points", *ACM Transactions on Mathematical Software*, **4**, 148-159.

Angevine, O.L. (1981) "Active acoustic attenuation of electric transformer noise", *Proceedings InterNoise 81*, 303-306.

Angevine, O.L. (1990) "Active cancellation of the hum of a simulated electric transformer", *Proceedings InterNoise 90*, 789-792.

Angevine, O.L. (1991) "Walk-away measurements of transformer hum", *Proceedings InterNoise 91*, 325-328.

Angevine, O.L. (1992) "Active cancellation of the hum of large electric transformers", *Proceedings InterNoise 92*, Toronto, 313-316.

Angevine, O.L. (1994) "The prediction of transformer noise", *Sound and Vibration*, October, 16-18.

References

Baumann, D.C. and Greiner, R.A. (1992) "Number of error microphones for multi-modal cancellation", *Proceedings of InterNoise 92*, 345-348.

Bailey, R. and Hicks, R. (1960) "Behaviour of perforated plates under plane stress", *Journal of Mechanical Engineering Science*, **2**, 143-161.

Berge, T., Pettersen, O.Kr.O. and Sϕrsdal, S. (1987) "Active noise cancellation of transformer noise", *Proceedings InterNoise 87*, 537-540.

Berge, T., Pettersen, O.Kr.O. and Sϕrsdal, S. (1988) "Active cancellation of transformer noise: field measurements", *Applied Acoustics*, **23**, 309-320.

Bolton, J.S., Gardner, B.K. and Beauvilain, T.A. (1995) "Sound cancellation by the use of secondary multipoles", *Journal of the Acoustical Society of America,* **98**(4), 2343-2362.

Borgiotti, G.V. (1990) "The power radiated by a vibrating body in an acoustic fluid and its determination from boundary measurements", *Journal of the Acoustical Society of America*, **88**(4), 1884-1893.

Brennan, M.J., Elliott, S.J. and Pinnington, R.J. (1995) "Active control of fluid waves in a pipe", *Proceedings of Active 95*, Newport Beach, USA, 849-860.

References

Bullmore, A.J., Nelson, P.A. and Elliott, S.J. (1986) "Active minimisation of acoustic potential energy in harmonically excited cylindrical enclosed sound fields", *AIAA paper 86-1958*. 1-10.

Burdisso, R.A. and Fuller, C.R. (1994) "Design of active structural acoustic control systems by eigenproperty assignment", *Journal of the Acoustical Society of America*, **96**(3), 1582-1591.

Caldersmith, G. (1978) "Guitar as a reflex enclosure", *The Journal of the Acoustical Society of America*, **63**, 1566-1575.

Chaplin, B. (1980) "The cancellation of repetitive noise and vibration", *Proceedings of InterNoise 80*, Miami, USA, 699-702.

Charette, F., Guigou, C., Berry, A. and Plantier, G. (1994) "Asymmetric actuation and sensing of a beam using piezoelectric materials", *Journal of the Acoustical Society of America*, **96**(4), 2272-2283.

Charette, F., Guigou, C. and Berry, A. (1995) "Development of volume velocity sensors for plates using PVDF film", *Proceedings of Active 95*, Newport Beach, USA, 241-252.

Cheuk, K.P., Man, K.F., Ho, Y.C. and Tang, K.S. (1994) "Active noise control for power transformers", *Proceedings of InterNoise 94*, Yokohama, Japan, 1365-1368.

References

Clark, R.L., Burdisso, R.A. and Fuller, C.R. (1993) "Design approaches for shaping polyvinylidene fluoride sensors in active structural acoustic control (ASAC)", *Journal of Intelligent Material Systems and Structures*, **4**, 354-365.

Clark, R.L and Fuller, C.R. (1991) "Control of sound radiation with adaptive structures", *Journal of Intelligent Material Systems and Structures*, **2**, 431-452.

Clark, R.L. and Fuller, C.R. (1992) "Modal sensing of efficient acoustic radiators with polyvinylidene fluoride distributed sensors in active structural control approaches", *Journal of the Acoustical Society of America*, **91**(6), 3321-3329.

Craig, S.E., and Angevine, O.L. (1993) "Active control of hum from large power transformers - the real world", *Proceedings of Recent Advances in Active Control of Sound and Vibration*, Technomic Publishing Company Inc., Lancaster, Pennsylvania, USA, 279-290.

Collins, S.A., Padilla, C.E., Notestine, R.J. and von Flotow, A.H. (1992) "Design, manufacture, and application to space robotics of distributed piezoelectric film sensors", *Journal of Guidance, Control, and Dynamics*, **15**(2), 396-403.

Conover, W.B. (1956) "Fighting noise with noise", *Noise Control*, **92**, 78-82.

References

Cunefare, K.A. (1991) "The minimum multimodal radiation efficiency of baffled infinite beams", *Journal of the Acoustical Society of America*, **90**(5), 2521-2529.

Cunefare, K.A. and Currey, M.N. (1994) "On the exterior acoustic radiation modes of structures", *Journal of the Acoustical Society of America*, **96**(4), 2302-2312.

Cunefare, K.A. and Koopmann, G.H. (1991) "Global optimum active noise control: Surface and far-field effects", *Journal of the Acoustical Society of America*, **90**(1), 365-373.

Curtis, A.R.D., Nelson, P.A., Elliott, S.J. and Bullmore, A.J. (1987) "Active suppression of acoustic resonance", *Journal of the Acoustical Society of America*, **81**(3), 624-631.

David, A. and Elliott, S.J. (1994) "Numerical studies of actively generated quiet zones", *Applied Acoustics*, **41**, 63-79.

Duncan, J.P. and Upfold R.W. (1963) "Equivalent elastic properties of perforated bars and plates", *Journal Mechanical Engineering Science*, **5**, 53-65.

Eatwell, G. (1989) "Active control of automobile cabin noise", *Proceedings of InterNoise 89, Newport Beach*.

References

Elliott, S.J., Joseph, P., Nelson, P.A. and Johnson, M.E. (1991) "Power output minimization and power absorption in the active control of sound", *Journal of the Acoustical Society of America*, **90**(5), 2501-2512.

Elliott, S.J. and Johnson, M.E. (1993) "Radiation modes and the active control of sound power", *Journal of the Acoustical Society of America*, **94**(4), 2194-2204.

Ffowcs-Williams, J.E. (1984) "Anti-Sound", *Proceedings of the Royal Society of London*, **395**, 63-88.

Forskitt, M., Moon, J.R. and Brook, P.A. (1991) "Elastic properties of plates perforated by elliptical holes", *Applied Mathematical Modelling*, **15**, 182-190.

Fuller, C.R. and Brevart, B.J. (1995) "Active control of coupled wave propagation and associated power in fluid-filled elastic long pipes", *Proceedings of Active 95*, Newport Beach, USA, 3-14.

Fuller, C.R., Hansen, C.H. and Snyder, S.D. (1991a) "Active control of sound radiation from a vibrating rectangular panel by sound sources and vibration inputs: An experimental comparison", *Journal of Sound and Vibration*, **145**(2), 195-215.

References

Fuller, C.R., Hansen, C.H. and Snyder, S.D. (1991b) "Experiments on active control of sound radiation from a panel using a piezoceramic actuator", *Journal of Sound and Vibration*, **150**(2), 179-190.

Fuller, C.R. and Jones, J.D. (1987) "Experiments on reduction of propeller induced interior noise by active control of cylinder vibration", *Journal of Sound and Vibration*, **112**, 389-395.

Gosselin, B., Fortin, J.C. and L'Espérance, A. (1992) "Measurement of noise emitted by electrical substations - Part I: Measurement method", *Proceedings InterNoise 92*, Toronto, 771-775.

Gosselin, B., Fortin, J.C., L'Espérance, A. and Laroche, C. (1993) "A new approach for the measurement of noise emitted by electrical substations", *Noise Control Engineering Journal*, **41**(3), 357-363.

Guicking, D. (1990) "On the invention of active noise control by Paul Lueg", *Journal of the Acoustical Society of America*, **87**(5), 2251-2254.

Guigou, C., Charette, F. and Berry, A. (1994) "Active control of sound by minimisation of volume velocity on finite beam", *Proceedings of the Third International Congress on Air- and Structure-Bourne Sound and Vibration*, Montreal, Canada, 1507-1514.

References

Hesselmann, N. (1978) "Investigation of noise reduction on a 100KVA transformer tank by means of active methods", *Applied Acoustics*, **11**, 27-33.

Horvay, G. (1952) "Bending of honeycombs and of perforated plates", *Journal of Applied Mechanics (Transactions of the ASME Vol 74)*, **19**, 122-123.

IMSL (1991) *FORTRAN subroutines for mathematical applications*, 620-623. User's Manual, IMSL, Houston, Texas.

Johnson, M.E. and Elliott, S.J. (1995) "Active control of sound radiation using volume velocity cancellation", *Journal of the Acoustical Society of America*, **98**(4), 2174-2186.

Junger, M.C. and Feit, D. (1986) *Sound, Structures and Their Interaction*. MIT, Cambridge.

Kinsler, L.E. and Frey, A.R. (1962) *Fundamentals of Acoustics*. (John Wiley and Sons, Inc. N.Y.)

Kowalewski, J., Sakuta, A. and Colbert, M. (1992) "Environmental noise control of transmission facilities at Ontario Hydro", *Proceedings InterNoise 92*, Toronto, 779-782.

References

La Fontaine, R.F. and Shepherd, I.C. (1983) "An experimental study of broadband active attenuation for cancellation of random noise in ducts", *Journal of Sound and Vibration*, **91**, 351-362.

Lamb, H. (1931) *Dynamical Theory of Sound.* (Edward Arnold & Co., London, Second Edition.)

Laroche, C., Rouffet, J.M., Gosselin, B. and Fortin, J. (1992) "Measurement of noise emitted by electrical substations - Part II: Measurement system", *Proceedings InterNoise 92*, Toronto, 775-778.

Lee, C.-K., Chiang, W.-W. and O'Sullivan, T.C. (1991) "Piezoelectric modal sensor/actuator pairs for critical active damping vibration control", *Journal of the Acoustical Society of America*, **90**(1), 374-383.

Lee, C.-K. and Moon, F.C. (1990) "Modal sensors/actuators", *ASME Journal of Applied Mechanics*, **57**, 434-441.

Leitch, P.R. and Tokhi, M.O. (1987) "Active noise control systems", *IEE Proceedings*, **134** pt. A.

References

Meijers, P. (1967) *Doubly-Periodic Stress Distributions in Perforated Plates*. Ph.D. thesis, University of Delft, Holland.

Meirovitch, L. and Baruh, H. (1982) "Control of self-adjoint distributed-parameter systems", *Journal of Guidance, Control and Dynamics*, **5**(1), 60-66.

Meirovitch, L. and Baruh, H. (1985) "The implementation of modal filters for control of structures", *Journal of Guidance, Control and Dynamics*, **8**(6), 707-716.

Meirovitch, L. and Bennighof, J.K. (1986) "Modal control of travelling waves in flexible structures", *Journal of Sound and Vibration*, **111**(1), 131-144.

Meirovitch, L. and Thangjitham, S. (1990) "Active control of sound radiation pressure", *ASME Journal of Vibration and Acoustics*, **112**, 237-243.

McLoughlin, M., Hildebrand, S. and Hu, Z. (1994) "A novel active transformer quieting system", *Proceedings of InterNoise 94*, Yokohama, Japan, 1323-1326.

Morgan, D.R. (1991) "An adaptive modal-based active control system", *Journal of the Acoustical Society of America*, **89**(1), 248-256.

References

Morse, P.M. (1986) *Vibration and Sound*, Chapt. 6, 234-235. (American Institute of Physics, Inc. N.Y.)

Morse, P.M. and Ingard, K.U. (1968) *Theoretical Acoustics*. (McGraw-Hill Book Co., New York)

Naghshineh, K., Koopmann, G.H. and Belegundu, A.D. (1992) "Material tailoring of structures to achieve a minimum radiation condition", *Journal of the Acoustical Society of America*, **92**(2), 841-855.

Naghshineh, K. and Koopmann, G.H. (1993) "Active control of sound power using acoustic basis functions as surface velocity filters", *Journal of the Acoustical Society of America*, **93**(5), 2740-2752.

Naghshineh, K., Chen, W. and Koopmann, G.H. (1995) "Active control of sound power radiated from a cylindrical shell", *Proceedings of Active 95*, Newport Beach, USA, 323-334.

Nashif, P.J. and Sommerfeldt, S.D. (1992) "An active control strategy for minimizing the energy density in enclosures", *Proceedings of InterNoise 92*, Toronto, Canada, 357-362.

References

Nelson, P.A., Curtis, A.R.D., Elliot, S.J. and Bullmore, A.J. (1987) "The minimum power output of free field point sources and active control of sound", *Journal of Sound and Vibration*, **116**, 397-414.

O'Donnell, W.J. and Langer, B.F. (1962) "Design of perforated plates", *Journal of Engineering for Industry*, 307-320.

O'Donnell, W.J. (1973) "Effective elastic constants for the bending of thin perforated plates with triangular and square penetration patterns", *Journal of Engineering for Industry*, 121-128.

Olson, H.F. and May, E.G. (1953) "Electronic sound absorber", *Journal of the Acoustical Society of America*, **25**, 1130-1136.

Olson, H.F. (1956) "Electronic control of noise, vibration, and reverberation", *Journal of the Acoustical Society of America*, **28**(5), 966-972.

Pan, J. and Hansen, C.H. (1990) "Active control of total power flow along a beam", *Proceedings of the International Congress on Recent Developments in Air- and Structure-Bourne Sound and Vibration*, Auburn University, USA, 229-236.

References

Pan, J., Hansen, C.H. and Bies, D.A. (1992a) "Use of a perforated panel for the active control of sound radiated from vibrating structures: I. Low frequency analysis", *Journal of Sound and Vibration*, **156**, 349-359.

Pan, J., Snyder, S.D., Hansen, C.H. and Fuller, C.R. (1992b) "Active control of farfield sound radiated by a rectangular panel - a general analysis.", *The Journal of the Acoustical Society of America*, **90**, 2056-2066

Pan, X. and Hansen, C.H. (1995) "Active control of vibratory power flow along a semi-infinite plate", *Journal of Sound and Vibration*, accepted for publication.

Photiadis, D.M. (1990) "The relationship of singular value decomposition to wave-vector filtering in sound radiation problems", *Journal of the Acoustical Society of America*, **88**(2), 1152-1159.

Porowski, J. and O'Donnell, W.J. (1974) "Effective plastic constants for perforated materials", *Journal of Pressure Vessel Technology*, 234-241.

Pritchard, R.L. (1960) "Mutual acoustic impedance between radiators in an infinite rigid plane", *Journal of the Acoustical Society of America*, **32**, 730-737.

References

Rex, J. and Elliott, S.J. (1992) "The QWSIS - a new sensor for structural radiation control", *Proceedings of the 1ˢᵗ International Conference on Motion and Vibration Control*, Yokohama, Japan, 339-343.

Ross, C.F. (1978) "Experiments on the active control of transformer noise", *Journal of Sound and Vibration*, **61**(4), 473-480.

Royston, T.J. (1995) "Technical note: Shaped polyvinylidene fluoride (PVDF) sensors for intelligent measurement of plane-wave acoustic pressure in liquid-filled pipes", *Noise Control Engineering Journal*, **43**(1), 15-20.

Sakuta, A., Kowalewski, J. and Colbert, M. (1992) "Assessment technique for controlling transformer noise", *Proceedings InterNoise 92*, Toronto, 783-786.

Sampson, R.C. (1960) "Photoelastic analysis of stresses in perforated material subject to tension or bending", *Bettis Technical Review*, WAPD-BT-18.

Savard, J. (1992) "The application of multi-spectrum technology to transformer noise identification", *Proceedings InterNoise 92*, 787-791.

Schuller, W.M. (1982) "Transformer noise", *Noise Control Engineering*, **18**(3), 111-116.

References

Schultz, T.J. (1986) *Acoustical Uses for Perforated Metals: Principles and Applications*, (Industrial Perforators Association, Inc.).

Silcox, R.J., Fuller, C.R. and Lester, H.C. (1987) "Mechanisms of active control in cylindrical fuselage structures", *AIAA paper 87-2703*. 1-10.

Silcox, R.J., Fuller, C.R. and Lester, H.C. (1990) "Mechanisms of active control in cylindrical fuselage structures", *AIAA Journal*, **28**(8), 1397-1404.

Silcox, R.J., Lester, H.C. and Abler, S.B. (1989) "An evaluation of active noise control in a cylindrical shell", *Journal of Vibration, Acoustics, Stress and Reliability in Design*, **111**, 337-342

Simpson, M.A., Luong, T.M., Swinbanks, M.A., Russel, M.A. and Leventhall, H.G. (1989) "Full scale demonstration tests of cabin noise reduction using active noise control", *Proceedings of InterNoise 89*, Newport Beach, USA, 459-462.

Simpson, M.A., Luong, T.M., Fuller, C.R. and Jones, J.D. (1991) "Full-scale demonstration tests of cabin noise reduction using active vibration control", *AIAA Journal of Aircraft*, **28**(3), 208-215.

References

Slot, T and O'Donnell, W.J. (1971) "Effective elastic constants for thick perforated plates with square and triangular penetration patterns", *Journal of Engineering for Industry*, 935-942.

Snyder, S.D. and Hansen, C.H. (1990) "Mechanisms of active noise control using vibration sources", *Journal of Sound and Vibration*, **147**, 519-525.

Snyder, S.D., Hansen, C.H. and Tanaka, N. (1993) "Shaped vibration sensors for feedforward control of structural radiation", *Proceedings of the Second Conference on Recent Advances in Active Control of Sound and Vibration*, Blacksburg, USA, 177-188.

Snyder, S.D. and Tanaka, N. (1993*a*) "To absorb or not to absorb: Control source power output in active noise control systems", *Journal of the Acoustical Society of America*, **94**(1), 185-195.

Snyder, S.D. and Tanaka, N. (1993*b*) "On feedforward active control of sound and vibration using vibration error signals", *Journal of the Acoustical Society of America*, **94**(4), 2181-2193.

Snyder, S.D., Tanaka, N., Burgemeister K.A. and Hansen, C.H. (1995*a*) "Direct-sensing of global error criteria for active noise control", *Proceedings of Active 95*, Newport Beach, USA, 849-860.

References

Snyder, S.D., Tanaka, N. and Kikushima, Y. (1995*b*) "The use of optimally shaped piezo-electric film sensors in the active control of free field structural radiation, part 1: Feedforward control", *ASME Journal of Vibration and Acoustics*, **117**(3A), 311-322.

Soler, A.I. and Hill, W.S. (1977) "Effective bending properties for stress analysis of rectangular tubesheets", *Journal of Engineering for Power*, 365-370.

Sommerfeldt, S.D. and Nashif, P.J. (1994) "An adaptive filtered-*x* algorithm for energy-based active control", *Journal of the Acoustical Society of America*, **96**(1), 300-306.

Sommerfeldt, S.D. and Parkins, J.W. (1994) "An evaluation of active noise attenuation in rectangular enclosures", *Proceedings of InterNoise 94*, Yokohama, Japan, 1351-1356.

Sommerfeldt, S.D., Parkins, J.W. and Park, Y.C. (1995) "Global active noise control in rectangular enclosures", *Proceedings of Active 95*, Newport Beach, USA, 477-488.

Sugiki, Y., Sugiyama, T., Naganawa, A. and Owaki, M. (1995) "A study of noise barrier using the active noise control for electric power facilities", *Proceedings of Active 95*, Newport Beach, USA, 707-716.

References

Tanaka, N., Kikushima, Y. and Kuroda, M. (1992) "Power flow control of a thin plate", *Proceedings of the First International Conference on Motion and Vibration Control*, Yokohama, Japan, 56-61.

Teplitzky, A.M. (1995) "Electric utility noise abatement", *Proceedings of InterNoise 95*, Newport Beach, USA, 165-168.

Thomas, D.R., Nelson, P.A. and Elliott, S.J. (1993*a*) "Active control of the transmission of sound through a thin cylindrical shell, part I: The minimization of vibrational energy", *Journal of Sound and Vibration*, **167**(1), 91-111.

Thomas, D.R., Nelson, P.A. and Elliott, S.J. (1993*b*) "Active control of the transmission of sound through a thin cylindrical shell, part II: The minimization of acoustic potential energy", *Journal of Sound and Vibration*, **167**(1), 113-128.

Tohyama, M. and Suzuki, A. (1987) "Active power minimization of a sound source in a closed space", *Journal of Sound and Vibration*, **119**(3), 562-564.

Tzou, H.S., Zhong, J.P. and Natori, M. (1991) "Modal filtering of distributed shell sensors using orthogonal functions", *Proceedings of the Second Joint Japan/U.S. Conference on Adaptive Structures*, Nagoya, Japan, 755-766.

References

Wallace, C.E. (1972) "Radiation resistance of a rectangular panel", *Journal of the Acoustical Society of America*, **51**, 946-952.

Yannucci, D. (1979) "Feasibility study of an active system for transformer noise abatement", *United States Department of Energy Contract* EE-77-C-02-4376.

Zander, A.C. and Hansen C.H. (1993) "A comparison of error sensor strategies for the active control of duct noise", *Journal of the Acoustical Society of America*, **94**(2), 841-848.

Zander, A.C. (1994) "Influence of error sensor and control source configuration and type upon the performance of active noise control systems", *Ph.D. Thesis, University of Adelaide.*

PUBLICATIONS ORIGINATING FROM THESIS WORK

Burgemeister, K.A. and Hansen, C.H. (1993) "Use of a secondary perforated panel to actively control the sound radiated by a heavy structure", *Proceedings of The American Society of Mechanical Engineers Winter Annual Meeting*, Pamphlet 93-WA/NCA-2, New Orleans, Louisiana.

Burgemeister, K.A. and Hansen, C.H. (1993) "Transmission of sound through apertures", *Proceedings of the Australian Acoustical Society Annual Conference*, Glenelg, South Australia.

Hansen, C.H. and Burgemeister, K.A. (1994) "Use of perforated panels as an active noise control source", *Proceedings of the 127th Conference of the Acoustical Society of America*, Boston, Massachusetts.

Burgemeister, K.A. and Hansen, C.H. (1995) "Reduction of radiated sound by use of actively controlled perforated panels", *International Journal of Active Control*, **1**(1), 45-64.

Snyder, S.D., Tanaka, N., Burgemeister, K.A. and Hansen C.H. (1995) "Direct-sensing of global error criteria for active noise control", *Proceedings Active 95*, Newport Beach, USA, 849-860.

Publications originating from thesis work

Burgemeister, K.A., Snyder, S.D. and Hansen C.H. (1995) "Acoustic sensing of global error criteria", *Proceedings Institution of Engineers, Australia: Vibration and Noise Symposium*, Newcastle, Australia, 9-10.

Burgemeister, K.A. and Hansen C.H. (1996) "Calculating resonance frequencies of perforated panels", *Journal of Sound and Vibration*, accepted for publication.

Snyder, S.D. and Burgemeister, K.A. (1996) "Performance enhancement of structural/acoustic active control systems via acoustic error signal decomposition", *Proceedings of Internoise'96*, Liverpool, U.K., in press.